TECHNISCHE UNIVERSITÄT WIEN
Vienna University of Technology

GEOWISSENSCHAFTLICHE MITTEILUNGEN

Heft Nr. 98, 2016

Determination of path delays in the atmosphere for geodetic VLBI by means of ray-tracing

Armin Hofmeister

Veröffentlichung des Departments für Geodäsie und Geoinformation
ISSN 1811-8380

Schriftenreihe der Studienrichtung VERMESSUNG UND GEOINFORMATION

TECHNISCHE
UNIVERSITÄT
WIEN
Vienna University of Technology

GEOWISSENSCHAFTLICHE MITTEILUNGEN

Heft Nr. 98, 2016

Determination of path delays in the atmosphere for geodetic VLBI by means of ray-tracing

Armin Hofmeister

Veröffentlichung des Departments für Geodäsie und Geoinformation
ISSN 1811-8380

Schriftenreihe der Studienrichtung VERMESSUNG UND GEOINFORMATION

2016
Published by the Department of Geodesy and Geoinformation
of the Vienna University of Technology
Gußhausstraße 27-29
1040 Vienna, Austria

Responsible for this issue: Univ.-Prof. Dipl.-Ing. Dr.techn. Johannes Böhm
Printed by: Grafisches Zentrum HTU GmbH

The digital version of the full document with colored figures is available online at:
http://katalog.ub.tuwien.ac.at/AC13248753
or
http://resolver.obvsg.at/urn:nbn:at:at-ubtuw:1-3444

Die Kosten für den Druck wurden vom Department für Geodäsie und Geoinformation übernommen.

Diese Arbeit wurde an der Fakultät für Mathematik und Geoinformation der Technischen Universität Wien zur Erlangung des akademischen Grades eines Doktors der technischen Wissenschaften eingereicht.

Begutachter:

Univ.-Prof. Dipl.-Ing. Dr.techn. Johannes Böhm
Department für Geodäsie und Geoinformation der Technischen Universität Wien
Gußhausstraße 27-29, 1040 Wien, Österreich

Assoc. Prof. Dipl.-Ing. Dr.techn. Thomas Hobiger
Department of Earth and Space Sciences of the Chalmers University of Technology
Observatorievägen 90, Råö SE-439 92 Onsala, Schweden

Tag der mündlichen Prüfung: 05.07.2016

Auflage: 20 Stück

ISSN 1811-8380

Prüfungssenat:

Ao. Univ.-Prof. Dipl.-Ing. Dr.techn. Robert Weber
Technische Universität Wien

Univ.-Prof. Dipl.-Ing. Dr.techn. Johannes Böhm
Technische Universität Wien

Assoc. Prof. Dipl.-Ing. Dr.techn. Thomas Hobiger
Chalmers University of Technology

Acknowledgements

First of all I would like to thank my supervisor Johannes Böhm for his great support of my work not only with respect to the one presented here, but basically throughout my whole academic career from the bachelor thesis across the master thesis to the present doctoral thesis. I am grateful that he always finds time for fruitful scientific discussions and that he is never short on helpful advices.

I also want to acknowledge Assoc. Prof. Dipl.-Ing. Dr.techn. Thomas Hobiger for providing highly appreciated feedback and reviewing my thesis.

Furthermore I would like to thank my family for the continuous support throughout the years. It is this support that gave me the chance to reach my goals.

I would also like to say a big thank you to all of my colleagues at the research group Advanced Geodesy for creating such a nice and familiar working atmosphere for everybody. Moreover I would like to particularly thank all those colleagues, who gave me valuable advices for my work throughout the years. In this respect I want to mention especially my office mates.

I am very grateful to the Austrian Science Fund (FWF) for the support of my work within project "Ray-traced Delays in der Atmosphäre für geodätische VLBI" (RADIATE VLBI) (P25320). Furthermore I would like to thank the European Centre for Medium-Range Weather Forecasts (ECMWF) for establishing and providing the meteorological data in form of the provided Numerical Weather Models (NWM) that build the very basement of this research. I also appreciate the International VLBI Service for Geodesy and Astrometry (IVS) for planning and carrying out the VLBI sessions and for providing the observational data, which have been used within this work.

Abstract

Observations of space geodetic techniques like the Very Long Baseline Interferometry (VLBI) are influenced by atmospheric effects that act on the signal path and the signal propagation. In order to be able to accurately analyse the observed data, it is necessary to reduce these effects in form of slant path delays from the observations. Today the influences of the atmosphere, i.e. of the troposphere as this part is the main unknown contributor with respect to VLBI observations, are a major error source in the analysis of space geodetic techniques. This fact is the fundamental motivation and incentive for this thesis. The current standard analysis approach of VLBI observations uses an indirect determination of the tropospheric slant path delays through a priori and estimated zenith delays and mapping functions. The presented research follows a different approach. The utilization of the ray-tracing technique, known from many different scientific fields, is a promising approach for the direct and accurate determination of the tropospheric slant path delays. The set goal is the improvement of the VLBI analysis by directly determining the tropospheric slant path delays using ray-tracing and applying them to the analysis. The important difference to the common correction approach is the utilization of true meteorological data along the actual signal path in order to calculate the tropospheric slant path delay. Furthermore both the actual signal path and the slant delay are determined together using the ray-tracing method and the meteorological parameters, which leads to a complete self-contained solution for the determination of the tropospheric slant path delays.

As part of the thesis a fast and accurate ray-tracing program called RADIATE for the operational determination of tropospheric slant path delays has been developed. Research on the optimal operational program design is carried out leading to the following conclusion for operational ray-tracing: An utilization of vertically high resolved meteorological profiles, applied to the fast piecewise-linear (PWL) ray-tracing approach, which is a simplified realization of the strict signal propagation determination in the atmosphere, delivers accurate tropospheric slant path delays for the application to the VLBI analysis.

The developed ray-tracing program RADIATE is validated in a comparison against ray-tracing packages of other institutions, which reveals a fully positive performance since the tropospheric slant total delays derived using the mapping factors agree very well with those from the other ray-tracing programs. At an elevation of 5° the individual differences of the RADIATE PWL results to those of the other programs, which use the same Numerical Weather Model (NWM) data input, are on average below 1.0 cm at station TSUKUB32 and below 2.4 cm at station WETTZELL. In a separate test zenith delays from program RADIATE are compared to estimates of a common VLBI analysis using the data set of the Continuous VLBI Campaign 2011 (CONT11) of the International VLBI Service for Geodesy and Astrometry (IVS). A good agreement is revealed also in this domain. The standard deviation of the differences regarding the zenith total delay is at almost all investigated stations below 1.5 cm, the one regarding the zenith hydrostatic delay is always

below 0.5 cm and the one regarding the zenith wet delay is at almost all stations below 1.5 cm.

Moreover the impact of the ray-traced delays from program RADIATE on the VLBI analysis is investigated. For this task ray-traced delays for all observations within the analysis are determined and applied to the analysis, which covers 16.5 years of observation data between January 1999 and the end of June 2015, i.e. 2 340 sessions. The impact of the ray-traced delays on the analysis results is investigated with respect to the baseline length repeatability (*BLR*) and the Terrestrial Reference Frame (TRF) solution. The results of the *BLR* reveal that the application of the ray-traced delays to the analysis leads to equal results on average like a standard VLBI analysis if both analysis parameterizations include zenith wet delay and tropospheric gradient estimation. However, 55.9% of the baselines benefit from the application of the ray-traced delays. The differences in the *BLR* are at the sub-mm level. The impact changes significantly if no tropospheric gradients are estimated within the analysis. Then the solution with applied ray-traced delays is significantly better than the one without applied ray-traced delays since the *BLR* of 90.6% of the baselines is improved. This assessment result is important with respect to two aspects. On the one hand the correctness of the ray-tracing results of program RADIATE is confirmed due to the homogeneous improvement of almost all baselines. On the other hand this means that the implicit tropospheric gradient information of the ray-traced delays is correctly introduced to the analysis. On average the *BLR* is improved by 1.0 mm due to the application of the ray-traced delays. The mean relative improvement compared to the case of not applying the ray-traced delays is 9.3%. In terms of the TRF solutions there is almost no impact if the ray-traced delays are applied in case the tropospheric gradients are estimated within the analysis. Only a minor average uplift of the stations of 0.7 mm is seen if a set of reliable stations is investigated. Horizontal station displacements reach at the maximum only 1.1 mm. The scale of the frame is affected by only 0.1 ppb. Thus, the frame stays almost the same. If no tropospheric gradients are estimated within the analysis, the application of the ray-traced delays has a more evident impact on the station heights and horizontal positions. On average the stations are uplifted by 1.1 mm and displaced horizontally by 2.7 mm if a set of reliable stations is investigated. Especially the impact on the horizontal station positions shows that the implicit tropospheric gradient information of the ray-traced delays is correctly introduced to the analysis. Again the scale of the frame is affected by only 0.1 ppb and in general the application of the ray-traced delays does not significantly alter the frame.

A comparison of the *BLR* results from applying RADIATE ray-traced delays or those from the National Aeronautics and Space Administration Goddard Space Flight Center (NASA GSFC) to the VLBI analysis of 2 085 sessions between January 2000 and the end of January 2015 reveals that the RADIATE delays have a slightly better performance. In case tropospheric gradients are estimated within the analysis, there is on average no difference in the *BLR* results, but the RADIATE ray-traced delays perform better for 51.3% of the baselines at sub-mm level. If no gradients are estimated, the RADIATE ray-traced delays lead to better *BLR* by 0.2 mm on average. They perform better for 63.0% of the baselines. A mean relative improvement of 1.5% compared to the NASA GSFC ray-traced delays is seen. The performance differences between the ray-traced delays from RADIATE and from NASA GSFC may mainly come from the different utilized NWM.

Kurzfassung

Bestimmung von Laufzeitverzögerungen in der Atmosphäre für geodätische VLBI mittels Strahlverfolgung

Die Beobachtungen weltraumgeodätischer Verfahren wie z.B. der Very Long Baseline Interferometry (VLBI) werden durch atmosphärische Effekte, die auf den Signalweg und die -ausbreitung wirken, beeinflusst. Um die Beobachtungsdaten korrekt auswerten zu können, müssen diese Effekte in Form von Laufzeitverzögerungen korrigiert werden. Heutzutage sind die Einflüsse der Atmosphäre bzw. genauer gesagt jener der Troposphäre, da diese den Hauptanteil der unbekannten atmosphärischen Einflüsse darstellt, eine der Hauptfehlerquellen bei VLBI-Auswertungen. Diese Tatsache liefert zugleich die grundlegende Motivation als auch die Ausgangslage für die vorliegende wissenschaftliche Arbeit. Der derzeitige Standardansatz zur Auswertung von VLBI-Beobachtungen verwendet eine indirekte Bestimmungsmethode der troposphärischen Laufzeitverzögerungen mit Hilfe von a priori und geschätzten Zenitlaufzeitverzögerungen und Projektionsfunktionen. Die vorliegende Arbeit verfolgt jedoch einen anderen Ansatz. Die Verwendung der Methode der Strahlverfolgung, bekannt aus verschiedenen Wissenschaftsgebieten, ist ein vielversprechender Ansatz für die direkte und genaue Bestimmung der troposphärischen Laufzeitverzögerungen. Zielsetzung ist die Verbesserung der VLBI-Auswertung mit Hilfe der direkten Bestimmung der troposphärischen Laufzeitverzögerungen mittels Strahlverfolgung und deren Anwendung in der Auswertung. Der essentielle Unterschied zum Standardansatz der Korrektur ist die Verwendung von echten meteorologischen Daten entlang des eigentlichen Signalpfades, um die troposphärische Laufzeitverzögerung zu berechnen. Weiters werden der tatsächliche Signalpfad und die Laufzeitverzögerung gemeinsam unter Anwendung der Methode der Strahlverfolgung und der meteorologischen Parameter bestimmt. Dies führt zu einer in sich geschlossenen Lösung für die Bestimmung der troposphärischen Laufzeitverzögerungen.

Als Teil der Dissertation wurde ein schnelles und genaues Strahlverfolgungsprogramm namens RADIATE für die operationelle Bestimmung von troposphärischen Laufzeitverzögerungen erstellt. Untersuchungen zum optimalen operationellen Programmdesign werden durchgeführt mit folgendem Ergebnis für die operationelle Strahlverfolgung: Die Verwendung vertikal hochaufgelöster meteorologischer Profile, angewandt auf den schnellen stückweise linearen (PWL) Strahlverfolgungsansatz, der seinerseits eine Vereinfachung der strikten Realisierung der Signalausbreitung in der Atmosphäre darstellt, liefert genaue troposphärische Laufzeitverzögerungen für die Anwendung in der VLBI-Auswertung.

Die Validierung des entwickelten Strahlverfolgungsprogramms RADIATE erfolgt mittels Vergleich gegen Softwarepakete von anderen Institutionen. Als Ergebnis zeigt sich ein gutes Abschneiden des Programms, da die totalen troposphärischen Laufzeitverzögerungen, berechnet

aus den Projektionsfaktoren, sehr gut mit jenen der anderen Programme übereinstimmen. Bei einem Elevationswinkel von 5° betragen die einzelnen Differenzen der RADIATE PWL-Resultate zu jenen der anderen Programme, die das gleiche numerische Wettermodell (NWM) verwenden, im Mittel weniger als 1,0 cm an der Station TSUKUB32 und weniger als 2,4 cm an der Station WETTZELL. In einem weiteren separaten Test werden die Zenitlaufzeitverzögerungen aus dem Programm RADIATE mit jenen verglichen, die in einer typischen VLBI-Auswertung bestimmt wurden. Dafür wird der Beobachtungsdatensatz der Continuous VLBI Campaign 2011 (CONT11) des International VLBI Service for Geodesy and Astrometry (IVS) verwendet. Auch auf diesem Gebiet kann eine gute Übereinstimmung erzielt werden. Die Standardabweichung der Differenzen beträgt in Bezug auf die totale Zenitlaufzeitverzögerung bei fast allen untersuchten Stationen weniger als 1,5 cm, jene in Bezug auf die hydrostatische Zenitlaufzeitverzögerung stets weniger als 0,5 cm und jene in Bezug auf die feuchte Zenitlaufzeitverzögerung bei fast allen Stationen weniger als 1,5 cm.

Darüber hinaus wird der Einfluss der mittels Strahlverfolgung bestimmten troposphärischen Laufzeitverzögerungen des Programms RADIATE auf die VLBI-Auswertung untersucht. Zu diesem Zweck werden mittels Strahlverfolgung die Laufzeitverzögerungen für alle Beobachtungen der Analyse bestimmt und in der Auswertung angebracht. Die Analyse umfasst Beobachtungsdaten von 16,5 Jahren zwischen Jänner 1999 und Ende Juni 2015, d.h. insgesamt 2 340 Sessions. Der Einfluss der mittels Strahlverfolgung bestimmten Laufzeitverzögerungen auf die Auswertung wird auf die Ergebnisse der Wiederholbarkeit der Basislinienlänge (BLR) und auf die Lösung für den terrestrischen Referenzrahmen (TRF) bezogen. Die BLR-Ergebnisse zeigen, dass die Anwendung der mittels Strahlverfolgung bestimmten Laufzeitverzögerungen in der Auswertung im Mittel zu den gleichen Ergebnissen führt wie eine Standardauswertung, wenn beide Auswertungsparameterisierungen die Schätzungen der feuchten Zenitlaufzeitverzögerung und der troposphärischen Gradienten beinhalten. Dennoch zeigt sich, dass immerhin 55,9% der Basislinien von der Verwendung der mittels Strahlverfolgung bestimmten Laufzeitverzögerungen profitieren. Die Unterschiede liegen in diesem Vergleich im Bereich von Sub-mm. Der Einfluss ändert sich wesentlich, wenn keine troposphärischen Gradienten innerhalb der Auwertung geschätzt werden. Dann hat jene Auswertung, die die mittels Strahlverfolgung bestimmten Laufzeitverzögerungen verwendet, signifikant bessere BLR-Ergebnisse als jene Auswertung ohne die mittels Strahlverfolgung bestimmten Laufzeitverzögerungen, da 90,6% der Basislinien verbessert werden. Diese Feststellung ist hinsichtlich zweier Aspekter wertvoll. Zum einen wird dadurch die Korrektheit der Strahlverfolgungsergebnisse des Programms RADIATE aufgrund der homogenen Verbesserung fast aller Basislinien bestätigt. Zum anderen bedeutet dies, dass die Information über die troposphärischen Gradienten, die implizit in den mittels Strahlverfolgung bestimmten Laufzeitverzögerungen enthalten ist, richtig in der Auswertung angebracht wird. Im Mittel wird die BLR um 1,0 mm durch die Anwendung der mittels Strahlverfolgung bestimmten Laufzeitverzögerungen verbessert. Die mittlere relative Verbesserung verglichen mit dem Verzicht auf deren Anwendung beträgt 9,3%. In Bezug auf die TRF-Lösungen zeigt sich, dass es fast keine Auswirkung gibt, wenn die mittels Strahlverfolgung bestimmten Laufzeitverzögerungen im Fall der Schätzung

der troposphärischen Gradienten in der Auswertung angewandt werden. Lediglich eine im Mittel geringfügige Hebung der Stationen um 0,7 mm kann beobachtet werden in Bezug auf eine Auswahl an zuverlässigen Stationen. Die horizontalen Stationsverschiebungen betragen maximal 1,1 mm. Der Maßstab des Rahmens wird nur um 0,1 ppb beeinflusst. Somit kann gesagt werden, dass der Rahmen annähernd unverändert bleibt. Werden keine troposphärischen Gradienten in der Auswertung geschätzt, dann zeigt die Anwendung der mittels Strahlverfolgung bestimmten Laufzeitverzögerungen einen klareren Einfluss auf die Stationshöhen und die horizontalen Stationspositionen. Im Mittel werden die Stationen um 1,1 mm gehoben und um 2,7 mm horizontal verschoben, bezugnehmend auf eine Auswahl an zuverlässigen Stationen. Besonders der Einfluss auf die horizontalen Stationspositionen zeigt, dass die Information über die troposphärischen Gradienten, die implizit in den mittels Strahlverfolgung bestimmten Laufzeitverzögerungen enthalten ist, richtig in der Auswertung angebracht wird. Wiederum wird der Maßstab des Rahmens nur um 0,1 ppb beeinflusst und es zeigt sich allgemein, dass die Anwendung der mittels Strahlverfolgung bestimmten Laufzeitverzögerungen den Rahmen nicht signifkant verändert.

Ein Vergleich der *BLR*-Ergebnisse, wenn die mittels Strahlverfolgung bestimmten Laufzeitverzögerungen vom Programm RADIATE oder jene vom National Aeronautics and Space Administration Goddard Space Flight Center (NASA GSFC) in der VLBI-Auswertung von 2 085 Sessions zwischen Jänner 2000 und Ende Jänner 2015 angewandt werden, zeigt, dass die mittels Strahlverfolgung bestimmten Laufzeitverzögerungen vom Programm RADIATE leicht bessere Resultate erzielen. Werden troposphärische Gradienten innerhalb der Auswertung geschätzt, so besteht zwar im Mittel kein Unterschied in den *BLR*-Ergebnissen, aber die mittels Strahlverfolgung bestimmten Laufzeitverzögerungen vom Programm RADIATE sind im Sub-mm Bereich besser für 51,3% der Basislinien. Werden keine troposphärischen Gradienten innerhalb der Auswertung geschätzt, so führt die Anwendung der mittels Strahlverfolgung bestimmten Laufzeitverzögerungen vom Programm RADIATE zu im Mittel um 0,2 mm besseren *BLR*-Ergebnissen. Sie sind insgesamt auch besser für 63,0% der Basislinien. Die mittlere relative Verbesserung beträgt 1,5% verglichen mit dem *BLR*-Ergebnis unter Verwendung der mittels Strahlverfolgung bestimmten Laufzeitverzögerungen vom NASA GSFC. Die Unterschiede zwischen den Leistungen der mittels Strahlverfolgung bestimmten Laufzeitverzögerungen vom Programm RADIATE und vom NASA GSFC kommen vermutlich hauptsächlich davon, dass unterschiedliche NWM zu deren Bestimmung verwendet werden.

Contents

Chapter 1

Introduction

The atmosphere plays an important role in many different kind of perspectives. In the first place of course, it actually makes life on Earth possible. Besides this fundamental fact, the atmosphere is naturally also a crucial subject in Earth sciences. In case of geodesy the system Earth is a primary subject of investigation. Thus, also the atmosphere is of particular interest. On the one hand the atmosphere serves here as direct object of research, e.g. in case of the study of atmospheric tides. On the other hand it is also indirectly part of the research, e.g. in case of the space geodetic techniques like the Very Long Baseline Interferometry (VLBI) and the Global Navigation Satellite Systems (GNSS). For these methods the atmosphere is in general not the primary subject of investigation as it is more the Earth itself that is monitored. Nevertheless the atmosphere contributes to VLBI and GNSS as the atmosphere is in the first place a disturbing influence for these Earth observing methods. The analysis of these techniques would be a lot easier and would lead to more accurate results, if the atmosphere was replaced by vacuum. Fortunately for mankind this is not the case. Thus, geodesists dealing with space geodetic techniques have to overcome the negative influences the atmosphere exerts on their observations. Therefore the assessment of the influence of the atmosphere in size through the determination of so-called path delays is of major importance in the field of space geodetic techniques like VLBI.

1.1 The atmosphere as important factor in space geodetic techniques like VLBI

In case of VLBI, the basic principle of the technique is degraded by the influences of the atmosphere, in particular of the so-called neutral atmosphere. The radio signals coming from quasars in outer space are received with radio telescopes installed on the surface of the Earth. Thus, the signals travel through the whole atmosphere until they are received. So, the signals coming from space are affected with respect to travel speed and path on their way through the atmosphere. These effects need to be taken into account in order to determine the VLBI target parameters correctly. It is therefore important to address the atmospheric influences in form of

so-called path delays as accurately as possible, because the accuracy of the VLBI results is directly related to the quality of the atmospheric corrections.

1.2 Motivation for and aims of the presented research

Directly from the previously described importance of the atmosphere for space geodetic techniques, here specifically investigated for the VLBI, the main goal of this work evolves.

Currently the atmospheric influence is still a major error source in VLBI. With respect to the ambitious goal of the upcoming new VLBI Global Observing System (VGOS), which aims at station position accuracies of 1 mm (Petrachenko et al. 2009), the need of an accurate determination of the atmospheric influences is even increased.

Therefore the primary target of this work is the determination of the impact of the atmosphere on the VLBI observations with high accuracy. For this task the ray-tracing approach is chosen and will be investigated in order to enhance the common way of data analysis in the field of VLBI since ray-tracing can utilize real meteorological data for the determination of the impact of the atmosphere on each individual observation by calculation of so-called ray-traced path delays.

In standard VLBI analysis the impact of the atmosphere is considered by applying a priori zenith delay models and estimating residual zenith delays by the use of mapping functions in order to be able to determine the slant delays of individual observations according to their elevation angles. Compared to that, ray-traced delays serve as a promising alternative way of determining the contribution of the atmosphere to the VLBI observations since real meteorological data are used for a direct estimation of the slant delays without the additional step of mapping functions. Thus, the VLBI analysis could be enhanced by applying ray-traced delays instead or additionally to the common modelling approach of the atmospheric influences.

The general topic of this work will therefore focus on the setup of an operational ray-tracing service for VLBI observations as realized through the program RADIATE, whose name stands for Ray-traced Delays in the Atmosphere. This ambitious target leads to different problems, when leaving the theoretical level towards the practical implementation. Ray-tracing is a quite demanding approach, because it has to be carried out for each observation separately. Furthermore it is an iterative technique. Thus, processing time is an important factor, which is on the other hand dependent on the desired accuracy of the results. So, with respect to the target of being able to deliver highly accurate ray-traced delays for operational purposes in an appropriate time, certain agreements and simplifications have to be made. Therefore this work focuses on one side on the theoretical aspects of ray-tracing, but on the other side also on practical problems with respect to the implementation, which will be documented by various investigations in order to find the best way of setting up an operational ray-tracing service for VLBI observations with the target of enhancing VLBI analysis.

1.3 Outline of the thesis

This work consists of 7 chapters and 2 appendices. In the first chapter the aim, motivation and content of the work is described.

In Chapter 2 an introduction to the space geodetic technique VLBI is given. The general principle is discussed as well as the practical observation technique. Also the analysis of the observations and the different estimated target parameters like the terrestrial and celestial reference frames (TRF and CRF) and the Earth Orientation Parameters (EOP) are described and explained.

Chapter 3 presents the theoretical background of the atmospheric effects on the observations. The focus is set on the influences of the neutral atmosphere on signals in the microwave frequency range in order to establish the theoretical prerequisites for ray-tracing of VLBI observations. A general description of the atmosphere and its structure is given. Subsequently, the wave propagation in the atmosphere is depicted. Based on these findings the theoretical calculation of the neutral atmosphere-induced path delay is described with respect to observations in the microwave frequency range. Finally different concepts for the practical determination of the slant path delay are shown.

In Chapter 4 the concept of ray-tracing for the estimation of the neutral atmosphere-induced path delays of geodetic VLBI observations is described in detail. At first the theoretical background of ray-tracing is presented, containing also the description of the implemented ray-tracing approaches within program RADIATE. Also the general structure of the ray-tracing program RADIATE is explained. The important main parts of the program are depicted in separate sections of the chapter , e.g. the vertical interpolation of the meteorological data.

Chapter 5 provides different investigations for the establishment of an optimal ray-tracing strategy with respect to operational application. At first the different possible meteorological data input sources are discussed in order to be able to establish the subsequently made appropriate choice for the practical application in program RADIATE. Following this, an investigation of the impact of the horizontal resolution of the Numerical Weather Model (NWM) is carried out since this may on the one hand be a key factor for the accuracy of the calculated ray-traced delays and the further resulting VLBI analysis results, but on the other hand it is certainly a major impact on the amount of data that needs to be (pre-)processed within the ray-tracing application. The influence of the horizontal resolution of the NWM is investigated in two ways. Firstly, the impact directly on the ray-traced delays is examined. Secondly, the influence on the VLBI analysis results is enquired, which should be the fundamental reason for a decision since the ray-traced delays are mainly generated for the application to the VLBI analysis. Moreover an investigation on the optimal ray-tracing approach is carried out based on the accuracies, advantages and disadvantages of different possible methods. Thus, the fundamental decision between a three-dimensional (3D) or a two-dimensional (2D) method is examined and further research is done with respect to the different implemented 2D ray-tracing approaches in program RADIATE for the final decision of the most suitable method for an operational ray-tracing service. In continuation of the search for the best suitable way of conduct for an optimal operational ray-tracing service, also the inner

accuracy of the ray-traced delay[1] needs to be considered, which is connected to and controlled by the accuracy with which the original outgoing elevation angle of the observation is reached by iteration of the ray path. Thus, a certain accuracy for the ray-traced outgoing elevation angle needs to be set. Therefore this setting of the appropriate accuracy of the ray-traced outgoing elevation angle for a specific desired inner accuracy of the ray-traced delay is investigated in a separate section of this chapter. With all these individual examinations an operational ray-tracing service can be established with the design of an optimal strategy with respect to ray-tracing and VLBI analysis result accuracy based on considering aspects of the amount of processing loads or processing times.

Chapter 6 presents different investigations of the ray-traced delay results from program RADIATE as well as research on their application to the VLBI analysis, i.e. their contribution and impact is examined for practical purposes.

As a very important first step the ray-tracing program must be validated to ensure proper quality of the delays. Thus, the results of program RADIATE are compared to those of other ray-tracing tools. In a separate section different samples of ray-traced delay results from program RADIATE for simulated VLBI observations are presented and investigated. In a next step the zenith delays in the total, hydrostatic and wet domains, which are also part of the ray-tracing solution, are compared to the estimated zenith delays from a normal VLBI analysis solution without applied ray-traced delays in order to verify the agreement and the differences. Furthermore it is of course fundamental to examine the impact of the ray-traced delays from program RADIATE on the VLBI analysis since this is the main target and purpose of the ray-tracing program and its results. Therefore the impacts on the baseline length repeatability (BLR) as well as on the Terrestrial Reference Frame (TRF) are investigated. Analysis solutions with applied ray-traced delays are compared against those without the application of ray-traced delays. These investigations are based on the analysis of VLBI sessions, which cover a long time span, in order to have a reliable assessment. Another important section in this chapter investigates the performance of the ray-traced delays from program RADIATE in comparison to the performance of the National Aeronautics and Space Administration Goddard Space Flight Center (NASA GSFC) ray-traced delays in terms of their application to the VLBI analysis. Therefore the BLR results of different VLBI analysis solutions are compared, where always one compared solution uses RADIATE ray-traced delays and the other solution uses ray-traced delays from NASA GSFC.

Chapter 7 gives a summary of the thesis and presents important conclusions as well as an outlook.

Appendix A contains additional tables, which deliver further or more detailed information than covered in the main matter of this work. In this part a closer look on the structures and implemented subroutines of program RADIATE and the auxiliary program Epochs_RADIATE is given.

[1] With inner accuracy of the ray-traced delay the accuracy of the delay within a specific ray-tracing approach is meant, not considering the overall accuracy of the approach itself.

Appendix B provides additional figures to the topics of the main part of the thesis. Thus, further or more detailed information on e.g. individual results of different investigations is presented in this part.

Chapter 2

Geodetic Very Long Baseline Interferometry

Since ray-traced delays for the application in VLBI analysis are determined and investigated, geodetic VLBI observations build the fundamental basis for the research of this work. Therefore this chapter should give a general overview of the principle of the VLBI technique as well as an insight to the practical data acquisition and target parameter estimation always with the focus on the geodetic application of VLBI. The main reference for this chapter is Schuh and Böhm (2013). If not stated differently the following information is taken from this reference.

2.1 General principle

The stations 1 and 2, i.e. radio telescopes or antennas, observe, as depicted in Figure 2.1, the same extragalactic source, e.g. a quasar, at the same time and receive the radiation in the microwave spectrum emitted from the source. Since these sources are extremely far away, the incoming wave fronts of the signals can be treated as plane wave fronts, whereas the incoming wave fronts of signals of extremely close sources like satellites of the GNSS would have to be treated as spherical wave fronts.

As the parallactic angles are eliminated through the assumed infinite distances to the sources, the geometric principle of the VLBI, which builds upon determining the baseline between the two stations, can be reduced to a rectangular triangle. This allows a direct relation between the baseline vector $\vec{b}$ and the direction to the source $\vec{s}_0$ through the scalar product (Campbell 2000; Schuh and Böhm 2013). Together with c as the speed of light, the observable of the VLBI for geodetic and astrometric purposes, the delay τ, can be calculated as described in Equation (2.1). This delay can also be described as the difference between the signal reception times t_1 and t_2 with the sign convention of $\tau = t_2 - t_1$ (Schuh and Böhm 2013):

$$\tau = -\frac{\vec{b} \cdot \vec{s}_0}{c} = t_2 - t_1. \tag{2.1}$$

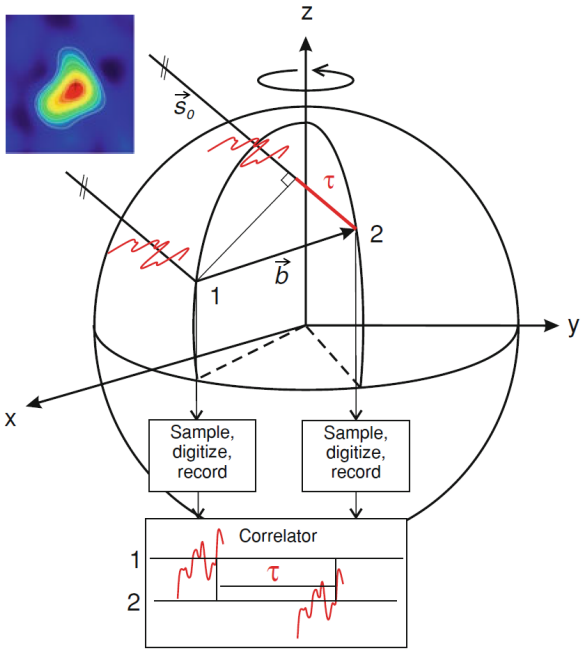

Figure 2.1: Geometric principle of the VLBI. Figure taken from Schuh and Böhm (2013) and slightly modified.

Since the stations are fixed to the Earth's surface the delay τ is time dependent because of the diurnal rotation of the Earth with respect to the celestial reference system (Schuh and Böhm 2013). Thus, the two stations have to observe the radio source simultaneously for a correct determination of τ.

VLBI has its origin in the radio astronomy that started in the 1930s. Later interferometry with cable-connected antennas was established to improve the resolution of the results. Today's VLBI was born in the mid of the 1960s with the removal of the physical connection and the use of station clocks instead. Now the separation of the antennas by arbitrary distances, very long baselines, was enabled (Sovers et al. 1998; Schuh and Böhm 2013).

Although so-called radio sources are observed, geodetic VLBI observations are actually carried out at microwave frequencies in the S-band (2.3 GHz, ∼13 cm wave length) and the X-band (8.4 GHz, ∼3.6 cm wave length) since the end of the 1970s (Schuh and Böhm 2013). With the approach of the next VLBI generation, called VLBI Global Observing System (VGOS), a change towards a broad frequency band between 2 GHz and 14 GHz is planned (Petrachenko et al. 2009).

In order to determine the reception time and take the time dependence of τ into account, the observed signals are time-tagged. For this task very stable and precise hydrogen masers (atomic clocks) are used[1]. As Figure 2.1 depicts at the bottom, the delay τ as the observable of the VLBI is determined from so-called fringes or interference patterns that are created by cross-correlation

[1]Frequency standards provide highly stable reference signals and are often called atomic clocks when periodic events derived from those signals are counted and provided as timing information.

of the time-tagged signals of the stations 1 and 2. For this step the recorded data are sent to specific correlation centres via hard disks or via e-transfer, i.e. transfer via high-speed broadband communication links (Schuh and Böhm 2013).

From the delay τ the target parameters of the geodetic VLBI can be derived by solving Equation (2.1) in its strict form where many different effects including relativistic effects are taken into account. For this task the vector $\vec{b}$ of the baseline and the vector $\vec{s}_0$ of the direction to the source have to be transformed into a common coordinate system. Then the baseline vector $\vec{b}$ can be determined with an accuracy of nowadays up to the sub-cm level. From the baseline vector also the station coordinates can be determined. Furthermore it is possible to estimate the source coordinates (Schuh and Böhm 2013). Since the sources are space-fixed, the angle between the Earth-fixed baseline vector $\vec{b}$ and the direction $\vec{s}_0$ to the sources changes with time, which can be determined with VLBI in high precision (Schuh 2000). This enables the derivation of the so-called Earth Orientation Parameters (EOP) that report the positioning of the Earth with respect to the celestial reference system of the sources. More details about the target parameters of the geodetic VLBI will be given in Section 2.3.

2.2 Observation technique

For geodetic VLBI two or more antennas, which form an observation network, observe simultaneously the same radio source. These observations are referred to as one scan. Through the observation of different sources a number of scans is created that form together a so-called session. Since the general goal, neglecting special purpose sessions, is a good global distribution of observing stations with a high sky-coverage of observed sources, it is not always possible that all participating stations can observe the same source simultaneously. Therefore so-called sub-networks of stations contribute with their scans to a session.

In order to coordinate the steering of the VLBI antennas for directing them to the sources that should be observed at the specific observation times, predefined observing schedules are needed. These schedules allow the beforehand definition of the desired observing strategy, e.g. best sky-coverage for optimal tropospheric delay estimation within the later analysis of the observations (Schuh and Böhm 2013).

In the following the signal reception and data preparation at a station is introduced. Considering a Cassegrain antenna, e.g. the 20 m antenna at the Geodetic Observatory Wettzell shown in Figure 2.2, the signal from the source is at first reflected by the primary paraboloidal dish up to the hyperboloidal subreflector from which it is finally deflected to the feed horn on the central axis. In case of a prime focus antenna the signal is directly reflected to the feed horn at the focus position (Sovers et al. 1998).

Following the reception of the signal by the feed horn, multiple signal processing steps are carried out. At first the signal is amplified and subsequently heterodyned from the radio (microwave) frequency down to an intermediate frequency of several hundred MHz before it is again

Figure 2.2: 20 m Cassegrain VLBI antenna at the Geodetic Observatory Wettzell, Germany. Photograph by A. Hofmeister, May 2014.

heterodyned down to so-called video-frequencies or baseband frequencies (Sovers et al. 1998). In modern receiving systems the signal is down-converted only once before it is fed to a backend system (Whitney et al. 2009). This process is done simultaneously in different frequency sub-bands of the original broadband. These channels are then limited to a width of a few MHz (Schuh and Böhm 2013). The splitting of the signal into single narrow bands is crucial for post-correlation processing where bandwidth synthesis (Rogers 1970) enables the reduction of the amount of data without reducing the accuracy of the determined delay (Sovers et al. 1998). The bandwidth synthesis results in a new bandwidth called effective bandwidth (Rogers 1970). The typical system temperatures are in the interval of 20 K to 100 K at the S- and X-bands. Finally the signal is digitized (Sovers et al. 1998). The thereby received raw VLBI data are stored on hard disks.

Now the data are ready for being shipped via hard disks or transferred via broadband communication link to the correlation centre for the retrieval of the needed (group-)delays τ that are used in the VLBI analysis, which will be discussed in Section 2.3.

Since the received signal flux density is in the order of 1 Jansky ($1\ Jy = 10^{-26}\ Wm^{-2}Hz^{-1}$) the sampling and recording rates need to be high and sensitive detectors and stable frequency standards (atomic clocks) are needed. Of major importance is also the size of the antenna's main dish that should be large on the one side in order to collect much signal flux, but on the other side the antenna must be able to perform position changes between widely separated sources within a few minutes (Sovers et al. 1998). Thus, the larger the antenna the slower, but the more signal

flux can be collected. This leads to the necessity of finding a suitable compromise between the two extreme opposites of large but slow and small but fast antennas. In the course of VGOS this compromise has been redefined since the new antennas are built smaller than the older ones, but with faster slewing rates, leading to more observations. Detailed information on VGOS can be found in Petrachenko et al. (2009).

In order to align the narrow channels during the bandwidth synthesis, the technique of phase calibration (Rogers 1975) is used, which detects phase shifts that are caused by the measurement instrumentation on the signal (Sovers et al. 1998). This method adds an artificial signal with known phase to the signal stream at its front end. By determining the phase after the way through the instrumentation possible phase shifts can be detected and corrected (Sovers et al. 1998). Additionally, in order to correct for length variations in the cable from the station clock to the antenna a correction called cable delay has to be applied (Schuh and Böhm 2013).

The correlation process to find the delays τ starts with the pairwise combination of the recorded signals from the stations at specific correlation centres in order to produce an interference pattern. These centres use special-purpose signal-processing hardware or nowadays mainly software for the determination of the delay τ as the difference in the arrival times at the combined stations 1 and 2, which is shown schematically in Figure 2.1. This is done by computing the cross-correlation function R_{corr} in Equation (2.2), where V_1 and V_2 denote the antenna voltage V as a function of time t. By shifting V_1 and V_2 relatively to each other in time, the cross-correlation maximum can be found, which delivers the searched value for τ. T_{int} is the averaging interval. The asterisk ($*$) stands for the complex conjugate (Sovers et al. 1998). Thus, according to Sovers et al. (1998) the cross-correlation is calculated by

$$R_{corr}(\tau) = \frac{1}{T_{int}} \int_0^{T_{int}} V_1(t) V_2^*(t-\tau) \, \mathrm{d}\, t. \tag{2.2}$$

Prior or during the correlation step the signals have to be counter-rotated since the Earth's rotation induces Doppler shifts on the observed signals (Sovers et al. 1998). The ionospheric effects on the signals due to charged particles can be removed by applying a simple model of dispersion since the ionosphere is a dispersive medium in the radio (microwave) frequency domain. Thus, it is sufficient in VLBI to determine the ionospheric effect from the difference in the delay results of two distinct frequencies, i.e. of the S- and X-band (Sovers et al. 1998; Schuh and Böhm 2013).

In order to reach a high resolution of the (group-)delay σ_τ, it is important to have a high signal-to-noise ratio SNR and a large effective bandwidth BW_{eff} from bandwidth synthesis since these quantities are inversely proportional to σ_τ as Equation (2.3) depicts (Rogers 1970):

$$\sigma_\tau = \frac{1}{2\pi} \cdot \frac{1}{SNR \cdot BW_{eff}}. \tag{2.3}$$

Unfortunately, as stated earlier, the flux density of the source signal is very weak compared to the background noise in space. Therefore the size of BW_{eff} becomes even more important.

The SNR itself is dependent on the recorded bandwidth BW as shown in Equation (2.4) (Böhm 2004):

$$SNR = \upsilon \cdot \frac{F_d}{2k_B} \cdot \sqrt{\frac{C_{A1} \cdot C_{A1}}{T_{S_1} \cdot T_{S_2}}} \cdot \sqrt{2 \cdot BW \cdot T_{int}} \tag{2.4}$$

with the digital loss factor υ, the flux density of the source F_d, the Boltzmann constant k_B, the effective antenna signal collection area C_A at station 1 and 2, the system temperature of the receiver T_S at station 1 and 2 and the integration interval T_{int}. Thus, from this equation it can be concluded that the size of the antennas and the bandwidth are the major parameters that can be adjusted to improve the SNR. As stated earlier, it is planned according to Petrachenko et al. (2009) to increase the bandwidth with VGOS.

2.3 Analysis and results

This section shows briefly what the target parameters of the geodetic VLBI are and how they are determined in an analysis of the delays. These delays, whose retrieval has been described in the last section, build the so-called observables for the analysis.

The analysis of the VLBI observables is based on a two stream approach as depicted in Figure 2.3, which serves as method to determine the VLBI target parameters (Schuh and Böhm 2013).

The goal of the first stream is to determine the reduced observed delay, i.e. the pure geometric part of the observed delay. Thus, starting with the actual observed delay multiple corrections and models are applied. At first, the observed delay is corrected due to instrumental effects, e.g. systematic clock instabilities and the electronic delays caused by the equipment, which are denoted as instrumental calibration in Figure 2.3 (Schuh and Böhm 2013). Secondly, the effect of the ionosphere is reduced. This has already been described briefly in the previous section. Of major relevance with respect to this work is the also necessary reduction of the tropospheric effects on the observed delay. The tropospheric influence and the modelling will be described in Chapter 3. Additionally antenna construction specific influences are reduced like the thermal deformation of the antenna and possible axis offsets. Furthermore the effects of source structure, which deals with the fact that sources can not generally be seen as perfect point sources, lead to influences on the observed delays and can also be corrected.

The second stream in VLBI data analysis is the calculation of the theoretical delay (Schuh and Böhm 2013). According to Figure 2.3 this means that without using the observation the delay is calculated by using a priori values and models with the goal to receive a delay value that is as accurate and close to the reduced observed delay as possible. For this task a priori station coordinates and source coordinates are needed. In a first step the a priori station coordinates are corrected due to deformations of the Earth because of solid Earth tides and station dependent loading effects. The latter are tidal and possibly also non-tidal ocean loadings, atmospheric tidal

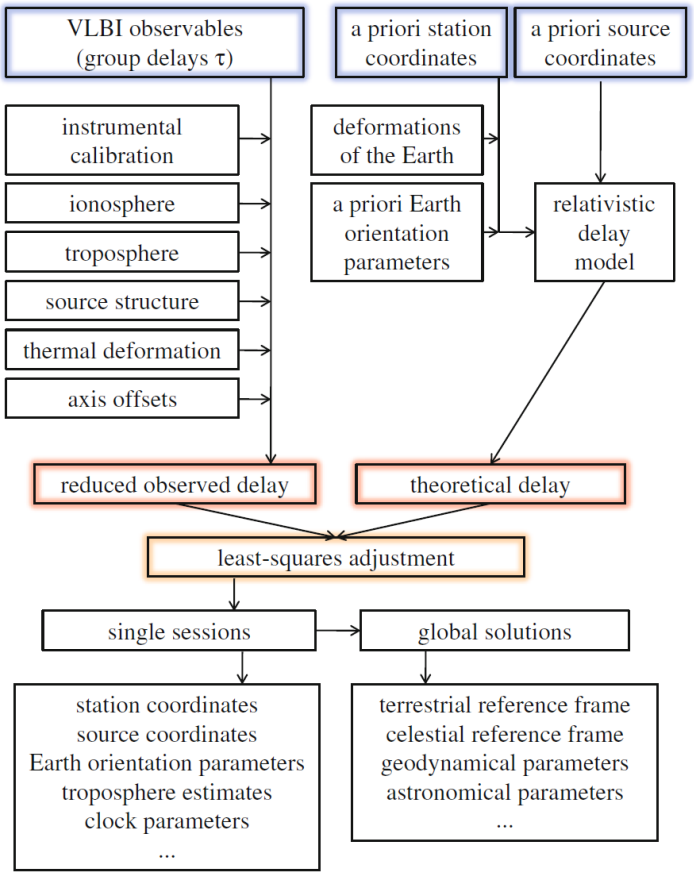

Figure 2.3: Flow chart of the VLBI analysis. Figure is taken from Schuh and Böhm (2013) and is according to Schuh (1987).

and non-tidal loadings, pole tides, ocean pole tides and possibly also hydrology loadings that act on the station positions at the time of the observation epoch. In a second step the station positions are transformed from the terrestrial reference system into a celestial reference system using a priori known EOP, so that the station and source positions are in the same system. Then the theoretical delay can be determined with included consideration of relativistic effects through a general relativistic delay model (Schuh and Böhm 2013).

Thus, having the reduced observed and the theoretical delay, the difference between these two entities can be formed in the way of "observed" − "computed". This difference is calculated for all observations in a VLBI session and serves as the main input to a least-squares adjustment, e.g. using the Gauß-Markov model or a Kalman-filter (Schuh and Böhm 2013). Having formed the differences and introduced to the least-squares adjustment, it is possible to solve for all parameters that are part of the observation equation described by Equation (2.1) since the differences build the reduced observation vector (Hofmeister 2013).

The parameters for which the analysis can solve are on the one side the target parameters of the VLBI, but on the other side needed auxiliary parameters that are usually not desired to be determined, but which are needed to correct for effects on the observations.

Auxiliary parameters are for example the clock parameters that describe the behaviour of the station clock as a linear or quadratic polynomial function. Also tropospheric parameters like the zenith wet delay and the horizontal gradients are usually part of the analysis solution, but only as auxiliary parameters since they are not in the main focus of a geodetic solution (Schuh and Böhm 2013). Imperfect or even no a priori modelling of the zenith wet delay or the horizontal gradients are the reasons why it is usually required to additionally estimate these parameters within the analysis in order to be able to accurately determine the target parameters.

The target parameters of the VLBI analysis are the station and source coordinates and the EOP. The EOP are five different parameters that describe the Earth orientation within a celestial reference system. This set of parameters contains the polar motion (2 parameters), the precession/nutation parameters that determine the location of the celestial pole (2 parameters) and the Earth rotation angle, which is related to the Universal Time 1 $UT1$. Since VLBI allows the determination of the value $\Delta UT1 = UT1 - UTC$, where UTC is the known Universal Time Coordinated, $UT1$ and therefore the Earth rotation angle can be determined directly with VLBI.

In a normal VLBI analysis all parameters are estimated on the basis of single sessions, which means that the results of the determined values are independent for each session. In order to connect the single session results and introduce a dependency between the individual sessions a "global" solution, i.e. a common least-squares adjustment, can be carried out in a succeeding step. Based on stacking of normal equations from the single sessions, station coordinates and velocities, source coordinates and EOP can be determined "globally". This also enables the creation of a terrestrial and celestial reference system realization (TRF and CRF) out of the free station and source networks determined by the VLBI analysis by applying No-Net-Translation (NNT) and No-Net-Rotation (NNR) conditions in case of station coordinates and NNR condition in case of source coordinates on selected datum defining stations or sources (Schuh and Böhm 2013).

From the above findings a conclusion of the importance of VLBI with respect to the parameters, which can be determined, may be given. Of major importance is that geodetic VLBI is the unique space geodetic technique, which can determine the full set of EOP due to the fact that no other method can directly provide the $UT1$ value. Furthermore only geodetic VLBI is capable of providing the celestial pole offsets over longer time spans. Regarding the determination of a CRF, geodetic VLBI also takes an unique position with the realization of the International Celestial Reference Frame (ICRF). With respect to TRF solutions geodetic VLBI provides an import advantage since it can determine the frame's scale just with the dependency on the natural constant of the speed of light, which is not the case for frames determined by space geodetic techniques based on satellite observations. Thus, especially in case of the International Terrestrial Reference Frame (ITRF) as a combination of solutions from different space geodetic techniques, VLBI can significantly contribute (Schuh and Böhm 2013).

Beside this important role in determining geodetic parameters, VLBI enables also the estimation of geodynamic parameters like the Love and Shida numbers h_L and l_S of the solid Earth tides model (see Krásná et al. 2013). Also ionospheric and tropospheric parameters can be determined in a VLBI analysis as it has already been described partly earlier in this section, where especially

the tropospheric part is of major importance for this work in the context of finding most accurate corrections for its influences rather than deriving meteorological parameters. Even astronomical parameters may be derived from VLBI observations like the gravitational deflection of radio (microwave) waves, which is due to the fact that the signals are affected by gravitational effects of the Sun, the Earth, Jupiter and of the Earth's moon and even of Saturn, Neptune or of the major satellites of Jupiter if the signals pass close to them. This, in turn, enables the determination of the post-Newtonian parameter γ, describing the light deflection resulting from the curvature of space due to gravity. Also a possible acceleration of the solar system barycentre may be determined from VLBI observations (Schuh and Böhm 2013).

Chapter 3

Atmospheric effects on observations

In this chapter the theoretical background of the atmospheric effects on observations is described. In the following, if speaking of atmospheric effects, the influence of the neutral atmosphere is meant since the ionospheric influences are not part of the research presented here. Furthermore, as this work deals with atmospheric path delays of VLBI observations, the focus is set on the influence of the atmosphere in the microwave frequency range. At first, a short introduction to the atmosphere with respect to its basic structure and important general knowledge is given. Then the wave propagation in the atmosphere is depicted. This serves as important background for the following description of the influence of the neutral atmosphere on the space geodetic techniques in the microwave frequency range like VLBI and GNSS in terms of path delay. In the last section an overview of different important approaches for the determination of path delays in the neutral atmosphere is given. A more detailed description of the ray-tracing approach will be depicted in Section 4.1 of Chapter 4. For Section 3.1 B. Klose and H. Klose (2015) serves as the main reference, whereas Nilsson et al. (2013) is the main reference for the remaining sections in this chapter.

3.1 Introduction to the atmosphere

The Earth's atmosphere can be described by a model of layers. Although there are also horizontal gradients of the meteorological parameters, it is sufficient for a general model to divide the atmosphere into a vertical layer structure since the vertical gradients of the meteorological parameters are significantly larger than the horizontal ones. Furthermore due to the influence of the gravity the regional horizontal differences become smoothed out towards higher altitudes. Thus, it can be said that the atmosphere has a quasi-horizontal structure of layers. This structure can be derived from vertical temperature profiles or the change in the chemical composition. Inhomogeneities in the vertical temperature gradient are used to separate adjacent layers (B. Klose and H. Klose 2015).

On the basis of vertical mean temperature profiles, the atmosphere can be divided into the troposphere, the stratosphere, the mesosphere, the thermosphere and the exosphere. This struc-

ture is established by the above mentioned inhomogeneities, which are changes in the sign of the vertical temperature gradient. At each of these occurrences a separation layer called "pause" is introduced to the layer structure. Therefore the additional intermediate layers tropopause, stratopause and mesopause are present in the atmospheric structure (B. Klose and H. Klose 2015). Figure 3.1 shows the layer structure of the atmosphere based on the vertical temperature gradient.

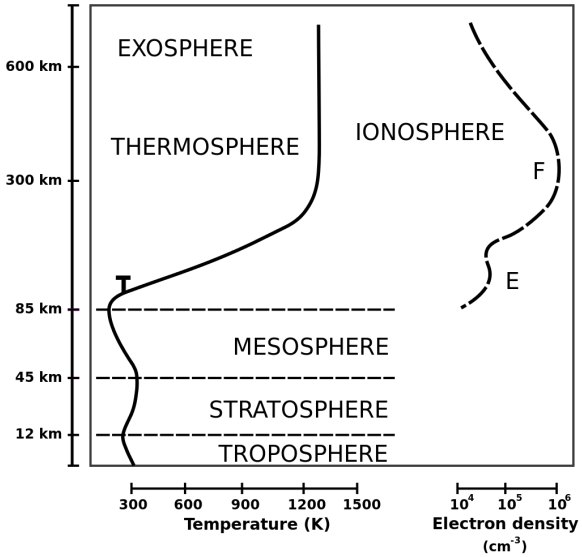

Figure 3.1: Layer structure of the atmosphere based on the vertical temperature gradient and representation of the ionosphere. Figure taken from https://commons.wikimedia.org/wiki/File:Atmosphere_with_Ionosphere.svg, Wikimedia Commons (2015).

The troposphere is the layer that has a direct connection to the Earth's surface over land and sea and is thus amongst other things also influenced by its shape. In this layer 70% to 90% of the atmospheric mass is contained and weather phenomena like cloud building and rainfall are taking place there. Throughout the troposphere the temperature gradient is negative with a mean value of about -6.5 K/km (B. Klose and H. Klose 2015). This is the result of the effects of the Earth's surface as heat source, of the expansion of air at its ascent and of the heat sink at height. At tropical regions a temperature minimum is reached at heights between 17 km and 18 km, whereas at higher latitudes the minimum is located at heights between 9 km and 13 km. The height of this temperature minimum defines the location of the tropopause. The latitude dependency of the temperature minimum is caused by, roughly formulated, the height limit of the water vapour content in the troposphere. Since the troposphere can contain more water vapour, if the surface temperature is higher, the minimum temperature height will be shifted to a larger height in these cases and thus the upper troposphere limit is raised. This leads to the fact that the troposphere limit is higher in tropical regions and thus also lower minimum temperatures are reached there (Roedel and Wagner 2011). The location and thickness of the tropopause is determined by the temperature gradient derived from radiosonde data. From definition, the tropopause is the layer

above the troposphere, where the temperature gradient is 0 K/km or only slightly negative or positive (B. Klose and H. Klose 2015).

Above the tropopause there is the stratosphere, which is characterized by a positive temperature gradient. This is due to the fact that this layer is very dry as there is almost no water vapour present and the contained ozone in the middle and upper parts of the stratosphere absorbs ultraviolet radiation, which leads to heat radiation. Therefore the temperature is in general increasing in the stratosphere (B. Klose and H. Klose 2015). The temperature gradient above the tropopause in the lower stratosphere is de facto 0 K/km at middle and higher latitudes, but +5 K/km at tropical regions. The mean gradient at the upper stratosphere is about +2 K/km (Roedel and Wagner 2011). The maximum temperature is reached at the stratopause, which separates the stratosphere and the mesosphere, at a height of about 50 km or at a total pressure of approximately 1 hPa (B. Klose and H. Klose 2015).

In the mesosphere the temperature is again decreasing with height. The temperature gradient is about -3 K/km. This temperature decrease stops at a height of approximately 85 km in summer. In middle and high latitudes the minimum temperature is reached at about 95 km in winter. At this change in the temperature gradient again a subdivisional layer is located, the mesopause. At this layer the lowest temperatures in the Earth's atmosphere are reached, which can be -95° C to -130° C in summer. In winter the mesopause is not only located at higher heights, but the minimum temperature is also significantly warmer. Due to the low density of the air in the mesosphere, the radiation absorption is very low, which leads to the fact that the temperature in this area underlies strong influences from the daily Earth rotation cycle and the yearly Sun cycle (B. Klose and H. Klose 2015).

Following the mesopause the thermosphere is located, where the ultraviolet radiation of the Sun is absorbed, mainly from oxygen, and transformed to heat leading again to a temperature increase with height up to a maximum of 1200 K to 1500 K, but with strong dependence on the daily Earth rotation cycle. In the thermosphere the ion content is significantly increasing, starting at heights of about 75 km (Roedel and Wagner 2011).

The uppermost layer of the atmosphere is the exosphere, which is located at heights above 1000 km, and can be described as the transition to space. In this layer the geostationary satellites and those on polar orbits as well as the space ships are located since the atmosphere's density there is that low that the orbits remain stable for long periods as the atmospheric drag is low (B. Klose and H. Klose 2015).

Switching from a vertical temperature gradient related structuring of the atmosphere to a subdivision regarding the propagation of signals from space geodetic techniques, the atmosphere can be divided into the neutral atmosphere and the ionosphere. The neutral atmosphere reaches from the Earth's surface up to about 100 km[1]. The ionosphere is located at heights between about 60 km and 2000 km with a dependence on latitude and time. This is also partly shown in

[1]In this work, i.e. for the ray-tracing, the neutral atmosphere is said to end at a height of 84 km, assuming that there is no contribution to the neutral atmosphere delay above this limit.

Figure 3.1. Concerning only observation signals in the microwave frequency range as it is done is this work, the influence of the neutral atmosphere in form of delays is of the same size for the phase and the group part. In the ionosphere the signals are experiencing phase advance and group delay. Due to dispersion the influence of the ionosphere can be eliminated by observing at more than one frequency, which is common practice in VLBI and also in GNSS. Since the neutral atmosphere is non-dispersive for microwave frequencies a different way of removing the influence has to be applied as described in Section 3.4, e.g. ray-tracing or mapping functions and horizontal gradients (Böhm et al. 2013).

Since this work focuses on the microwave frequency based observations of VLBI, the ionosphere is not explicitly treated here as its influence can be eliminated with the observations at two frequencies. Nevertheless the ionospheric effects on the signals are briefly described in the following. The density of free electrons and ions is high enough in the ionosphere to affect the propagation of microwave signals, which is called the ionosphere refraction effect (Böhm et al. 2013). Though the ionosphere is located between 60 km and 2000 km, its particles are concentrated mainly between 300 km and 400 km (Rishbeth and Garriott 1969; Hargreaves 1995). The neutral gas in the ionosphere is ionized by the extreme ultraviolet radiation from the Sun at wave lengths <130 nm. A further ionization is exhibited by energetic particles from the solar wind and cosmic rays, but the total share of this contribution is much smaller (Hunsucker and Hargreaves 2002). The free electrons in the ionosphere are produced due to the interaction of the solar radiation with the atoms and molecules (Böhm et al. 2013).

3.2 Wave propagation in the atmosphere

For the derivation of the path delays induced by the neutral atmosphere the mechanism of the wave propagation of electromagnetic waves in the atmosphere has to be known. In the following, the term atmospheric delay always denotes the delay induced by the neutral atmosphere only, i.e. without contributions of the ionosphere.

In general all variables in the upcoming equations are applied with their SI-units except for total pressure, dry pressure and water vapour pressure, which are always supposed to be used in [hPa]. In case any variable in an equation is not following these guidelines the unit is explicitly declared.

The propagation of electromagnetic waves can be described by Maxwell's equations (see Jackson 1998). The troposphere can be considered as a propagation medium, which is non-conducting and neutral (Nilsson et al. 2013). Maxwell's equations have according to Jackson (1998) in the absence of sources in a non-conducting infinite medium with spatially constant permeability and

susceptibility the form

$$\nabla \cdot (\varepsilon \vec{E}) = 0, \tag{3.1a}$$

$$\nabla \cdot \vec{B} = 0, \tag{3.1b}$$

$$\nabla \times \vec{E} = -\frac{\partial \vec{B}}{\partial t}, \tag{3.1c}$$

$$\nabla \times \vec{B} = \mu\varepsilon \frac{\partial \vec{E}}{\partial t}, \tag{3.1d}$$

where $\vec{E}$ and $\vec{B}$ denote the electric and magnetic field vectors, ε the electric permittivity of the medium, μ the magnetic permeability of the medium and t the time. By combining Equations (3.1c) and (3.1d) the wave equation for the electric field can be formed (Demtröder 2013a; Demtröder 2013b). Under the assumption of only small spatial and temporal variations in ε and μ (Nilsson et al. 2013) its equation can be written according to Demtröder (2013b) and Nilsson et al. (2013) as

$$\nabla^2 \vec{E} = \mu\varepsilon \frac{\partial^2 \vec{E}}{\partial t^2} = \frac{n^2}{c^2} \frac{\partial^2 \vec{E}}{\partial t^2} \tag{3.2}$$

with the speed of light c in vacuum according to Demtröder (2013a)

$$c = \frac{1}{\sqrt{\mu_0 \varepsilon_0}} \tag{3.3}$$

and with the refractive index n of the medium according to Jackson (1998)

$$n = \sqrt{\frac{\mu\varepsilon}{\mu_0 \varepsilon_0}}, \tag{3.4}$$

where μ_0 is the vacuum permeability or magnetic constant and ε_0 is the vacuum permittivity or electric constant. Analogous to Equation (3.2) the equation for the magnetic field can be formed (Demtröder 2013b).

Thus, in order to solve the propagation of electromagnetic waves, e.g. waves in the microwave frequency range, in the neutral atmosphere with Equation (3.2) the refractive index n needs to be known. It represents a factor $\geqslant 1$ for the calculation of c' as the speed of light in a medium by (Demtröder 2013b)

$$c' = \frac{c}{n}. \tag{3.5}$$

Since the value of n is very close to 1 in the neutral atmosphere an alternative representation of this quantity can be used, which is called refractivity N. N has the unit [mm/km] or [ppm] or [N-unit] and is determined by (Nilsson et al. 2013)

$$N = (n-1) \cdot 10^6. \tag{3.6}$$

Generally N is a complex number and can be separated into three terms (Nilsson et al. 2013):

$$N = N_0 + N'(\nu) - iN''(\nu), \tag{3.7}$$

where ν denotes the frequency. In case of signals of space geodetic techniques the effects of the real and imaginary terms of the refractivity on the wave propagation can be treated separately since the spatial and temporal variations of N are negligible over one wavelength, i.e. over maximal a few decimetres. The real terms N_0 and $N'(\nu)$ cause the refraction and delay of the signal. N_0 is frequency independent and therefore called the non-dispersive part, whereas $N'(\nu)$ is dependent on the signal frequency and therefore the dispersive part. The imaginary term $N''(\nu)$ causes absorption and is frequency dependent (Nilsson et al. 2013).

Considering space geodetic techniques the imaginary part can be neglected since the techniques are based on travel time measurements and the absorption does not influence the propagation delay of the signals. Only when considering the SNR the absorption may be of importance. Thus, with respect to the effect on the signal propagation delay it is sufficient to deal only with the real part of the refractivity (Nilsson et al. 2013).

According to Debye (1929) the real part of the refractivity N can be represented as the contributions of densities of the different atmospheric gases:

$$N = \sum_i \left(\Lambda_i(\nu)\rho_i + \Gamma_i(\nu)\frac{\rho_i}{T} \right) \tag{3.8}$$

with the index i for the different gases and the densities ρ_i, the temperature T and the constants Λ_i and Γ_i that are dependent on the frequency ν. The term $\Lambda_i(\nu)\rho_i$ describes the induced dipole moments on the gases, whereas $\Gamma_i(\nu)\frac{\rho_i}{T}$ describes the effect of the permanent dipole moment of the molecules, i.e. the water vapour, since it is the only major gas in the atmosphere that has a permanent dipole moment (Nilsson et al. 2013). As the relative concentrations of the dry atmospheric gases are roughly constant with the exception of carbon dioxide, it is possible to assume that the density ρ_i of each gas can be expressed as the product of the density of dry air ρ_d with a constant factor x_i in form of $\rho_i = x_i\rho_d$. Thus Equation (3.8) can be altered and rewritten as a function of pressure, temperature and humidity according to Essen and Froome (1951):

$$\begin{aligned} N &= \sum_i \Lambda_i(\nu)x_i\rho_d + \Lambda_w(\nu)\rho_w + \Gamma_w(\nu)\frac{\rho_w}{T} + \Lambda_{lw}(\nu)\rho_{lw} \\ &= k_1(\nu)\frac{p_d}{T}Z_d^{-1} + k_2(\nu)\frac{p_w}{T}Z_w^{-1} + k_3(\nu)\frac{p_w}{T^2}Z_w^{-1} + k_4(\nu)\rho_{lw}. \end{aligned} \tag{3.9}$$

The constants Λ_w and Γ_w, which are dependent on the frequency ν, are related to the water vapour. ρ_w is the density of wet air. Λ_{lw} and ρ_{lw} denote the constant and density for liquid water. k_1, k_2, k_3 and k_4 are the refractivity coefficients that are dependent on the frequency ν. p_d is the partial pressure of dry air and p_w is the partial pressure of water vapour. For the liquid water droplets the

assumption is made that they are small compared to the wavelength, otherwise Equation (3.9) would have to be enhanced (see Solheim et al. 1999). Furthermore the contribution of liquid water to N is normally neglected since it is small, in particular outside of clouds. Z_d and Z_w are the compressibility factors for dry air and water vapour, which can be determined by

$$Z_d = \frac{p_d M_d}{\rho_d R T}, \tag{3.10}$$

$$Z_w = \frac{p_w M_w}{\rho_w R T} \tag{3.11}$$

with the molar masses of dry and wet air M_d and M_w and the universal gas constant R. Z_d and Z_w represent the divergence of the constituent from an ideal gas. An ideal gas has $Z_i = 1$ (Nilsson et al. 2013).

For the practical determination of the inverses of Z_d and Z_w Owens (1967) has determined empirical expressions from a least-squares polynomial curve fitting of thermodynamic data as

$$Z_d^{-1} = 1 + p_d \left[57.90 \cdot 10^{-8} - \frac{9.3250 \cdot 10^{-4}}{T} + \frac{0.25844}{T^2} \right], \tag{3.12}$$

$$Z_w^{-1} = 1 + p_w \left[1 + \left(3.7 \cdot 10^{-4} \right) p_w \right] \cdot \cdot \left[-2.37321 \cdot 10^{-3} + \frac{2.23366}{T} - \frac{710.792}{T^2} + \frac{7.75141 \cdot 10^4}{T^3} \right] \tag{3.13}$$

with p_d and p_w in [hPa] and T in [K]. Note that Equation (3.12) is valid for the standard composition of dry air containing 0.03% carbon-dioxide.

3.3 Neutral atmosphere-induced path delays of observations in the microwave frequency range

As described by Equation (3.9) the refractivity is dependent on the signal's frequency. Thus, since the target of this work is the determination of tropospheric path delays for VLBI observations, the focus of the frequency range is set hereafter on the microwave frequencies. Figure 3.2 shows the impact of different frequencies and concentrations of liquid water on the refractivity. Around 50 GHz to 70 GHz the refractivity shows a higher variation with respect to the in general relatively small change in the dependence on the frequency in the range of 0 GHz to 100 GHZ. This is due to absorption lines from oxygen. At frequencies below 40 GHz there is almost no change in the refractivity. Thus, since microwave-based space geodetic techniques like VLBI and GNSS typically use frequencies below 40 GHz, frequency independence of the refractivity can be assumed for these techniques. This leads to the fact that the phase and group velocities are equal in the troposphere. The variations in the refractivity due to the water vapour absorption line at around 22.235 GHz are also typically neglected. The impact of liquid water on the refractivity is relatively small and thus usually neglected, although dense clouds exhibit an influence on the refractivity

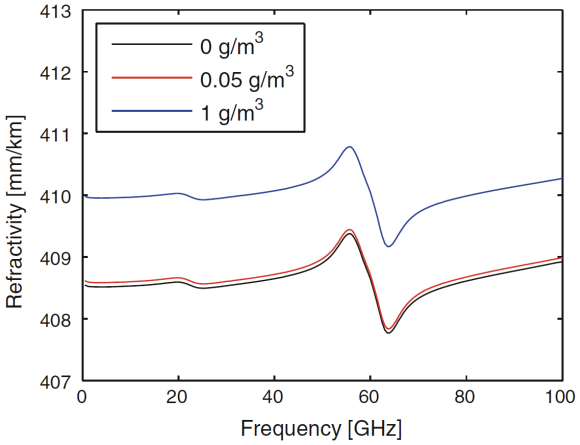

Figure 3.2: Influence of frequency and liquid water concentration on the refractivity. Refractivity has been calculated under the assumptions of a total pressure of 1013 hPa, a temperature of 300 K and a relative humidity of 100% using the Millimeter-wave Propagation Model (MPM) (Liebe 1985; Liebe 1989; Liebe et al. 1993). The impact of three different concentrations of liquid water on the refractivity is shown. A concentration of 0 g/m^3 represents dry conditions, 0.05 g/m^3 simulates fog and 1 g/m^3 can be found inside clouds. Figure and information are taken from Nilsson et al. (2013).

that should be taken into account in case of high accuracy demands (Nilsson et al. 2013).

Thus, following Nilsson et al. (2013) and ignoring the frequency dependence and the liquid water contribution, Equation (3.9) can be rewritten as

$$\begin{aligned} N &= k_1 \frac{p_d}{T} Z_d^{-1} + k_2 \frac{p_w}{T} Z_w^{-1} + k_3 \frac{p_w}{T^2} Z_w^{-1} \\ &= N_d + N_v, \end{aligned} \tag{3.14}$$

where N_d is the dry refractivity coming from the dry gases and N_v is the wet refractivity coming from the water vapour as according to Smith and Weintraub (1953) and Kleijer (2004).

By applying Equation (3.10) and Equation (3.11) to Equation (3.14), it can be written as

$$N = k_1 \frac{R}{M_d} \rho_d + k_2 \frac{R}{M_w} \rho_w + k_3 \frac{p_w}{T^2} Z_w^{-1} \tag{3.15}$$

with the molar masses of dry and wet air M_d and M_w and the universal gas constant R. According to Davis et al. (1985) and Kleijer (2004) the total density of moist air ρ, which is defined as

$$\rho = \rho_d + \rho_w, \tag{3.16}$$

can be used to rewrite Equation (3.15) as

$$\begin{aligned} N &= k_1 \frac{R}{M_d}\rho - k_1 \frac{R}{M_d}\rho_w + k_2 \frac{R}{M_w}\rho_w + k_3 \frac{p_w}{T^2} Z_w^{-1} \\ &= k_1 \frac{R}{M_d}\rho + \left(k_2 - k_1 \frac{M_w}{M_d}\right) \frac{R}{M_w}\rho_w + k_3 \frac{p_w}{T^2} Z_w^{-1}. \end{aligned} \tag{3.17}$$

By defining the refractivity coefficient k_2' as

$$k_2' = k_2 - k_1 \frac{M_w}{M_d} \tag{3.18}$$

Equation (3.17) can be brought into the form

$$\begin{aligned} N &= k_1 \frac{R}{M_d}\rho + k_2' \frac{R}{M_w}\rho_w + k_3 \frac{p_w}{T^2} Z_w^{-1} \\ &= k_1 \frac{R}{M_d}\rho + k_2' \frac{p_w}{T} Z_w^{-1} + k_3 \frac{p_w}{T^2} Z_w^{-1} \\ &= k_1 \frac{R}{M_d}\rho + \left(k_2' \frac{p_w}{T} + k_3 \frac{p_w}{T^2}\right) Z_w^{-1} \\ &= N_h + N_w, \end{aligned} \tag{3.19}$$

where N_h is the hydrostatic part of the refractivity and N_w is the non-hydrostatic part of the refractivity, which will be though called wet refractivity in the following. They can be determined separately as

$$N_h = k_1 \frac{R}{M_d}\rho, \tag{3.20}$$

$$N_w = \left(k_2' \frac{p_w}{T} + k_3 \frac{p_w}{T^2}\right) Z_w^{-1}. \tag{3.21}$$

Equation (3.19) is also used within ray-tracing to determine the needed refractivity values, which will be described in Chapter 4.

For the determination of the hydrostatic refractivity N_h only the dependence on the total density of moist air ρ is important, whereas in case of the non-hydrostatic (wet) refractivity N_w the dependence on the partial pressure of water vapour p_w and the temperature T is crucial. The hydrostatic part accounts for the major part of the total refractivity N, whereas the wet refractivity is smaller, but has a much higher variability and is therefore difficult to express in terms of a model (Nilsson et al. 2013).

Please note that there is a significant difference between the separation of N into the dry refractivity N_d and the wet refractivity N_v as shown in Equation (3.14) and the separation into the hydrostatic part of the refractivity N_h and the non-hydrostatic (also called wet) part N_w in Equation (3.19). This is due to the reformation of Equation (3.14) to Equation (3.19) by using the total density of moist air ρ and k_2'. The dry refractivity accounts only for the dry part, whereas

the hydrostatic refractivity accounts for all hydrostatic parts, also those of the true wet refractivity. Therefore N_w is strictly speaking only the non-hydrostatic refractivity.

Both separation approaches have their advantage. From a practical point of view it is more useful to separate into hydrostatic and non-hydrostatic refractivity (Nilsson et al. 2013).

The refractivity coefficients k_1, k_2 and k_3 have been determined in several laboratory measurements (Nilsson et al. 2013). Rüeger (2002a) and Rüeger (2002b) calculated so-called "best-average" values for the coefficients, which are shown in Table 3.1. The reported accuracy for k_1, i.e. the dry refractivity is 0.012% and for the wet refractivity it is 0.15% (Rüeger 2002a; Rüeger 2002b). Exactly these values are used for the ray-tracing program RADIATE, which will be described in Section 4.2, to calculate the refractivity or the refractive index as shown in Section 4.2.2.

Table 3.1: "Best-average" values from Rüeger (2002a) and Rüeger (2002b) for the refractivity coefficients k_1, k_2 and k_3.

k_1 [K/hPa]	k_2 [K/hPa]	k_3 [K^2/hPa]
77.6890	71.2952	375463

Basically k_1 is dependent on the relative concentrations of the different dry gases in the atmosphere. Fortunately most of the dry gases have a stable concentration. Carbon dioxide is the only of the major atmospheric gases that shows a variability. The carbon dioxide concentration increases by between 1.5 ppm to 2 ppm per year, but it also has an annual variation cycle of the size of 5 ppm. Thus k_1 is in principle changing with time. The total impact of carbon-dioxide on k_1 is only 0.03% (Nilsson et al. 2013). Thus, the ray-tracing program RADIATE does not account for changes of k_1 and uses the value for k_1 shown in Table 3.1 that has been determined by Rüeger (2002a) for the then expected carbon dioxide concentration of the year 2004.

Having described the way of retrieving the refractivity that is needed for determining the propagation of the signal in the neutral atmosphere, it is now possible to show how the path delay is defined and how it can be estimated.

Referring to space geodetic techniques travel times as in case of GNSS or differences in travel times, so-called delays, as in case of VLBI are measured. The resulting time measurement can be converted to a distance by multiplying it with the speed of light in vacuum. This distance is affected by the atmosphere as the signal travels through it. Thus, the atmosphere is inducing an error on the distance measurement (Nilsson et al. 2013). This error can be therefore described as the difference in the observed distance and the theoretical distance, that would be received in case the atmosphere was vacuum. Since the geometric principles of the techniques need the theoretical distance as input, the error induced by the atmosphere has to be determined and corrected.

The atmosphere influences the signal propagation in two different ways. Firstly, since the speed of light is lower in the atmosphere than in vacuum, the signal propagates slower. Secondly, the signal path is affected by refraction due to the changing composition of the atmosphere with

height.

To describe these effects on the signal propagation the geometrical optics approximation can be used in case the amount of changes in the refractivity across the distance of one wavelength of the signal can be neglected. In case of space geodetic techniques with maximum wavelengths of a few decimeters, the geometrical optics approximation can be used. Therefore the propagation of the signal, i.e. the electromagnetic wave, can be considered as a ray. Hence, the propagation time can be determined using the refractivity just along the ray path of the signal (Nilsson et al. 2013). The electric path length L is defined as

$$L = \frac{t_{signal}}{c}, \tag{3.22}$$

where t_{signal} is the propagation time of the signal and c is the speed of light in vacuum. L of a signal travelling along the ray path S can be determined with the refractive index n at the arc length s along the ray through (Nilsson et al. 2013)

$$L = \int_S n(s)\ \mathrm{d}s. \tag{3.23}$$

Compared to the length of the geometric path G, which is a straight line as it assumes that the signal travels through vacuum instead of the atmosphere, the electric path is longer due to the beforehand mentioned two reasons. On one hand the signal travels at a lower speed through the atmosphere since the speed of light is smaller than in vacuum. On the other hand the geometric signal path S is different from a straight line due to Fermat's principle, which minimizes the electric path length L with respect to propagation time. The geometry behind the atmospheric effect on the signal propagation is depicted in Figure 3.3. Thus, the atmospheric delay ΔL, which

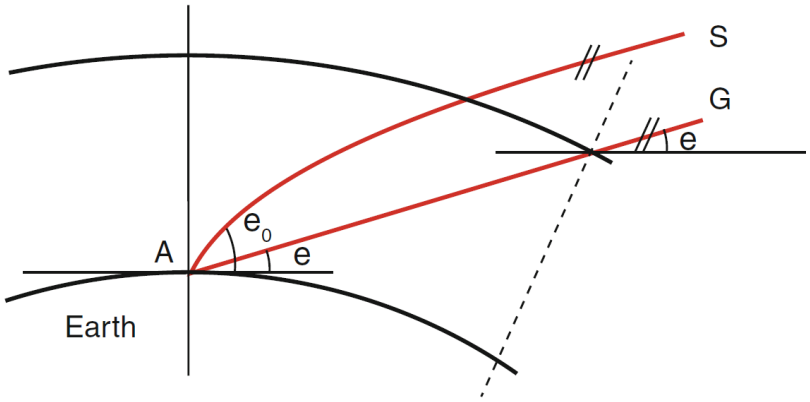

Figure 3.3: Path geometry of a signal S through the atmosphere compared to the geometric path G in vacuum. Figure taken from Nilsson et al. (2013).

expresses the excess in the electric path length L due to the atmosphere, can be defined as (Nilsson

et al. 2013)

$$\begin{aligned}\Delta L &= L - G \\ &= \int_S n(s)\ \mathrm{d}s\ - G \\ &= \int_S [n(s)-1]\ \mathrm{d}s\ + \int_S \mathrm{d}s\ - G \\ &= 10^{-6} \int_S N(s)\ \mathrm{d}s\ + S - G.\end{aligned} \tag{3.24}$$

By applying Equation (3.19) the equation can be splitted into a hydrostatic and a wet part:

$$\begin{aligned}\Delta L &= 10^{-6} \int_S N_h(s)\ \mathrm{d}s\ + 10^{-6} \int_S N_w(s)\ \mathrm{d}s\ + S - G \\ &= \Delta L_h + \Delta L_w + S - G \\ &= \Delta L_h + \Delta L_w + g_{bend},\end{aligned} \tag{3.25}$$

where N_h is the hydrostatic refractivity and N_w is the wet refractivity. $S - G$ accounts for the so-called geometric bending effect g_{bend}. ΔL_h is the slant hydrostatic delay and ΔL_w is the slant wet delay. In common practice the geometric bending effect g_{bend} is added to the slant hydrostatic delay. Therefore also the hydrostatic mapping function includes the geometric bending effect (Nilsson et al. 2013). The mapping functions will be described in Section 3.4.2. Due to this convention usually also the slant total delay includes the geometric bending effect as described in Equation (3.25). In order to distinguish between the different representations a special notation is used in case the geometric bending effect is already added to the slant total and hydrostatic delays. Accordingly the slant total, hydrostatic and wet delays will be noted as STD, SHD and SWD, although the slant wet delay does not include the geometric bending effect. This notation will be used especially in case of results of slant total and hydrostatic delays from program RADIATE, which already contain the geometric bending effect. In case of Equations (3.24) and (3.25), please be aware that the slant total delay is denoted as ΔL and not as STD, although the geometric bending effect is included. This is due to the reason not to complicate the readability of its derivation.

The value for the geometric bending effect g_{bend} is in principle dependent on the elevation angle of the observation. Assuming azimuthal symmetry of the atmosphere, the geometric bending effect is only present in a vertical plane and observations in the zenith direction are not affected by geometric bending. The amount of the geometric bending effect increases with decreasing elevation and can reach values of up to around 20 cm at 5° elevation depending on the meteorology above the station. Examples of the elevation dependency of g_{bend} are presented in Section 6.2.3 and in Appendix Section B.3.

Also ΔL_h and ΔL_w increase with decreasing elevation angle. ΔL_h can reach more than 20 m and ΔL_w at humid sites also even a few metres at around 5° elevation. ΔL_w is strongly dependent

on the meteorology in terms of water vapour content above the station along the slant path.

The delays in the zenith direction, which are also of major importance in space geodesy in combination with mapping functions, can be determined through

$$\Delta L_h^z = 10^{-6} \int_{h_0}^{\infty} N_h(z)\ \mathrm{d}z, \tag{3.26}$$

$$\Delta L_w^z = 10^{-6} \int_{h_0}^{\infty} N_w(z)\ \mathrm{d}z \tag{3.27}$$

with the station height h_0 and the refractivities along the zenith direction. ΔL_h^z is the zenith hydrostatic delay (later also denoted as ZHD) and ΔL_w^z is the zenith wet delay (later also denoted as ZWD) (Nilsson et al. 2013).

Assuming typical conditions of the atmosphere, ΔL_h^z is typically 2.3 m for a station at sea level pressure, whereas ΔL_w^z is dependent on the latitude and increases from a few millimetres at polar regions to around 40 cm at the equator (Nilsson et al. 2013).

According to findings of Saastamoinen (1972) and Davis et al. (1985) accurate determination of the zenith hydrostatic delay can also be done by using the surface pressure at the station. Thus, the so-called zenith hydrostatic delay from Saastamoinen's equation ZHD^S in [m] can be determined by

$$ZHD^S[m] = 0.0022768 \frac{p_0}{f(\varphi_0, h_0)} \tag{3.28}$$

with

$$f(\varphi_0, h_0) = 1 - 0.00266\cos(2\varphi_0) - 0.28 \cdot 10^{-6} h_0 \tag{3.29}$$

and with the total pressure p_0 in [hPa] at the station, the (ellipsoidal) station latitude φ_0 and the (ellipsoidal) station height h_0 in [m] (Nilsson et al. 2013). Thus, ΔL_h^z can be easily found without detailed knowledge about the hydrostatic refractivity above the station as required by Equation (3.26).

Since the zenith wet delay ΔL_w^z is dependent on the temperature, but also on the water vapour pressure, which is highly variable both in location and time and which can not be predicted accurately, the determination of ΔL_w^z through a model is more difficult compared to the hydrostatic domain. Therefore various models for the zenith wet delay have been developed like those shown in Saastamoinen (1972), Böhm et al. (2015), Hopfield (1969), Ifadis (1986), Mendes and Langley (1998) and Mendes (1999). These models can serve as a priori values for the accurate determination of ΔL_w^z, which is usually done within the VLBI analysis. The above referenced zenith wet delay models basically also rely only on the knowledge of the meteorology at the surface similar to the case of the zenith hydrostatic delay. Therefore in most cases at least water vapour pressure or water vapour pressure and temperature at the surface need to be known for such models. Nevertheless the values at the surface can not be seen as representative for the

air-masses situated in the atmosphere above (Nilsson et al. 2013). According to Saastamoinen (1972) the zenith wet delay, denoted here as zenith wet delay from Saastamoinen's equation ZWD^S, can be determined by

$$ZWD^S[m] = 0.0022768(1255 + 0.05T_0)\frac{p_{w0}}{T_0} \tag{3.30}$$

based on the surface water vapour pressure p_{w0} in [hPa] at the station and the surface temperature T_0 in [K] at the station. The factor 0.0022768 is taken from Davis et al. (1985) as they refine the finding of 0.002277 by Saastamoinen (1972).

As a rule of thumb for a rough estimate of the zenith wet delay ZWD, it can be said that the surface water vapour pressure p_{w0} in [hPa] at the station approximates the expectable zenith wet delay in [cm] (Nilsson et al. 2013):

$$ZWD[cm] \approx p_{w0}[hPa]. \tag{3.31}$$

3.4 Concepts of determining path delays in the neutral atmosphere

For the determination of the neutral atmosphere-induced delays of space geodetic observations in principle two different approaches are possible. One is the determination of the delays by external measurements and calculations. The second, more common way is to estimate the delay within the data analysis of the space geodetic technique (Nilsson et al. 2013).

In case the path delays are determined within the analysis, zenith delays are needed in a first step,which are then mapped to the according elevation angles of the observations using so-called mapping functions, which will be described in Section 3.4.2. Since the zenith hydrostatic delays can be determined with sufficient accuracy from surface pressure data with Equation (3.28) that has been described in Section 3.3, no additional estimation of them needs to be done within the analysis. Due to the limited accuracy of zenith wet delays derived from surface data, which has also been described in Section 3.3, it is necessary to estimate the zenith wet delay within the data analysis (Nilsson et al. 2013).

The second possibility of determining the path delays are external sources. Here, ray-tracing or more accurately expressed ray-tracing through Numerical Weather Models (NWM) is an important opportunity to both determine the delays in the neutral atmosphere and contribute to establishing new tropospheric mapping functions. This approach will be described very briefly in the upcoming Section 3.4.1 of this chapter, but extensively in Chapter 4. Besides, also measurements of external instruments like a Water Vapour Radiometer (WVR) can be used directly to infer atmospheric wet delays, i.e. zenith and slant wet delays, from its measurements (Nilsson et al. 2013). A short introduction to the WVR will be given in Section 3.4.3. Furthermore, radiosondes deliver meteorological data applicable for the determination of atmospheric delays together with ray-tracing, but due to the measurement principle their data are not directly used, but serve as an input to enhance the NWM that are then used for ray-tracing. Radiosondes and their data

acquisition will be described in more detail in Section 5.1.1.

3.4.1 Ray-tracing

As already described in Section 1.2, the ray-tracing approach is a promising alternative of determining atmospheric path delays. Instead of utilizing zenith delays from models and/or least-squares adjustment within the data analysis of the space geodetic technique together with mapping functions, ray-tracing can determine the slant path delays directly.

With the use of radiosonde data or NWM, as utilized in this work, refractivity fields can be created. The refractivity values along the signal path are integrated as shown in Equation (3.25) to finally obtain the slant path delay induced by the neutral atmosphere. Since the real propagation path of the signal is usually not known beforehand, it has to be determined in a first step. For this task the ray-tracing technique can be used, which is utilized in many different scientific fields since it quantifies the propagation of an electromagnetic wave through a stratified medium (Nilsson et al. 2013). Since the ray-tracing technique is the dominant part of the determination of the atmospheric path delay, the whole method is simply called ray-tracing.

The slant path delays obtained from ray-tracing can be applied to different space geodetic techniques in order to remove the atmospheric influence from their observations. Besides the application to the VLBI analysis, which is the main target of this work, the ray-traced slant delays can also be applied to GNSS observations. Hobiger et al. (2008b) show the utilization of ray-traced slant delays for GNSS Precise Point Positioning (PPP). Furthermore it is also possible to apply slant delays obtained from ray-tracing to the remote sensing technique Interferometric Synthetic Aperture Radar (InSAR) as described by Hobiger et al. (2010a).

The application of the directly determined slant delays from ray-tracing through NWM data has an important advantage compared to the concept of slant delays derived from zenith delays and mapping functions. As Hobiger et al. (2010b) show for an example of GNSS positioning estimates, the application of ray-traced slant delays received using NWM data improves the results significantly in case of extreme weather situations like a typhoon since the standard mapping functions approach is not able to accurately model such events.

More details on the ray-tracing technique and its formal description by general equations as well as specific equations for different realizations with respect to atmospheric path delay estimation will be given in Chapter 4.

3.4.2 Mapping functions and gradients

In case the path delays are determined within the analysis of the space geodetic method, the delay ΔL (already including the geometric bending effect) can be described using the following equation:

$$\Delta L(e) = \Delta L^z \cdot mf(e), \tag{3.32}$$

where the zenith total delay ΔL^z is mapped to the elevation angle e using the elevation dependent mapping function mf (Nilsson et al. 2013). In detail the elevation angle e is the outgoing or vacuum elevation angle that is determined through the geometry of the observation between the station and the source in case of VLBI. The outgoing elevation angle is needed since the geometric bending effect is already accounted for by the mapping function (Nilsson et al. 2013). Equation (3.32) assumes azimuthal symmetry of the atmosphere, i.e. the delay induced by the atmosphere is thus independent of the azimuth of the observation. Section 3.4.2.2 will describe more realistic approaches by considering the effect of the actual azimuthal asymmetry by gradients.

From Equation (3.32) it can be seen that a mapping function provides the ratio of the slant delay to the zenith delay (Schuh and Böhm 2013).

Equation (3.32) can be used on one side to determine a priori slant delays for the analysis and on the other side the mapping function serves as the partial derivative for the estimation of residual zenith delays within the analysis. In this way residual zenith delays are usually determined within the VLBI or GNSS analysis in intervals of 20-60 minutes. In case of the VLBI analysis this can be done with a least-squares adjustment since there is only one observation per station at a time (Nilsson et al. 2013). Unfortunately, there are correlations between the zenith delays, the station heights and the station clocks (Nothnagel et al. 2002). Therefore, if an erroneous mapping function is introduced to the least-squares adjustment, the estimated station heights and station clocks will also be affected by errors. With respect to Equation (3.32) the following statement can be made: In case the mapping function mf is too large, then the determined zenith delay ΔL^z will be too small since the slant delay is considered not to change. As a consequence the station height is affected and moves upwards (Nilsson et al. 2013). The rule of thumb from Böhm (2004) predicts that the station height error is approximately one fifth of the error in the delay at an elevation angle of 5°. The zenith delay decreases by one half of the according station height increase (Nilsson et al. 2013).

From the observational point of view the correlations between the zenith delays, the station heights and the station clocks can be reduced by observing at low elevations. The drawback in this approach is that the errors in the mapping functions increase rapidly at small elevation angles like 5° or smaller (Schuh and Böhm 2013).

3.4.2.1 Mapping functions and azimuthal symmetry

Assuming azimuthal symmetry, the delay induced by the atmosphere is independent of the azimuth of the observation and thus only dependent on the elevation angle. In case azimuthal symmetry of the atmosphere is assumed, Equation (3.32) can be rewritten according to Davis et al. (1985) as

$$\Delta L(e) = \Delta L_h^z \cdot mf_h(e) + \Delta L_w^z \cdot mf_w(e), \tag{3.33}$$

where ΔL is again the slant total delay and already contains the geometric bending effect. The mapping function is now split into a hydrostatic mapping function mf_h and a wet mapping function mf_w. ΔL, mf_h and mf_w are dependent on the elevation angle e of the observation, i.e. the outgoing elevation angle. The outgoing elevation angle is needed since the bending effect is accounted for by the hydrostatic mapping function (Nilsson et al. 2013). Thus, the zenith delays in the hydrostatic and wet domains ΔL_h^z and ΔL_h^z are mapped to the outgoing elevation angle.

In common practice of VLBI analysis, the zenith wet delays are fully estimated within the analysis (Schuh and Böhm 2013), whereas the zenith hydrostatic delays are a priori determined. This split strategy is possible since the actually for the analysis required a priori zenith total delays in principle have the same mapping function as the instead used a priori zenith hydrostatic delays in case no constraints are applied on the estimated zenith delays (Nilsson et al. 2013). Nevertheless errors are introduced if wrong a priori zenith hydrostatic delays are used, which can not be completely absorbed by the estimated zenith wet delays due to the fact that the hydrostatic and wet mapping functions are different. Therefore the use of a total mapping function would be an advantage. In turn, the downside of this approach is that the value of the total mapping function is similar to that of the hydrostatic one and thus not capable of considering the short-time variations in the wet part, i.e. estimating fast changing zenith wet delays appropriately (Böhm et al. 2006b). This leads to the conclusion of using the split mapping function strategy at least for cases of time resolutions of the mapping functions of 3 hours or lower (Nilsson et al. 2013).

The hydrostatic part has a scale height in the troposphere of about 8 km. The scale height of the wet part is about 2 km (Nilsson et al. 2013). This is also depicted in Figure 3.4, which shows the ratios that define the mapping functions according to Nilsson et al. (2013):

$$mf_h = \overline{P_1P_3} : \overline{Q_3P_3}, \qquad mf_w = \overline{P_1P_2} : \overline{Q_2P_2}, \tag{3.34}$$

where P_1, P_2 and P_3 are points along the ray trajectory at the station position, at the scale height of the wet part and at the scale height of the hydrostatic part. Q_1, Q_2 and Q_3 are the points on the surface corresponding to the points P_1, P_2 and P_3 along the ray trajectory.

From Equation (3.34) and Figure 3.4 it can be seen that the hydrostatic mapping function has a smaller value than the wet mapping function due to the larger hydrostatic scale height and the Earth's curvature. Only for very small elevation angles the hydrostatic mapping function may be larger than the wet one due to the added geometric bending effect that is significantly increased at very low elevations (Nilsson et al. 2013).

In general it can be said that the hydrostatic mapping function is approximately the ratio of the thickness of the atmosphere to the Earth radius (Niell 1996). The flatter, i.e. the thinner, the atmosphere is the more the mapping function approaches the expression $\frac{1}{\sin e}$. Thus, if the atmosphere was totally flat and evenly stratified, the mapping function would be $\frac{1}{\sin e}$ (Nilsson et al. 2013). Since the atmosphere is not totally flat, a more sophisticated formula is needed. According to Marini (1972) any kind of horizontally stratified atmosphere can be described by a

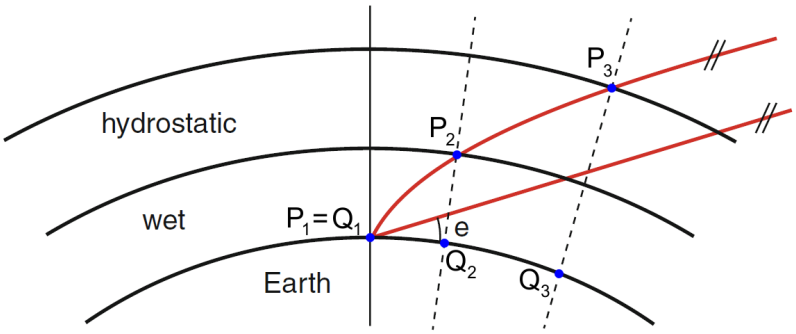

Figure 3.4: Scale heights of the troposphere: about 8 km for the hydrostatic domain and about 2 km for the wet domain. The mapping functions thus can be described using the scale heights in ratios to the according slant path segments. The hydrostatic mapping function has the ratio $mf_h = \overline{P_1P_3} : \overline{Q_3P_3}$. The wet mapping function has the ratio $mf_w = \overline{P_1P_2} : \overline{Q_2P_2}$ (Nilsson et al. 2013). Figure taken from Nilsson et al. (2013) and slightly modified.

continued fraction as

$$mf(e) = \cfrac{1}{\sin(e) + \cfrac{y_1}{\sin(e) + \cfrac{y_2}{\sin(e) + \cfrac{y_3}{\sin(e) + \dots}}}}, \tag{3.35}$$

where the $y_1, y_2, y_3, \dots$ are constants.

A further development has been made by Herring (1992) with the Massachusetts Institute of Technology Temperature (MTT) mapping function, where the y_i are introduced as parameters, which are dependent on latitude, height and temperature at the station. Herring (1992) also altered the continued fraction to

$$mf(e) = \cfrac{1 + \cfrac{y_1}{1 + \cfrac{y_2}{1 + y_3}}}{\sin(e) + \cfrac{y_1}{\sin(e) + \cfrac{y_2}{\sin(e) + y_3}}}, \tag{3.36}$$

which is today a widely accepted form. The numerator is introduced to normalize the fraction in the zenith direction, i.e. the mapping function is 1 in the zenith direction (Niell 2001).

The MTT mapping function (see Herring 1992) shows a strong dependence on the surface temperature. Therefore, Niell (1996) developed the New or also called Niell Mapping Functions

(NMF) (Nilsson et al. 2013). The hydrostatic mapping function is dependent on the station latitude, the height of the station above the sea level and the day of the year. The wet mapping function is only dependent on the station's latitude (Niell 1996). For the NMF no meteorological data at the station are needed, which enables their use at stations without meteorological sensors, which is often a true circumstance at GNSS stations (Nilsson et al. 2013). Niell (1996) derived the NMF, which are valid for elevation angles from the zenith down to 3°, from ray-tracing at nine different elevation angles through profiles of the U.S. Standard Atmosphere at different latitudes and different times. The principal form of the NMF follows Equation (3.36) from Herring (1992). In a least-squares fit the coefficients y_1, y_2 and y_3 have been determined using the ray-traced delays. Thus, with sufficient accuracy of the coefficients the mapping functions in the form of Equation (3.36) are accurate enough to reach 1 mm accuracy at elevation angles down to 3° both in the hydrostatic and the wet domain (Niell 1996).

Today, the most accurate mapping functions, that are available on a global scale, are the Vienna Mapping Functions 1 (VMF1) (see Böhm et al. 2006b) (Schuh and Böhm 2013). This is especially true for the hydrostatic mapping function, whereas in recent times new and probably more accurate wet mapping functions have been developed. Strictly speaking the VMF1 are a further enhanced version of the Vienna Mapping Functions (VMF) (see Böhm and Schuh 2004) through updated coefficients within the mapping functions. The VMF1 are based on the Equation (3.36). The coefficients y_2 and y_3 for the hydrostatic and wet mapping functions have been determined using the NWM data of the ECMWF 40 years re-analysis (ERA-40) model[1] for the year 2001. Ray-tracing through the NWM data has been done at 10 different initial elevation angles at the station down to 3.2° with a subsequent least-squares adjustment for the coefficient determination (Böhm et al. 2006b). The coefficients y_2 and y_3 are dependent on the day of the year and the station latitude and therefore provided as an analytical function (Schuh and Böhm 2013). The coefficient y_1 is determined by using the already known best available coefficients y_2 and y_3 together with the mapping function values determined from ray-tracing at an initial elevation angle of 3.3°. By inverting Equation (3.36) the coefficient y_1 can be calculated (Böhm et al. 2006b). The coefficients y_1 for the hydrostatic and wet mapping functions are determined with a temporal resolution of 6 hours and provided on either a global grid with a resolution of 2° in latitude and 2.5° in longitude or directly for the locations of the specific VLBI stations. As meteorological data for the ray-tracing with respect to the determination of the coefficients y_1 for the hydrostatic and wet mapping functions, operational analysis data and forecast data from the European Centre for Medium-Range Weather Forecasts (ECMWF) are used (Schuh and Böhm 2013). In case of the gridded coefficients y_1 the height correction according to Niell (1996) has to be applied. As a side note it should be mentioned that the ray-tracing approach for the determination of the coefficients for the VMF1 is a one-dimensional (1D) method, i.e. one single refractivity profile in the zenith direction at a station position is used, leading to azimuthally symmetric delays (Nilsson et al. 2013).

[1] ECMWF is the European Centre for Medium-Range Weather Forecasts.

Since the coefficients y_1 of the VMF1 are provided as a continuous time series, regular updates are required in order to be able to use the mapping functions also for the analysis of new observations. Thus, it may be sometimes preferable to have mapping functions that can be used independent of needed updates, i.e. empirical mapping functions. Such a mapping function is provided by the Global Mapping Function (GMF) (see Böhm et al. 2006a). The GMF has again the form of Equation (3.36) for both the hydrostatic and the wet domain. The coefficients y_1, y_2 and y_3 are dependent on the station coordinates, i.e. also a longitude dependence is implicit, and on the day of the year. The coefficients y_2 and y_3 are the same as for the VMF1. Considering the hydrostatic and wet realizations of the coefficient y_1, ray-tracing through the global NWM data of the ERA-40 model of the period September 1999 to August 2002 with a horizontal resolution of 15° x 15° has been done according to the strategy of the VMF1, i.e. at an initial elevation angle of 3.3° (Böhm et al. 2006a). According to the method described by Böhm et al. (2006b) the resulting mapping function values from ray-tracing have been used together with the known coefficients y_2 and y_3 to derive the hydrostatic and wet coefficients for y_1 by inverting Equation (3.36). A drawback of the empirical GMF compared to the VMF1 is that it does not account for special meteorological conditions such as the El Niño event in 2009/10 (Nilsson et al. 2013).

3.4.2.2 Mapping functions and azimuthal asymmetry

In a more realistic modelling of the atmosphere the assumption of azimuthal symmetry has to be rejected since certain climatic and weather phenomena lead to azimuthal asymmetry and thus the delays induced by the atmosphere are dependent on the azimuth angle of the observation. In case of stations at northern latitudes larger delays are received if the observation points towards the South than if the observation points towards the North. This is due to the latitudinally dependent height limit of the troposphere, which is higher above the equator than above the poles (Nilsson et al. 2013). Therefore the signal has a longer path through the troposphere in case of a northern station pointing towards the South than pointing towards the North. Besides this general property of the troposphere also local weather phenomena play a role in the azimuthal asymmetry (Schuh and Böhm 2013).

In order to consider the azimuthal asymmetry horizontal gradients are introduced. Their derivation is described by Davis et al. (1993). In common practice gradients in the North- and East-direction are used to account for the azimuthal asymmetry.

Within the VLBI analysis these North- and East-gradients are usually estimated every 2-24 hours (Schuh and Böhm 2013).

The hydrostatic gradients which are induced by pressure and temperature gradients have a spatial resolution of around 100 km (MacMillan 1995; Gardner 1976). Their temporal scale is in the order of days. The wet gradients are dependent on water vapour content and temperature and have a spatial scale of less than 10 km and a temporal variability of hours or less (MacMillan 1995). However, a stable behaviour on longer time scales is also possible, e.g. at coastal locations (Nilsson et al. 2013). Thus, in general the wet gradients behave similar to the wet delay and show

a much higher variability at both the spatial and the temporal domain.

For the formal description of the atmospheric delays by mapping functions including the accounting for azimuthal asymmetry different approaches have been found. According to findings of MacMillan (1995) the delay can be calculated in dependence on azimuth α and elevation e as

$$\Delta L(\alpha, e) = \Delta L_0(e) + mf_h(e)\cot(e)[G_N\cos(\alpha) + G_E\sin(\alpha)], \tag{3.37}$$

where $\Delta L_0(e)$ is the atmospheric delay from Equation (3.33) assuming azimuthal symmetry. G_N and G_E are the gradients in North- and East-direction, which are used together with the hydrostatic mapping function mf_h. This model is similar to findings of Davis et al. (1993) and Herring (1992) and presented as denoted in (Nilsson et al. 2013). A strict form of Equation (3.37) would require the usage of the refracted elevation angle instead of the vacuum elevation angle e within the $\cot(e)$ according to Davis et al. (1993).

A different model is proposed by Chen and Herring (1997), where the delay including the azimuthal asymmetry treatment can be calculated according to the equation in the form presented in Nilsson et al. (2013) by

$$\Delta L(\alpha, e) = \Delta L_0(e) + mf_g(e)[G_N\cos(\alpha) + G_E\sin(\alpha)] \tag{3.38}$$

with

$$mf_g(e) = \frac{1}{\sin(e)\tan(e) + C_{grad}}, \tag{3.39}$$

where

$$C_{grad} = \frac{3h_{scale}}{R_E}. \tag{3.40}$$

$\Delta L_0(e)$ is again the atmospheric delay from Equation (3.33) assuming azimuthal symmetry. For the gradient mapping function mf_g the coefficient C_{grad} is used, which depends on the scale height of the neutral atmosphere h_{scale} for the hydrostatic or wet part and on the Earth radius R_E. Chen and Herring (1997) have found the following values for C_{grad}: Assuming a scale height for the hydrostatic part of 6.5 km, $C_{grad} = 0.0031$ and assuming a scale height for the wet part of 1.5 km, $C_{grad} = 0.0007$. In case of total gradients they use $C_{grad} = 0.0032$ (Chen and Herring 1997; Herring 1992; Nilsson et al. 2013).

According to Rothacher et al. (1998) the atmospheric gradients can also be described as a tilting of the mapping function by an angle β. This is depicted in Figure 3.5. According to the formalism presented in Nilsson et al. (2013), the delay, including the effect of an atmospheric

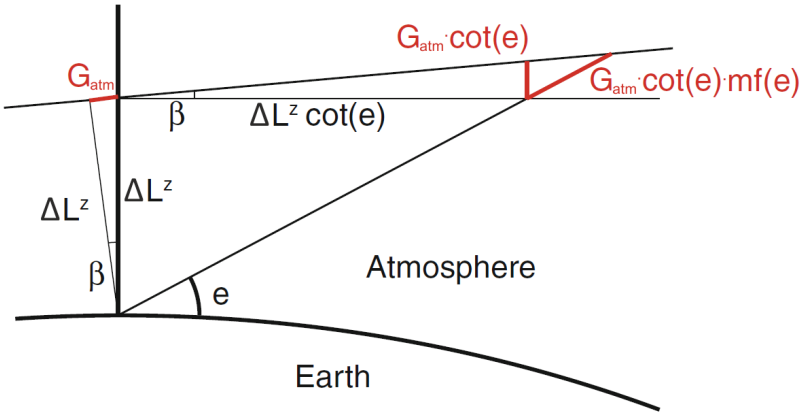

Figure 3.5: Atmospheric gradients can be described according to Rothacher et al. (1998) by the tilting of the mapping function by the angle β under the assumption of a horizontally stratified atmosphere. Figure taken from Nilsson et al. (2013) and slightly modified.

gradient G_{atm} through a tilting of the mapping function, can be described as

$$\Delta L(e-\beta) = \Delta L^z \cdot mf(e-\beta) \approx \Delta L^z \left(mf(e) + \frac{\partial mf}{\partial e}(-\beta) \right). \tag{3.41}$$

Note that due to the mf the geometric bending effect is included in ΔL. Under the assumption of a flat atmosphere, $\frac{1}{\sin(e)}$ can be used as mapping function. Furthermore it is assumed that the zenith delay ΔL^z is not altered due to the tilting (Nilsson et al. 2013). The tilting angle β can be derived from Figure 3.5 through trigonometry as

$$\sin\beta = \frac{G_{atm}}{\Delta L^z}, \tag{3.42}$$

which can be approximated for a small β to

$$\beta \approx \frac{G_{atm}}{\Delta L^z}. \tag{3.43}$$

Thus, from the above assumptions and declarations Equation (3.41) can be rewritten as (Nilsson et al. 2013)

$$\Delta L(e-\beta) = \Delta L^z \cdot mf(e) + \cot(e) mf(e) G_{atm}, \tag{3.44}$$

which is exactly the finding of MacMillan (1995) given in Equation (3.37). In case of a gradient G_{atm} of 1 mm the corresponding tilting angle β is 1.5' for the hydrostatic and 17' for the wet domain. In principle the tilting also affects the zenith delay, but due to sizes of $2 \cdot 10^{-4}$ mm for the zenith hydrostatic and $2 \cdot 10^{-5}$ mm for the zenith wet delay, these influences are negligible (Nilsson et al. 2013).

For the analysis of space geodetic observations it is necessary to determine the atmospheric

gradients. This is especially crucial for observations at low elevations. The application of a priori gradients to the analysis is not needed as long as there are no constraints applied on their residual estimation (Nilsson et al. 2013). Thus, in a standard analysis approach gradients are only estimated within the analysis, e.g. by a least-squares adjustment.

3.4.3 Water vapour radiometer

Using the instrumentation of a Water Vapour Radiometer (WVR) it is possible to derive the atmospheric wet delay from its measurements of the thermal radiation in the sky. The observations are carried out at those microwave frequencies at which the atmospheric attenuation is relatively high due to the absorption by the water vapour. The attenuation of the measurement signal is generally dependent on frequency, temperature, pressure, humidity and liquid water content. Therefore it is possible to determine humidity profiles from WVR measurements, which can in turn be used to estimate the atmospheric wet delay (Nilsson et al. 2013). This means that slant wet delays can be determined from WVR measurements for e.g. VLBI observations.

Due to the fact that the beam width of most WVR is quite large, covering several degrees, the application of the WVR is limited to elevation angles larger than 15° to 20° in order to avoid interference with radiation from the ground. Therefore slant wet delays for observations at smaller elevation angles can only be derived using extrapolation of WVR measurements, which may lead to errors. Furthermore the utilization of a WVR is not possible during rain fall (Nilsson et al. 2013).

Chapter 4

Ray-tracing for geodetic VLBI

This chapter builds upon the findings of the last chapter with regard to the propagation of microwave signals in the neutral atmosphere and its effects on the signal compared to vacuum propagation. In the beginning the formal prerequisites of ray-tracing in form of the equation systems are presented. These are needed to derive the propagation path of microwave signals in the neutral atmosphere for the determination of the path delays. A main focus is set in this chapter also on different applied realizations of the ray-tracing approach, which are implemented in the operational ray-tracing program RADIATE. Following the theoretical background and the practical implementations of ray-tracing in Section 4.1, further important parts of a complete ray-tracing program are introduced with regard to program RADIATE. Therefore the remaining major steps from the preparation of the meteorological data to the final delay calculation are presented in Section 4.2.

4.1 Theoretical background of ray-tracing and applied realizations

As already stated in Section 3.3 the geometrical optics approximation is assumed to be valid for atmospheric ray-tracing for space geodetic techniques. Thus, the electromagnetic wave propagation can be considered as a ray. The basic equation for ray-tracing is the so-called Eikonal equation, which needs to be solved in order to get the ray path and the optical path length. The Eikonal equation itself is the solution of the so-called Helmholtz equation with respect to electromagnetic waves that propagate through a medium with only slow variations in refractivity, i.e. the variation over a distance equal to the wavelength is insignificant, under the assumption that diffraction effects can be neglected (Iizuka 2008; Wheelon 2001; Nilsson et al. 2013; Gegout et al. 2011; Nafisi et al. 2012b).

The Eikonal equation can be derived from Maxwell's equations (3.1a) to (3.1d) with the assumptions of no free charges and zero conductivity in the medium and a small vacuum wavelength of the signal according to Wheelon (2001), Born and Wolf (1999) and Nilsson et al. (2013) as

$$\|\nabla L\|^2 = n(\vec{r})^2, \tag{4.1}$$

where L is the optical path length, although initially defined as electric path length, since the geometrical optics approximation has been assumed to be valid leading to the propagation as a ray. The components of ∇L describe the ray directions. The refractive index n of the medium has already been defined by Equation (3.4). The vector $\vec{r}$ represents the position vector (Nilsson et al. 2013). The basic equation of the geometrical optics is represented through the Eikonal equation (4.1). $L(\vec{r}) = constant$ define so-called geometrical wave surfaces or geometrical wave-fronts (Born and Wolf 1999).

The Eikonal equation represents a partial differential equation of the first order for $n(\vec{r})$. Upon many different forms of alternatively representing the equation one important is the Hamiltonian canonical formalism as it is represented here according to Born and Wolf (1999), Červený (2005), Nafisi et al. (2012a) and Nilsson et al. (2013):

$$H(\vec{r}, \nabla L) \equiv \frac{1}{a}\left\{(\nabla L \cdot \nabla L)^{\frac{a}{2}} - n(\vec{r})^a\right\} = 0, \tag{4.2a}$$

$$\frac{\mathrm{d}\vec{r}}{\mathrm{d}u} = \frac{\partial H}{\partial \nabla L}, \tag{4.2b}$$

$$\frac{\mathrm{d}\nabla L}{\mathrm{d}u} = -\frac{\partial H}{\partial \vec{r}}, \tag{4.2c}$$

$$\frac{\mathrm{d}L}{\mathrm{d}u} = \nabla L \cdot \frac{\partial H}{\partial \nabla L}. \tag{4.2d}$$

Equations (4.2a) to (4.2d) enable the definition of a ray-tracing system by setting the scalar a to a suitable value (Nafisi et al. 2012a). Generally a is a real number, but in the presented context it can be considered to be an integer number. By setting a, the type of the parameter of interest u is defined (Nilsson et al. 2013). Table 4.1 lists different possible cases for a. $H(\vec{r}, \nabla L)$ is the so-called

Table 4.1: Different cases for a in order to set the type of the parameter of interest u in the Hamiltonian formalism. Table is according to Nafisi et al. (2012a) and according to the findings of Červený (2005).

a	$\mathrm{d}u$	Parameter of interest u
0	$\mathrm{d}u = \mathrm{d}t$	Travel time t along the ray
1	$\mathrm{d}u = \mathrm{d}s$	Arc length s along the ray
2	$\mathrm{d}u = \mathrm{d}\sigma = \frac{\mathrm{d}t}{n^2}$	Natural variables along the ray

Hamiltonian function or simply Hamiltonian. In case of a three-dimensional (3D) coordinate system the Hamiltonian canonical formalism consists of seven equations. Equations (4.2b) and (4.2c) need to be solved together and lead to six equations that deliver the result $\vec{r} = \vec{r}(u)$, i.e. the trajectory of the propagating signal. The seventh equation is Equation (4.2d), whose solution is independent of the other equations and can be solved for the optical path length L[1] (Nafisi et al. 2012a).

[1] Due to the geometrical optics approximation the electric path length L is equivalent to the optical path length.

In order to solve the Hamiltonian for the atmospheric delay along the ray path, $a = 1$ is chosen[1] according to Table 4.1. As a coordinate system in principle any curvilinear system, also a non-orthogonal system, may be chosen, but a spherical polar coordinate system (r, φ, λ) suits usually best for the atmospheric ray-tracing application. Thus Equation (4.2a) can be written as

$$H(r,\vartheta,\lambda,L_r,L_\vartheta,L_\lambda) \equiv \left(L_r^2 + \frac{1}{r^2}L_\vartheta^2 + \frac{1}{r^2\sin^2\vartheta}L_\lambda^2\right)^{\frac{1}{2}} - n(r,\vartheta,\lambda,t) = 0 \tag{4.3}$$

with the radial distance r, the co-latitude ϑ ($0 \leqslant \vartheta \leqslant \pi$) and the longitude λ ($0 \leqslant \lambda \leqslant 2\pi$). The components of L in the ray directions are $L_r = \partial L/\partial r$, $L_\vartheta = \partial L/\partial\vartheta$ and $L_\lambda = \partial L/\partial\lambda$ (Nafisi et al. 2012a). Additionally to the spatial dependence, a temporal dependence on the time t is introduced to the refractive index n due to its temporal variability.

Equation (4.3) is now substituted into Equations (4.2b) and (4.2c) to receive the first six equations of the equation system, as stated before, in a 3D medium in spherical coordinates:

$$\frac{\mathrm{d}r}{\mathrm{d}s} = \frac{1}{\omega}L_r, \tag{4.4a}$$

$$\frac{\mathrm{d}\vartheta}{\mathrm{d}s} = \frac{1}{\omega}\frac{L_\vartheta}{r^2}, \tag{4.4b}$$

$$\frac{\mathrm{d}\lambda}{\mathrm{d}s} = \frac{1}{\omega}\frac{L_\lambda}{r^2\sin^2\vartheta}, \tag{4.4c}$$

$$\frac{\mathrm{d}L_r}{\mathrm{d}s} = \frac{\partial n(r,\vartheta,\lambda,t)}{\partial r} + \frac{1}{\omega r}\left(\frac{L_\vartheta^2}{r^2} + \frac{L_\lambda^2}{r^2\sin^2\vartheta}\right), \tag{4.4d}$$

$$\frac{\mathrm{d}L_\vartheta}{\mathrm{d}s} = \frac{\partial n(r,\vartheta,\lambda,t)}{\partial\vartheta} + \frac{1}{\omega}\frac{L_\lambda^2}{r^2\sin^3\vartheta}, \tag{4.4e}$$

$$\frac{\mathrm{d}L_\lambda}{\mathrm{d}s} = \frac{\partial n(r,\vartheta,\lambda,t)}{\partial\lambda} \tag{4.4f}$$

with the auxiliary parameter ω:

$$\omega = \left(L_r^2 + \frac{1}{r^2}L_\vartheta^2 + \frac{1}{r^2\sin^2\vartheta}L_\lambda^2\right)^{\frac{1}{2}} = n(r,\vartheta,\lambda,t) \tag{4.5}$$

(Nafisi et al. 2012a). Again the variation of n with time t is considered.

The six partial differential equations (4.4a) to (4.4f) have to be solved together. This can be done by numerical integration for example with the Runge-Kutta method leading to the positions of the points along the ray trajectory (Nafisi et al. 2012a). Thus, the signal propagation path can be determined.

According to (Červený 2005; Nafisi et al. 2012a) the following initial conditions at the starting point, i.e. at the station position, can be used to solve these partial differential equations which

[1] In principle the setup of the equations for the application of atmospheric ray-tracing can also be done with $a = 2$ as shown by Gegout et al. (2011).

build the ray-tracing system:

$$r = r_0, \tag{4.6a}$$
$$\vartheta = \vartheta_0, \tag{4.6b}$$
$$\lambda = \lambda_0, \tag{4.6c}$$
$$L_{r_0} = n_0 \cos\zeta_0, \tag{4.6d}$$
$$L_{\vartheta_0} = n_0 r_0 \sin\zeta_0 \cos\alpha_0, \tag{4.6e}$$
$$L_{\lambda_0} = n_0 r_0 \sin\zeta_0 \sin\alpha_0 \sin\vartheta_0, \tag{4.6f}$$

where r_0, ϑ_0, λ_0, n_0, L_{r_0}, L_{ϑ_0} and L_{λ_0} describe initial values for the individual quantities. α_0 is the initial geodetic azimuth and ζ_0 is the initial geodetic zenith angle.

Concerning the 3D case, the gradient of the refractive index $\nabla n(r,\vartheta,\lambda)$ must be taken into account since it influences the ray bending and thus acts on the result of the total delay (Nafisi et al. 2012a). In case of spherical coordinates it is defined according to Nafisi et al. (2012a) as

$$\nabla n(r,\vartheta,\lambda) = \frac{\partial n(r,\vartheta,\lambda,t)}{\partial r} + \frac{1}{r}\frac{\partial n(r,\vartheta,\lambda,t)}{\partial \vartheta} + \frac{1}{r\sin\vartheta}\frac{\partial n(r,\vartheta,\lambda,t)}{\partial \lambda}. \tag{4.7}$$

Equations (4.4d), (4.4e) and (4.4f) contain the gradient components ∇n_r, ∇n_ϑ and ∇n_λ of the refractive index in the domains of the spherical coordinate system, which are explicitly

$$\nabla n_r = \frac{\partial n(r,\vartheta,\lambda,t)}{\partial r}, \tag{4.8a}$$
$$\nabla n_\vartheta = \frac{\partial n(r,\vartheta,\lambda,t)}{\partial \vartheta}, \tag{4.8b}$$
$$\nabla n_\lambda = \frac{\partial n(r,\vartheta,\lambda,t)}{\partial \lambda}. \tag{4.8c}$$

Their determination is needed in order to be able to solve the ray-tracing equation system (Nafisi et al. 2012a).

After having found the solution for the signal trajectory, the optical path length L[1] needs to be determined since it is the goal of atmospheric ray-tracing to estimate the path delay. According to Nafisi et al. (2012a) the substitution of Equation (4.3) into Equations (4.2d) delivers the seventh equation of the ray-tracing system out of the Hamiltonian formalism, whose result is the optical path length

$$L = \int_S n(r,\vartheta,\lambda,t)\,\mathrm{d}s, \tag{4.9}$$

which has already been depicted in Section 3.3 by Equation (3.23). Again the temporal dependence of the refractive index is additionally accounted for here. With the trajectory of the ray

[1] Due to the geometrical optics approximation the electric path length L is equivalent to the optical path length.

calculated by Equations (4.4a) to (4.4f) the refractive indices along the path can be determined and thus the optical path length can be calculated with Equation (4.9) (Nafisi et al. 2012a).

Thus, the atmospheric delay ΔL can be determined by

$$\Delta L = L - G, \tag{4.10}$$

which has also already been described in Section 3.3 by Equation (3.24), through the simple subtraction of the geometric path in vacuum G, which is the straight line distance, from the optical path length L of the propagation of the signal in the atmosphere (Nilsson et al. 2013).

The 3D ray-tracing system can be reduced to a two-dimensional (2D) system by limiting the ray path to a vertical plane, which means that a fixed azimuth is assumed for the ray-tracing. In this case the gradient components of the refractive index in the direction of the co-latitude ∇n_ϑ and in the direction of the longitude ∇n_λ are set to zero:

$$\nabla n_\vartheta = \frac{\partial n(r,\vartheta,\lambda,t)}{\partial \vartheta} = 0, \tag{4.11a}$$

$$\nabla n_\lambda = \frac{\partial n(r,\vartheta,\lambda,t)}{\partial \lambda} = 0 \tag{4.11b}$$

(Nafisi et al. 2012a). This leads to the vanishing of the horizontal gradients and just the gradient in the radial direction is preserved. If this is applied to Equations (4.4a) to (4.4f), the system of the six partial differential equations is reduced to the following four equations:

$$\frac{\mathrm{d}r}{\mathrm{d}s} = \frac{1}{\omega} L_r, \tag{4.12a}$$

$$\frac{\mathrm{d}\vartheta}{\mathrm{d}s} = \frac{1}{\omega}\frac{L_\vartheta}{r^2}, \tag{4.12b}$$

$$\frac{\mathrm{d}L_r}{\mathrm{d}s} = \frac{\partial n(r,\vartheta,\lambda,t)}{\partial r} + \frac{1}{\omega r}\left(\frac{L_\vartheta^2}{r^2} + \frac{L_\lambda^2}{r^2\sin^2\vartheta}\right), \tag{4.12c}$$

$$\frac{\mathrm{d}L_\vartheta}{\mathrm{d}s} = \frac{1}{\omega}\frac{L_\lambda^2}{r^2\sin^3\vartheta} \tag{4.12d}$$

with ω as described by Equation (4.5) (Nafisi et al. 2012a). In the 2D case the seventh equation of the 3D case (Equation (4.9)) remains unchanged and is still valid (Nafisi et al. 2012a).

From the above findings different 2D ray-tracing approaches have been developed with different applied further simplifications of the strict solution of the Eikonal equation and thereby valuable savings in computational efforts compared to the strict 3D solution of the Eikonal equation. Three of these 2D approaches will be described in the following sections as they are implemented in the ray-tracing program RADIATE, which will be discussed in Section 4.2 in more detail.

4.1.1 Piecewise-linear ray-tracing approach

A simple but powerful 2D ray-tracing approach with respect to processing speed and accuracy is the so-called piecewise-linear (PWL) method as described by Böhm (2004). The basic equations for this approach are taken from Böhm (2004), who describes the one-dimensional (1D) application of this ray-tracing method since he uses only a single vertical profile of the refractive index at the station position in his work.

The geometry of the PWL approach is shown in Figure 4.1. For the use of this method in a

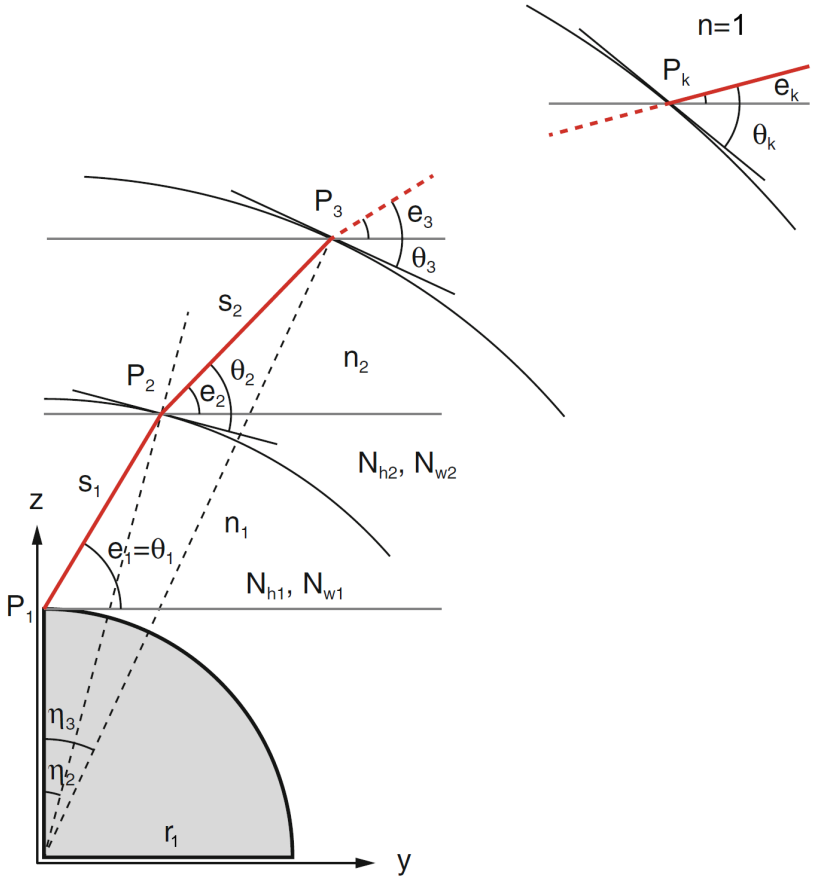

Figure 4.1: Geometry of the PWL ray-tracing approach. For 2D ray-tracing the refractive indices are dependent on both the vertical and the horizontal location. For simplicity the figure only shows the 1D case, where the refractive indices are only changing with height. The η_i are the geocentric angles to the ray points P_i. Figure taken from Nilsson et al. (2013) and slightly modified and corrected.

2D-way, just like for all other multi-dimensional ray-tracing approaches, it is necessary to have a 3D field of refractive indices $n^*(\varphi, \lambda, h)$. In detail this means that the total, hydrostatic and wet refractive indices n^*, n_h^* and n_w^* need to be known at discrete horizontal locations of latitude φ and longitude λ as well as at specific height levels h. According to Hobiger et al. (2008a) the used height system should be geometric or ellipsoidal heights since the ray-tracing is done in a geodetic reference system. In case of program RADIATE ellipsoidal heights are used. The height

levels should reach from the station height (level 1) up to the height (level k) at which the neutral atmosphere does not contribute to the delay any more, i.e. the heights above can be considered as free space, which does not affect the signal propagation. The denser the different height levels are available the more accurate the PWL ray-tracing approach works since for the signal propagation in the intermediate layer between two height levels a constant mean refractive index will be assumed. Thus, smaller level spacing increases the resolution of the later determined ray path and delay. The topic of the vertical resolution will be described in Section 4.2.2. For nomenclature clarification it should be stated that the total refractive index and thus also the delay is separated into the hydrostatic and non-hydrostatic part as described in Section 3.3. For convenience the non-hydrostatic part of the refractive index as well as the one of the delay will be called wet part. For a better readability the dependence of the refractive index on the horizontal position as described above will be implicitly assumed in the following without explicit annotation. Only the height level dependence is explicitly noted as it is the most essential part of the ray-tracing method.

As a first step it is necessary to determine the mean total, hydrostatic and wet refractive index values between two adjacent height levels in order to get the value for the covered height interval between the levels, i.e. the so-called intermediate layer. These mean values will be used for the ray-tracing and the delay calculation. Averaging leads to

$$n_i = \frac{n_i^* + n_{i+1}^*}{2} \qquad i = 1, \ldots, k-1 \tag{4.13a}$$

$$n_{h,i} = \frac{n_{h,i}^* + n_{h,i+1}^*}{2} \qquad i = 1, \ldots, k-1 \tag{4.13b}$$

$$n_{w,i} = \frac{n_{w,i}^* + n_{w,i+1}^*}{2} \qquad i = 1, \ldots, k-1 \tag{4.13c}$$

where n_i, $n_{h,i}$ and $n_{w,i}$ are the resulting mean total, hydrostatic and wet refractive indices valid at the intermediate height between the adjacent discrete levels with the total, hydrostatic and wet refractive indices n^*, n_h^* and n_w^*. Thus, $k-1$ mean refractive indices are determined in each domain. As the upcoming ray-tracing system needs also a k-th value, the refractive indices for the layer above the neutral atmosphere representing vacuum are set to

$$n_k = 1, \tag{4.14a}$$

$$n_{h,k} = 1, \tag{4.14b}$$

$$n_{w,k} = 1. \tag{4.14c}$$

The distances r_i of each discrete height level to the Earth's centre can be determined using the Earth radius R_E and the individual heights h_i, i.e. ellipsoidal heights, of the levels i above the surface through (Böhm 2004)

$$r_i = R_E + h_i \qquad i = 1, \ldots, k. \tag{4.15}$$

A detailed description for determining the Earth radius R_E will be given in Section 4.2.3.

For the start of the ray-tracing the elevation angle e_1 at the station position must be known. Usually only the so-called outgoing elevation angle $e_{out} = e_k$, which represents the elevation angle at the transition from the atmosphere to the non-influencing space, is known from the observation geometry between the station and the radio source in case of VLBI. This angle is also called the vacuum elevation angle since it is the elevation angle of the unaffected signal in case the atmosphere was replaced by vacuum. Therefore this value is normally used together with an a priori geometric bending effect correction g_{apbend} in order to approximate the actual elevation angle e_1 at the station position and to use it as starting point for the ray-tracing. At the end of the first ray-tracing calculation the outgoing elevation angle from ray-tracing e_{outrt} is received and may not firsthand correspond to the outgoing elevation angle of the observation e_{out}. In case of the PWL ray-tracing approach this angle is denoted as e_k. Thus, iterations of the ray-tracing need to be made by altering the previously used elevation angle e_1 at the station position by the difference in the outgoing elevation angle Δe_{out} of the actual and the ray-traced outgoing elevation angle:

$$\Delta e_{out} = e_{out} - e_{outrt}. \tag{4.16}$$

Only in case of the first ray-tracing run the elevation angle at the station e_1 is set to

$$e_1 = e_{out} + g_{apbend}, \tag{4.17}$$

where g_{apbend} is the a priori geometric bending correction. This value can be determined using a model. One sufficient empirical model for this task that delivers g_{apbend} in [deg] is proposed by Hobiger et al. (2008a):

$$\Delta g_{apbend}(e_{out}, h_0)[deg] = \frac{C_b \exp\left(\frac{-h_0}{6000}\right)}{\tan e_{out}} \tag{4.18}$$

with the (ellipsoidal) height of the station h_0 in [m] and the empirical constant $C_b = 0.02$, that has been determined from fitting of different ray-tracing results. This model is accurate enough to reduce the number of iterations of ray-tracing, but it is also simple enough not to cost too much extra processing time itself (Hobiger et al. 2008a). Therefore this model is used in program RADIATE. Examples for more sophisticated models are presented by Choi (1996) and Schulkin (1952).

For upcoming iterations e_1 is set without using g_{apbend}, but instead Δe_{out} from Equation (4.16) is used, which implies the result of e_{outrt} of the latest ray-tracing result inside:

$$e_1 = e_{out} + \Delta e_{out}. \tag{4.19}$$

The ray-tracing iteration is stopped if Δe_{out} is smaller than a certain threshold, i.e. the ray-

tracing has reached the targeted e_{out} with a defined accuracy. The definition of an appropriate value for this limit in order to reach a predefined inner accuracy of the delay[1] will be described in Section 5.5.

For the ray-tracing calculations itself not the elevation angles e_i are used, whose reference is fixed to the horizontal plane at the station position, but instead θ_i are used, which reference the elevation angles always to the horizontal plane at each point i along the ray trajectory. I.e. the θ_i are defined as the angles between the ray trajectory and the tangent of the height layer at each ray point. Thus, at the initial position, i.e. the station position,

$$\theta_1 = e_1. \tag{4.20}$$

Constraining the ray path to the vertical plane of constant azimuth leads to the reduction from a 3D to a 2D ray-tracing system. Thus, the PWL ray-tracing can be done in a 2D Cartesian Y-Z-coordinate system, which has its origin at the Earth's centre. The Z-axis is defined through the straight line between the Earth's centre and the station position. The Y-axis is perpendicular and set to the azimuth-direction of the observation that is ray-traced. Hence the first point of the ray trajectory (P_1), i.e. the station position, has the following coordinates:

$$Z_1 = r_1, \qquad Y_1 = 0. \tag{4.21}$$

Approximation of the ray trajectory as the sum of piecewise-linears establishes the PWL ray-tracing approach as depicted in Figure 4.1. This stepwise reconstruction of the signal path can be done inside a loop of $i = 1 : (k-1)$ using the upcoming Equations (4.22) to (4.27) for the determination of the point P_{i+1} in each cycle. This leads to the full determination of the signal path through the discrete points P_1 to P_k.

From geometry the distance s_i between the ray point P_i at height level i to the next point P_{i+1} along the trajectory located at height level $i+1$ can be determined by (Böhm 2004)

$$s_i = -r_i \sin\theta_i + \sqrt{r_{i+1}^2 - r_i^2 \cos^2\theta_i}. \tag{4.22}$$

Accordingly, the next point P_{i+1} can then be determined from trigonometry as (Böhm 2004)

$$Z_{i+1} = Z_i + s_i \sin e_i, \qquad Y_{i+1} = Y_i + s_i \cos e_i. \tag{4.23}$$

The angle θ_{i+1} at which the ray leaves the newly determined point P_{i+1} can be determined according to Böhm (2004) by Equation (4.24). Remember that the value of θ_1 has already been

[1] With inner accuracy of a delay the accuracy of a delay within a specific ray-tracing approach is meant, not considering the overall accuracy of the approach itself.

determined by the elevation angle at the station (see Equation (4.20)).

$$\theta_{i+1} = \arccos\left(\frac{n_i}{n_{i+1}}\cos(\theta_i + \eta_{i+1} - \eta_i)\right), \tag{4.24}$$

where η_i and η_{i+1} are the geocentric angles to the ray points P_i and P_{i+1}. Note that the value of η_1 is defined through the coordinate system to be

$$\eta_1 = 0. \tag{4.25}$$

η_{i+1} is determined by (Böhm 2004)

$$\eta_{i+1} = \arctan\frac{y_{i+1}}{z_{i+1}}. \tag{4.26}$$

Equation (4.24) applies Snell's law of refraction and therefore needs the total refractive index n_i in the intermediate height layer i and the total refractive index n_{i+1} in the intermediate height layer $i+1$ determined by Equation (4.13a) or Equation (4.14a). Since there is beside the height dependence of n also a dependence on the latitude φ and longitude λ, each n_i has to be determined from the 3D field of mean refractive indices with respect to the spherical position $(\varphi_i, \lambda_i, h_i)$ of the ray point P_i. As the radial component is already given from the layer structure, only the latitude φ_i and longitude λ_i in case of the ray point P_i have to be determined in order to retrieve the according refractive index in the 3D field. In case of program RADIATE the latitude and longitude of each ray point is determined by the use of azimuth and geocentric angles. The detailed method is described in Section 4.2.4.

Thus, with the gained knowledge of φ and λ of a ray point the total refractive index at the desired (horizontal) position in a specific height layer of the discrete 3D field of mean refractive indices can be determined by using a horizontal interpolation method like the bilinear interpolation as in case of program RADIATE, which is described in Section 4.2.5.

With respect to the later determination of the delays in the total, hydrostatic and wet domains it is reasonable to simultaneously calculate also the hydrostatic and wet refractive indices at the ray point.

The elevation angle at the ray point P_{i+1} can be determined by (Böhm 2004)

$$e_{i+1} = \theta_{i+1} - \eta_{i+1}. \tag{4.27}$$

After incrementally reconstructing the signal path from the station point P_1 to the point P_k at which the signal enters or leaves the delay relevant part of the atmosphere and after successful iteration of the ray path to reach the actual outgoing elevation angle with the desired accuracy, the final ray trajectory that represents the observation path is determined. This information, i.e. the values of the refractive indices along the path, can now be used to determine the atmospheric delay. Using the findings of Equation (3.25) the slant total delay ΔL (without geometric bending

effect), slant hydrostatic delay ΔL_h and slant wet delay ΔL_w can be calculated according to Böhm (2004) as the sums of the incremental delays along the slant distances s_i:

$$\Delta L = \sum_{i=1}^{k-1}[(n_i - 1)s_i], \qquad \Delta L_h = \sum_{i=1}^{k-1}[(n_{h,i} - 1)s_i], \qquad \Delta L_w = \sum_{i=1}^{k-1}[(n_{w,i} - 1)s_i], \tag{4.28}$$

where the total, hydrostatic and wet refractive indices n_i, $n_{h,i}$ and $n_{w,i}$ have been determined during the ray-tracing at the horizontal positions of the ray points at the intermediate height levels from the according 3D field of refractive indices.

The geometric bending effect g_{bend} as part of the atmospheric delay described by Equation (3.25) is calculated by (Böhm 2004)

$$g_{bend} = \sum_{i=1}^{k-1}[s_i - \cos(e_i - e_k) \cdot s_i], \tag{4.29}$$

where the individual elevation angles e_i at each ray point are used together with the final outgoing elevation angle $e_{out} = e_k$ and the slant distances s_i.

As already mentioned in Section 3.3, the geometric bending effect is usually applied to the hydrostatic delay and therefore it is also part of the total delay. Thus, the notation for the slant total delay STD, the slant hydrostatic delay SHD and the slant wet delay SWD that is used for referring to results of program RADIATE are meant to include the geometric bending effect in the total and hydrostatic domains:

$$STD = \Delta L + g_{bend}, \qquad SHD = \Delta L_h + g_{bend}, \qquad SWD = \Delta L_w. \tag{4.30}$$

Additionally to the slant delays also the zenith total delay ZTD, the zenith hydrostatic delay ZHD and the zenith wet delay ZWD, as they will be denoted in the following, can be determined by (Böhm 2004)

$$ZTD = \sum_{i=1}^{k-1}[(n_i^z - 1)\Delta h_i], \quad ZHD = \sum_{i=1}^{k-1}[(n_{h,i}^z - 1)\Delta h_i], \quad ZWD = \sum_{i=1}^{k-1}[(n_{w,i}^z - 1)\Delta h_i]. \tag{4.31}$$

For this task the signal path derived from ray-tracing is not needed, but the height differences Δh_i between each two consecutive height levels h in zenith direction:

$$\Delta h_i = h_{i+1} - h_i \qquad\qquad i = 1, \ldots, k-1. \tag{4.32}$$

Furthermore the mean refractive indices in zenith direction (n^z, n_h^z and n_w^z) are needed. They can be determined from the 3D fields of mean refractive indices (as determined by Equations (4.13a) to (4.13c)) by horizontal interpolation at the station position at all intermediate height layers, e.g. using again a bilinear interpolation as in case of program RADIATE. From Equation (4.29)

it can be seen that the geometric bending effect vanishes in the zenith direction, so the zenith delays do not contain a contribution originating from the geometric bending effect.

A fundamental requirement of the PWL approach is a sufficient high resolution of the vertical domain in terms of a high number of discrete height levels at which the linear segments start and end in order to sufficiently approximate the originally curved ray path. Thus, as described in Thayer (1967) and presented in Section 4.1.3 a more accurate approach that introduces curved ray paths can remedy the disadvantage of the high number of needed height levels for accurate ray-tracing. However, also the simple PWL approach can be further enhanced, as described by Hobiger et al. (2008a), in a way that the impact of the vertical resolution of the refractive index can be reduced, so that also a sparser distribution of height levels can be used for accurate ray-tracing. This alternative version of the basic PWL approach will be described in the upcoming Section 4.1.2.

4.1.2 Refined piecewise-linear ray-tracing approach

The PWL approach uses a very rough way of applying the refractive index values to the ray-tracing approach. As shown by Equations (4.13a) to (4.13c) the refractive indices given at discrete height levels are simply averaged in order to define the values for the complete intermediate layer between the two discrete levels used for applying Snell's law of refraction and the delay calculation. Thus, in case of a sparse vertical distribution of height levels in the 3D field of refractive indices inaccuracies are introduced since the refractive index does not follow a linear function with height. A possible way to overcome this problem is presented by the so-called refined piecewise-linear (ref. PWL) approach as described by Hobiger et al. (2008a). This modified version of the PWL method allows a more accurate determination of the refractive indices used for ray-tracing, especially in case of a low vertical resolution of the 3D field of refractive indices. Since the azimuth is again fixed, assumming a horizontally stratified atmosphere, the ref. PWL method is again a 2D ray-tracing approach. In terms of processing costs the refined determination of the refractive indices means of course a more sophisticated and thus increased calculation effort, which leads to increased processing times compared to the simple PWL approach. A comparison between the results of the PWL and the ref. PWL approaches under the same prerequisites of available data is shown in Section 5.4. The definition of the vertical resolution of the meteorological data and thus of the refractive index with respect to program RADIATE will be given in Section 4.2.2.

In the following the ref. PWL approach is described according to Hobiger et al. (2008a). Figure 4.2 show the geometry of the ref. PWL approach. Like for the PWL approach discrete height levels are present, whose radial distances are determined according to Equation (4.15). Now, instead of using these for the application of Snell's law of refraction together with mean refractive indices in the intermediate layers in between, new discrete height levels at radial distances $\overline{r}_i$ are introduced at the half height between the original height levels as (Hobiger et al. 2008a)

$$\overline{r}_i = \frac{r_i + r_{i+1}}{2} \qquad i = 1, \ldots, k-1. \tag{4.33}$$

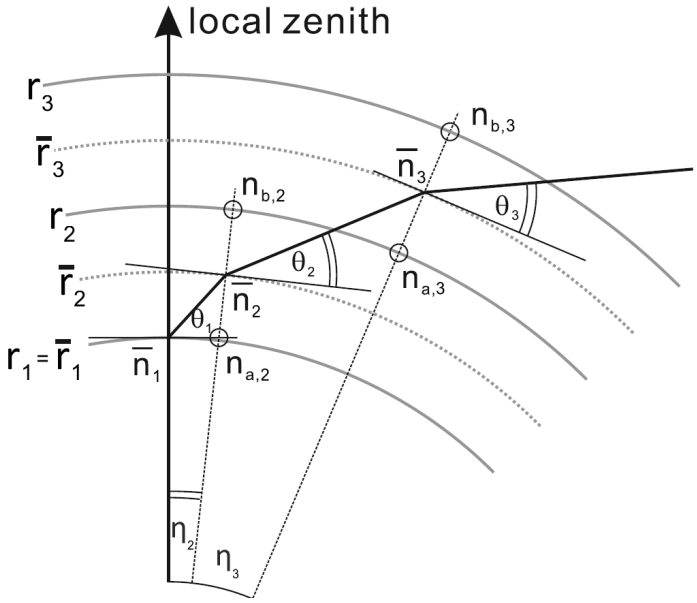

Figure 4.2: Geometry of the ref. PWL ray-tracing approach. For 2D ray-tracing the refractive indices are dependent on both the vertical and the horizontal location. For simplicity the figure only shows the 1D case, where the refractive indices are only changing with height. The η_i are the geocentric angles to the ray points. Figure taken from Hobiger et al. (2008a) and slightly modified and corrected.

The height level r_1 is also part of the newly created intermediate layers as $\overline{r}_1$ and marks the start of the ray-tracing, which basically follows the same formalism and equations as the PWL approach. Thus, almost all equations from (4.16) to (4.27) also apply to the ref. PWL approach in the identical form and the iterative reconstruction of the ray path is again needed. Only due to the use of discrete intermediate height levels and the changed calculation of the refractive indices for the ray-tracing and the delay estimation differences occur. Thus, Equation (4.24) of the PWL approach has now the form

$$\theta_{i+1} = \arccos\left(\frac{\hat{n}_{a,i+1}}{\hat{n}_{b,i+1}}\cos\left(\theta_i + \eta_{i+1} - \eta_i\right)\right), \tag{4.34}$$

where $\hat{n}_{a,i+1}$ is the refined calculated mean refractive index for Snell's law of refraction at the horizontal position of the ray point valid for the medium below the ray point and $\hat{n}_{b,i+1}$ is the refined calculated mean refractive index for Snell's law of refraction at the horizontal position of the ray point valid for the medium above the ray point. The refined refractive indices for Snell's law of refraction are calculated according to Hobiger et al. (2008a) (mistakes in reported

formulas are corrected according to personal communication with Thomas Hobiger) as

$$\begin{aligned}\hat{n}_{a,i+1} &= \frac{1}{r_{i+1}-r_i}\int_{r_i-\frac{r_{i+1}-r_i}{2}}^{\frac{r_i+r_{i+1}}{2}} n(r)\ \mathrm{d}\,r \\ &= 1+\frac{n_{a,i+1}-1}{C_{n,i+1}(r_{i+1}-r_i)}\left(\sqrt{\frac{n_{b,i+1}-1}{n_{a,i+1}-1}}-\sqrt{\frac{n_{a,i+1}-1}{n_{b,i+1}-1}}\right)\end{aligned} \tag{4.35}$$

and

$$\begin{aligned}\hat{n}_{b,i+1} &= \frac{1}{r_{i+1}-r_i}\int_{\frac{r_i+r_{i+1}}{2}}^{r_{i+1}+\frac{r_{i+1}-r_i}{2}} n(r)\ \mathrm{d}\,r \\ &= 1+\frac{n_{a,i+1}-1}{C_{n,i+1}(r_{i+1}-r_i)}\left(\sqrt{\left(\frac{n_{b,i+1}-1}{n_{a,i+1}-1}\right)^3}-\sqrt{\frac{n_{b,i+1}-1}{n_{a,i+1}-1}}\right),\end{aligned} \tag{4.36}$$

where $n_{a,i+1}$ is the refractive index at the horizontal position of the ray point in the original height level r_i, i.e. below the current mean height level $\overline{r}_{i+1}$, and $n_{b,i+1}$ is the refractive index at the horizontal position of the ray point in the original height level r_{i+1}, i.e. above the current mean height level $\overline{r}_{i+1}$. These two refractive indices can be derived from horizontal, e.g. bilinear, interpolation (see Section 4.2.5) using the refractive index grid at the according height level. For this interpolation the latitude and longitude of the ray point are needed since the refractive indices are given in a latitude and longitude grid. The ray point's latitude and longitude can be determined using the geocentric angles and the azimuth together with the initially known latitude and longitude of the station position as described in Section 4.2.4. C_n is the coefficient for the exponential decrease of the refractive index and is calculated as (Hobiger et al. 2008a)

$$C_{n,i+1} = \frac{\log\left(\frac{n_{b,i+1}-1}{n_{a,i+1}-1}\right)}{r_{i+1}-r_i}. \tag{4.37}$$

The slant total delay of each linear segment (ΔL_i) of the ray path (without the geometric bending effect) can be calculated according to Hobiger et al. (2008a) by

$$\Delta L_i = \frac{\overline{n}_{i+1}-\overline{n}_i}{\log\left(\frac{\overline{n}_{i+1}-1}{\overline{n}_i-1}\right)}s_i, \tag{4.38}$$

where the refined refractive index $\overline{n}_{i+1}$ at each ray point P_{i+1} is used, determined by (Hobiger et al. 2008a)

$$\overline{n}_{i+1} = 1+(n_{a,i+1}-1)\sqrt{\frac{n_{b,i+1}-1}{n_{a,i+1}-1}}. \tag{4.39}$$

The needed slant distances s_i have already been calculated during the preceding ray-tracing part again according to Equation (4.22), but by the use of the radial distances $\overline{r}$ of the intermediate height levels. Note that $\overline{n}_1$ is directly received from the refractive index at the station position without application of Equation (4.39).

Thus, the sum of the individual $k-1$ ray path delays results in the total delay. Applying Equations (4.38) and (4.39) to the hydrostatic and wet domains by the use of the hydrostatic and wet refractive indices allows the calculation of the delay also in these domains. Thus, the slant total, hydrostatic and wet delays are

$$\Delta L = \sum_{i=1}^{k-1} \Delta L_i, \qquad \Delta L_h = \sum_{i=1}^{k-1} \Delta L_{h,i}, \qquad \Delta L_w = \sum_{i=1}^{k-1} \Delta L_{w,i}. \tag{4.40}$$

The geometric bending effect is again calculated by Equation (4.29). According to the common practice Equation (4.30) is used to represent the delays.

The delays can also be determined in the zenith direction. Their estimation is independent from the ray-tracing, i.e. the slant distances s_i are not needed. Instead the height differences Δh_i between each two consecutive intermediate height levels $\overline{r}$ are needed, calculated as

$$\Delta h_i = \overline{r}_{i+1} - \overline{r}_i \qquad\qquad i = 1, \ldots, k-1 \tag{4.41}$$

as well as the refractive indices in the zenith direction. Thus the individual segments of the total delay along the zenith (ΔL^z) are determined similarly to Equation (4.38) as

$$\Delta L_i^z = \frac{\overline{n}_{i+1}^z - \overline{n}_i^z}{\log\left(\frac{\overline{n}_{i+1}^z - 1}{\overline{n}_i^z - 1}\right)} \Delta h_i, \tag{4.42}$$

where the refined refractive index $\overline{n}^z{}_{i+1}$ at each height level h_{i+1} in the zenith direction is used, that is determined similarly to Equation (4.39) by

$$\overline{n}_{i+1}^z = 1 + (n_{a,i+1}^z - 1)\sqrt{\frac{n_{b,i+1}^z - 1}{n_{a,i+1}^z - 1}}, \tag{4.43}$$

where the $n_{a,i+1}^z$ is the refractive index in the zenith direction in the original height level r_i and $n_{b,i+1}^z$ is the refractive index in the zenith direction in the original height level r_{i+1}. These two can again be derived from horizontal, e.g. bilinear, interpolation (see Section 4.2.5) using the refractive index grid at the according height level at the horizontal station position.

Application of Equations (4.42) and (4.43) to the hydrostatic and wet domains is straightforward. Thus, by separate summation of the increments ΔL^z, ΔL_h^z and ΔL_w^z from Equation (4.42)

the total, hydrostatic and wet delays ZTD, ZHD and ZWD are determined as

$$ZTD = \sum_{i=1}^{k-1} \Delta L_i^z, \qquad ZHD = \sum_{i=1}^{k-1} \Delta L_{h,i}^z, \qquad ZWD = \sum_{i=1}^{k-1} \Delta L_{w,i}^z. \tag{4.44}$$

From the presented formalism of the ref. PWL approach it can be stated that through the refined calculated mean refractive indices $\hat{n}_{a,i+1}$ and $\hat{n}_{b,i+1}$ for the application to Snell's law of refraction within Equation (4.34) the modelling of the exponential decrease of the refractive index with height is improved for the ray-tracing approach enabling the application of PWL ray path calculation even in case of a relatively low vertical resolution of height levels with according refractive indices (Hobiger et al. 2008a).

4.1.3 Thayer ray-tracing approach

Thayer (1967) developed an analytical 2D ray-tracing approach, i.e. for a horizontally stratified atmosphere using a fixed azimuth angle. The approach is based on the relation of the refractive indices n_1 and n_2 of the according height levels r_1 and r_2

$$\frac{n_2}{n_1} = \left(\frac{r_2}{r_1}\right)^A, \tag{4.45}$$

as proposed by Schelleng et al. (1933), and it is in accordance to the radial distance power-law model (Thayer 1967). A is the exponential coefficient for the relation of radial distances to refractive indices. Since Thayer (1967) assumes that the refractive index is only dependent on the height, the calculation of A from Equation (4.45) is straightforward and can be derived directly. Nevertheless azimuthal asymmetry, i.e. a dependence of the refractive index on the horizontal location, is taken into account for program RADIATE and thus an iterative solution of A needs to be carried out. In the following the therefore adapted original Thayer formalism is presented as described by Hobiger et al. (2008a). In this way the Thayer approach is also implemented in program RADIATE. Figure 4.3 shows the geometry of the Thayer ray-tracing approach. Equal to the PWL and ref. PWL approaches discrete height levels are present, whose radial distances r_i from the Earth's centre to the height levels are determined according to Equation (4.15). The basic principle of the iterative way of ray-tracing in order to reproduce the known outgoing elevation angle is also needed in case of the Thayer approach. Thus, the initial procedures of each iteration covered by Equations (4.16) to (4.20) also apply to the Thayer approach. The geocentric angle of the first ray point, i.e. the station position, is again defined to be zero as described in Equation (4.25) due to the setting of the coordinate system. In case of the Thayer approach it is sufficient to define the coordinates of the ray points at the intersection with the height levels through the according geocentric angle and the azimuth of the observation. An extra Cartesian representation as used within the PWL and ref. PWL approaches is not needed. The refractive indices at the ray-traced points along the path can be determined again by horizontal interpol-

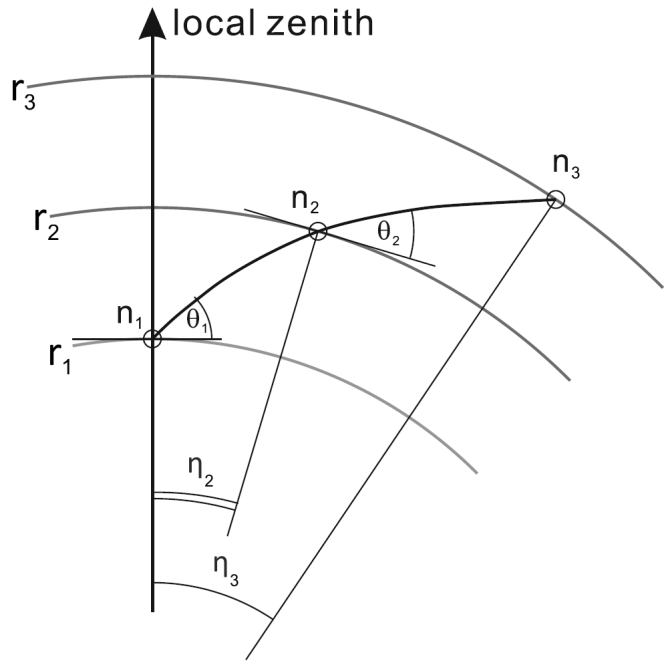

Figure 4.3: Geometry of the Thayer ray-tracing approach. For 2D ray-tracing the refractive indices are dependent on both the vertical and the horizontal location. For simplicity the figure only shows the 1D case, where the refractive indices are only changing with height. The η_i are the geocentric angles to the ray points. Figure taken from Hobiger et al. (2008a) and slightly modified and corrected.

ation, i.e. bilinear interpolation (see Section 4.2.5), at each height level from the 3D field. For this task, since the refractive indices are available in a latitude and longitude grid, the latitude and longitude of the ray points are needed, which can be determined using the geocentric angles and the azimuth together with the initially known latitude and longitude of the station position as described in Section 4.2.4.

In a loop of $i = 1 : (k-1)$, i.e. from the first to the last but one height level, the ray path through the atmosphere is reconstructed. At each height level the determination of the coefficient A is the key factor of the Thayer ray-tracing approach. As already mentioned, an iterative solution of A is needed at each height level. This iteration is stopped when the position of the next ray point, determined with the iterated A, has changed only within a certain threshold compared to the previous iteration (Hobiger et al. 2008a). As threshold program RADIATE uses the mean coordinate accuracy, which is set to $1 \cdot 10^{-7}$ degrees for the updated ray point position. In order to avoid too many or even infinite iteration loops in case of non-convergence a maximum number of allowed iterations is additionally introduced. According to Hobiger et al. (2008a) the equations presented in Thayer (1967) can be used as a starting point for the iterative determination of A. For each new height level $i+1$ the following starting conditions are used for the coefficient A_{i+1}

and the refractive index n_{i+1}:

$$A_{i+1}^{initial} = 0, \qquad n_{i+1}^{initial} = n_i. \tag{4.46}$$

This means that the initially unknown coefficient A_{i+1} is set to zero and the initially unknown, but needed, n_{i+1} is set to the value of the previous level, which is n_i. These starting conditions are applied to the first iteration cycle in order to determine the location dependent elevation angle θ_{i+1} according to Thayer (1967) and Hobiger et al. (2008a) as

$$\theta_{i+1} = \arccos\left(\frac{r_i n_i \cos\theta_i}{r_{i+1} n_{i+1}}\right) \tag{4.47}$$

and following this, the geocentric angle η_{i+1} is calculated according to Thayer (1967) and Hobiger et al. (2008a) by

$$\eta_{i+1} = \eta_i + \frac{\theta_{i+1} - \theta_i}{1 + A_{i+1}}. \tag{4.48}$$

Note that for the evaluation of this equation the knowledge of the geocentric angle η_i, i.e. the value of the last ray point, is also needed. Like for the PWL and ref. PWL approach the value of η_1 at the station position is defined to be zero.

Thus, by the gained knowledge of θ_{i+1} and thereby the knowledge of the new ray point at the height level $i+1$, the refractive index n_{i+1} can now be determined from the 3D refractive index field utilizing horizontal interpolation, i.e. bilinear horizontal interpolation (see Section 4.2.5), using the grid at the height level $i+1$. With the more accurate knowledge of n_{i+1} compared to the starting condition also A_{i+1} can be newly calculated according to Thayer (1967) by

$$A_{i+1} = \frac{\log n_{i+1} - \log n_i}{\log r_{i+1} - \log r_i}. \tag{4.49}$$

At this step the check of the mean coordinate accuracy of the newly determined ray point at the level $i+1$ is introduced for all iteration cycles after the first, since at least one cycle is needed for an updated and thus accurate value of A_{i+1} and at least a second cycle is needed for an updated and thus accurate position of the new ray point. The result of this test decides if the newly calculated position of the ray point has still significantly changed compared to the last result, which would require the continuation of the iteration, i.e. the calculation of Equations (4.47) to (4.49) using the latest updates of A_{i+1} and n_{i+1}. In case the mean coordinate accuracy of the newly determined ray point is good enough, i.e. it is smaller than the introduced threshold, the ray-tracing can be continued at the next height level. The mean coordinate accuracy σ_{coor} is calculated by

$$\sigma_{coor} = \sqrt{\frac{(\varphi_{previous} - \varphi_{new})^2 + (\lambda_{previous} - \lambda_{new})^2}{2}} \tag{4.50}$$

with the coordinates $\varphi_{previous}$ and $\lambda_{previous}$ of the ray point from the previous iteration cycle and the ones from the latest iteration cycle φ_{new} and λ_{new}.

The elevation angle e at each ray point can be calculated according to Equation (4.27). After iterating also the complete ray-tracing result in order to reach the actual observed outgoing elevation angle with the desired accuracy, the ray path is finally known. Thus, the atmospheric path delay can be calculated. This is done according to Equation (4.28) in the domains of the total, hydrostatic and wet delay. For the application of this equation the mean refractive indices in these domains are needed, which means that the refractive indices that have been calculated at the discrete height levels need to be averaged between each two consecutive height levels according to Equations (4.13a) to (4.13c). Furthermore the slant distances s_i of all curved ray segments between the discrete height levels are needed. These can be calculated according to Thayer (1967) and Hobiger et al. (2008a) by

$$s_i = \frac{r_i n_i \cos\theta_i}{(1+A_{i+1})} \tan\theta_{i+1} - \tan\theta_i. \tag{4.51}$$

Please note that in this equation the refractive indices at the discrete height levels are needed and not the averaged ones. Since this equation cannot be applied in case of an observation very close to the zenith direction due to numeric reasons, a threshold has to be used to define at which elevation angles, that are too close to the zenith, instead of the slant delay the zenith delay is calculated.

In order to get the usual representation of the slant delays according to Equation (4.30) the geometric bending effect g_{bend} needs to be calculated with Equation (4.29) and is then added to the slant delays in the total and hydrostatic domains.

The zenith delays can be calculated according to Equation (4.31) together with the height differences Δh_i between each two consecutive height levels h in zenith direction, which can be determined according to Equation (4.32). For this task also the refractive indices at each height level in the zenith direction above the station have to be determined firsthand and then averaged between each two consecutive levels to receive intermediate values for the height interval between the discrete height levels.

As a conclusion to the presented Thayer approach it can be stated that the major advantage of this method of ray-tracing is the use of curved ray paths instead of linear pieces, which is due to the exponential decrease in the refractive index. Moreover a significant difference to the PWL and ref. PWL approach is that the end of the last curved segment has the same tangent as the beginning of the next segment (Hobiger et al. 2008a). Thus the Thayer approach is more accurate than a PWL approach and it is faster than the strict 3D solution of the Eikonal equation. A disadvantage is the additional iterative step for the calculation of the coefficient A at each height level. Thus, an increased number of operations is introduced compared to the simple PWL approach.

4.2 Ray-tracing with program RADIATE

In this section the important parts of a ray-tracing program for space geodetic observations with focus on VLBI will be described. This is done on the practical example of program RADIATE. The description of the workflow is done chronologically, so that it represents a typical process run. Details of the ray-tracing approaches implemented in program RADIATE have already been described in Section 4.1. Thus, the ray-tracing itself is not covered in this section. The operational version of program RADIATE is written in Fortran. The fundamental developments including different basic program approaches have been done in MATLAB®. The decision of Fortran as programming language for the operational version is based on the fact that it is a language, which is very fast in terms of processing[1]. A complete program run for the determination of the ray-traced delays is much faster using Fortran code than using equivalent MATLAB® code. An example for this will be given in Section 6.2. In contrary, the development of a mathematical program is faster and simpler in MATLAB®. Therefore the fundamental development of program RADIATE has been carried out in MATLAB®, already considering requirements of the later development of the operational version in Fortran. A further argument for the decision of writing the operational version of program RADIATE in Fortran has been the thereby gained possibility to run program RADIATE on the ECMWF supercomputers.

4.2.1 General structure of the ray-tracing program RADIATE

With respect to program RADIATE the general structure of a ray-tracing program is described in this section. The general structures of all modern ray-tracing programs for space geodetic applications follow similar guidelines to those presented in the following. In practice the implementations of them may differ.

A more detailed insight into the structure of the operational Fortran version of program RADIATE is given by a description of all subroutines implemented in the program including a short overview of their individual targets. This closer insight into program RADIATE can be found in Appendix Section A.1 in Table A.1 on page 174. Additionally short descriptions of the different stand-alone MATLAB® versions of program RADIATE are also given in Appendix Section A.1.

4.2.1.1 Inputs to the program

In a first step of the program the input of various data is executed in order to have all basic parameters and values available, which will be needed during the processing.

The first major input source are the observations. The observation time together with the name of the observing station, the azimuth angle and the outgoing elevation angle build a single observation. All observations, e.g. from a VLBI session, are read in. The coordinates of the

[1]This is also expressed in the name Fortran, which stands for "FORmula TRANslation", as the language has been originally developed for scientific computing on large computers for the evaluation of formulas (Adams et al. 2009).

observing stations are needed as well for the observation data. Therefore a station catalogue, i.e. coordinate file, is used as an input in order to find the coordinates of every observing station. All of these different parameters provide together the fundamental geometry of the ray-tracing. The station position defines the starting point of the ray-tracing. Azimuth and outgoing elevation angle roughly determine the direction of the ray path. The outgoing elevation angle also sets the target of the ray-tracing iteration as described within Section 4.1.1 on the example of the PWL ray-tracing approach. The observation time basically defines, which epochs of the NWM data will be used later for the ray-tracing, i.e. it determines the time for which the ray-traced delay will be calculated. This is described in Section 4.2.6 in more detail. Furthermore this means that in order to be able to calculate the ray-traced delays the NWM data at the specific epochs, which are required according to the observation times, have to be available. To ensure this availability the needed epochs of the NWM can be determined before the start of the ray-tracing program by an auxiliary program called Epochs_RADIATE. Further details on this program are given in Appendix Section A.2 on page 188.

The second major input source to the ray-tracing program are the meteorological data. Primarily this means the data of the NWM epochs needed according to the observation times and according to the time interpolation strategy (see again Section 4.2.6). Furthermore supplementary meteorological data from a standard atmosphere are needed for height levels above those supported by the NWM up to the defined limit of the atmosphere, where no further contribution to the atmospheric delay is induced. The reasons why NWM data and a standard atmosphere have been selected as basic meteorological input sources are described in Section 5.2.

4.2.1.2 Data preparations and pre-calculations

In order to save processing time during the later ray-tracing it is reasonable to execute some pre-calculations. Basically this means that the input data is prepared for the application to the ray-tracing algorithm.

The observations are assigned to the needed epochs of the NWM data, so that later the ray-traced delays, valid at the specific time of the epoch, are available and can be input to the time interpolation as described in Section 4.2.6 in case this is desired.

Furthermore the appropriate station coordinates have to be assigned to each observation since from the pure observation data only the station names are known in case of VLBI observations. For this step the loaded station catalogue is used.

The major workload prior to the actual ray-tracing is due to data preparations and pre-calculations of the meteorological data. This means that the data delivered by the NWM is used to determine a 3D field of the refractive index with an increased vertical resolution compared to the input resolution. In order to reach this goal the vertically low resolved meteorological data from the NWM are vertically interpolated after some preparative pre-calculations. Additionally a standard atmosphere is used to vertically extrapolate the limited NWM data. This fundamental part of preparing the refractive index field within the ray-tracing program is described in Section 4.2.2

in detail.

4.2.1.3 Ray-tracing of the observations

The main part of a ray-tracing program is of course the ray-tracing approach itself, which is executed after the above described preliminary steps. The detailed implementations of the different approaches present in program RADIATE have been described in the Sections 4.1.1 to 4.1.3. The needed inputs to the ray-tracing are the observation data together with the 3D refractive index fields in the total, hydrostatic and wet domains in order to be able to calculate the slant and zenith delays in these domains along the ray-traced signal path and the zenith direction.

4.2.1.4 Outputs after the ray-tracing and final results

After the successful execution of ray-tracing for the individual observations, different results and outputs can be derived. Of main interest are of course the slant and zenith delays in the total, hydrostatic and wet domains. Additionally the geometric bending effect and the total, hydrostatic and wet mapping factors, i.e. the ratios of the specific slant delays to the zenith delays, are a valuable information source. Furthermore the elevation angle at the station as well as the outgoing elevation angle, which have been both derived or reconstructed by ray-tracing, are reported. Also the total pressure, temperature and water vapour pressure at the station position determined from the vertically interpolated NWM data are outputs since these meteorological data provide valuable information for further applications.

Depending on the time interpolation mode the output values of program RADIATE are valid at the exact observation time or only at the timely closest epoch of the NWM. The detailed process of the time interpolation will be described in Section 4.2.6.

As final step of the ray-tracing program RADIATE the observation data with the according ray-tracing results are written to files. One file is the so-called ".radiate" text file that contains all of the important results that have been determined. Also a second output text file called ".trp" is created, which reports only the most important ray-tracing results in a more standardized format, i.e. in accordance to the format by the National Aeronautics and Space Administration Goddard Space Flight Center (NASA GSFC). The ".trp" files can be applied directly to the VLBI analysis in case of using the analysis software Vienna VLBI Software (VieVS) (see Böhm et al. 2012, for more information on VieVS). The creation of the ".trp" file can optionally be turned off.

4.2.2 Establishing a vertically high-resolved refractive index field for ray-tracing

For the ray-tracing a 3D field of the refractive index is needed, which can be determined from the meteorological data provided by a NWM. The fundamental horizontal resolution of the later determined refractive index field is left as defined by the horizontal resolution of the NWM. In order to determine the refractive indices at the exact horizontal locations of the ray points during the ray-tracing an interpolation is carried out using the available horizontal grid as described in

Section 4.2.5. An investigation of the influence of the input horizontal resolution of the NWM data on the ray-traced delays is presented in Section 5.3.

Program RADIATE uses the ECMWF operational NWM for all observational data since 01.01.2008. Earlier observations are processed using the ECMWF Re-Analyis-Interim (ERA-Interim) NWM, because the operational NWM is available only with a reduced number of total pressure levels for earlier epochs. Both models are used with the same output specifications, relevant to program RADIATE: The two ECMWF NWM provide amongst other possible parameters temperature, specific humidity and geopotential at 25 certain total pressure levels[1] with a global coverage. The data are reported at epochs every 6 hours. The basic properties of the NWM are summarized in Table 4.2. In the following the NWM used within program RADIATE will always be denoted as the ECMWF operational NWM for simplification with implicitly addressing the ERA-Interim NWM in case of observational data before 01.01.2008.

Table 4.2: Properties of the ECMWF operational NWM and the ERA-Interim NWM as used within program RADIATE.

Horizontal coverage	Global, i.e. in latitude [90°, -90°] and in longitude [0°, 360°[
Horizontal resolution	Various possibilities, e.g.: 0.125° x 0.125° and 1° x 1° used for RADIATE
Vertical coverage	25 total pressure levels in [hPa]: 1000, 950, 925, 900, 850, 800, 700, 600, 500, 400, 300, 250, 200, 150, 100, 70, 50, 30, 20, 10, 7, 5, 3, 2, 1
Epochs	Every 6 hours, i.e. 0 h, 6 h, 12 h and 18 h UTC
Parameters	Temperature, specific humidity, geopotential

Within ray-tracing the 3D refractive index field is needed to be available in a spherical coordinate system, i.e. a geodetic reference system, as described e.g. in Section 4.1.1 as this is the basic coordinate system used for the ray-tracing application. In order to reach this goal, some pre-calculations using the provided meteorological parameters from the NWM at the individual total pressure levels are necessary.

As a first pre-calculation step the water vapour pressure p_w, which will be needed later for the determination of the refractive index, is calculated according to Nafisi et al. (2012a) and Wallace and Hobbs (2006) as

$$p_w = \frac{qp}{\psi + (1-\psi)q} \tag{4.52}$$

[1] Depending on the model and the epoch time more total pressure levels could be in principle provided, but program RADIATE always uses the NWM with the same 25 total pressure levels.

with

$$\psi = \frac{M_w}{M_d} \approx \frac{18.01528 \ \frac{kg}{kmol}}{28.9644 \ \frac{kg}{kmol}} = 0.622, \tag{4.53}$$

which leads to

$$p_w \approx \frac{qp}{0.622 + 0.378q} \tag{4.54}$$

with the specific humidity q, which is according to Böhm et al. (2013) the ratio of the densities of water vapour and wet air. The molar mass of water vapour M_w and the molar mass of dry air M_d, whose values are set according to Mendes (1999) and Lide (1997), form the auxiliary parameter ψ.

The further pre-calculations concern the coordinate system of the present meteorological parameters. The used ECMWF NWM provides the horizontal grid in latitude and longitude, which can be treated as to be conform to the geodetic system that is used for ray-tracing. Thus, a horizontal coordinate transformation is not necessary. In the vertical domain the meteorological data are referenced to specific levels of the total pressure. Additionally the geopotential values for each grid point at the different total pressure levels of the NWM are reported. In order to establish the needed geodetic reference system for the ray-tracing algorithm, which uses ellipsoidal heights in case of program RADIATE, the geopotentials need to be transformed to be able to use the available meteorological data within the vertical interpolation.

In a first step of this transformation the geopotential height h_d, which is also called dynamic height in geodetic research fields (Böhm et al. 2013), is determined from the geopotential C_p according to Böhm et al. (2013) by

$$h_d = \frac{C_p}{g_n}, \tag{4.55}$$

where $g_n = 9.80665 \frac{m}{s^2}$, which is a constant gravity value (normal gravity) that is normally used by meteorologists to divide the geopotential (Böhm et al. 2013). Following this, the geopotential height h_d needs to be transformed to the orthometric (geometric) height h_{orth}. According to Hobiger et al. (2008a) the strict determination of the orthometric height h_{orth} is given by

$$h_{orth} = \frac{C_p}{\overline{g}(\varphi, \lambda, h_{orth})} = \frac{h_d g_n}{\overline{g}(\varphi, \lambda, h_{orth})} \tag{4.56}$$

with $\overline{g}$ as the mean acceleration due to the gravity between the geoid and the position of the point (Hobiger et al. 2008a). Thus, $\overline{g}$ is dependent on the position of the point, i.e. dependent on the latitude φ, the longitude λ and on the point's orthometric height h_{orth}. According to Böhm et al. (2013) a realistic, but more simplified gravity value g at the half value of the desired height h_{orth}

at the latitude φ of the point can be used within Equation (4.56). The longitude dependence of the gravity value is neglected. Thus, the equation can be rewritten as

$$h_{orth} = \frac{h_d g_n}{g\left(\varphi, \frac{h_{orth}}{2}\right)}. \tag{4.57}$$

According to Kraus (2001) the gravity g can be determined by

$$g(\varphi, h_{orth}) = g_n\left[1 - 0.0026373\cos(2\varphi) + 0.0000059\cos^2(2\varphi)\right] \cdot \left(1 - 3.14 \cdot 10^{-7} \cdot h_{orth}\right), \tag{4.58}$$

where g_n is again the above defined normal gravity constant. Equation (4.58) uses an approximation for the height dependence through the expression $\left(1 - 3.14 \cdot 10^{-7} \cdot h_{orth}\right)$, which would be in a strict sense according to Newton's law of universal gravitation $1/(1 + h_{orth}/R_E)^2$ with the Earth radius R_E (Kraus 2001). Thus, the orthometric height h_{orth} has to be determined iteratively. In practice, the first calculation of Equation (4.57) should be sufficient (Böhm et al. 2013). Therefore Equation (4.58) can be applied to Equation (4.57). This results in a quadratic equation of h_{orth}, which leads to the correct solution for h_{orth} through

$$h_{orth} = \frac{1}{2 \cdot 1.57 \cdot 10^{-7}} - \sqrt{\frac{1}{(1.57 \cdot 10^{-7})^2} - \frac{1}{1.57 \cdot 10^{-7}} \frac{h_d}{1 - 0.0026373\cos(2\varphi) + 0.0000059\cos^2(2\varphi)}}. \tag{4.59}$$

In a last transformation step the orthometric height h_{orth} is transformed to the ellipsoidal height h_{ell} by adding the geoid undulation h_N:

$$h_{ell} = h_{orth} + h_N. \tag{4.60}$$

In case of program RADIATE the geoid undulations h_N are taken from the Earth Gravitational Model 2008 (EGM2008) (see Pavlis et al. 2012).

Thus at this stage, the fundamental meteorological parameters that will be needed for the calculation of the refractive index are known at discrete grid points through latitude and longitude and at specific levels of total pressure. The ellipsoidal height of each horizontal grid point at each total pressure level is also available, enabling the determination of a 3D refractive index field.

Since the vertical resolution of 25 total pressure levels provided by the ECMWF NWM is not sufficient for high accuracy ray-tracing, a vertical refinement, i.e. a vertical interpolation, of the meteorological data is reasonable. The vertical interpolation should be done prior to the refractive index calculation, because the refractive index calculation as according to Equation (3.19) is based on non-linear contributions, i.e. non-linear combinations, of the total pressure (as part of the calculation of the total density), the water vapour pressure and the temperature. Therefore

a direct vertical interpolation of the refractive index is not recommended as it would not be adequate (Hobiger et al. 2008a; Nafisi et al. 2012a). An individual vertical interpolation of the constituents leads to a more accurate vertically refined refractive index.

As a first step of the vertical interpolation, the specific vertical interpolation steps in form of ellipsoidal heights, due to the use of a geodetic reference system, should be defined. As described by Hobiger et al. (2008a) the choice of the number of height levels predefines the possible accuracy of the ray-traced delays as well as the necessary computational efforts with respect to memory usage and numbers of operations. The simple approach of using equally dense distributed height levels from the lowest to the uppermost level would lead to an incredibly high number of levels. Using a spacing of 10 m for the levels ranging from -100 m to 84 km would result in 8411 height levels, which would have to be interpolated (extrapolated) and stored in the memory. Thus, a more sophisticated approach should be chosen. According to Hobiger et al. (2008a) the fact that the pressure decreases exponentially with height should be considered since this parameter mainly influences the magnitude of the refractive index. Therefore they developed an approach that determines the height levels based on a sophisticated exponential algorithm.

For program RADIATE the height levels are defined according to the findings of Rocken et al. (2001). They verified that these increment definitions lead to an agreement with an equal 5 m spacing of the height levels at the sub-mm level at 1° elevation. Thus, these definitions are suitable for program RADIATE with respect to the set accuracy goals that will be described in Section 5.5. Table 4.3 shows these increments of the height levels. In case of program RADIATE the 10 m

Table 4.3: Increments and increment intervals according to Rocken et al. (2001) for the vertical interpolation.

Increments in [m]	10	20	50	100	500
Increment intervals in [km]	0-2	2-6	6-16	16-36	36-136

increment of the height levels is also used for all levels below 0 m. In the operational version of the program the lowest height level for which interpolation is done, is defined by the lowest station of all observing ones in the specific ray-tracing session. Thus according to the increments and the increment intervals shown in Table 4.3 the vertical interpolation starts at the last height level that is just below the lowest station height. The uppermost height level, i.e. the upper limit of the neutral atmosphere, for which interpolation is done, is set to 84 km since this height should be sufficiently high to make sure that upper heights can be treated as non-contributing to the neutral atmosphere delay. According to Nafisi et al. (2012a) this limit should be the point where it can be said that the air density is equal to zero, i.e. the refractive index is almost exactly 1. Hobiger et al. (2008a) use 86 km as the limit. Nafisi et al. (2012a) decided to use 76 km after testing different upper and also lower limits and their influence on the ray-traced delays at low elevation. In case of program RADIATE 84 km is chosen as limit of the neutral atmosphere since the U.S. Standard Atmosphere 1976 (see COESA 1976), which is used for the extrapolation at heights above the pressure level data of the NWM, can be easily utilized for the determination

of total pressure and temperature for geometric heights up to 86 km or geopotential heights up to 84.852 km. Since at these heights the different height systems do not significantly alter the results of the total pressure and temperature the ellipsoidal heights are treated as geopotential heights when using the standard atmosphere. The general definition of the individual height levels according to the definitions of Rocken et al. (2001) are used for all horizontal grid points of the global grid in order to determine a 3D grid.

As already mentioned, the used NWM does unfortunately not provide meteorological data up to the height of the desired 84 km. The utilized ECMWF NWM provides data up to a total pressure level of 1 hPa. The according ellipsoidal height is highly dependent on the horizontal position. Furthermore it is depending on the season and the time of day of the epoch. Thus, for the epoch at 15.09.2011 18:00:00 h UTC the ellipsoidal heights on a global grid at the 1 hPa level vary between about 42.697 km and about 48.662 km, i.e. there is a span of about 6 km. For all height levels that should be interpolated above these heights extrapolation has to be carried out. Therefore a standard atmosphere model can be used. More details on standard atmospheres are provided in Section 5.1.3. In case of program RADIATE the U.S. Standard Atmosphere 1976 (see COESA 1976) is used. To unify the transition between the use of meteorological data from the NWM and from the standard atmosphere for all horizontal grid points, the switching limit, which is called NWM limit in the following, is set to be the minimum ellipsoidal height provided by the uppermost total pressure level of the NWM. On one side this means that at some horizontal grid points the information of the NWM is not used up to the very last possible interpolation height level, but on the other side this enables an equal treatment of all height levels above the NWM limit with the same source of meteorological data, i.e. with data from the standard atmosphere.

Thus, in the first part of the vertical interpolation the meteorological data from the NWM are used up to the NWM limit. In the second part, i.e. above this limit, the U.S. Standard Atmosphere 1976 (see COESA 1976) is used up to the set upper limit of the troposphere, i.e. of the neutral atmosphere.

The desired output of the vertical interpolation are dense 3D fields of refractive indices in the total, hydrostatic and wet domains since these are needed for the ray-tracing and the delay calculations. The hydrostatic, wet and total refractive indices n_h, n_w and n are calculated according to Equation (3.19) and (3.6) as

$$n_h = 1 + \left(k_1 \frac{R}{M_d} \rho \right) \cdot 10^{-6}, \tag{4.61}$$

$$n_w = 1 + \left(k_2' \frac{p_w}{T} + k_3 \frac{p_w}{T^2} \right) Z_w^{-1} \cdot 10^{-6}, \tag{4.62}$$

$$n = n_h + n_w - 1. \tag{4.63}$$

Strictly speaking, n_w is the non-hydrostatic refractive index, but it will be called wet refractive index in the following for simplicity.

Some of the needed values for the calculation of the refractive index can be defined beforehand. These are the universal gas constant R, the molar mass of dry air M_d and the molar mass

of water vapour M_w with the values

$$R = 8314.510 \quad \left[\frac{J}{kmol \cdot K} = \frac{kg \cdot m^2}{kmol \cdot K \cdot s^2}\right], \tag{4.64}$$

$$M_d = 28.9644 \quad \left[\frac{g}{mol} = \frac{kg}{kmol}\right], \tag{4.65}$$

$$M_w = 18.01528 \quad \left[\frac{g}{mol} = \frac{kg}{kmol}\right] \tag{4.66}$$

as according to Mendes (1999) and Lide (1997). With these parameters the specific gas constants of dry and wet air R_d and R_w can be determined (Mendes 1999):

$$R_d = \frac{R}{M_d} = 287.0596 \quad \left[\frac{J}{K \cdot kg} = \frac{m^2}{K \cdot s^2}\right], \tag{4.67}$$

$$R_w = \frac{R}{M_w} = 461.5254 \quad \left[\frac{J}{K \cdot kg} = \frac{m^2}{K \cdot s^2}\right]. \tag{4.68}$$

Furthermore the refractivity coefficients k_1, k_2 and k_3 are needed. For these the so-called "best-average" values from Rüeger (2002a) and Rüeger (2002b) are used, which are shown in Table 3.1. k_2' is determined according to Equation (3.18).

With these prerequisites the actual vertical interpolation can be carried out to determine those meteorological parameters in a higher resolution, which are needed for the refractive index calculation. In a first step of the vertical interpolation the pressure level data of the NWM is used up to the determined NWM limit.

At first the total pressure is interpolated using an exponential approach according to Wallace and Hobbs (2006), Kleijer (2004) and Nafisi et al. (2012a):

$$p_{int} = p_i \exp\left(-\frac{(h_{int} - h_i) g_i}{R_d T_{v,i}}\right). \tag{4.69}$$

Hobiger et al. (2008a) suggest, in order to follow the natural exponential decrease of the total pressure with height, a linear interpolation of the logarithm-transformed pressure values, which results in the above shown exponential interpolation in the pressure domain. For the evaluation of Equation (4.69) the knowledge of the gravity g and the virtual temperature T_v at the height h_i of the closest pressure level i below or above the interpolation height h_{int} are needed. g_i can be determined again by Equation (4.58) with the use of the latitude of the interpolation position and the height h_i of the closest pressure level to the interpolation height h_{int}. $T_{v,i}$ can be calculated following Wallace and Hobbs (2006) and Nafisi et al. (2012a) as

$$T_{v,i} = \frac{T_i p_i}{p_i - \left(1 - \frac{M_v}{M_d}\right) p_{w,i}}, \tag{4.70}$$

where the subscript i always refers to the meteorological values (temperature T, total pressure

p and partial pressure of water vapour p_w) from the pressure level closest to the interpolation height h_{int}.

The virtual temperature describes the temperature, which dry air should have in order to possess the same density like moist air at the same pressure. Due to the lower density of moist air at the same pressure and temperature as dry air, the virtual temperature is always larger than the actual temperature (Wallace and Hobbs 2006).

Following Hobiger et al. (2008a) and Nafisi et al. (2012a) it is sufficient to use a linear interpolation in case of the temperature in order to increase the vertical resolution. Thus, the temperature is interpolated as

$$T_{int} = T_{i+1} + \frac{T_i - T_{i+1}}{h_i - h_{i+1}} (h_{int} - h_{i+1}) . \tag{4.71}$$

The subscripts i and $i+1$ address the specific values from the lower and the upper pressure levels in between which the interpolation height h_{int} is located.

The third fundamental meteorological parameter that is vertically interpolated is the partial pressure of water vapour p_w. According to Böhm et al. (2013) it can be done by an exponential approach:

$$p_{w,int} = p_{w,i} \exp\left(\frac{h_{int} - h_i}{C_{p_w}} \right), \tag{4.72}$$

where the coefficient for the exponential decrease of the water vapour pressure with height C_{p_w} is determined according to Nafisi et al. (2012a) by

$$C_{p_w} = \frac{h_{i+1} - h_i}{\log\left(\frac{p_{w,i+1}}{p_{w,i}} \right)}. \tag{4.73}$$

The subscripts i and $i+1$ address again the specific values from the lower and the upper pressure levels in between which the interpolation height h_{int} is lying.

In case the water vapour pressures of the pressure levels i and $i+1$ are the same or if one of them is zero, the exponential interpolation fails since the coefficient C_{p_w} can not be evaluated. Thus, in those cases linear interpolation is an adequate remedy leading to the following interpolation scheme:

$$p_{w,int} = p_{w,i} + \frac{p_{w,i+1} - p_{w,i}}{h_{i+1} - h_i} (h_{int} - h_i) . \tag{4.74}$$

In case of the same vapour pressures at the pressure levels i and $i+1$ even the linear interpolation is redundant since directly one of the pressure level values can be taken as the interpolated water vapour pressure. Due to programming concerns the common linear interpolation for all exception cases may still be favourable although it might be sometimes unnecessary from a theoretical point of view.

At this point the three fundamental meteorological parameters for the refractive index calculation, i.e. the total pressure, the temperature and the water vapour pressure, have been vertically interpolated to derive a dense, high resolved and accurate vertical tropospheric profile up to the supported height of the NWM data.

In order to be able to calculate the refractive indices some further parameters need to be calculated using the vertically interpolated fundamental parameters. For the calculation of the hydrostatic refractive index with Equation (4.61) the total density of moist air ρ is needed, which is according to Equation (3.16) the sum of the density of dry air ρ_d and the density of wet air ρ_w, which in turn can be determined according to Wallace and Hobbs (2006) by

$$\rho_d = \frac{p - p_w}{R_d T}, \tag{4.75}$$

$$\rho_w = \frac{p_w}{R_w T} \tag{4.76}$$

with the total pressure p, the partial pressure of water vapour p_w, the specific gas constants of dry and wet air R_d and R_w as defined by Equations (4.67) and (4.68) and the temperature T.

For the evaluation of Equation (4.62) in order to determine the wet refractive index, the compressibility factor of water vapour Z_w is needed as inverse, which is therefore calculated with Equation (3.13).

Finally with the availability of all needed constituents the calculation of the refractive indices in the hydrostatic, wet and total domains can be carried out according to Equations (4.61) to (4.63).

At this point the refractive index is available as 3D field in each domain for all interpolation height levels up to the NWM limit. Therefore the second part of the refinement of the vertical resolution deals with all interpolation heights above the determined NWM limit. For this task the U.S. Standard Atmosphere 1976 (see COESA 1976) is utilized in program RADIATE as data source.

Due to the large height of roughly 40 km at which the standard atmosphere model overtakes the vertical interpolation, a simplification can be introduced. The water vapour pressure can be set to zero for all heights above the NWM limit since the atmosphere is dry at these heights. Therefore only the total pressure and the temperature are required from the standard atmosphere model. Thus, these values need to be interpolated from the model.

The temperature is again linearly interpolated with respect to the provided standard atmosphere data. The total pressure is interpolated on the basis of the hydrostatic equation (COESA 1976). The specific values of the total pressure and the temperature from the U.S. Standard Atmosphere 1976 at the different heights are shown in Figure 5.1. At this step the fundamental meteorological parameters total pressure, temperature and water vapour pressure are now also known for the interpolation heights above the NWM data. Therefore the refractive indices in the domains hydrostatic, wet and total can again be determined using Equations (4.61) to (4.63) with the prior evaluation of the total density of moist air ρ again according to Equations (3.16), (4.75)

and (4.76) and the determination of the inverse of the compressibility factor of water vapour Z_w again according to Equation (3.13).

Since the refractive indices are also needed at the exact horizontal position and height of the observing stations for the ray-tracing algorithm, the total pressure, temperature and water vapour pressure values are horizontally and vertically interpolated at a separate stage of program RADIATE right after the vertical interpolation of the complete horizontal grid. At first the horizontal interpolation of the meteorological parameters at the exact horizontal location of the station is done according to the description that will be given in Section 4.2.5 on the example of the refractive index. The horizontal interpolation is carried out with those two height levels gained from the previous vertical interpolation, that are located just below and above the station height for which vertical interpolation will be carried out in the next step. With the horizontally interpolated meteorological parameters below and above the station height, the vertical interpolation at this station height can be carried out. This is done in the same way as it has been done for the complete horizontal grid and thus with the same equations as described previously in this section.

Finally at this stage, the refractive indices have been determined as dense 3D fields and locally at the station positions in the total, hydrostatic and wet domains just as they are needed for the ray-tracing and the delay calculations.

In Figure 4.4 results of the vertical interpolation scheme, that has been described above, are presented on the example of a specific vertical profile. All above described settings for the vertical interpolation have been taken into account in the equal manner as described, e.g. the upper limit of the NWM, the upper limit of the neutral atmosphere and the general increments between the interpolation height levels. Note that the strict vertical interpolation mode of program RADIATE, which will be denoted as "profilewise" mode in the following, has been used to derive the values. More information on the different modi of the vertical interpolation in program RADIATE will follow in Section 4.2.2.1. Figure 4.4 shows the vertical profile at the closest horizontal grid point of the ECMWF operational NWM with a horizontal resolution of 0.125° x 0.125° to the exact station position of WETTZELL ($\varphi = 49.1450°, \lambda = 12.8775°$). As lowest interpolated ellipsoidal height 0 m has been chosen. Note the discontinuity in the water vapour pressure decrease near the surface that is visible in Figure 4.4c. This apparently also affects the wet refractivity shown in Figure 4.4d.

Further examples of vertical interpolation results are shown for the profiles next to the stations KOKEE and TSUKUB32 in Figures B.1 and B.2 in Appendix Section B.1 on the pages 215 and 216.

4.2.2.1 Different modi of the vertical interpolation within program RADIATE

Program RADIATE has two implemented modi for the vertical interpolation called "profilewise" and "gridwise". The fundamental interpolation strategy is the same for both modi and it is according to the interpolation equations that have been presented above. The only but significant difference is the way the pressure level data of the NWM are used.

In case of the "profilewise" approach the vertical interpolation is done separately for each ver-

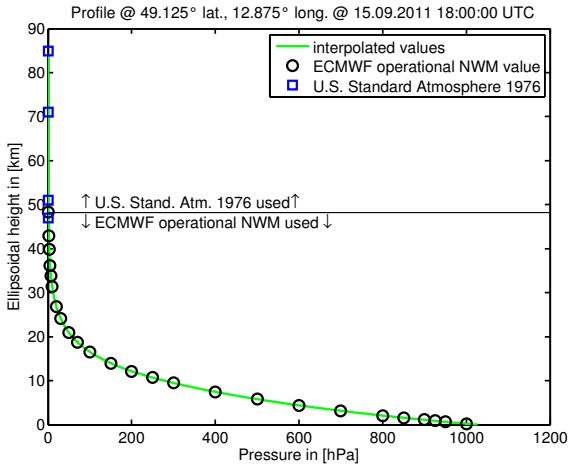

(a) Vertical profile of the pressure.

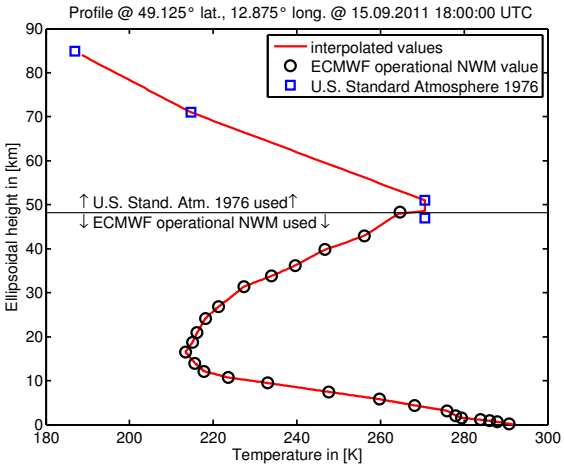

(b) Vertical profile of the temperature.

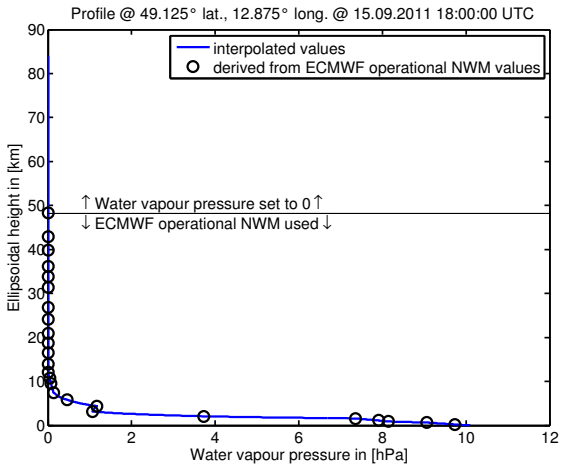

(c) Vertical profile of the water vapour pressure.

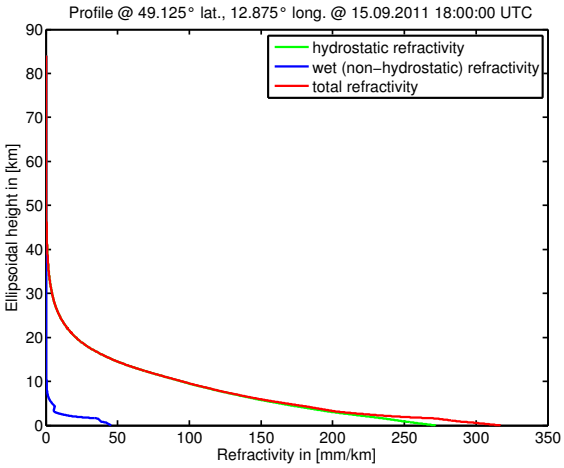

(d) Vertical profiles of the hydrostatic, wet and total refractivity.

Figure 4.4: Vertical profiles of pressure, temperature, water vapour pressure and refractivity. The horizontal position of the profiles ($\varphi = 49.1250°, \lambda = 12.8750°$) is the nearest grid point of the NWM to the station WETTZELL ($\varphi = 49.1450°, \lambda = 12.8775°$). The epoch of the NWM is 15.09.2011 18:00:00 h UTC. The defined NWM limit is represented by a horizontal line. Up to this point the ECMWF operational NWM data from 25 pressure levels, which are delivered in a horizontal resolution of 0.125° x 0.125°, have been used to interpolate the pressure, the temperature and the derived water vapour pressure. Above this limit the U.S. Standard Atmosphere 1976 has been used to interpolate the pressure and the temperature. The water vapour pressure has been set to 0 for these heights. For a better readability the refractivities are presented instead of the refractive indices. These values have been calculated according to Equations (4.61) to (4.63) using the interpolated pressure, temperature and water vapour pressure.

tical profile, i.e. at one specific horizontal grid point vertical interpolation is carried out at the sequential desired height levels starting at the lowest height upwards. After finishing one profile the next one, located at a new horizontal grid point, is vertically interpolated. This "profilewise" approach is the strict method of the vertical interpolation for the derivation of a dense 3D re-

fractive index field since the pressure level data are used during the vertical interpolation always appropriately according to the specific heights for which they are valid due to the fact that the heights represented by the pressure level data are dependent on the horizontal location of the processed profile.

The "gridwise" approach inherits a simplification in order to save valuable processing time in case of programming languages that especially support simultaneous array calculations like MATLAB®. For programming languages with limited performance gain in case of simultaneous array calculations like Fortran the "gridwise" approach may not provide improved processing speed or even leads to increased processing time.

Within the "gridwise" approach all horizontally distributed profiles are vertically interpolated together. Since the vertical interpolation always requires the meteorological data from two supporting total pressure levels of the NWM, i.e. the lower and the upper level with the interpolated height lying in between, an approximation has to be made. The reason for this is that the meteorological data of the NWM are provided as total pressure level data and used in this form for the vertical interpolation. Despite the fact of the same total pressure at one specific pressure level, the according ellipsoidal height, that has been determined in the pre-calculations, differs for every horizontal grid point since the total pressure at a specific height varies with horizontal position. Within the vertical interpolation the upper and lower pressure levels have to be changed in case the interpolation height exceeds the according height of the upper pressure level. At this stage a simplification has to be introduced, because at some horizontal points the upper pressure level may still be the correct one, i.e. the according height at the horizontal position is still higher than the interpolation height, but at other horizontal locations the upper pressure level may not be the correct one any more as the according height at the horizontal position may be lower. The decision and thus the introduced simplification within the "gridwise" approach when to change the supporting lower and upper pressure levels is based on the mean ellipsoidal height of the complete upper pressure level horizontal grid. So, after the pressure level change when the interpolation height exceeded the mean height of the former upper pressure level some profiles may still require the previous upper and lower pressure levels. Therefore an error in the vertical interpolation at these profiles is introduced, which is visible as a discontinuity in the interpolated meteorological data profiles. This is the drawback of simultaneously interpolating the whole horizontal grid at once. The benefit of this strategy is the increase of processing speed during the vertical interpolation in programming languages with special support of simultaneous array calculations. Figure 4.5 schematically shows the above described "gridwise" vertical interpolation approach and describes the inherited error source because of the applied simplification in order to simultaneously interpolate all vertical profiles.

In case of a global vertical interpolation of a field of refractive indices, the "gridwise" approach should be avoided since the ellipsoidal heights at the poles are very different to those at the equator for the same total pressure level. In the example of using the ECMWF operational NWM in a 1° x 1° horizontal resolution for the ray-tracing of the first session of the Continuous VLBI Campaign 2011 (CONT11) of the International VLBI Service for Geodesy and Astrometry (IVS)

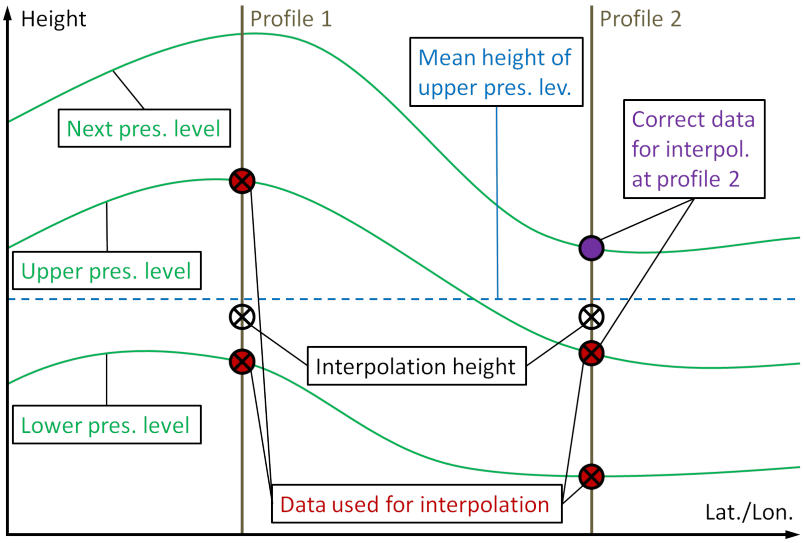

Figure 4.5: Schematic representation of the "gridwise" vertical interpolation approach. At profile 1 the total pressure level data are used for the vertical interpolation in the correct way as it would also be done within the strict "profilewise" approach. The upper and lower pressure levels have been set according to the fact that the interpolation height is lower than the mean ellipsoidal height of the complete horizontal grid of the selected upper pressure level. At profile 2, which is interpolated simultaneously with profile 1, the vertical interpolation is shown for the same interpolation height. Thus, the same total pressure levels are used for deriving the data for the vertical interpolation at the horizontal position of profile 2. In the "profilewise" and thus strict vertical interpolation the total pressure levels would be changed for the vertical interpolation at profile 2 since the true height of the selected upper pressure level is lower than the interpolation height at the horizontal position of profile 2. Therefore an error is introduced to the vertical interpolation of profile 2 in case of the "gridwise" approach, which will be visible as a discontinuity in the interpolated meteorological data profile when the pressure levels used for the vertical interpolation will be changed at a higher interpolation height.

(see IVS 2015) on September 15 in 2016, the simplification within the "gridwise" approach leads to errors in the vertical interpolation that result in differences mainly at the mm level for the slant total delays compared to the results when using the strict "profilewise" approach, whereas the "profilewise" approach always delivers smaller delay values. At low elevation the differences reach up to about 2.5 cm.

Thus, in order to avoid any influences from the vertical interpolation it may be better to use the strict "profilewise" approach in case of global grids or to utilize the "gridwise" approach only in case the horizontal extent of the interpolated grid is limited, e.g. 10° x 10°, which minimizes the interpolation errors since the mean height used for the pressure level change is then more accurate for all evaluated profiles. The approach of limiting the horizontal extent of the grid for the vertical interpolation is used in an alternative development version of program RADIATE. In this specific program version only a horizontally limited grid around each station is used for the ray-tracing. This alternative version is described in the following section.

4.2.2.2 Different modi for the horizontal extent of the dense refractive index field within program RADIATE

In order to be able to determine ray-traced delays for any number and horizontal distribution of different stations on the world, the program is designed in the operational Fortran version and the according MATLAB® development version to exhibit the vertical interpolation always on the global scale, i.e. for the whole global grid provided through the NWM a vertically interpolated field of refractive indices is established for the ray-tracing.

For small scale applications, i.e. with a very limited number of stations, a different strategy may be more suitable, where from the globally provided NWM data a subgrid around each station is extracted for which the vertical interpolation is done. This reduces the interpolation load in case of only few observing stations for which ray-tracing should be done. Nevertheless, the horizontal extent of the subgrids should be chosen wisely in order to avoid that ray-traces leave the subgrid in case of small elevation angles. This version of program RADIATE that uses subgrids has been developed only in MATLAB® as a first development step towards the operational version in Fortran.

4.2.3 Determination of the Earth radius

Since the coordinate systems of space geodetic techniques are based on reference ellipsoids such as the World Geodetic System 1984 (WGS84), ray-tracing should be done in ellipsoidal coordinates, but this leads to ray-tracing algorithms that are not efficient and fast. A solution to this issue is the use of an approximation by local spherical coordinates, i.e. site dependent spherical coordinates. This means that geodetic latitudes and longitudes are used as spherical coordinates together with the ellipsoidal heights referenced to an osculating sphere of a certain radius dependent on the local site for the ray-tracing (Hobiger et al. 2008a). This radius will be denoted in the following as Earth radius.

The data from the NWM are given in a coordinate frame of spherical latitudes and longitudes and geopotentials (at specific total pressure levels). As an approximation, the latitudes and longitudes of the NWM are treated as geodetic latitudes and longitudes within the ray-tracing. Through transformation and application of geoid undulations the geopotentials can be converted to ellipsoidal heights. This has already been described in Section 4.2.2.

Considering the Earth radius that is needed within the ray-tracing approach, different approximations are possible. The simplest one is setting the radius to a constant value, i.e. the Earth is then approximated by a sphere. Since a highly accurate ray-tracing result is desired, more sophisticated solutions should be considered.

A more accurate representation of the Earth radius is the Gaussian curvature radius, which introduces a latitude dependency of the approximating radius. It represents the radius of a local osculating sphere (Nafisi et al. 2012b). The Gaussian curvature radius R_G can be calculated by

(Torge and Müller 2012)

$$R_G = \sqrt{R_M(\varphi)R_N(\varphi)}, \tag{4.77}$$

where R_M is the meridian radius of curvature

$$R_M(\varphi) = \frac{a_{ell}(1-e_{cc}^2)}{(1-e_{cc}^2\sin^2\varphi)^{\frac{3}{2}}} \tag{4.78}$$

and R_N is the radius of curvature in the prime vertical, also called polar radius of curvature

$$R_N(\varphi) = \frac{a_{ell}}{(1-e_{cc}^2\sin^2\varphi)^{\frac{1}{2}}} \tag{4.79}$$

in dependence on the latitude φ of the point, where the radius should be calculated, e.g. the station position in case of ray-tracing. a_{ell} is the semi-major axis of the reference ellipsoid and e_{cc}^2 is the squared first numerical eccentricity of the reference ellipsoid, i.e. of the WGS84 in case of program RADIATE,

$$e_{cc}^2 = \frac{a_{ell}^2 - b_{ell}^2}{a_{ell}^2} \tag{4.80}$$

with the semi-minor axis b_{ell} of the reference ellipsoid.

Another even more accurate approximation of the Earth radius is the Euler radius of curvature. Besides the latitude dependency, it is also introduces a dependency on the azimuth α of the observation for which ray-tracing should be done. The Euler radius of curvature R_α represents the radius of an ellipsoid (Nafisi et al. 2012b). It is received from Euler's formula (Torge and Müller 2012):

$$\frac{1}{R_\alpha} = \frac{\cos^2\alpha}{R_M} + \frac{\sin^2\alpha}{R_N}. \tag{4.81}$$

R_M and R_N are determined again by evaluation of Equations (4.78) and (4.79).

Figure 4.6 shows the differences between the determined Earth radius in case either the Gaussian curvature radius or the Euler radius of curvature are used. In Figure 4.6a the differences are shown at a fixed latitude but at different azimuth angles in order to highlight the azimuth-dependency of the Euler radius of curvature. Figure 4.6b presents the differences at different latitudes but for the same azimuth.

These differences between the Euler and the Gaussian curvature radius do not largely impact the results of the ray-traced delays. Results for the CONT11 campaign, which is described in Section 5.3.1.2, show that the maximum impact of the Euler compared to the Gaussian curvature radius is a difference of about 4 mm in the slant total delay, whereas all of the very few comparably

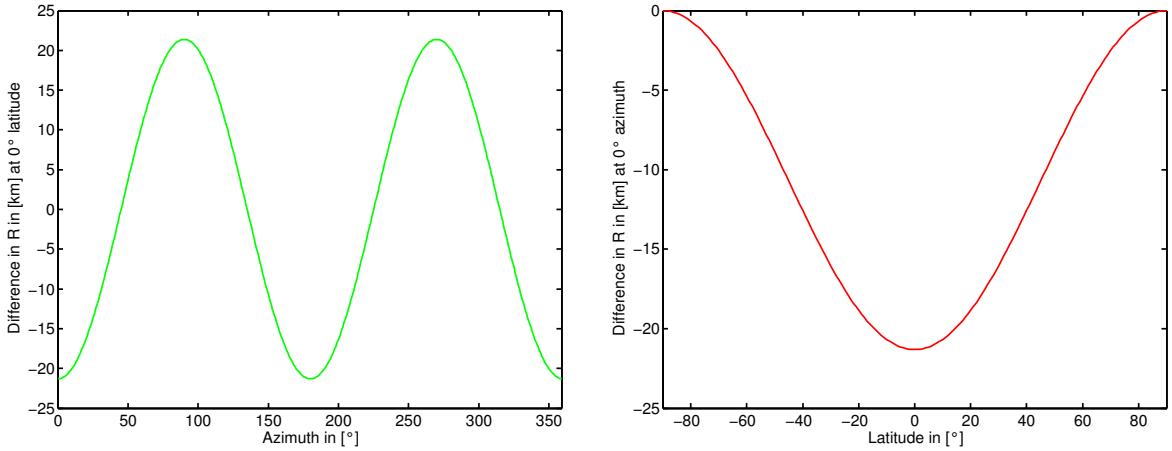

(a) Differences in the resulting radius with respect to the azimuth dependency of the Euler radius of curvature at the latitude 0°.

(b) Differences in the resulting radius with respect to the latitude dependency of the Euler radius of curvature and the Gaussian curvature radius at the azimuth 0°.

Figure 4.6: Differences between the Euler radius of curvature R_α and the Gaussian curvature radius R_G in the form $R_\alpha - R_G$.

large differences occur at very low elevation angles of about 5.5°.

Program RADIATE uses the Euler radius of curvature for the representation of the Earth radius when calculating ray-traced delays. In earlier stages of the program development the Gaussian curvature radius has been used, e.g. for the comparison of RADIATE against other ray-tracing programs as described in Section 6.1. In order to enhance the accuracy of the Earth radius a switch to the more accurate Euler radius of curvature has been made.

4.2.4 Determination of the spherical coordinates of the points along the ray trajectory

Within ray-tracing the ray path is sequentially determined as described for the PWL, ref. PWL and the Thayer approaches in the Sections 4.1.1 to 4.1.3. Thus, with each new segment a new point along the ray path is determined. Within the ray-tracing itself the location of this point is determined by a height (with added Earth radius), the known (fixed) azimuth angle of the observation and a geocentric angle that is referenced to the starting position of the ray, i.e. the station position. Now, in order to be able to derive the needed refractive index for each new ray point for the further ray-tracing, it is necessary to know the latitude, the longitude and the height of each point since the data base (3D field) of the refractive indices is given in spherical coordinates. Since the refractive index field has been set up during the vertical interpolation phase in the same height system (ellipsoidal heights) as used for the ray-tracing, no further calculations are needed with respect to the height of the ray point. Thus, only the latitude and the longitude of the ray point need to be determined in order to be able to retrieve the according refractive index from the data field at the desired horizontal and vertical position.

In the following the calculation of the latitude φ_{i+1} and longitude λ_{i+1} of the ray point P_{i+1} is described. A graphical representation can be found in Figure 4.7. Initially latitude φ_1, longitude

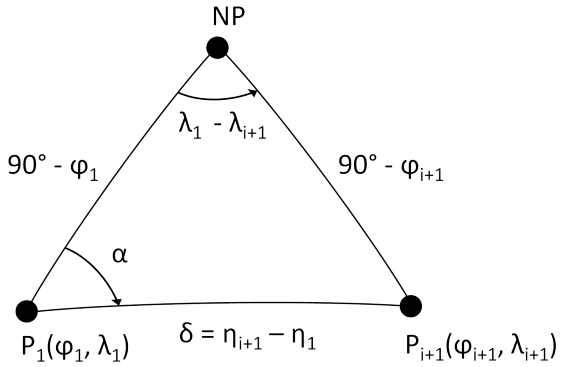

Figure 4.7: Spherical geometry for the calculation of the latitude φ_{i+1} and the longitude λ_{i+1} of the point P_{i+1} using the point P_1, the azimuth α and the geocentric angles η_1 and η_{i+1}. NP is the North-pole.

λ_1 and geocentric angle η_1 of the first ray point P_1, i.e. of the station position, as well as the (fixed) azimuth α of the observation are known. Together with the geocentric angle η_{i+1} of the ray point P_{i+1}, known from ray-tracing, the latitude φ_{i+1} and the longitude λ_{i+1} of the ray point P_{i+1} can be determined from the following equations, which are derived from spherical trigonometry:

$$\varphi_{i+1} = \arcsin\left(\sin\varphi_1 \cos\delta + \cos\varphi_1 \sin\delta \cos\alpha\right), \tag{4.82}$$

$$\lambda_{i+1} = \lambda_1 + \arctan\left(\frac{\sin\alpha}{\cot\delta \cos\varphi_1 - \sin\varphi_1 \cos\alpha}\right), \tag{4.83}$$

where λ_{i+1} is lying in the interval [-180°, 180°] through the use of a four-quadrant arctan function, which is often implemented in programming languages as atan2. δ is determined by

$$\delta = \eta_{i+1} - \eta_1. \tag{4.84}$$

In the 2D ray-tracing approaches the ray path is fixed to the azimuth angle of the observation. In order to retain this azimuth within the above shown coordinate determination, it is necessary to use always the first ray point, e.g. the station position, as reference for the coordinate calculations of the sequential ray points as the given azimuth is referenced to this point. In case a different ray point would be used instead of the station point for the calculation of the sequential ray points, the azimuth would be changed.

4.2.5 Horizontal interpolation method

After vertically interpolating the input meteorological data, these are available as 3D fields in a spherical coordinate system with the domains of latitude φ, longitude λ and height h with a suitable high vertical resolution, i.e. an appropriate number of dense height levels. With respect

to the ray-tracing approach and the delay calculation especially the derived total, hydrostatic and wet refractive index fields are of main interest.

Since the basic input of the meteorological data is given by the NWM in case of program RADIATE, the horizontal resolution of the 3D data fields are initially set by the horizontal resolution of the NWM. As described in the Sections 4.1.1, 4.1.2 and 4.1.3, which present different ray-tracing methods, the refractive indices are always needed at the exact horizontal locations of specific points, mostly directly at points along the ray, which usually do not coincide with one of the available horizontal grid nodes of the 3D data field. Therefore a horizontal interpolation has to be performed.

A suitable method for the horizontal interpolation of a specific value, e.g. the refractive index, is the bilinear interpolation as described by Hobiger et al. (2008a). In the following the bilinear interpolation is shown with respect to the interpolation of the refractive index as needed within the ray-tracing approach in order to determine the value at the exact horizontal location of the ray point with the known latitude φ_{int} and longitude λ_{int}.

At a certain height level of the 3D field and thus assuming a 2D grid with discrete nodes at specific latitude and longitude values the interpolated refractive index $n_{\varphi_{int},\lambda_{int}}$ can be found by using those four refractive indices n_{φ_1,λ_1}, n_{φ_1,λ_2}, n_{φ_2,λ_2} and n_{φ_2,λ_1} from the discrete grid, which are given at the grid nodes (φ_1,λ_1), (φ_1,λ_2), (φ_2,λ_2) and (φ_2,λ_1), that surround the interpolation location $(\varphi_{int},\lambda_{int})$. A schematic diagram of the geometry for the bilinear interpolation is given by Figure 4.8. The surrounding grid nodes have to fulfil the following conditions (Hobiger et al.

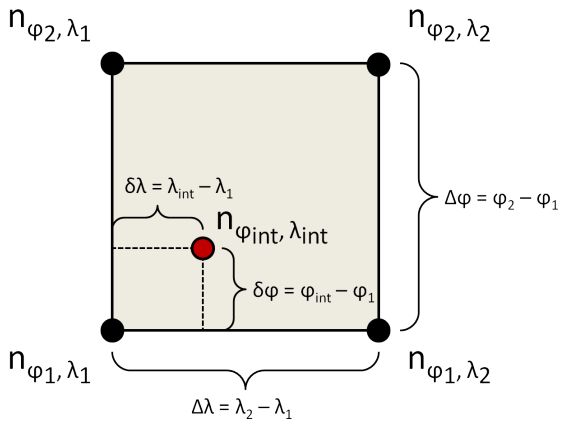

Figure 4.8: Geometry for the bilinear interpolation of the refractive index $n_{\varphi_{int},\lambda_{int}}$ using the surrounding refractive indices n_{φ_1,λ_1}, n_{φ_1,λ_2}, n_{φ_2,λ_2} and n_{φ_2,λ_1} at the grid nodes.

2008a):

$$\varphi_1 \leqslant \varphi_{int} \leqslant \varphi_2, \qquad \lambda_1 \leqslant \lambda_{int} \leqslant \lambda_2. \tag{4.85}$$

$n_{\varphi_{int},\lambda_{int}}$ is then determined according to Hobiger et al. (2008a) by

$$n_{\varphi_{int},\lambda_{int}} = (1-\chi)(1-\xi)n_{\varphi_1,\lambda_1} + (1-\chi)\xi n_{\varphi_1,\lambda_2} + \chi\xi n_{\varphi_2,\lambda_2} + \chi(1-\xi)n_{\varphi_2,\lambda_1}, \tag{4.86}$$

where ξ and χ denote the auxiliary parameters used for the weighting of the contribution of each grid node value to the interpolation result with respect to longitude and latitude of the interpolation location. They are determined as (Hobiger et al. 2008a)

$$\chi = \frac{\varphi_{int} - \varphi_1}{\varphi_2 - \varphi_1}, \qquad \xi = \frac{\lambda_{int} - \lambda_1}{\lambda_2 - \lambda_1}. \tag{4.87}$$

An alternative strategy to the direct horizontal interpolation of the refractive index is the horizontal interpolation of the constituent parameters of the refractive index, which are the total pressure, the water vapour pressure and the temperature, using the adopted Equations (4.85) to (4.87) with the subsequent refractive index calculation from these interpolated values. The reason for this lies inside the refractive index calculation as it is according to Equation (3.19) based on non-linear contributions, i.e. non-linear combinations, of the total pressure (as part of the calculation of the total density), the water vapour pressure and the temperature (Hobiger et al. 2008a; Nafisi et al. 2012a). Thus, the beforehand horizontal interpolation of the constituents may lead to a more accurate refractive index. Unfortunately this also leads to a significant increase in the number of processing operations. Furthermore the variability of the constituents total pressure, water vapour pressure and temperature is not as large in the horizontal domain as it is in the vertical domain supposing a reasonable high horizontal resolution of the basic grid from the NWM. Therefore this alternative horizontal interpolation strategy has been implemented only in a separate development version of program RADIATE for research and only in the programming language MATLAB®.

For the operational mode of program RADIATE it is sufficient to directly horizontally interpolate the refractive index values. For the vertical domain the separate beforehand vertical interpolations of the total pressure, the water vapour pressure and the temperature as described in Section 4.2.2 are reasonable.

4.2.6 Time dependency of the ray-traced delays

The NWM provides the meteorological data for certain epochs. In program RADIATE each calculated ray-traced delay has been determined using the meteorological data from one specific epoch. Thus, the resulting ray-traced delays are only valid at a specific time, i.e. they are time dependent with respect to the meteorological data used for their calculation. In order to determine ray-traced delays at the exact observation times, which do not normally coincide with the epoch of the NWM, it is therefore necessary to calculate for a specific observation ray-traced delays at different epochs of the NWM and use an interpolation method like the Lagrange interpolation to derive the final ray-traced delay at the exact observation time.

In case of program RADIATE NWM data with a temporal resolution of 6 hours, i.e. at the epochs 0 h, 6 h, 12 h and 18 h UTC are used. With this fundamental time resolution of the meteorological data it is sufficient to calculate ray-traced delays at those two epochs that temporally surround the time of the observation. Thus, the applied Lagrange interpolation reduces to a linear interpolation between the two ray-traced delays determined at the surrounding epochs, leading to the final delay at the exact observation time. Equation (4.88) describes the linear interpolation with respect to the time domain:

$$\Delta L_{t_{obs}} = \Delta L_{t_{ep1}} + \frac{\Delta L_{t_{ep2}} - \Delta L_{t_{ep1}}}{t_{ep2} - t_{ep1}}(t_{obs} - t_{ep1}), \tag{4.88}$$

where $\Delta L_{t_{obs}}$ is the interpolated ray-traced delay at the exact observation time t_{obs}. t_{ep1} and t_{ep2} are the epoch times at which the ray-traced delays $\Delta L_{t_{ep1}}$ and $\Delta L_{t_{ep2}}$ have been calculated beforehand using the according meteorological data. Since in program RADIATE the ray-traced delays are calculated at the two surrounding epochs of the NWM t_{obs}, t_{ep1} and t_{ep2} additionally fulfil the following condition:

$$t_{ep1} \leqslant t_{obs} < t_{ep2}. \tag{4.89}$$

This means that the epoch t_{ep1} of the NWM is the last one before or exactly at the observation time t_{obs} and the epoch t_{ep2} of the NWM is the first one after the observation time t_{obs}.

In case no time interpolation is needed or desired, program RADIATE calculates ray-traced delays using the data of only one NWM epoch. This means that according to the time of an observation, the closest epoch in time of the meteorological data is used for the calculation of the ray-traced delays. Subsequently, no interpolation is needed. In case of a time resolution of 6 hours as in case of the NWM data used in program RADIATE, the meteorological data and therefore the calculated final delays may be offset to the observation time by a maximum of 3 hours if no time interpolation is carried out.

Chapter 5

Research on optimal operational ray-tracing strategy

In this chapter different investigations for the establishment of an optimal ray-tracing strategy for an operational application are presented. Each section focuses on a specific main aspect that contributes to enable the complete ray-tracing application to perform in an optimized way. This optimum search is seen under two different general points of view. The first and basic objective of the ray-tracing application is to deliver the results, i.e. the tropospheric delays, with the highest accuracy possible. The second objective is to ensure that the ray-tracing calculations perform best with respect to processing time and computer memory usage. These two aspects are often not directly compatible and compromises need to be made. So, within this chapter a best-performing strategy of ray-tracing is considered that combines these two aspects to realize an application that delivers very accurate results, but which is nevertheless still competitive with respect to the needed time and memory to achieve these results.

5.1 Meteorological data sources

The first very important aspect of ray-tracing is the choice of the input sources for the meteorological data. Basically there are different options to receive the needed meteorological data. Following Nievinski (2009), important sources are radiosondes, Numerical Weather Models (NWM) and climatologies, i.e. standard atmosphere models. These will be discussed shortly within the following subsections.

5.1.1 Radiosondes

The following basic information about radiosondes is mainly taken from Dabberdt et al. (2003).

A radiosonde is in its conventional version a measuring device attached to a carrier balloon. Through different sensors the device measures in-situ a vertical profile of meteorological para-

meters while the balloon ascends from the land or the ocean surface, where it has been exploited, up to heights of about 30 km or respectively pressures of about 11 hPa. Generally pressure, temperature and humidity are measured as a they vary with altitude. Modern radiosondes carry out these measurements at intervals between 1 s and 6 s (Dabberdt et al. 2003). Also wind-speed and -direction can be measured. During the measurement the data are transmitted to a ground station, where they are processed. The measurements are typically carried out twice a day at stations in the USA and Europe, but only once per day at other sites (Dabberdt et al. 2003). In addition to this rather coarse temporal data acquisition intervals, also the horizontal coverage is very limited as each radiosonde measurement is only valid for a sparse horizontal extent and the global coverage with the, according to Nievinski (2009), about 800 operational radiosonde stations worldwide is also limited.

The obtained profiles serve as the core of the global weather observing system, which is in turn an important input to numerical weather prediction models. Therefore the meteorological parameters are reported at various standard pressure levels and also at significant levels at which specific meteorological changes occur (Dabberdt et al. 2003).

The general objectives of radiosonde profiling are to gain knowledge of the current weather patterns and to deliver important data inputs to short- and medium-range computer-based weather prediction models. Further application fields are climate studies, hurricane investigation and hurricane movement forecasting, air pollution research and aviation operations (Dabberdt et al. 2003).

Besides the conventional balloon-type other types of radiosondes exist. The dropsonde is released from an aircraft attached to a balloon-like parachute and descends to the surface while it is measuring and sending the data back to the aircraft by radio transmission. Dropsondes have the advantage that they can be released also at places over the Earth, which can not or only very difficultly reached on the surface, e.g. polar regions. With a driftsonde system the measurement equipment is carried up to a specific height by a balloon where it then drifts at a specific height level for up to five days releasing dropsondes at specific locations and at specific times with the goal to densify the data availability in sparsely covered areas. The concept of a rocketsonde is in principle the same as that of a dropsonde, but instead of an aircraft a rocket is used for the uplift (Dabberdt et al. 2003).

5.1.2 Numerical weather models

With the term Numerical Weather Model (NWM) in principle the results of a model that describes the Earth's atmosphere is meant in the following. There are different kinds of models, which therefore need to be differentiated into (re-)analysis, operative and prediction models addressing different time steps of data processing through backward, present and forecast modelling. Nevertheless all results are bound to a specific epoch of time, where they are valid. The epoch specification can be seen as the moment where a snapshot of the atmospheric conditions is taken. The differences in the results of the NWM from (re-)analysis, operative and prediction

processing come from the different models and input data used for their determination.

The processing of the NWM is done at specific weather centres, where the atmosphere-relevant parts of the observations of different measurement techniques like radiosondes, satellite techniques and surface measurements are combined and assimilated according to their observing positions and error characteristics (Salstein 2013). Through the use of physical equations, e.g. the equation of motion and the equation of thermodynamics, etc., together with information about gas physics, chemistry and radiative transfer it is possible to build models of the atmosphere, which are in turn the framework of the NWM. Depending on the purpose, i.e. analysis, short-term forecast or climate projections, these models are different. If the knowledge about basic meteorological parameters like temperature, pressure, geopotential height and moisture is needed, observational data from the sources described above serve as input to the NWM (Böhm et al. 2013).

What is addressed as NWM here is a three-dimensional (3D) field of different meteorological parameters that represent the state of the atmosphere at a certain time, which is specified by the epoch of the NWM. In case of the European Centre for Medium-Range Weather Forecasts (ECMWF) the NWM are available on a gridded global scale with different horizontal and vertical resolutions displaying the parameters coarser or finer, but the underlying basic data stays the same with respect to a specific processing model.

5.1.3 Standard atmospheres

Vaughan (2003) declares that standard atmospheres vertically describe the atmospheric parameters temperature, pressure and density on an international agreement basis, which means that they are reference models for the representation of the Earth's atmosphere.

So, a standard atmosphere model does not report atmospheric conditions really observed at a specific epoch since it is meant to be a reference that should fit as a kind of standardization model for the Earth's atmosphere.

For example the U.S. Standard Atmosphere 1976 (see COESA 1976) in its representation for geometric heights up to 86 km or geopotential heights up to 84.852 km is defined by specifying, amongst other parameters, initial parameters for pressure and temperature at the surface and temperature lapse rates for specific height intervals. With these parameters is it possible to interpolate pressure and temperature values at any desired height covered by the underlying model. Therefore this model can be seen as a simplified projection of the complex atmosphere through a description equal to that one of the basic structure of the atmosphere in Section 3.1.

Figure 5.1 shows the temperature and pressure values that can be obtained from the U.S. Standard Atmosphere 1976. The temperature is linearly interpolated with respect to the provided standard atmosphere data. The pressure is interpolated on the basis of the hydrostatic equation with respect to the provided standard atmosphere data (COESA 1976).

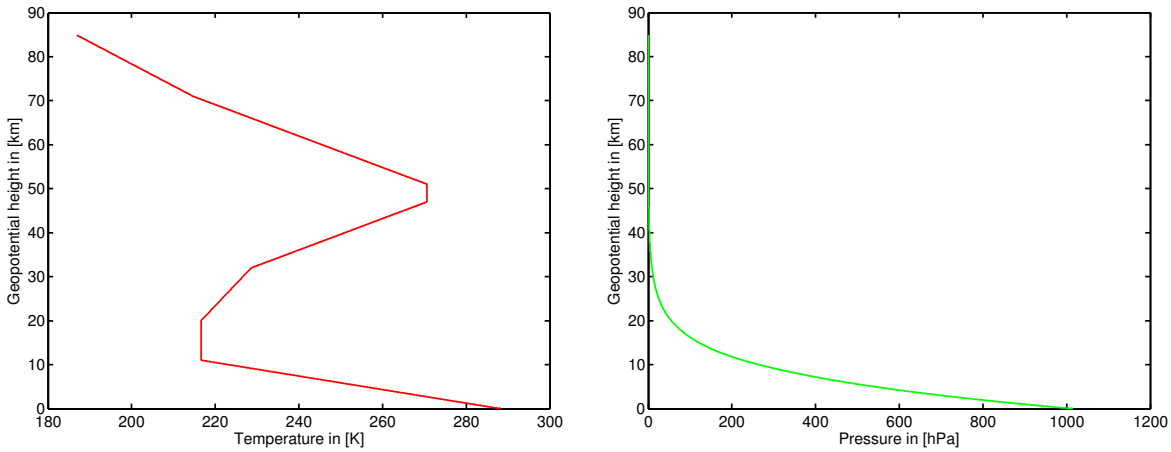

(a) Temperature profile.

(b) Pressure profile.

Figure 5.1: Temperature and pressure profiles of the U.S. Standard Atmosphere 1976 for geopotential heights up to 84.852 km (corresponds to the geometric height of 86.0 km).

5.2 Selection of appropriate meteorological data

The demands on the meteorological data used for the ray-tracing of geodetic VLBI observations are challenging. As it should be possible to calculate ray-traced delays for observations at any station position on the Earth, it is necessary that the meteorological data have a global coverage. Furthermore an adequate temporal resolution of these globally provided data is needed to ensure that the ray-tracing can work with data that reasonably fit the time of the observation. Therefore the use of a NWM as primary input source for the meteorological data is a favourable decision to meet these requirements as radiosonde data are limited with respect to both positional availability and temporal resolution.

Nevertheless the stand-alone use of a NWM as meteorological data input is not sufficient. Program RADIATE uses the operational or the ERA-Interim NWM of the ECMWF always in a setup with 25 total pressure levels[1] ranging from 1000 hPa to 1 hPa at which meteorological data are delivered. So, for heights above, where the total pressure is lower than 1 hPa, the NWM does not deliver any meteorological data. This limit of the NWM data is reached at an ellipsoidal height of approx. 42 km or higher (depending on the horizontal position and the general condition of the atmosphere at the epoch of the NWM). In order to reach a high accuracy for the ray-traced delays, the available meteorological data needs to be expanded above this limit of the NWM. Thus, a standard atmosphere model, i.e. the U.S. Standard Atmosphere 1976 (see COESA 1976) is used to extend the available meteorological data up to an ellipsoidal height of 84 km, which is treated in program RADIATE as the final limit up to which the neutral atmosphere contributes to the tropospheric delays.

[1] Depending on the model and the epoch time more total pressure levels could be in principle provided, but program RADIATE always uses the NWM with the same 25 total pressure levels.

5.3 Research on the impact of the horizontal resolution of the numerical weather model

At this stage a short clarification needs to be made. The term NWM will be mainly used for denoting the data, i.e. the results of the model, and not for referencing to the theoretical model in the background.

As mentioned in Section 5.1.2 there are different forms of models and input data for the determination of the NWM data that is used for ray-tracing. Actually there are many options for the choice of a suitable NWM. At first there is the possibility to choose a specific weather centre that produces the NWM, e.g. the European Centre for Medium-Range Weather Forecasts (ECMWF) or the Global Modeling and Assimilation Office (GMAO). Furthermore it is of course possible to select which model for the NWM is used, e.g. (re-)analysis, operational or prediction model. Additionally it may be possible to choose the spatial representation of the NWM, i.e. if the data are delivered in a three-dimensional (3D) grid or as spherical harmonics as mentioned by Nievinski (2009). In case of a gridded data representation a spatial discretization of the meteorological data in the horizontal and the vertical direction is necessary and realized by setting specific resolutions in these domains. In the vertical domain the NWM data may be represented in two different ways, e.g. via total pressure levels or terrain following model levels. Thus, many different options are available for a perfectly fitting NWM for the application to the ray-tracing.

In this section the focus is set on the horizontal resolution of a gridded and total pressure level-based NWM as this parameter, besides all others that define a NWM, is of special interest for the ray-tracing processing. On the one hand this basic setting may be a direct driver for the accuracy of the ray-traced delays. On the other hand the horizontal resolution definitely is a driver for the amount of data that needs to be processed within the ray-tracing. Therefore the horizontal resolution of the NWM must be chosen adequately to both satisfy accuracy and processing speed concerns for ray-tracing.

Hereinafter a research on the effect of the horizontal resolution of the NWM on ray-traced delays and on VLBI analysis is presented, which is also summarized in Hofmeister et al. (2015). The main goal of this investigation is to determine the actual impact of the horizontal resolution of the NWM and to find an appropriate resolution that is reasonable to be used in operative ray-tracing processing.

5.3.1 Ray-tracing settings and data for the research

In general the ray-tracing program RADIATE with its main processing characteristics as described in Section 4.2 is used to determine the ray-traced delays for the research on the impact of the horizontal resolution of the NWM. The PWL method (see Section 4.1.1) is used as ray-tracing approach. Within the processing of the delays, meteorological and observational data are needed. With respect to the meteorological data the findings of Section 5.2 are used. This means that both a NWM and a standard atmosphere model are utilized in the processing. The NWM that is used

for this research will be described in Section 5.3.1.1. As standard atmosphere model the U.S. Standard Atmosphere 1976 (see COESA 1976) is utilized to extend the data up to 84 km. For the ray-tracing a subgrid of the meteorological data of 10° x 10° around each station is used (see Section 4.2.2.2 for more details) for which the vertical resolution is increased using the "gridwise" approach as described in Section 4.2.2.1. For the approximation of the Earth radius the Gaussian curvature radius is used (see Section 4.2.3). Section 5.3.1.2 describes the observational data for which ray-traced delays are calculated. In order to get the ray-traced delays at the exact observation times, ray-traced delays at the two surrounding NWM epochs are calculated and linearly interpolated as it has been described in Section 4.2.6.

5.3.1.1 Numerical weather model

As input NWM to the ray-tracing, the gridded global ECMWF operational NWM with 25 total pressure levels and a temporal resolution of 6 hours, starting at 00:00 h UTC each day, is utilized. These settings of the NWM are said to define one specific NWM for this research. Now, for the investigation of the impact of the horizontal resolution, this NWM is used with two different horizontal resolutions of 0.125° x 0.125° and 1° x 1°. Referring to the horizontal resolution, these two realizations of the NWM will be called NWM(0.125°) and NWM(1°) in the following.

5.3.1.2 Observational data

Concerning the observational data input, two different data sets are used. The first is the Continuous VLBI Campaign 2011 (CONT11) of the International VLBI Service for Geodesy and Astrometry (IVS) (see IVS 2015). This set of observations is chosen, because it provides a well-prepared data sample for the research. This campaign contains 15 days of 24 h VLBI observations from September 15 to September 29 in 2011[1]. In total 14 different stations participated[2]. Figure 5.2 shows the station network. See Table A.3 in Appendix Section A.3 on page 191 for more information about the stations.

As second data set simulated observations for all CONT11 stations at the epochs of the NWM every 6 hours for the time span from September 15 00:00 h UTC to September 30 18:00 h UTC in 2011[3] are used. The simulated data set contains artificial observations for each station at each NWM epoch for all of the 144 combinations of azimuths in the interval [0°:22.5°:337.5°] with the elevation angles of [1°, 2°, 3°, 5°, 7°, 10°, 15°, 30°, 70°].

[1] This interval needs 61 epochs of NWM data in case of the used temporal resolution of 6 hours.

[2] Unfortunately the station WARK12M has only a very limited number of observations. This is due to the occurrence of technical problems during the campaign (IVS 2015).

[3] This interval results in a total of 64 NWM epochs.

Figure 5.2: Station network of the IVS CONT11 campaign. Figure taken from http://ivscc.gsfc.nasa.gov/program/cont11/, IVS (2015).

5.3.2 Influence directly on the ray-traced delays

In a first step it is important to quantize how much the horizontal resolution of the NWM affects the results of the ray-traced delays directly. Therefore ray-traced delays for each of the two observational data sets are calculated twice with the PWL approach implemented in program RADIATE (see Section 4.1.1). The calculations are carried out once using the meteorological data from NWM(0.125°) leading to ray-traced delays, which will be denoted as RD(0.125°) in the following, and once using the meteorological data from NWM(1°) leading to ray-traced delays, which will be denoted as RD(1°) in the following.

To determine the change between the ray-tracing results RD(0.125°) and RD(1°), ΔSTD, ΔSHD and ΔSWD, which denote the differences Δ in the domains slant total delay STD, slant hydrostatic delay SHD and slant wet delay SWD, are estimated. Please note that the slant total and slant hydrostatic delays contain the geometric bending effect. Equations (5.1) to (5.3) show how the differences are built. The subscripts denote the used ray-tracing solution, i.e. which horizontal resolution of the NWM has been used to calculate it.

$$\Delta STD = STD_{RD(0.125^\circ)} - STD_{RD(1^\circ)}, \tag{5.1}$$

$$\Delta SHD = SHD_{RD(0.125^\circ)} - SHD_{RD(1^\circ)}, \tag{5.2}$$

$$\Delta SWD = SWD_{RD(0.125^\circ)} - SWD_{RD(1^\circ)}. \tag{5.3}$$

Additionally ΔSTD_{mf}, ΔSHD_{mf} and ΔSWD_{mf} are determined, where the differences Δ are determined from the results of the STD_{mf}, the SHD_{mf} and the SWD_{mf}, which are in turn calculated using the total, hydrostatic or wet mapping factors mf, mf_h or mf_w that can be determined from the slant and zenith total delays (STD and ZTD), the slant and zenith hydrostatic delays (SHD and ZHD) and the slant and zenith wet delays (SWD and ZWD). Through the introduc-

tion of the mf a kind of scaling of the differences is done. See Equations (5.4) to (5.8) for the formalisms. The subscripts denote again the used ray-tracing solution, i.e. which horizontal resolution of the NWM has been used to calculate it. The zenith delays from the RD(0.125°) are used as the reference zenith delays to calculate the slant delays from the specific mf.

$$\Delta STD_{mf} = \underbrace{mf_{RD(0.125^\circ)} \cdot ZTD_{RD(0.125^\circ)}}_{STD_{RD(0.125^\circ)}} - mf_{RD(1^\circ)} \cdot ZTD_{RD(0.125^\circ)} \tag{5.4}$$

with

$$mf_i = \frac{STD_i}{ZTD_i} \tag{5.5}$$

$$\Delta SHD_{mf} = \underbrace{mf_{h,RD(0.125^\circ)} \cdot ZHD_{RD(0.125^\circ)}}_{SHD_{RD(0.125^\circ)}} - mf_{h,RD(1^\circ)} \cdot ZHD_{RD(0.125^\circ)} \tag{5.6}$$

with

$$mf_{h,i} = \frac{SHD_i}{ZHD_i} \tag{5.7}$$

$$\Delta SWD_{mf} = \underbrace{mf_{w,RD(0.125^\circ)} \cdot ZWD_{RD(0.125^\circ)}}_{SWD_{RD(0.125^\circ)}} - mf_{w,RD(1^\circ)} \cdot ZWD_{RD(0.125^\circ)} \tag{5.8}$$

with

$$mf_{w,i} = \frac{SWD_i}{ZWD_i} \tag{5.9}$$

Figure 5.3 shows the impact of the horizontal resolution of the NWM in the domain of the STD for the CONT11 observations of station WETTZELL including the scaled results when determined via mf. Please refer to Figures B.3 and B.4 in the Appendix Section B.2 on the pages 217 and 218 for a presentation of the results for the CONT11 observations of the station WETTZELL in the domains SHD and SWD. Furthermore Figure B.5 on page 219 shows the plots of the impact on the simulated observations of station WETTZELL. Please note that the differences are always built in the form $RD(0.125^\circ) - RD(1^\circ)$ with respect to the specific domain of the differences, i.e. ΔSTD, ΔSHD, ΔSWD or those differences using the mapping factor.

In the following all statements are made with respect to all CONT11 stations and the observational results of both the CONT11 campaign and the simulated observations. If we look at the ΔSTD, e.g. in Figure 5.3a for station WETTZELL, it is visible that the horizontal resolution of the NWM definitely has an impact directly on the ray-traced delays. This influence is increasing with decreasing elevation angles. If the elevation angles are larger than 10° then the differences between the solutions RD(0.125°) and RD(1°) reach up to only a few centimetres for the majority

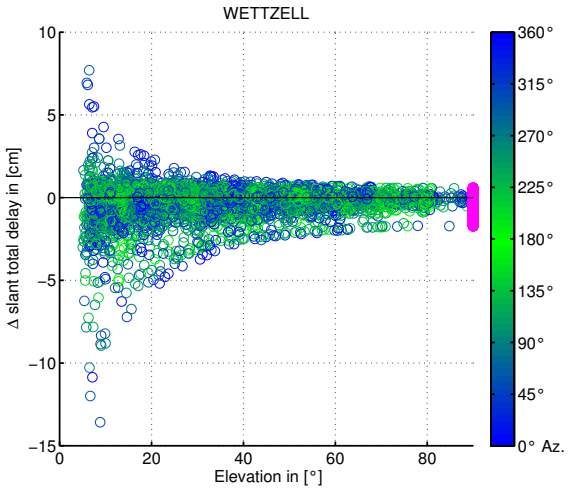

(a) ΔSTD are plotted with respect to the elevation angles, the respective azimuths are shown colour-coded.

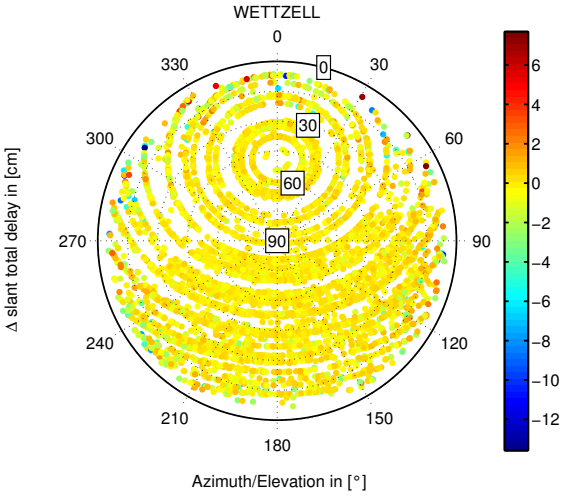

(b) ΔSTD are colour-coded in a skyplot of the observations.

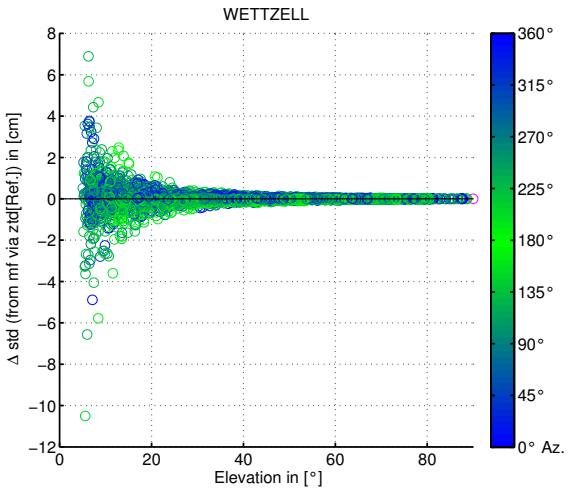

(c) ΔSTD_{mf} are plotted with respect to the elevation angles, the respective azimuths are shown colour-coded.

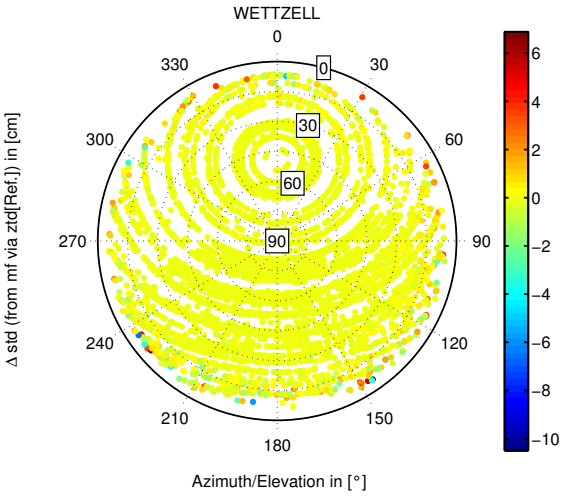

(d) ΔSTD_{mf} are colour-coded in a skyplot of the observations.

Figure 5.3: ΔSTD and ΔSTD_{mf} for the CONT11 observations of station WETTZELL. The differences are built in the form $RD(0.125°) - RD(1°)$ with respect to the specific domain of the differences.

of stations. For most of the elevation angles larger than 10° at most of the stations the differences even remain around only 1-2 cm. But at elevation angles smaller than 10° the differences rise significantly and can even reach up to a few decimetres in case of very low elevations as visible in case of the simulated observations. Please refer to the Appendix Section B.2 Figure B.5a on page 219 to see the ΔSTD of the simulated observations for station WETTZELL. The total amount of the ΔSTD mainly arises from the ΔSWD. Please refer again to the Appendix Section B.2 Figure B.3 on page 217 and Figure B.4 on page 218 for the results of the ΔSHD and the ΔSWD

based on the CONT11 observations of the station WETTZELL.

If we now study the ΔSTD_{mf}, we can basically see a kind of scaled version of the ΔSTD as expected due to the formalism of Equation (5.4). This means that the ΔSTD_{mf} from the ray-tracing results RD(0.125°) and RD(1°) are in general reduced compared to the ΔSTD. See Figure 5.3c for the results of the ΔSTD_{mf} of the station WETTZELL. This finding holds of course also true for the ΔSHD_{mf} and the ΔSWD_{mf}, which are shown in Figures B.3c and B.4c in Appendix Section B.2 on page 217 and page 218. Nevertheless the usage of the mf deliver no true scaled versions as there are some distinct differences compared to the ordinary calculated differences without the use of the mf. Firstly, there are significant outliers especially at at low elevations. Secondly, a few stations, but especially the stations KOKEE and TSUKUB32, show a special behaviour in the ΔSTD_{mf}. At these stations a steeper rise of the ΔSTD_{mf} as expected due to the scaling can be seen at low elevations. This leads to the fact that compared to the homogeneously equally small differences between the ray-tracing solutions RD(0.125°) and RD(1°) at higher elevations, the ΔSTD_{mf} are significantly increased at low elevations and remain at a high level compared to the ΔSTD. An example for this is given in Figure 5.4, which shows the plots of the ΔSTD and the ΔSTD_{mf} for the CONT11 observations of the station KOKEE.

The plots of the differences in the SHD and SWD for the CONT11 observations of the station KOKEE can be found in Appendix Section B.2 in Figure B.6 on page 221 and in Figure B.7 on page 222. Figure B.8 on page 223 shows the results for the simulated observations.

Please refer to the Appendix Section B.2 for the figures of the results for the CONT11 and the simulated observations of the stations FORTLEZA and TSUKUB32. Figures B.9 to B.12 on the pages 225 to 228 show the results for station FORTLEZA and Figures B.13 to B.16 on the pages 230 to 233 show the ones for station TSUKUB32.

5.3.3 Influence on the VLBI analysis with applied ray-traced delays

For a further, more application-oriented, investigation of the effect of the horizontal resolution of the NWM the ray-traced delays RD(0.125°) and RD(1°) are applied to the VLBI analysis to see the influence on the results. For the impact assessment the baseline length repeatability (BLR) and the station coordinate repeatability (SCR) derived from the analysis results are used. BLR and SCR are calculated as the standard deviations of the baseline lengths and of the station coordinates received from the VLBI analysis. As analysis software the Vienna VLBI Software (VieVS) is used (see Böhm et al. 2012, for more information on VieVS). For the influence assessment three different parameterizations are used for the analysis:

Parameterization 1: *Ray-tracing only*

- Ray-traced slant total delays of RD(0.125°) respectively RD(1°) used as a priori input.
- No a priori tropospheric gradient model used.
- No estimation of ZWD or tropospheric gradients.

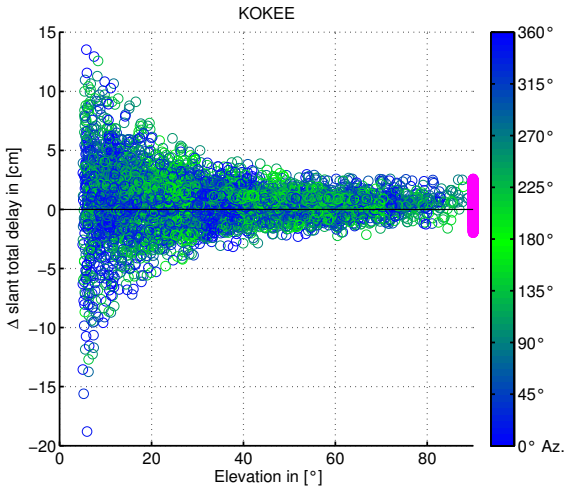

(a) ΔSTD are plotted with respect to the elevation angles, the respective azimuths are shown colour-coded.

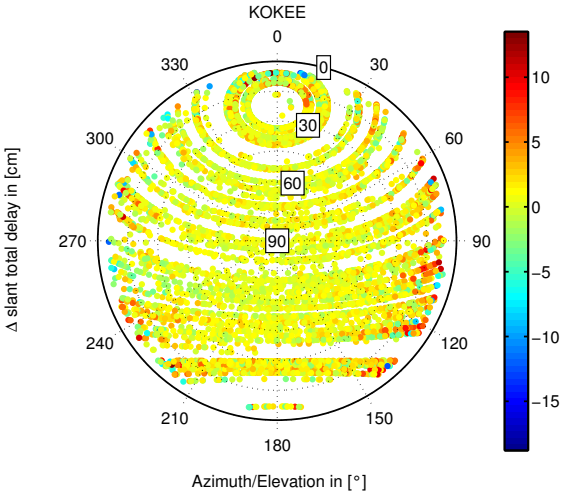

(b) ΔSTD are colour-coded in a skyplot of the observations.

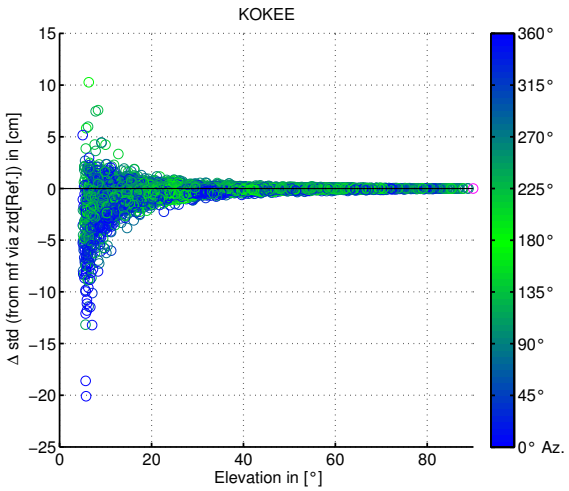

(c) ΔSTD_{mf} are plotted with respect to the elevation angles, the respective azimuths are shown colour-coded.

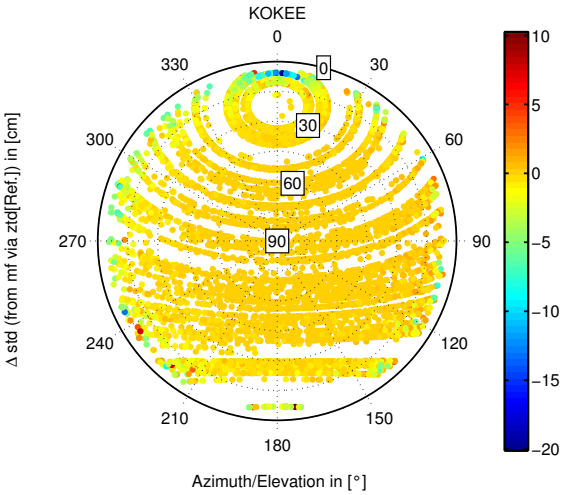

(d) ΔSTD_{mf} are colour-coded in a skyplot of the observations.

Figure 5.4: ΔSTD and ΔSTD_{mf} for the CONT11 observations of station KOKEE. The differences are built in the form $RD(0.125°) - RD(1°)$ with respect to the specific domain of the differences.

Parameterization 2: *Ray-tracing, est. ZWD 3h, est. gradients 24h*

- Ray-traced slant total delays of RD(0.125°) respectively RD(1°) used as a priori input.
- No a priori tropospheric gradient model used.
- Estimation of ZWD every 3 hours with a relative constraint of 10 cm after 3 hours.
- Estimation of tropospheric North- and East-gradients every 24 hours with a relative constraint of 0.01 cm after 24 hours for both gradient directions.

Parameterization 3: *Ray-tracing, est. ZWD 1h, est. gradients 6h*

- Ray-traced slant total delays of RD(0.125°) respectively RD(1°) used as a priori input.
- No a priori tropospheric gradient model used.
- Estimation of ZWD every hour with a relative constraint of 1.5 cm after 1 hour.
- Estimation of tropospheric North- and East-gradients every 6 hours with a relative constraint of 0.05 cm after 6 hours for both gradient directions.

The VLBI analysis is only carried out for the real CONT11 observations, not for the simulated observations as for these no true VLBI observational data are available since they have been defined just for the ray-tracing calculations. Thus, analysis for each of the above defined parameterizations is done two times, once using the RD(0.125°) and once using the RD(1°) for CONT11.

In order to estimate the influence of the horizontal resolution of the NWM on the VLBI analysis, the weighted BLR and the weighted SCR are calculated for each of the in total 6 analysis results. As weights for the estimation of the BLR the inverses of the squared formal baseline length errors are used. These are derived in a calculation using the estimated coordinates and the according covariances of the baseline-forming stations. The weights for the calculation of the SCR are the inverses of the squared formal coordinate errors of the estimated station coordinates. Equations (5.10) and (5.12) describe the formalisms of the BLR and SCR calculations used in the following investigations in this section. The BLR is calculated as

$$BLR = \sqrt{\frac{\sum_{i=1}^{n} w_i \left(b_i - \overline{b}_w\right)^2}{\sum_{i=1}^{n} w_i - \frac{\sum_{i=1}^{n} w_i^2}{\sum_{i=1}^{n} w_i}}} \tag{5.10}$$

with the weight w_i of each length estimate b_i of a specific baseline. The weighted mean baseline length $\overline{b}_w$ is determined as

$$\overline{b}_w = \frac{\sum_{i=1}^{n} w_i b_i}{\sum_{i=1}^{n} w_i}. \tag{5.11}$$

Equation (5.10) is the unbiased[1] weighted estimate of the standard deviation according to the formalism presented in Wikipedia (2016) and Galassi et al. (2015). For short time spans with respect to geological time scales, which is true for the CONT11 campaign, it is not necessary to subtract a trend term from the baseline length estimates before the calculation of the BLR. On

[1] This means that the standard deviation is determined with a degree of freedom of $n-1$.

the example of the X-coordinate the SCR can be determined for any Cartesian coordinate as

$$SCR = \sqrt{\frac{\sum_{i=1}^{n} w_i \left(X_i - \overline{X}_w\right)^2}{\sum_{i=1}^{n} w_i - \frac{\sum_{i=1}^{n} w_i^2}{\sum_{i=1}^{n} w_i}}}, \tag{5.12}$$

where w_i is the weight of each X-coordinate estimate X_i of a specific station. The weighted mean X-coordinate $\overline{X}_w$ is determined as

$$\overline{X}_w = \frac{\sum_{i=1}^{n} w_i X_i}{\sum_{i=1}^{n} w_i}. \tag{5.13}$$

Equation (5.12) is again the unbiased weighted estimate of the standard deviation according to the formalism presented in Wikipedia (2016) and Galassi et al. (2015). Also for the determination of the SCR within the time span of CONT11 it is not necessary to subtract a trend term from the station coordinate estimates before the calculation of the SCR.

The results for the BLR and the SCR from the use of the RD(0.125°) or RD(1°) are compared for each analysis parameterization. Equations (5.14) and (5.15) describe how the assessed parameters, namely the difference in the baseline length repeatability ΔBLR and the difference in the station coordinate repeatability ΔSCR, are calculated. The subscripts describe, which ray-traced delays have been applied to the VLBI analysis. So, with the formalisms described by Equations (5.14) and (5.15) negative differences indicate an improvement of the specific quantity BLR or SCR if the horizontally higher resolved NWM(0.125°) has been used for calculating the ray-traced delays applied to the VLBI analysis.

$$\Delta BLR = BLR_{RD(0.125°)} - BLR_{RD(1°)}, \tag{5.14}$$

$$\Delta SCR = SCR_{RD(0.125°)} - SCR_{RD(1°)}. \tag{5.15}$$

The results for the ΔSCR will be presented with respect to the local topocentric station coordinates in the North-, East- and up-direction. Therefore a transformation from the Cartesian to the local topocentric coordinate system is done in a pre-calculation step of the ΔSCR determination. The transformation equation is described in Section 6.4.3.4 by Equation (6.12).

The plots in Figure 5.5 show the impact of the horizontal resolution of the NWM on the VLBI analysis in terms of ΔBLR and ΔSCR if the analysis parameterization 1, described on page 92, is used. These results are described in the following.

The average of the ΔBLR of all baselines in the solution delivers a value of -0.5 mm. This means that on average the BLR is only slightly worse if the horizontally lower resolved NWM(1°) has been used for determining the ray-traced delays applied to the analysis. Going into more detail, only 34 of the 66 calculated baselines are improved by using the horizontally higher resolved NWM(0.125°). On average the baselines formed by the station KOKEE are influenced the most

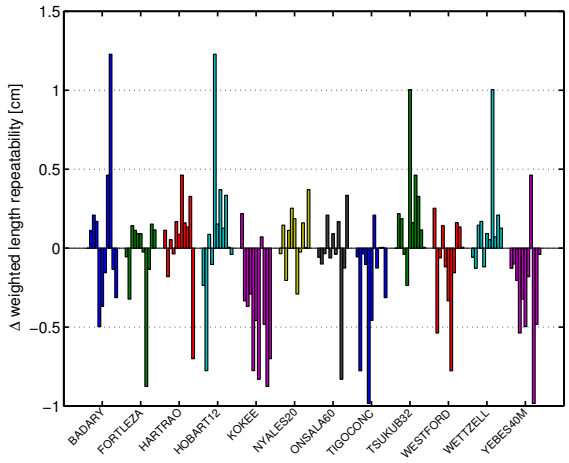

(a) ΔBLR from parameterization 1. The values are presented on a per-station basis, sorted by the weighted mean baseline length. Therefore each specific baseline is contained twice in the plot.

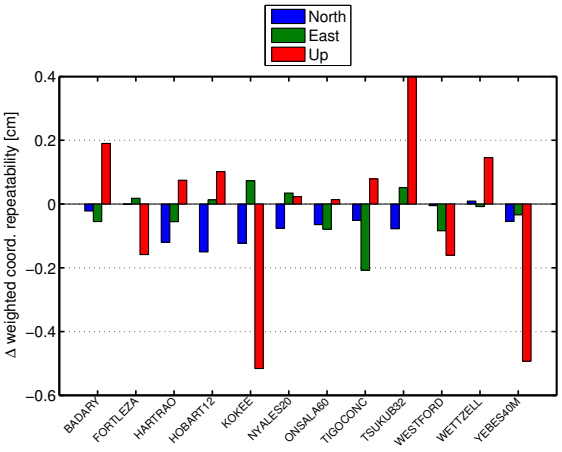

(b) ΔSCR from parameterization 1 in the local coordinate system.

Figure 5.5: Impact of the horizontal resolution of the NWM on the VLBI analysis with parameterization 1, described on page 92. Negative differences indicate that the ray-traced delays derived from the horizontally higher resolved NWM(0.125°) would improve the solution.

with -4.4 mm for the ΔBLR as almost all are at least slightly improved by the use of NWM(0.125°). Nevertheless, in general no clear trend of an improvement can be derived if NWM(0.125°) is used. For 57 of the 66 calculated baselines the ΔBLR is in between ±5 mm.

Concerning the results of the SCR the averaged differences in the local coordinates of all stations are -0.6 mm for the North-, -0.3 mm for the East- and -0.3 mm for the up-direction. In general, looking at the single station results, the ΔSCR are at a very low mm level. Only the stations KOKEE, TSUKUB32 and YEBES40M show increased differences in the up-components, which may come from their significantly increased ΔSTD_{mf}, which has been described in Section 5.3.2. Interestingly, the up-direction of the station TSUKUB32 is oppositely influenced compared to the stations KOKEE and YEBES40M, yielding a positive impact of the usage of NWM(1°). The North-components seem to be improved by the use of NWM(0.125°), but due to the very small amounts this is not significant. For the other coordinate directions there is no clear trend for the impact derivable.

In Figure 5.6 the differences in the analysis results from parameterization 2, described on page 93, are shown. These are discussed in the following.

The individual ΔBLR are in general reduced compared to the parameterization 1 and on average the horizontal resolution of the NWM does not influence the BLR at all for this parameterization. Exactly half of the baselines seem to improve if the RD(0.125°) and the other half if the RD(1°) are applied to the VLBI analysis. With +1.1 mm for the ΔBLR on average for its baselines station KOKEE is again mostly influenced, but this time oppositely compared to the analysis parameterization 1. For 59 of the 66 calculated baselines the ΔBLR is in between ±2 mm. Compared

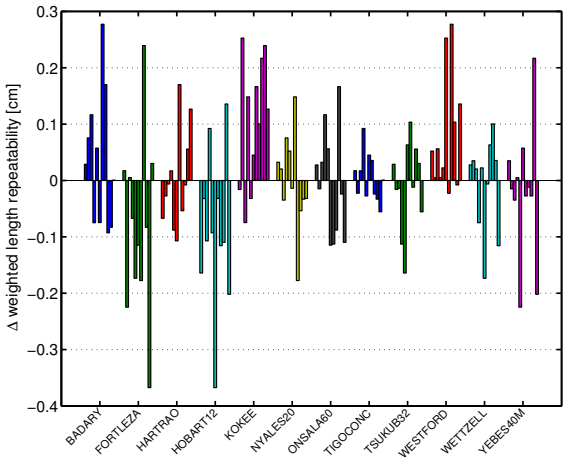

(a) ΔBLR from parameterization 2. The values are presented on a per-station basis, sorted by the weighted mean baseline length. Therefore each specific baseline is contained twice in the plot.

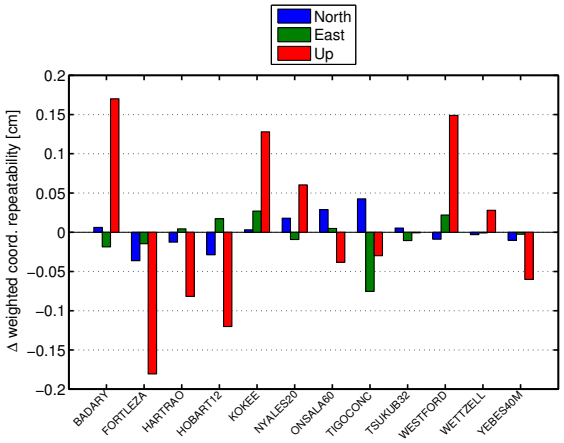

(b) ΔSCR from parameterization 2 in the local coordinate system.

Figure 5.6: Impact of the horizontal resolution of the NWM on the VLBI analysis with parameterization 2, described on page 93. Negative differences indicate that the ray-traced delays derived from the horizontally higher resolved NWM(0.125°) would improve the solution.

to the parameterization 1 the influence of the horizontal resolution of the NWM on the BLR is reduced.

Also the ΔSCR are reduced. On average the differences in the North-direction are close to 0.0 mm, in the East-direction -0.05 mm and in the up-direction +0.02 mm. The individual differences of all stations in the North- and East-direction are at the sub-mm level. Only for some stations the difference in the up-direction is slightly increased. No trend for the impact of the horizontal resolution of the NWM on the SCR can be derived as the differences are very small and not clearly distributed for any of the local coordinate components.

Figure 5.7 shows the differences in the analysis results from parameterization 3, described on page 94, which are discussed in the following.

The BLR differs on average only by +0.2 mm between the analysis solution with applied RD(0.125°) and the one with applied RD(1°). On average the baselines of the station KOKEE are again influenced the most with +1.5 mm for the ΔBLR and again oppositely compared to the analysis parameterzation 1. Looking at the ΔBLR of all baselines, only 25 of the calculated 66 baselines improve with the use of the RD(0.125°). Furthermore for 51 baselines the ΔBLR is between ±1 mm. Thus the impact of the horizontal resolution of the NWM is very low and again reduced compared to the parameterizations 1 and 2 with no clear trend for the impact.

Also the ΔSCR are reduced compared to the results of the previous parameterizations for the VLBI analysis. The North-components of all stations differ on average by about 0.0 mm, the East-components by +0.01 mm and the up-components by +0.4 mm. The ΔSCR are at the sub-mm level at all stations in the North- and East-direction. At some stations the difference in the

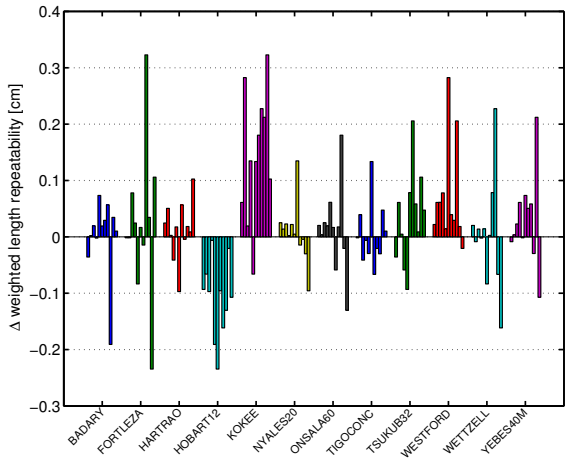

(a) ΔBLR from parameterization 3. The values are presented on a per-station basis, sorted by the weighted mean baseline length. Therefore each specific baseline is contained twice in the plot.

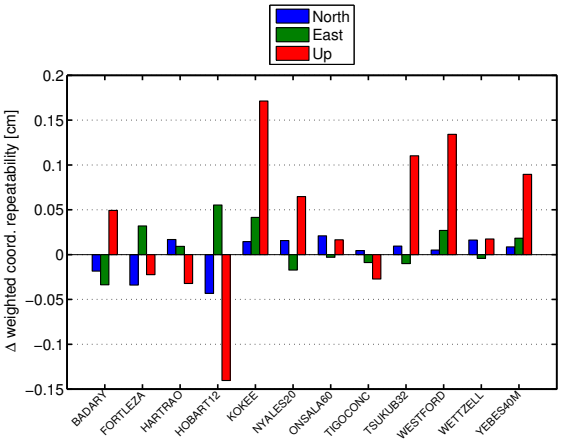

(b) ΔSCR from parameterization 3 in the local coordinate system.

Figure 5.7: Impact of the horizontal resolution of the NWM on the VLBI analysis with parameterization 3, described on page 94. Negative differences indicate that the ray-traced delays derived from the horizontally higher resolved NWM(0.125°) would improve the solution.

up-direction is again slightly increased. In all three coordinate directions no clear trend of an improvement or degradation based on the influence of the horizontal resolution of the NWM can be derived. Furthermore the general impact on the SCR is too small to be significant.

5.3.4 Conclusions on the impact of the horizontal resolution of the numerical weather model

The direct influence of the horizontal resolution of the NWM on the ray-traced delays is increasing with decreasing elevation angle. Nevertheless a really significant impact is only given at elevation angles smaller than 10°.

If the ray-traced delays are applied to the VLBI analysis, the impact of the horizontal resolution of the NWM is relatively small with respect to the BLR and the SCR and no clear trend of an improvement can be derived in case a higher horizontal resolution of the NWM is used for the ray-tracing calculations. Additionally, the analysis parameterization affects the size of the impact. In case of estimating ZWD and tropospheric gradients within the analysis, the influence of the horizontal resolution of the NWM is negligible.

So, from these findings and concerning the operational application of ray-tracing respectively the calculation of ray-traced delays for large datasets spanning long time intervals with many needed epochs of the NWM data, it is appropriate to use a lower horizontal resolution of the NWM, e.g. 1° x 1°. This significantly reduces the number of processing operations and therefore also the processing time of the ray-tracing due to the reduced amounts of meteorological data, which need to be prepared for their utilization. Although there are influences of the horizontal resolution of

the NWM directly on the ray-traced delay results, which are acting mainly on observations at low elevations, the deterioration of the accuracy of the delays is not significant for the conventional usage of the ray-traced delays as they are applied to the VLBI analysis, where neither the higher nor the lower horizontal resolution of the NWM leads to a clear improvement or deterioration of the results.

Nafisi et al. (2012a) investigated the impact on the slant total delays calculated from mapping factors for the case of using the two different NWM horizontal resolutions of 0.5° and 1° and they concluded to use the higher horizontal resolution of 0.5° for determining ray-traced delays for VLBI analysis. Interestingly, the ΔSTD_{mf} found by Nafisi et al. (2012a) are of equal orders of magnitude as the ones that have been presented in this work from NWM data with horizontal resolutions of 0.125° and 1°. This interesting discrepancy in the findings may be explained by the facts that on the one hand the NWM data in its original representation used for ray-tracing may have different accuracies and on the other hand the horizontal interpolation strategy during the ray-tracing follows a completely different approach in Nafisi et al. (2012a) compared to program RADIATE.

Thus, from the findings presented here in this work concerning the application of the ray-traced delays to the VLBI analysis, a horizontal resolution of 1° x 1° of the NWM data still seems to be a good choice in order to reduce processing times without reducing the slant delay accuracies too much. In case of a direct utilization of the ray-traced delays without the application to the VLBI analysis, the use of the NWM data in a higher horizontal resolution would be an option.

5.4 Ray-tracing approach

Based on the theoretical background of ray-tracing, which has been described in Section 4.1, various practical approaches for ray-tracing have been established (like those described in Sections 4.1.1, 4.1.2 and 4.1.3). The differences between these realizations of the strict theoretical background are due to different degrees of simplification or approximation. On the one hand it is true that the closer the implemented method stays to the theoretical background the more accurate the results are. On the other hand simplifications of the strict theory of ray-tracing may be desirable in order to reduce the calculation effort, so that, especially advantageous for a large number of observations, the processing speed can be increased without a significant decrease of the results' accuracy. So, for an operational ray-tracing application the implemented approach needs to satisfy two important aspects: highest accuracy at lowest processing costs.

In a first fundamental step of the decision of the applied ray-tracing approach it is important to decide if ray-tracing should be done in a full three-dimensional (3D) way or if a two-dimensional (2D) approach is sufficient. In a 3D approach the ray path has the freedom to travel in the vertical- and the horizontal-direction, including the possibility of a change of the azimuth. This implementation strictly follows the solution of the Eikonal equation (see Section 4.1 Equation (4.1)) and is therefore processing-cost intensive. In contrast, a 2D approach denies the ray to change the

azimuth by setting it to a constant value. Therefore the ray can not leave the plane determined by the azimuth- and the height-direction. This is the reason why such an approach is accordingly denoted as 2D. In a 2D approach the formalism of the ray-tracing is significantly simplified and the processing costs are reduced correspondingly. The theoretical derivation of the 2D ray-tracing out of the 3D ray-tracing has been described in Section 4.1.

Concerning the differences in the resulting ray-traced delays between 3D and 2D approaches the results of the research of Hobiger et al. (2008a) will be discussed in the following. Hobiger et al. (2008a) compared a 3D approach, which is the solution of the Eikonal equation, against the 2D approaches Thayer and (ref.) PWL (see again Section 4.1 for more information on the theoretical background). The comparison of the 3D approach against both 2D approaches reveal for complex weather conditions that the differences of the slant total delays at elevation angles larger than 10° do not exceed 1 mm. At elevation angles of 5° the differences may be up to only 3 mm. Thus, the 2D approaches Thayer and (ref.) PWL deliver results equivalent to the processing-cost-intensive 3D approach. Furthermore Nafisi et al. (2012b) found that the impact of a different NWM is significantly larger as the slant total delays can differ at the dm level just because of different NWM inputs. So, the small differences of the 2D approaches to the 3D approach can be neglected.

After the fundamental finding of a 2D ray-tracing approach as being sufficient for the operational application, the second step of the decision is to choose, which specific 2D method from the available should be used. Three different 2D methods have been implemented in program RADIATE. These are the PWL, the ref. PWL and the Thayer approach. The details on these models have been described in Sections 4.1.1, 4.1.2 and 4.1.3.

For a general quality assessment of the RADIATE ray-tracing results a comparison against the results of ray-tracing programs of different institutions has been carried out by Hofmeister and Böhm (2014). More details on this comparison will be given in Section 6.1. Within this comparison the three implemented ray-tracing approaches of program RADIATE have been tested. Their results can be used to quantify the differences in the delays just from using a different approach. The results described in the following originate from the comparison by Hofmeister and Böhm (2014). For the calculation of the delays sufficiently high resolved meteorological data in the vertical domain have been used in the comparison since the input NWM data have been interpolated. The PWL, ref. PWL and Thayer approach deliver very similar results for the STD, which are shown in Figure 5.8 for the stations WETTZELL and TSUKUB32. In Table 5.1 statistical details on the differences between the ref. PWL and the PWL approach and statistical details on the differences between the Thayer and the PWL approach can be found.

As the resolution of the refractivity in the vertical direction is high enough in case of the default setting of program RADIATE, which is described in Section 4.2.2, the PWL and the ref. PWL approach deliver equal results. Therefore the application of the more sophisticated approach of the ref. PWL method with the refined refractivity determination is not necessary and is just leading to increased processing costs. Furthermore the difference of the PWL solution to the Thayer approach can be described by an offset that may come on the one side from the fact that

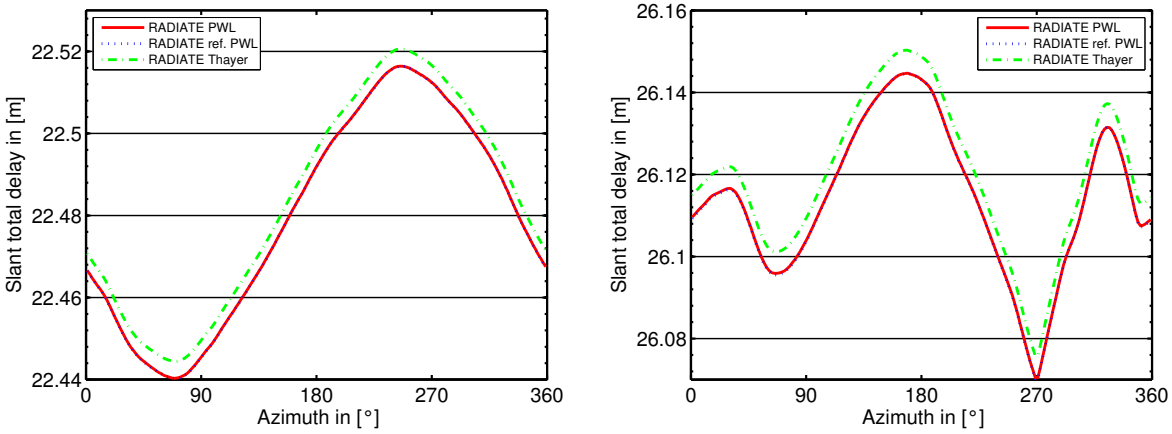

(a) STD for station WETTZELL at 5° elevation angle for January 1, 2008 at 00:00:00 h UTC.

(b) STD for station TSUKUB32 at 5° elevation angle for August 12, 2008 at 00:00:00 h UTC.

Figure 5.8: Impact of different 2D ray-tracing approaches on the STD results. Results have been taken from the comparison of Hofmeister and Böhm (2014).

Table 5.1: Statistical details on the differences between the ref. PWL and the PWL approach and statistical details on the differences between the Thayer and the PWL approach according to the values shown in Figure 5.8.

Ref. PWL - PWL in [mm]	WETTZELL	TSUKUB32
Min.	-0.2	-0.4
Max.	0.0	0.1
Mean	-0.1	-0.2
Standard deviation	0.1	0.1
Thayer - PWL in [mm]	**WETTZELL**	**TSUKUB32**
Min.	4.0	5.3
Max.	4.2	5.8
Mean	4.1	5.5
Standard deviation	0.1	0.1

the Thayer approach uses curved ray paths instead of linear pieces and on the other side from the more sophisticated calculation of the refractivity values. Although there is a more or less constant offset of about 4.1 mm at station WETTZELL and of about 5.5 mm at station TSUKUB32 between the results of the PWL and the Thayer approach at an elevation angle of 5°, the results of the PWL approach are not significantly different with respect to the very low elevation. Referring again to the comparison results of Hobiger et al. (2008a) they receive even smaller differences between the PWL and the Thayer approach of up to only 1.2 mm at an elevation angle of 5°. This might be due to a different way of calculating the slant distance that is used for the determination of the

slant delay since the formula used for the Thayer approach implemented in program RADIATE introduces slight overheads for the slant distances at elevations almost equal to the zenith, which leads to increased overheads for the slant distances at low elevations as the overheads become scaled. This may explain the resulting increased difference between the PWL and the Thayer approach compared to the results of Hobiger et al. (2008a). The comparison between the PWL and the Thayer approach leads to the conclusion that it is sufficient to use the simple but less processing-cost intensive PWL method instead of the more sophisticated but therefore also more processing-cost intensive Thayer approach since the ray-tracing accuracy is good enough in case of the PWL method.

In order to compare the processing times of the different approaches, a test using the operational Fortran version of program RADIATE is carried out. Using simulated observations at different azimuth and elevation angles, the processing time, which is needed solely for the ray-tracing and delay calculations, of each implemented ray-tracing approach is derived. Please refer to Section 6.2.1 for the observation data details and the main processing settings used for this test. As a result, the implementation of the PWL approach shows the best performance and is able to process on average[1] 1000 observations in only 0.8 seconds. In contrast, both the implementation of the ref. PWL and the Thayer approach need on average 1.6 seconds for calculating the ray-traced delays of 1000 observations, i.e. due to the increased processing costs of these approaches the processing times are doubled.

As a conclusion from all of the above findings, it is an adequate choice to use the PWL method for ray-tracing in order to satisfy both the aspects of accuracy and of processing costs, i.e. needed processing time, as this method delivers an acceptable accuracy with a simple and fast-performing algorithm.

5.5 Inner accuracy of the ray-traced delays

Another important aspect of ray-tracing is the setting of the desired target accuracy of the calculated delays. As described in Section 4.1 the signal path has to be determined in the first step of the delay determination, i.e. in the actual ray-tracing process. This is an iterative operation in case of VLBI observations because of the stepwise adjustment of the initial elevation angle at the station in order to determine a ray path that fits the outgoing elevation angle of the observation (see also Section 4.1.1 for more details on this task with respect to the PWL approach). In order to reduce the number of iterations and avoid infinite iteration in case of a non-convergence, an adequate stopping criterion has to be set. This criterion is defined to be the difference of the outgoing elevation angle that has been been determined from ray-tracing to the original outgoing

[1] The value is said to be on average since the processing time is taken from ray-tracing at different elevation angles and a small elevation angle leads to a significantly higher processing time than a larger elevation angle, because more iterations of the ray-path are needed to reach the desired accuracy of the outgoing elevation angle. Thus, the reported processing time has to be seen as a mean value and it can not be said that the processing of every observation takes the same time.

elevation angle from the observation. The iteration stopping criterion therefore directly defines the achievable inner accuracy of the delay[1] with respect to the used ray-tracing approach since the delay is calculated in the second step after the final ray path has been determined through ray-tracing. Thus, the inner accuracy of the delay is connected to the accuracy with which the original outgoing elevation angle is reached by iteration of the ray path.

For program RADIATE the inner accuracy goal is defined through the inner accuracy of the slant hydrostatic delay. Precisely, the SHD should have an inner accuracy of at least 0.1 mm at an elevation angle of 3°. This quite challenging setting is necessary in order not to leave too much additional margin of error for the delays since the use of a not strict ray-tracing approach[2] already introduces an error to them as it has been described in Section 5.4.

To reach this inner accuracy goal of the delay, which is defined purely by the iteration accuracy, the maximum allowed absolute difference value between the ray-traced outgoing elevation angle and the outgoing elevation angle from the observation has to be known so that it can be set as the stopping criterion for the iterative ray path determination. In order to determine this allowed maximum absolute deviation in the ray-traced outgoing elevation angle, calculations using the Global Mapping Function (GMF) (see Böhm et al. 2006a) are carried out. For the calculations a ZHD of 2 m at a station located at 0° latitude φ and 0° longitude λ at an ellipsoidal height h_{ell} of 0 m at the modified Julian date mjd 51544 (01.01.2000 00:00:00 h) is assumed. The basic equation to determine the SHD at a specific elevation angle e from the ZHD and from the hydrostatic global mapping factor gmf_h of the GMF (see Böhm et al. 2006a) is

$$SHD = ZHD \cdot gmf_h(mjd, \varphi, \lambda, h_{ell}, e). \tag{5.16}$$

From this it can be derived that

$$gmf_h(mjd, \varphi, \lambda, h_{ell}, e) = \frac{SHD}{ZHD}. \tag{5.17}$$

If the SHD is now changed by a specific amount of ΔSHD, also the value for gmf_h changes. This change can be passed on to a change of the input elevation angle for gmf_h by a value of Δe whilst all other dependencies are fixed to their original value:

$$gmf_h(mjd, \varphi, \lambda, h_{ell}, e + \Delta e) = \frac{SHD + \Delta SHD}{ZHD}. \tag{5.18}$$

Therefore an iteration of the input elevation angle $e + \Delta e$ in Equation (5.18) can be used to determine at which value of Δe the ΔSHD becomes smaller than a desired value. Assuming a maximum ΔSHD of 0.1 mm the Δe must not exceed $1.62 \cdot 10^{-5}$ degree[3] in case of an elevation

[1] With inner accuracy of a delay the accuracy of a delay within a specific ray-tracing approach is meant, not considering the overall accuracy of the approach itself.

[2] A strict ray-tracing approach means the 3D solution of the Eikonal equation. Thus, the 2D approaches used in program RADIATE are not strict.

[3] $\approx 2.83 \cdot 10^{-7}$ rad

angle of 3°. Therefore the stopping criterion for the iteration of the ray path in program RADIATE is set to $1 \cdot 10^{-7}$ rad $\approx 5.7 \cdot 10^{-6}$ degree to ensure that the inner accuracy of the SHD at an elevation angle of 3° is at least 0.1 mm.

The possible case of a non-convergence of the iteration with respect to the desired iteration accuracy is solved by introducing an ultimate stopping criterion through defining a number of maximum allowed iterations. This threshold is set to 10 iterations for program RADIATE since typical ray-tracing calculations showed that this value is sufficiently high enough in order not to break converging iterations before the iteration accuracy is reached.

5.6 Conclusions for an operational service

The findings of the previous sections helped to reveal the requirements and desired specifications of an operational ray-tracing service. In contrast to ray-tracing with the target of maximized accuracy by using the best available original resolution of the NWM data and the most accurate ray-tracing strategy, the goal of an optimal ray-tracing service for operational tasks is to combine two antagonists, namely high processing speed and high accuracy of the results.

Considering the choice of the optimal sources for the meteorological data, Section 5.2 showed that the combination of NWM data with a standard atmosphere model provides a good basis for the input of meteorological data to the ray-tracing application.

The general selection of the type of the NWM is more difficult. According to Nafisi et al. (2012b) the use of different NWM from different weather forecasting centres can lead to differences in the slant delays at the dm level. For program RADIATE the operational NWM of the ECMWF with 25 total pressure levels is selected. For the processing of observational data before 01.01.2008 the ECMWF Re-Analyis-Interim (ERA-Interim) NWM is utilized. Both models are used with the same output specifications as described in Table 4.2 on page 63. Nevertheless a further choice has to be made as the models are available in different horizontal resolutions. This decision is of major importance for an operational ray-tracing service as the highest available resolution would on the one hand significantly increase the processing time and would additionally lead to a higher memory demand. On the other hand Section 5.3.2 revealed that the ray-traced delays, especially for low elevations, are affected by the horizontal resolution of the NWM data and thus may benefit from higher resolved meteorological data. Nevertheless the primary purpose of the calculation of ray-traced delays[1] is to use them for the application to the VLBI analysis on which the impact of the horizontal resolution of the NWM ranges from quite small to insignificant depending on the parameterization of the analysis as it has been revealed in Section 5.3.3. Therefore it is sufficient for an operational VLBI ray-tracing service to use a horizontally lower resolved NWM, e.g. 1° x 1° in case of program RADIATE, and to take the advantages of shorter processing time and lower memory demand.

According to the descriptions and findings of the Sections 4.2.2.1 and 4.2.2.2 the operational

[1] at least in this research

Fortran version of program RADIATE uses the "profilewise" and thus strict vertical interpolation mode by default since the meteorological data from the NWM are interpolated vertically on the global scale. The use of the not strict "gridwise" mode on the global scale would lead to inaccuracy effects on the resulting ray-traced delays.

The ray-traced delays are usually determined at the exact observation times in the operational version of program RADIATE by using the time interpolation approach, which is described in Section 4.2.6.

The choice of the appropriate ray-tracing method is again a decision between processing speed and accuracy. With respect to the small differences between the strict 3D approach and the 2D methods and the found small differences between the in program RADIATE implemented different 2D approaches PWL, ref. PWL and Thayer, found in Section 5.4, it is appropriate to take the benefit of the fast processing speed of the PWL method with the drawback of only a small loss of accuracy of the ray-traced delays.

The decision of the iteration depth, i.e. the accuracy with which the ray path is determined, is of minor importance with respect to the processing speed as the utilized ray-tracing algorithm usually converges fast and only a few iterations are needed to reach the set accuracy of the outgoing elevation angle. Thus, program RADIATE is set up in a way to determine the ray path very accurately (see Section 5.5). The reason for this is the inner accuracy of the delays, i.e. the accuracy of the delays within a specific ray-tracing approach, not considering the overall accuracy of the approach itself. Program RADIATE is set up to iteratively reconstruct the ray path until the outgoing elevation angle from the observation is reached with an accuracy of at least $1 \cdot 10^{-7}$ rad in order to reach an inner accuracy of the SHD of at least 0.1 mm at an elevation angle of 3°.

The processing speed of the ray-tracing program, i.e. the number of operations per second and not considering the total number of operations executed within the program, is in general limited by the speed of one core of the computer's Central Processing Unit (CPU), which carries out all operations within a program run. The operational Fortran version of program RADIATE is capable of determining ray-traced delays for one session, e.g. a VLBI session, at each call of the program. Thus, through the use of a multi-core CPU and parallel runs of the ray-tracing program, it is possible to increase the processing speed in case of a large number of sessions.

A strategy for the increase of the processing speed within one session would be the application of parallel processing inside the ray-tracing program for the use together with a multi-core CPU. The realization of this strategy requires a modification of the source code. As Hobiger et al. (2009) show in their investigation an even further increase in the processing speed within one session can be reached by implementing the ray-tracing in parallel mode on a Graphics Processing Unit (GPU). The performance gain is dependent on the number of rays that should be calculated for one session. This is due to the fact that the individual cores of a CPU perform better than the individual cores of a GPU. The performance boost through the utilization of a GPU is generated by the larger number of cores compared to a CPU. Therefore the GPU enables a performance gain in case of a large number of rays, whereas the CPU outperforms the GPU in case of a small number of rays (Hobiger et al. 2009).

Chapter 6

Investigations on ray-tracing for geodetic VLBI

In this chapter different investigations on ray-tracing for geodetic VLBI and their results are presented. The spectrum of the shown researches ranges from basic aspects like a general quality assessment of the ray-traced delays to very detailed investigations of different results.

6.1 Validation of RADIATE against other ray-tracing programs

In order to validate the results of program RADIATE and to get a knowledge of the expectable accuracy of the ray-traced delays a comparison of RADIATE against other ray-tracing programs is useful as a first basic quality assessment.

For this reason the results of program RADIATE are validated against the results of a ray-tracing program comparison campaign by Nafisi et al. (2012b). Five different institutions have taken part in this campaign, each with their own ray-tracing program. Table 6.1 shows the institutions and their ray-tracing program. For more details on the different programs please refer to Nafisi et al. (2012b).

In the comparison campaign by Nafisi et al. (2012b) from which the following information is taken, common data sets have been used wherever possible to ensure an optimal environment for the direct comparison of the ray-tracing results. For the validation of program RADIATE against this comparison campaign, RADIATE therefore also uses the same data sets. In detail this means that the ECMWF operational NWM with 25 total pressure levels, a horizontal resolution of 0.1° x 0.1° and a horizontal extent of 20° x 20° around the station position is used, which provides the needed parameters geopotential, temperature and specific humidity. Additionally the geoid undulations from the Earth Gravitational Model 1996 (EGM96) (see Lemoine et al. 1998) are used in the same horizontal resolution. The observational data for the ray-tracing consists of observations at 5° elevation angle at azimuths in the interval [1°:2°:359°]. The delays are calculated for these observation geometries at the station TSUKUB32 at the epoch August 12, 2008 00:00:00 h UTC and at the station WETTZELL at the epoch January 1, 2008 00:00:00 h

Table 6.1: Ray-tracing programs of the institutions that participated in the comparison campaign of Nafisi et al. (2012b).

Program	Approach	Institution	Developers
GFZ	2D	GFZ (German Research Centre for Geosciences)	Florian Zus and Jens Wickert
Horizon	Eikonal (2D)	GRGS (Groupe de Recherche de Géodésie Spatiale)	Pascal Gegout
KARAT	Thayer (2D) and Eikonal (3D)	NICT (National Institute of Information and Communications Technology)	Thomas Hobiger and Ryuichi Ichikawa
UNB-bent	2D and 3D	UNB (University of New Brunswick)	Landon Urquhart, Marcelo Santos, Felipe Nievinski
VIE	2D and 3D	Vienna University of Technology	Vahab Nafisi, Johannes Böhm, Dudy D. Wijaya

UTC for the same observation geometries. Nafisi et al. (2012b) chose these two different stations at two different epoch times on purpose since station TSUKUB32 is facing humid conditions in August, whereas station WETTZELL faces rather dry conditions in January. Thus, two opposite tropospheric conditions can be investigated. Please note, that the programs GFZ and Horizon used ECMWF native model level data with 91 model levels instead of the ECMWF pressure level data with 25 total pressure levels like the other programs in the past comparison campaign (Nafisi et al. 2012b).

In the following the results of program RADIATE for its different ray-tracing approaches will be compared to the results of the past comparison campaign by Nafisi et al. (2012b). A summary of this research can also be found in Hofmeister and Böhm (2014).

Table 6.2 gives an overview of the main settings of program RADIATE for the calculations of the ray-traced delays for the comparison. The ray-tracing approaches PWL, ref. PWL and Thayer, which are implemented in program RADIATE, have been described in the Sections 4.1.1, 4.1.2 and 4.1.3. All main settings of and processes within program RADIATE for this comparison comply with those that have been described in Section 4.2. Please note that for the Earth's curvature approximation the Gaussian curvature radius is used (see Section 4.2.3) and that the vertical interpolation is done with the "gridwise" approach (see Section 4.2.2.1) for a subgrid with a horizontal extent of 20° x 20° around the station position (see Section 4.2.2.2). The characteristics of the other ray-tracing programs can be found in Nafisi et al. (2012b).

In a first step of the comparison of the results of program RADIATE to those of the other ray-tracing packages, the zenith delay results shall be investigated. Figure 6.1 shows the differences in different zenith delay domains with respect to the results of the RADIATE PWL approach. Please note that the results for the presented different zenith domains are not available from all ray-tracing packages. Furthermore please be aware of the fact that the ZTD, ZHD and ZWD of all ray-tracing packages except those of RADIATE are taken from Nafisi et al. (2012b). Unfortunately,

Table 6.2: Main settings of program RADIATE for the comparison.

Methods (all 2D)	NWM	Upper height limit	Suppl. atm. model	Treatment of the Earth's curvature	Vertical interpolation of the meteorological parameters
PWL, ref. PWL, Thayer	ECMWF pressure level data	84 km	U.S. Stand. Atm. 1976	Gaussian curvature radius	Temperature: linear, pressure and water vapour pressure: exponential

these reported ZHD and ZWD values do not fit to the reported ZTD values since their sums are not equal to the ZTD values. Therefore the ΔZTD shown in Figure 6.1a are not equal to the sums of the ΔZHD and the ΔZWD presented in Figures 6.1b and 6.1c, although this should be the case like the RADIATE results show.

All three RADIATE ray-tracing approaches yield the same results in any of the zenith delay domains. This important fact yields a first positive assessment since the zenith delay in each domain should stay the same independent of the ray-tracing approach as the implementations in RADIATE strictly separate the slant and the zenith delay determinations. Thus, the method of the ray path determination itself does not affect the determined zenith delays. Nevertheless the zenith refractive indices are calculated differently in case of the ref. PWL method compared to the PWL and the Thayer approach. Receiving equal results for all three approaches strengthens the impression of the correct implementation of each approach. Since the differences between the zenith delays of the RADIATE PWL solution and the other two RADIATE solutions are zero, the bars for the RADIATE solutions are not visible in the plots of Figure 6.1.

In Figure 6.1a the differences in the zenith total delay ΔZTD with respect to the RADIATE PWL solution are investigated. The comparison reveals that especially at the station WETTZELL the results of RADIATE fit quite well to the other ray-tracing packages since the differences only reach up to around 2.2 mm. As most of the differences show a positive sign, RADIATE mostly delivers ZTD that are a bit lower than those of the other programs. Concerning the results for station TSUKUB32 the differences of the other ray-tracing programs to RADIATE are a bit increased, especially the results of the programs GFZ and Horizon. As mentioned earlier GFZ and Horizon used a different kind of NWM for calculating their results. The significantly increased differences between the ZTD results of RADIATE and those of GFZ and Horizon arise from the ZWD part as the alternative NWM is supposed to show differences especially in the wet domain. Compared to the remaining ray-tracing packages the results of RADIATE still fit quite well at station TSUKUB32 as the ΔZTD do not exceed 3.7 mm. Also for station TSUKUB32 RADIATE delivers ZTD values, which are in general a bit lower compared to those of the other ray-tracing packages since the differences are always positive.

Figure 6.1b shows the differences in the zenith hydrostatic delay ΔZHD with respect to the RADIATE PWL solution. Also concerning this quantity, the RADIATE results have a good agreement at both stations with the results of the other ray-tracing packages. Please remember that the values of the other ray-tracing packages are not too reliable since their ZHD and ZWD do

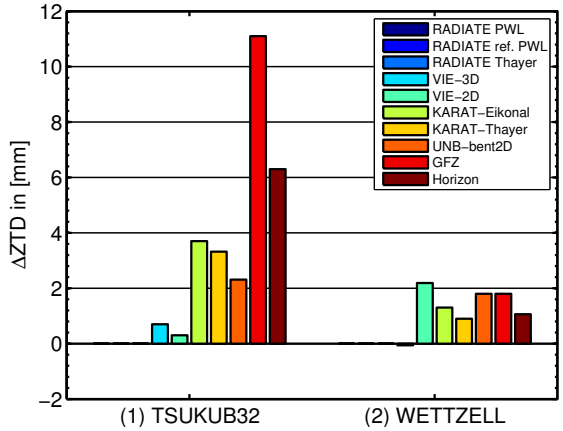

(a) $\Delta ZTD = ZTD - ZTD_{RADIATE\ PWL}$. $ZTD_{RADIATE\ PWL}$ for (1) TSUKUB32: 2.5716 m and (2) WETTZELL: 2.2057 m.

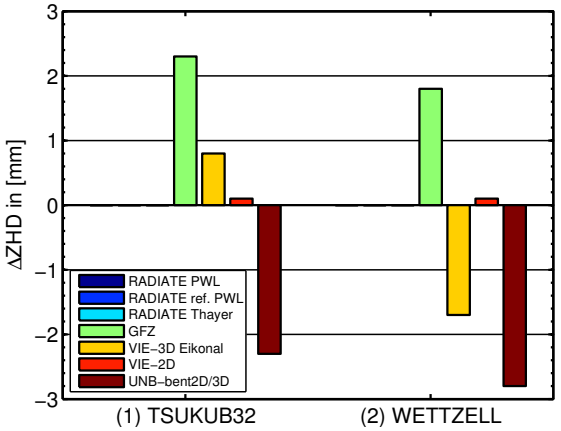

(b) $\Delta ZHD = ZHD - ZHD_{RADIATE\ PWL}$. $ZHD_{RADIATE\ PWL}$ for (1) TSUKUB32: 2.2969 m and (2) WETTZELL: 2.1688 m.

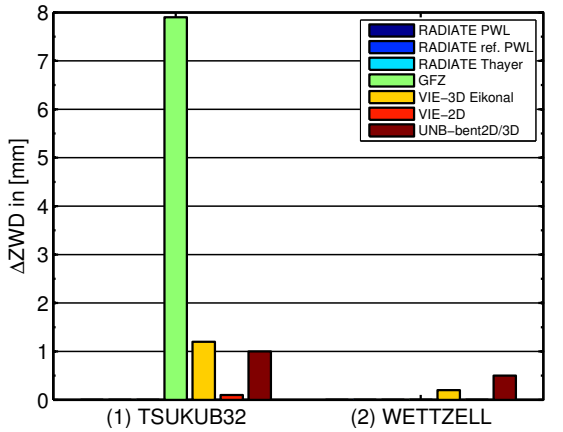

(c) $\Delta ZWD = ZWD - ZWD_{RADIATE\ PWL}$. $ZWD_{RADIATE\ PWL}$ for (1) TSUKUB32: 0.2747 m and (2) WETTZELL: 0.0369 m.

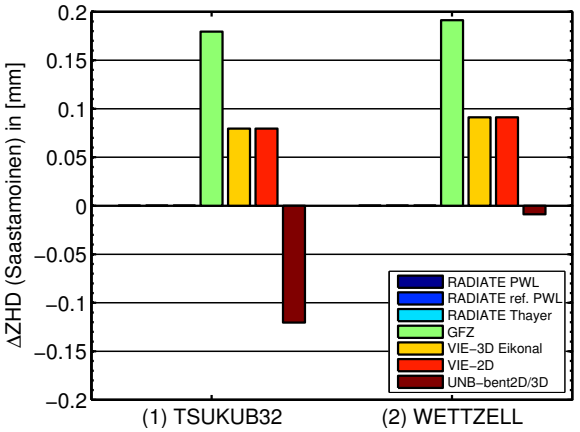

(d) $= ZHD^S - ZHD^S_{RADIATE\ PWL}$. $ZHD^S_{RADIATE\ PWL}$ for (1) TSUKUB32: 2.2948 m and (2) WETTZELL: 2.1662 m.

Figure 6.1: Differences of the results of the different ray-tracing packages in the individual zenith domains with respect to the results of RADIATE PWL. Observation times are August 12, 2008 00:00:00 h UTC for station TSUKUB32 and January 1, 2008 00:00:00 h UTC for station WETTZELL. Results have been taken from Hofmeister and Böhm (2014), respectively the underlying past comparison campaign results from Nafisi et al. (2012b).

not fit to their ZTD and program GFZ used a different NWM in the comparison of Nafisi et al. (2012b). Erroneous ZWD values may especially be the case for program UNB-bent2D/3D since the sum of its ΔSHD and its ΔSWD for each station is far away from its according ΔSTD.

The comparison of the ZWD is shown in Figure 6.1c, where the ΔZWD with respect to the RADIATE PWL solution are presented. Neglecting the result of program GFZ since this program used a different NWM, also in this domain the RADIATE results have a good agreement at both stations with the results of the other ray-tracing packages. Please remember again that the values of the other ray-tracing packages are not too reliable due to the reasons discussed before.

In order to reduce the impact of the meteorological data to only the pressure at the station level also the results for the zenith hydrostatic delay from Saastamoinen's equation ZHD^S are investigated. The formalism has already been presented in Section 3.3 in Equation (3.28). The advantage of this formula is that only the total pressure at the station position, the station's latitude and the station's height must be known to be able to evaluate it. Thus, the utilization of this equation reduces the impact of the NWM data on the ZHD significantly, which enables a better direct comparison of the different ray-tracing packages. Figure 6.1d presents the differences in the zenith hydrostatic delay from Saastamoinen's equation ΔZHD^S with respect to the RADIATE PWL solution. The agreement of the RADIATE results with the results of the other ray-tracing packages is very good since the ΔZHD^S only reach up to about 0.2 mm at both stations TSUKUB32 and WETTZELL if the results of GFZ, which uses a different NWM as already stated earlier, are included. If not, the results of RADIATE fit even better to those of the remaining ray-tracing packages with differences of around only 0.1 mm at both stations.

Figure 6.2 shows the STD results of program RADIATE and of the other ray-tracing packages for the stations TSUKUB32 and WETTZELL. The results of the other ray-tracing packages are again taken from Nafisi et al. (2012b). Please note that only the 2D mode results of the ray-tracing package UNB are shown in Figure 6.2 and not its 3D mode results. Nafisi et al. (2012b) describe that the differences between the UNB 2D mode results and the UNB 3D mode results are smaller than 0.01 mm at both stations and that the STD of the UNB 2D mode are always slightly larger than those of the UNB 3D mode.

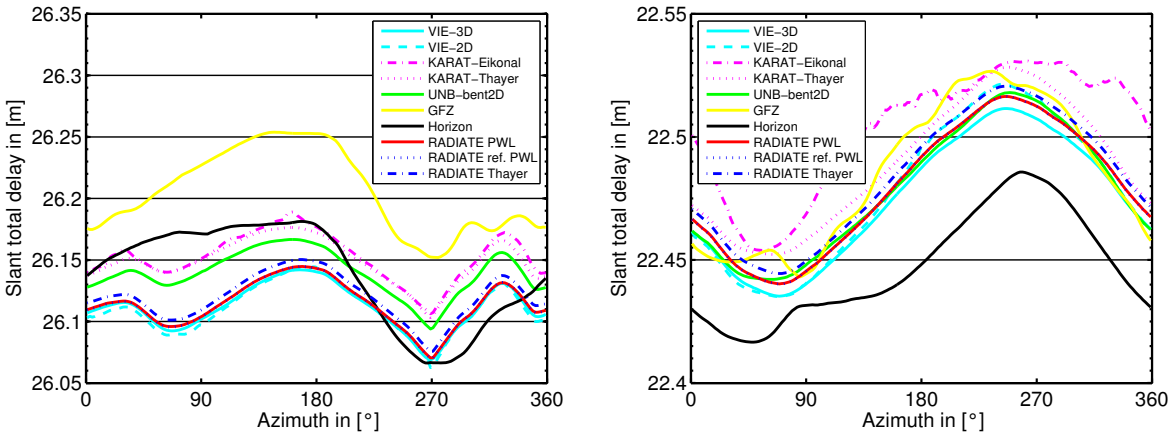

(a) STD for station TSUKUB32 at 5° elevation angle on August 12, 2008 00:00:00 h UTC.

(b) STD for station WETTZELL at 5° elevation angle on January 1, 2008 00:00:00 h UTC.

Figure 6.2: STD of different ray-tracing programs. Results have been taken from Hofmeister and Böhm (2014), respectively the past comparison campaign results from Nafisi et al. (2012b).

In case of station TSUKUB32, shown in Figure 6.2a, the results of RADIATE fit very well to the general trend of the STD of the other ray-tracing programs. Please note again that the packages GFZ and Horizon used a different NWM than the others as described before. Therefore their trends in the STD across the full azimuth range are different. This is due to the fact that the

wet part of the delay is an important factor at the station TSUKUB32 for observations in August and the alternative NWM is supposed to show differences especially in the wet domain. The differences of the RADIATE results to those of the other ray-tracing packages are at a low cm-level if the results of GFZ and Horizon are neglected. In case of the RADIATE PWL solution the individual mean differences to the other solutions, neglecting the solutions of GFZ and Horizon, are below 3.9 cm with standard deviations below 0.6 cm.

Figure 6.2b presents the results for the STD at station WETTZELL. Again the RADIATE results fit very well to the trends of the other ray-tracing programs. In this case also the trends of GFZ and Horizon fit to those of the other ray-tracing packages. This is due to the fact that the impact of the wet part of the delay on observations at the station WETTZELL in January is significantly smaller than on observations at the station TSUKUB32 in August. Therefore the different NWM used by GFZ and Horizon does not influence their results in the STD too much compared to the results of the other ray-tracing packages. Looking at the individual mean differences of the RADIATE PWL solution to the other solutions, neglecting the solution of Horizon, only values below 2.4 cm are found with standard deviations below 1 cm. Interestingly, the solution of KARAT-Eikonal does not fit to the other solutions at station WETTZELL besides the solution of Horizon. Neglecting both the solutions of Horizon and KARAT-Eikonal the individual mean differences of the RADIATE PWL solution to the remaining solutions do not even exceed 1 cm with standard deviations below 0.4 cm. Generally all different RADIATE solutions fit better to the solutions of the other ray-tracing packages at station WETTZELL compared to the findings at station TSUKUB32. This can be explained by the reduced humidity at station WETTZELL compared to station TSUKUB32 at the investigated observation times since the humidity has a key impact on the delays.

Looking closer at the results for the STD of each ray-tracing approach of program RADIATE at each station, it is obvious that they are quite similar. The detailed descriptions of the expectable and actual differences between the specific ray-tracing approaches of RADIATE have already been given in Section 5.4. In general the STD trends across the full azimuth range are equal and also the absolute results are very similar.

As Nafisi et al. (2012b) state, the correspondence of the mapping factor results of the different ray-tracing packages is in practice even more important than the agreement of the STD results since in VLBI analysis, where the ray-traced delays are applied, usually residual zenith delays are estimated. Therefore also the agreement of the STD calculated from mapping factors is investigated here. The application of mapping factors reduces general offsets in the absolute delay values. Equation (6.1) repeats the formalism of the calculation of the mapping factor mf in the total domain as it has already been presented by Equation (5.5):

$$mf = \frac{STD}{ZTD}. \tag{6.1}$$

With Equation (6.1) the slant total delay from mapping factor STD_{mf} can be determined by

$$STD_{mf} = mf \cdot ZTD. \tag{6.2}$$

For the following comparisons the STD_{mf} of all ray-tracing packages are determined. For the calculations of the STD_{mf} the mf of the individual ray-tracing packages are always used together with the ZTD of the RADIATE PWL solution. The mf value of each ray-tracing package has been calculated beforehand using its individual STD and ZTD results. With this approach a kind of scaling with respect to the RADIATE PWL solution is introduced compared to the normal STD values. As all three RADIATE ray-tracing methods have the same ZTD, which is used for the calculation of their individual mf, there is no scaling for the RADIATE solutions. Figure 6.3 shows the STD_{mf} at the stations TSUKUB32 and WETTZELL.

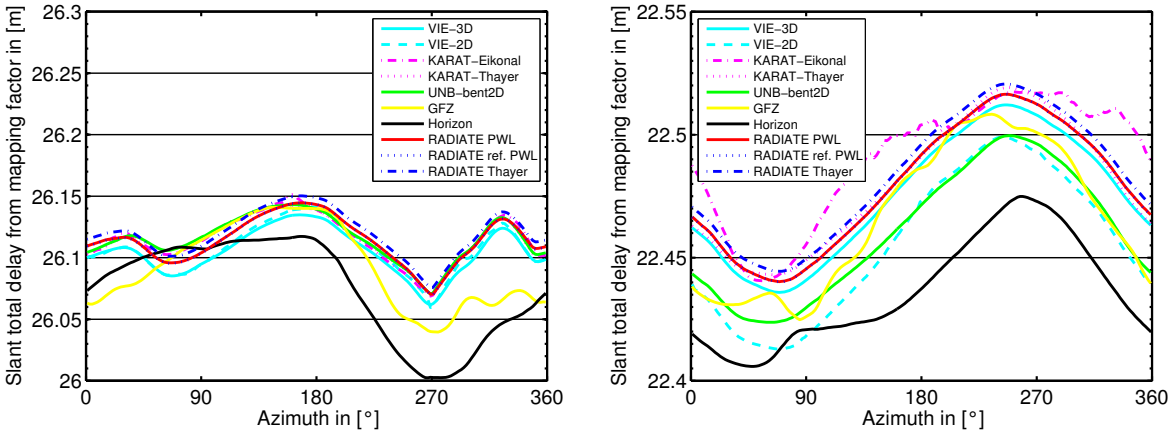

(a) STD_{mf} for station TSUKUB32 at 5° elevation angle on August 12, 2008 00:00:00 h UTC. ZTD of RADIATE PWL solution (2.5716 m) used for the calculation of the STD_{mf} from the mf of each solution.

(b) STD_{mf} for station WETTZELL at 5° elevation angle on January 1, 2008 00:00:00 h UTC. ZTD of RADIATE PWL solution (2.2057 m) used for the calculation of the STD_{mf} from the mf of each solution.

Figure 6.3: STD_{mf} of different ray-tracing programs. For the calculation of the STD_{mf} the mf of each solution are always used together with the ZTD of the RADIATE PWL solution. Results have been taken from Hofmeister and Böhm (2014), respectively the past comparison campaign results from Nafisi et al. (2012b).

Looking at the results for station TSUKUB32, the agreement of the RADIATE solutions with the solutions of the other ray-tracing packages has improved compared to the agreement of the comparisons of the normal STD, neglecting the solution of Horizon due to the known reason. The individual mean differences between the RADIATE PWL solution and the other solutions are now less than 1 cm with standard deviations below 0.6 cm, if the results of GFZ and Horizon are neglected. Thus, again a good agreement between the comparable ray-tracing packages is achieved.

In case of the station WETTZELL the individual means of the ΔSTD_{mf} between the RADIATE PWL solution and the other solutions, neglecting the solutions of GFZ and Horizon, are less than 2.4 cm with standard deviations below 1 cm. Generally all different RADIATE solutions for the station WETTZELL yield in principle the same good agreements of the STD and of the STD_{mf} with the solutions of the other ray-tracing packages in these domains.

As a final conclusion of the comparison of the RADIATE results to the results of the other ray-tracing packages it can be stated that program RADIATE agrees very well with those ray-tracing packages which used the same NWM data, especially with respect to the STD_{mf} solutions. Therefore the quality assessment of the ray-tracing program RADIATE can be seen very positive as it provides a certain confidence for delivering accurate ray-traced delays with program RADIATE for the application to VLBI analysis. Nevertheless Nafisi et al. (2012b) showed that different NWM can influence the ray-traced slant delays significantly, which has also been shown above in case of the results of the packages GFZ and Horizon which both used an ECMWF NWM, but a different one than all other ray-tracing programs in the comparison.

6.2 Sample ray-traced tropospheric path delay results determined with the operational Fortran version of program RADIATE

In this section some sample ray-traced tropospheric path delay results determined with the operational Fortran version of RADIATE are presented. Additionally the processing time, which is needed to derive the ray-traced delays, is described.

Furthermore the processing time of the specific MATLAB® development version of program RADIATE, which is equivalent to the operational Fortran version, is described in order to see the drastic differences in the needed amount of time for deriving the exactly same ray-traced delay results in case different programming languages are used.

6.2.1 Determination of sample ray-traced tropospheric path delays

For simulated VLBI observations on 15.09.2011 at 18:00:00 h UTC ray-traced delays are determined at the five stations FORTLEZA, KOKEE, TSUKUB32, WETTZELL and ZELENCHK. At each station observations at different combinations of azimuth directions and elevation angles are simulated. The chosen azimuth directions form the equally spaced interval [0°:10°:360°[. These azimuths are combined with all elevation angles in the equally spaced interval [0.5°:0.5°:90°]. Thus, each station has a set of 6 480 different observations, which leads to the total number of 32 400 simulated observations.

The ray-traced delays of these simulated observations are determined utilizing the operational Fortran version of program RADIATE. The settings and options of the program are defined according to the findings of Section 5.6. Therefore the ECMWF operational NWM is used with a horizontal resolution of 1° x 1°, 25 total pressure levels and a time resolution of 6 hours. The PWL method is utilized for the ray-tracing. The vertical resolution of the NWM data is improved by a vertical interpolation with the "profilewise" approach, which is described in Section 4.2.2.1. Since every observation is defined to be at the epoch 18:00:00 h UTC of the NWM, an extra time interpolation in order to determine the delays at the exact observation time is not needed. Therefore the final ray-traced delay of each observation is directly the ray-traced delay which is determined from using the meteorological data at the closest NWM epoch, which is the desired observation

time anyway. A determination of a second ray-traced delay at the next closest epoch of the NWM and a subsequent linear time interpolation between the two ray-traced delays is therefore not needed. The details on the different time interpolation modi of program RADIATE can be found in Section 4.2.6.

6.2.2 Processing time

For the computations a 64-bit Microsoft Windows® 7 machine with an Intel® Core™ i3-2120 CPU at 3.3 GHz and with 8 GB RAM is used. Only one of the four CPU cores is used for the processing.

The complete program run of the operational Fortran version of RADIATE for the determination of the ray-tracing results of the 32 400 simulated observations takes only 40.4 seconds. From these 0.6 seconds are needed for the station and observation data preparations. The loading, the preparation and the vertical interpolation of the meteorological data including the refractivity calculations take 13.4 seconds. The ray-tracing and delay calculations of all 32 400 simulated observations take only 25.8 seconds. The final steps including the creation of the ".radiate" and ".trp" text files, which contain the ray-tracing results, need 0.6 seconds. Please note, that the ray-tracing at a small elevation angle significantly increases the processing time since more iterations of the ray-path are needed to reach the desired accuracy of the outgoing elevation angle. Thus, it can not be said that the processing of every observation takes the same time. The presented processing time information has to be seen with respect to elevation angles ranging from 0.5° to 90°. Thus, the pure ray-tracing and delay calculations of a single observation at one specific epoch of the NWM need on average only 0.8 milliseconds. Observations at smaller elevation angles may need more and observations at larger elevation angles may need less time.

In order to investigate the processing speed benefit of the operational Fortran version, the simulated observations are also processed with the equivalent MATLAB® development version with the identical processing settings. The received results of the MATLAB® version are exactly the same as derived with the operational Fortran version.

The complete program run of the equivalent MATLAB® version of RADIATE needs in total 124.83 minutes for the determination of the ray-tracing results of the same 32 400 simulated observations. This is more than 185 times the time amount of the operational Fortran version, which needs only 40.4 seconds. At this point it shall be stressed that both the Fortran and the MATLAB® version have been carefully optimized with respect to processing speed, but the MATLAB® version does not make full use of intrinsic functions since these are not available in Fortran for which the development was intended. In the MATLAB® version it takes 8.5 seconds to prepare the station and observation data, i.e. more than 14 times the time amount of the Fortran version. The following loading, the preparation and the vertical interpolation of the meteorological data including the refractivity calculations require 35.21 minutes, which is more than 157 times the time amount of the Fortran version, although the same algorithm is used. The ray-tracing and delay calculations of all 32 400 simulated observations take in the MATLAB® version 89.12 minutes,

i.e. more than 207 times the time amount of the Fortran version with the same ray-tracing approach and algorithm. The final steps including the creation of the ".radiate" and ".trp" text files, but in case of the MATLAB® version also with an additional storage of an extra variable data file, needs 21.3 seconds, which is more than 35 times the time amount of the Fortran version. The MATLAB® version needs on average 165.0 milliseconds to process the pure ray-tracing and delay calculations of a single observation at one specific epoch of the NWM. Compared to this, the Fortran version needs only 0.8 milliseconds. Accordingly, the MATLAB® version requires on average 2.75 minutes for processing 1000 observations.

Table 6.3 gives an overview of the processing times of the different program steps with respect to the operational Fortran or the equivalent MATLAB® development version of program RADIATE regarding the processing of the simulated observations.

Table 6.3: Processing times using the operational Fortran or the equivalent MATLAB® development version of program RADIATE regarding the processing of the simulated observations.

Program section	Fortran	MATLAB®	X-times Fortran for 1 time MATLAB®
Station and observation data preparations	0.6 sec.	8.5 sec.	> 14 times
Loading, preparation and vertical interpolation of the meteorological data including refractivity calculations	13.4 sec.	35.21 min.	> 157 times
Ray-tracing and delay calculations of all 32 400 simulated observations	25.8 sec.	89.12 min.	> 207 times
Final steps including the creation of the ".radiate" and ".trp" text files	0.6 sec.	21.3 sec.[a]	> 35 times
Total time	40.4 sec.	124.83 min.	> 185 times
Average[b] processing time for pure ray-tracing and delay calculations of 1000 observations	0.8 sec.	2.75 min.	> 207 times

[a] Includes in case of the MATLAB® version also the additional time needed for the storage of an extra variable data file.

[b] Due to the fact that the time needed for the ray-tracing of one observation is dependent on the elevation angle of the observation, the reported time is an average for the simulated observations at different elevation angles.

This comparison of the processing times between the operational Fortran version and the equivalent MATLAB® version shows clearly why it is essential to use a fast-performing low-level programming language, although the algorithms are already fast, which is evident from the performance of the Fortran version.

6.2.3 Sample ray-traced tropospheric path delay results

In the following the results of the ray-tracing processing are discussed. Figure 6.4 presents the STD, SHD, SWD and the geometric bending effect g_{bend} at station WETTZELL for the simulated observations at different elevation angles at 0° azimuth at 15.09.2011 18:00:00 h UTC. The geometric bending effect is already added to the STD and SHD according to common practice. It is clearly visible that the STD, which is presented in Figure 6.4a, has similar values for elev-

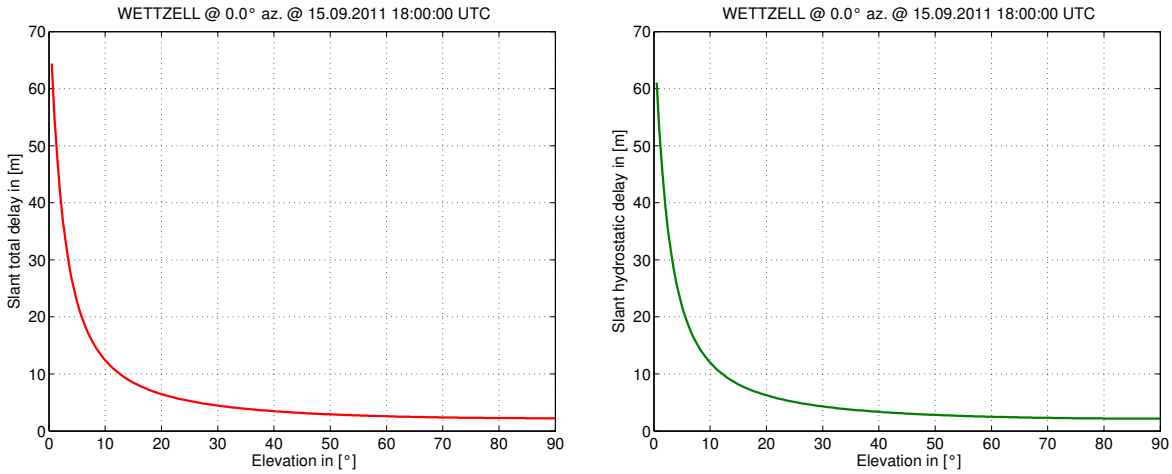

(a) STD.

(b) SHD.

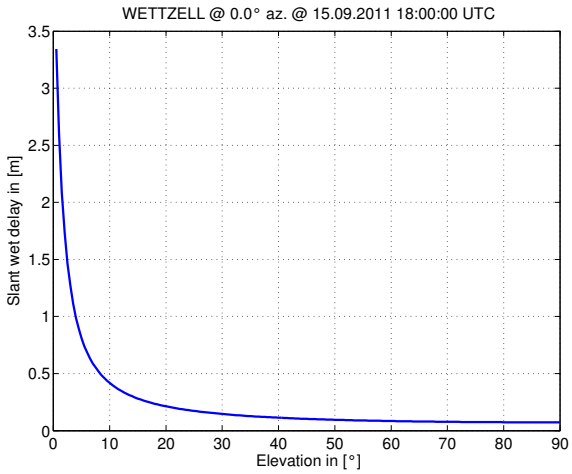

(c) SWD.

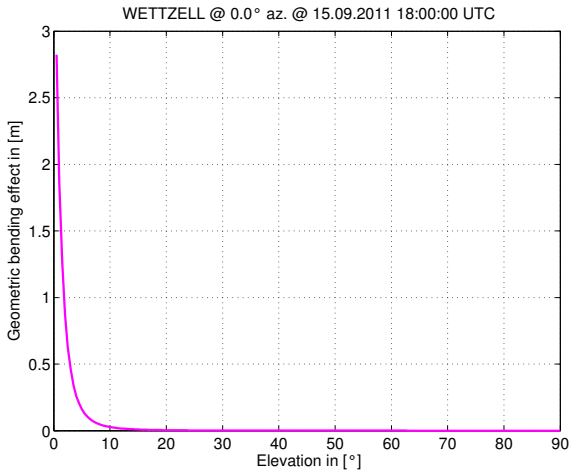

(d) g_{bend}.

Figure 6.4: STD, SHD, SWD and g_{bend} at station WETTZELL for simulated observations at different elevation angles at 0° azimuth at 15.09.2011 18:00:00 h UTC. The geometric bending effect is already added to the STD and SHD.

ation angles from the zenith down to 40°. Approaching smaller elevation angles the STD rises significantly. This effect can also be seen in the domains of the SHD, SWD and g_{bend}. The SHD, which is shown in Figure 6.4b, is the largest contributor to the STD. The SWD results, which are presented in Figure 6.4c, show that their contribution to the STD is especially at very low

elevations essential. The geometric bending effect has the steepest slope as visible in Figure 6.4d. Starting at the sub-cm level at 14.5° elevation, the g_{bend} rises to 2.8 m if the elevation angle decreases to 0.5°.

The observations in the other azimuth directions show equal results in terms of the elevation-dependent behaviour, but due to the meteorological differences along the signal path significant differences between the ray-tracing results at the individual azimuth angles can be found. These differences increase with decreasing elevation. At an elevation angle of 0.5° the STD varies by up to 0.43 m just because of a different azimuth direction. Every constituent of the STD, i.e. the SHD, SWD as well as the g_{bend}, which is already part of the SHD, shows this azimuthal dependence. Figure 6.5 presents a closer look on the azimuthal dependence of the SWD at station WETTZELL.

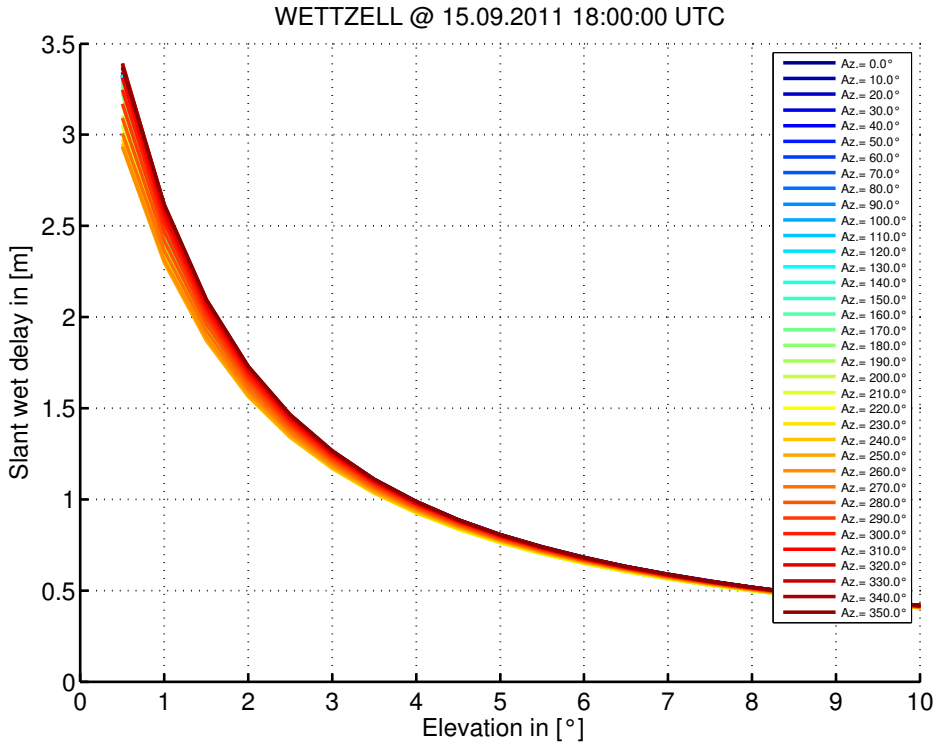

Figure 6.5: Azimuthal dependence of the SWD at small elevation angles at 15.09.2011 18:00:00 h UTC at station WETTZELL.

Figure 6.6 depicts the STD, SHD, SWD and the g_{bend} at station KOKEE for the simulated observations at different elevation angles at 0° azimuth at 15.09.2011 18:00:00 h UTC. The geometric bending effect is again already added to the STD and SHD. Also in case of station KOKEE the elevation dependent increase of the different delays and of the geometric bending effect is clearly visible and similar to the results of station WETTZELL. The geometric bending effect shows again the steepest slope as visible in Figure 6.6d. Starting at the sub-cm level at 14° elevation, the g_{bend} rises to 2.9 m if the elevation angle decreases to 0.5°.

Also at station KOKEE the need of accounting for the azimuthal dependence of the ray-tracing

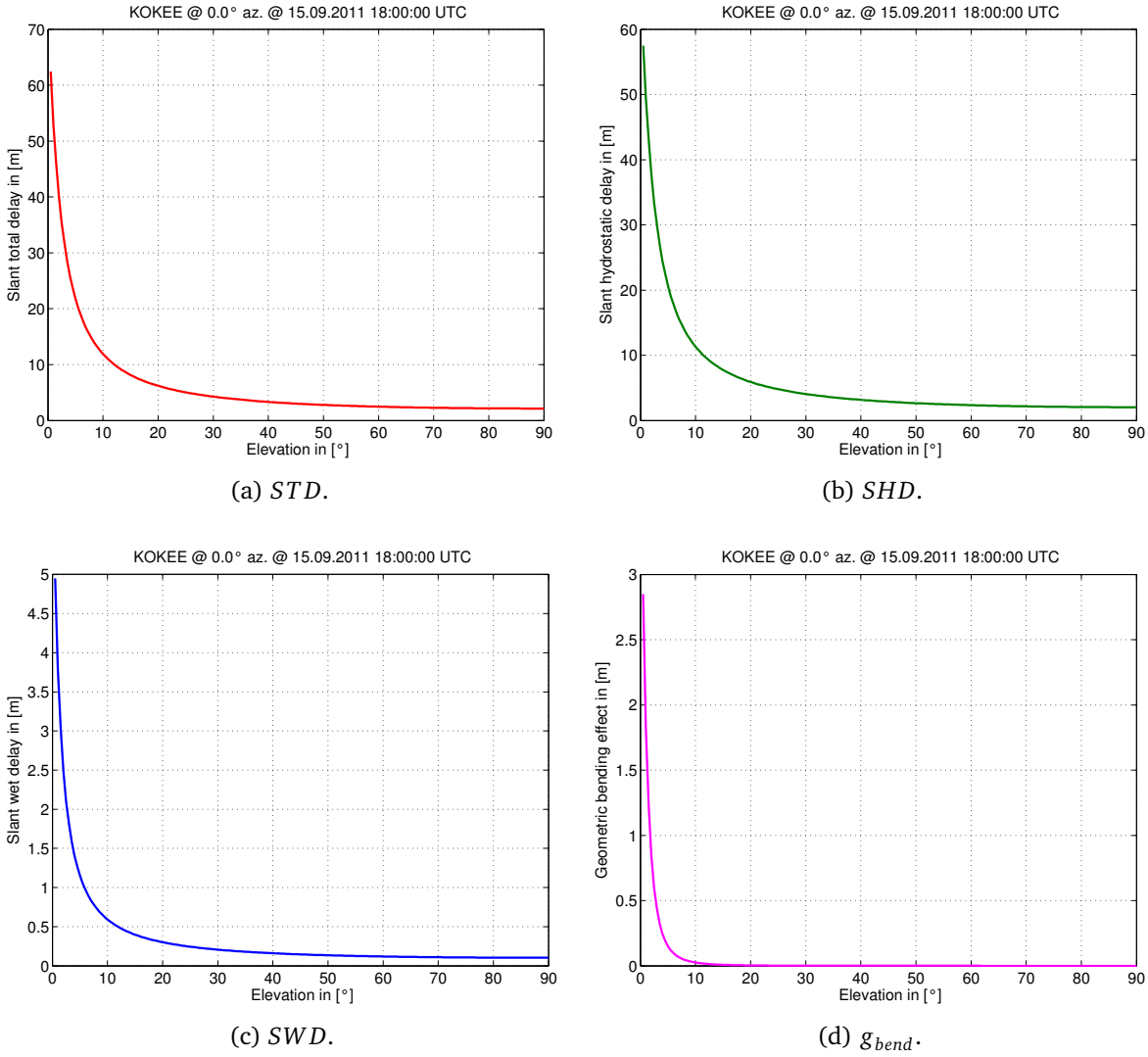

(a) STD. (b) SHD.

(c) SWD. (d) g_{bend}.

Figure 6.6: STD, SHD, SWD and g_{bend} at station KOKEE for simulated observations at different elevation angles at 0° azimuth at 15.09.2011 18:00:00 h UTC. The geometric bending effect is already added to the STD and SHD.

results due to the meteorological differences along the signal path is evident since the differences increase with decreasing elevation angle. At an elevation angle of 0.5° the STD varies by up to 1 m just because of a different azimuth direction. Again every constituent of the STD, i.e. the SHD, SWD as well as the g_{bend}, which is already part of the SHD, shows this azimuthal dependence. At station KOKEE the contribution of the SWD to the STD is higher compared to station WETTZELL and also the variation of the SWD with respect to different azimuth directions is increased. Figure 6.7 presents a closer look on the azimuthal dependence of the SWD at station KOKEE.

The results of the STD, SHD, SWD and the g_{bend} at the stations FORTLEZA, TSUKUB32 and ZELENCHK are presented in Appendix Section B.3 on page 235. There also the plots of the azimuthal dependence of the SWD at these stations are shown.

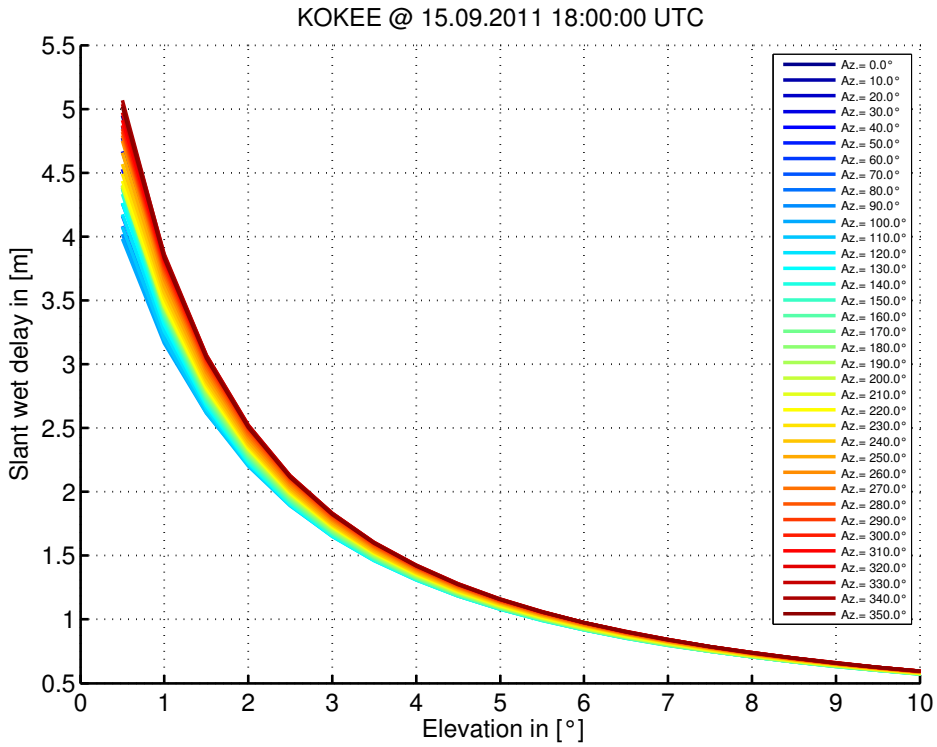

Figure 6.7: Azimuthal dependence of the SWD at small elevation angles at station KOKEE.

6.3 Comparison of zenith delays from RADIATE and from VLBI analysis on the example of CONT11

In this section the zenith delays in the total, hydrostatic and wet domains, determined by the ray-tracing program RADIATE, are compared to the estimated values from a VLBI analysis. As observational data input for both the ray-tracing and the VLBI analysis, the CONT11 campaign is utilized since it provides a good data base for a comparison in this respect. A description of the CONT11 campaign is given in Section 5.3.1.2 on page 88.

For the comparison the ZTD, ZHD and ZWD have been determined for all available observations of CONT11 by ray-tracing with the operational Fortran version of program RADIATE. This means that program RADIATE has been executed with the settings and options according to the conclusions for the operational service of the program, which have been described in Section 5.6. Thus, as NWM the ECMWF operational model with a horizontal resolution of 1° x 1°, 25 total pressure levels and a time resolution of 6 hours has been utilized as meteorological data input. The resolution of the vertical domain of the meteorological data has been improved with the "profilewise" vertical interpolation mode, which is the strict mode in program RADIATE, according to the description given in Section 4.2.2.1. The PWL ray-tracing approach has been utilized. In order to get the delays at the exact observation times, the time interpolation strategy as described in Section 4.2.6, using ray-traced delays at the NWM epochs directly before and after the time of each observation, has been used.

The VLBI analysis has been carried out using the Vienna VLBI Software (VieVS) (see Böhm et al. 2012, for more information on VieVS). The parameterization that has been used for the analysis of CONT11 shall represent a standard VLBI analysis. A detailed description of the settings and models can be found in Section 6.4.2 in Tables 6.5 and 6.6, which provide the basic settings for the a priori models and for the parameter estimation within the analysis. Additional to these, the settings of parameterization 1, described in Table 6.7, have been used to complete the entire setup of the analysis. Thus, the ZHD has been determined for each considered observation[1] within the analysis through the zenith hydrostatic delay from Saastamoinen's equation ZHD^S (see Equation (3.28)) using the total pressure at the station provided by the data file of the processed session. The ZWD has been estimated as a function of PWL offsets every 30 minutes within the least-squares adjustment of the analysis. Via a linear interpolation the ZWD is determined at the observation time in a separate processing after the analysis. The sum of ZHD and ZWD delivers then the ZTD. It is important to note that no NWM model data has been used within the described VLBI analysis for the determination of the zenith delays, at least not directly since the utilized VMF1 are based on NWM data.

Table 6.4 provides the standard deviations of the ΔZTD, ΔZHD and ΔZWD, which are used to assess the agreement of the results of the ZTD, ZHD and ZWD between RADIATE and the VLBI analysis estimates of VieVS. The differences are determined at the epoch times of the NWM data, which have been used for the ray-tracing and which are covered by the individual session data. At these epochs the zenith delays in the different domains have been interpolated using the VieVS estimates and the RADIATE zenith delays from which the differences are then built.

Figure 6.8 presents the comparison of the ZTD, ZHD and ZWD at station WETTZELL determined by a pure VLBI analysis with VieVS and determined by program RADIATE for the observations of CONT11. There is a good overall agreement in terms of the ZTD, presented in Figure 6.8a, between the results from RADIATE and the analysis solution estimates of VieVS with a standard deviation of the differences of 9.5 mm. Only at some events of extreme variability within the VieVS estimates, the RADIATE results may not follow these changes closely. Since the ZHD determined by RADIATE and VieVS, which are shown in Figure 6.8b, are very similar, i.e. with a standard deviation of the differences of only 0.9 mm, it is the ZWD, which mainly contributes to the differences present in the domain of the ZTD. Taking a closer look at the results of the ZWD, presented in Figure 6.8c, it can be seen that here the extreme variability of the VieVS estimates is not always followed closely by the results from RADIATE. The determined standard deviation of the differences in the ZWD is therefore 9.3 mm. The reason for the differences in the ZWD domain between the VieVS and the RADIATE results may be on one side due to the fact that for the ray-tracing NWM data with a horizontal resolution of 1° x 1° and a time resolution of 6 hours has been used, but the analysis results are estimated every 30 minutes. This may lead to situations where severe weather and thus also humidity changes may not be recognized by the NWM data

[1] Due to certain restrictions concerning e.g. the quality of an observation or other analysis optimizing aspects, not all available observations are considered within the analysis.

Table 6.4: Standard deviations of the ΔZTD, ΔZHD and ΔZWD from VieVS - RADIATE. The differences are determined using the interpolated data at the epochs of the NWM, which have been used for determining the ray-traced zenith delays. Only those epochs are considered, which are covered by the observational data of each individual session. Unfortunately no reliable standard deviation can be derived for station WARK12M since the station has too few observations in order to cover a sufficient number of epochs.

Station	St. dev. [mm] of ΔZTD	St. dev. [mm] of ΔZHD	St. dev. [mm] of ΔZWD
BADARY	10.4	1.4	10.7
FORTLEZA	12.5	4.6	13.3
HARTRAO	11.6	0.7	11.9
HOBART12	7.8	0.9	7.7
KOKEE	14.8	0.8	14.9
NYALES20	5.6	1.2	5.5
ONSALA60	9.9	0.8	9.5
TIGOCONC	11.3	1.1	11.1
TSUKUB32	12.3	0.9	12.4
WARK12M	-	-	-
WESTFORD	11.0	0.8	11.0
WETTZELL	9.5	0.9	9.3
YEBES40M	12.6	0.7	12.6
ZELENCHK	16.0	1.5	16.1

at a specific location and time, although a time interpolation using zenith delays at two neighbouring epochs has been used to determine the ray-traced zenith delay at the observation time according to the approach described in Section 4.2.6. Please note, that for the reported standard deviation of the zenith delay differences the time resolution of the NWM does not matter since the differences are determined using only data at the exact epochs. Nevertheless the horizontal resolution of the NWM may not be sufficient to resolve local small scale weather phenomena, although a horizontal interpolation of neighbouring data points has been carried out within the ray-tracing according to the approach described in Section 4.2.5. On the other side the ZWD from the VieVS solution might be influenced. This means that beside the estimated parameter further effects like clock errors may affect the ZWD estimates as the clock is correlated with the zenith delay according to Nothnagel et al. (2002) (see also Section 3.4.2). Furthermore it is the case that the VieVS estimates of the ZWD show oscillations (Runge's phenomenon) at the beginning and at the end of some sessions. Therefore some of the peaks in the VieVS results are not due to the meteorology, but due to numerical solution effects. At these peaks the not coinciding

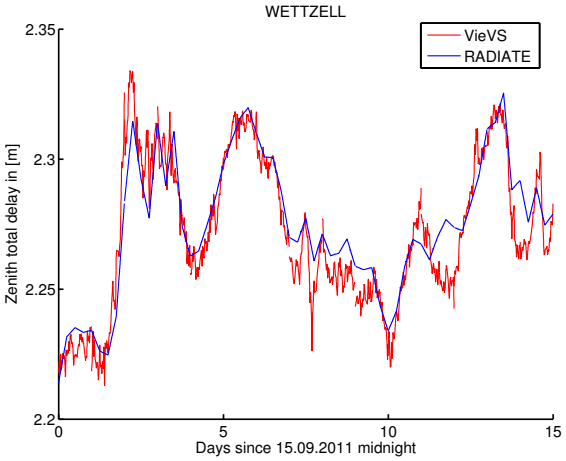

(a) ZTD.

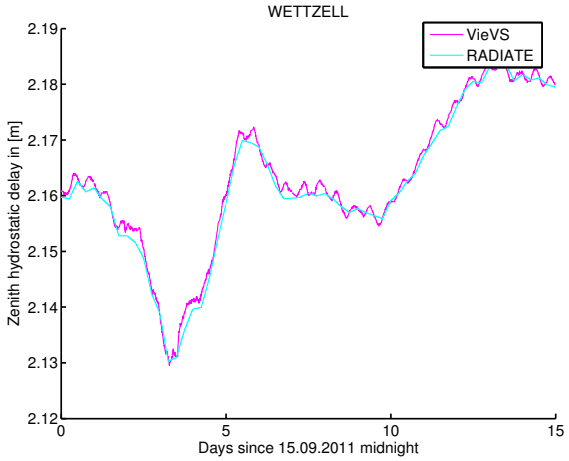

(b) ZHD.

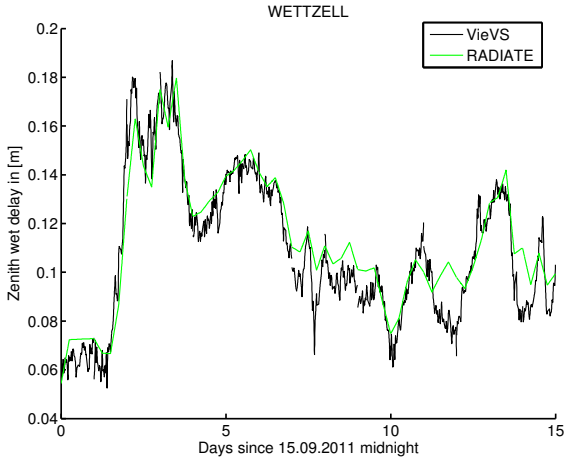

(c) ZWD.

Figure 6.8: Comparison of the ZTD, ZHD and ZWD at station WETTZELL for the observations of CONT11 from a VLBI analysis with VieVS and from ray-tracing with program RADIATE. Breaks in the plotted lines may be visible after the last observation of the station in a specific session of CONT11.

RADIATE results are of course more reliable.

Figure 6.9 presents the comparison of the ZTD, ZHD and ZWD at station FORTLEZA for the observations of CONT11. The results at station FORTLEZA are explicitly shown since they reveal a new aspect in the ZHD compared to the results at station WETTZELL. Again significant oscillation effects in the VieVS estimates of the ZWD are visible in some sessions, presented in Figure 6.9c. Additionally now also the estimates of the ZHD of VieVS, shown in Figure 6.9b, seem to be affected by another problem. Compared to the obvious diurnal and semi-diurnal changes in the RADIATE results, which come from the atmospheric tides, the VieVS estimates determined from Saastamoinen's equation (see Equation (3.28)) show only a linear behaviour across the complete 15 days of CONT11. The reason for this are incorrect total pressure data at

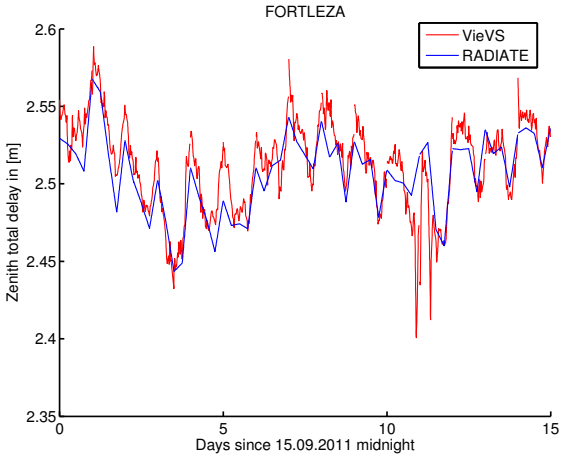

(a) ZTD.

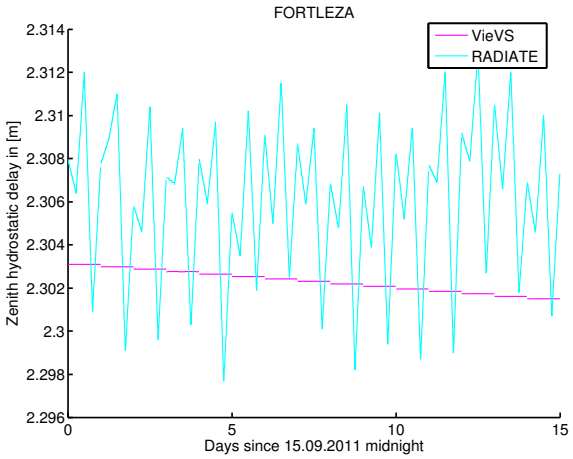

(b) ZHD.

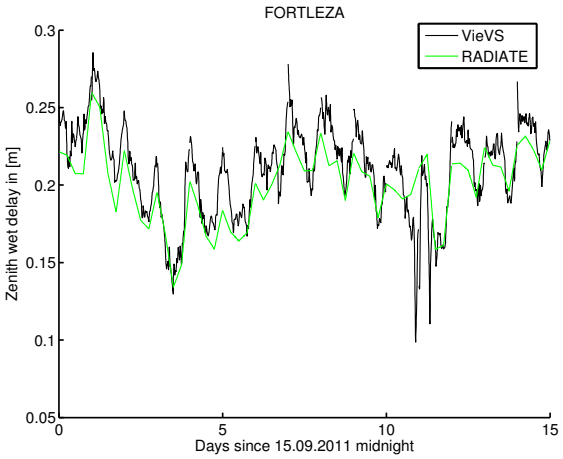

(c) ZWD.

Figure 6.9: Comparison of the ZTD, ZHD and ZWD at station FORTLEZA for the observations of CONT11 from a VLBI analysis with VieVS and from ray-tracing with program RADIATE. Breaks in the plotted lines may be visible after the last observation of the station in a specific session of CONT11.

the station as reported in and used from the observation data file. This difference between the VieVS and RADIATE ZHD leads to a significant higher standard deviation of the differences of 4.6 mm compared to station WETTZELL. Maybe due to the sometimes extreme oscillation effects in the ZWD of VieVS also the standard deviation of the differences in this domain is increased to 13.3 mm. The standard deviation of the differences in the ZTD is 12.5 mm.

Further station specific results are presented in Appendix Section B.4 on page 241, which contains the results for the stations KOKEE, TSUKUB32 and ZELENCHK.

According to the results described in Table 6.4 the standard deviation of the differences in the ZTD is at almost all stations below 15 mm. In case of the ZHD it is always below 5 mm and in case of the ZWD it is at almost all stations below 15 mm. This leads to the conclusion that the

ray-traced zenith delays from program RADIATE have a good agreement with the estimates of a pure VLBI analysis, which uses Saastamoinen's equation for the ZHD and the VMF1 for the ZWD estimates.

6.4 Application of ray-traced delays to VLBI analysis of the years 1999.0 to 2015.5

In this section the main validation of the ray-traced delays from program RADIATE and their impact on the VLBI analysis are presented. The sessions used for this research cover the time span between January 1999 and the end of June 2015. This interval will be denoted as 1999.0 to 2015.5 in the following.

For the quality check and the impact assessment of the ray-traced delays from program RADIATE on the VLBI analysis results the baseline length repeatability (BLR) is used. Furthermore the impact of the ray-traced delays on the Terrestrial Reference Frame (TRF) determination is investigated.

6.4.1 Data for the research

For the assessment of the impact of the ray-traced delays on the VLBI analysis the time span of 1999.0 to 2015.5, which covers 16.5 years of VLBI observations, is used. Unfortunately not all sessions between 1999.0 and 2015.5 fulfil the prerequisites for an optimal assessment basis. On one side this is because of session type reasons, i.e. all so-called intensive sessions in which only two or three stations participate with the goal of determining $\Delta UT1$ are excluded, but on the other side also because of accuracy reasons of individual sessions. Therefore a selection of suitable sessions from all of the available is done based on a so-called process list of sessions between 1979.0 and 2015.5, which has been explicitly designed for reference frame determinations. This process list has been created and kindly provided by David Mayer. From this predefined process list all sessions in the interval between 1999.0 and 2015.5 are taken and form the fundamental process list called "pl_long-run" for the investigations presented in the following. This process list covers in total 2 461 sessions between January 1999 and the end of June 2015. For these sessions VLBI analysis is carried out.

Ray-traced delays have been determined for each session on the process list "pl_long-run" using the operational Fortran version of program RADIATE[1]. Program RADIATE has been executed with the settings and options according to the conclusions for the operational service of the program, which have been described in Section 5.6. Thus the ECMWF NWM[2] data as specified in Table 4.2 on page 63 with a horizontal resolution of 1° x 1° have been used, the vertical inter-

[1] Actually ray-traced delays have been determined for all available sessions between January 1999 and the end of December 2015, which are in total 8 595 sessions.

[2] The ERA-Interim NWM is used for observations before 01.01.2008 and the ECMWF operational NWM is used for later observations.

polation of the meteorological data has been done in the "profilewise" and thus strict mode as described in Section 4.2.2.1 and the PWL ray-tracing approach has been utilized. The ray-traced delays have been determined at the exact observation times by applying the time interpolation strategy as described in Section 4.2.6 using ray-traced delays at the NWM epochs directly before and after the time of each observation. The determined ray-traced delays are provided directly to the VLBI analysis software VieVS via the so-called ".trp" files written by program RADIATE.

6.4.2 VLBI analysis

For the analysis of the VLBI observations of all sessions on the process list "pl_long-run" the software VieVS is used. For the investigation of the impact of the ray-traced delays on the analysis results four parameterizations with the following names are used:

Parameterization 1: *VieVS*

- A typical VLBI analysis parameterization.

Parameterization 2: *VieVS no gradients*

- A typical VLBI analysis parameterization, but without the estimation of tropospheric gradients.

Parameterization 3: *RADIATE*

- A VLBI analysis parameterization with applied ray-traced tropospheric delays from program RADIATE.

Parameterization 4: *RADIATE no gradients*

- A VLBI analysis parameterization with applied ray-traced tropospheric delays from program RADIATE, but without the estimation of tropospheric gradients.

In Table 6.5 those a priori model settings are described, which are common to all of the above defined parameterizations 1 to 4 used for the VLBI analysis with VieVS.

Table 6.5: A priori model settings common to all of the defined parameterizations 1 to 4.

Option	Setting
Analysis optimization	
OPT files	Use of so-called "OPT" files for problematic sessions in order to optimize their results by correcting clock breaks, excluding stations, etc.
Outlier files	Use of files containing outlier observations, which have been determined in a first analysis run.

Table 6.5 (continued): A priori model settings common to all of the defined parameterizations 1 to 4.

Option	Setting
Quality code limit	0, only best quality observations are taken.
Cut-off elevation angle	0°.
Reference frames	
TRF	VieVS-TRF, a collection of most accurate station coordinates from different sources or solutions.
CRF	ICRF2 (see Fey et al. 2009).
Ephemerides	Model JPL 421 (see Folkner et al. 2009) from the National Aeronautics and Space Administration Jet Propulsion Laboratory (NASA JPL).
Ionosphere	Ionospheric delay applied as reported by the NGS data file of the session. NGS stands for National Geodetic Survey.
Station correction models	
Solid Earth tides	According to the IERS Conventions 2010 (see Petit and Luzum 2010). IERS is the International Earth Rotation and Reference Systems Service.
Tidal ocean loading	FES2004 (see Lyard et al. 2006).
Tidal atmosphere loading	Atmospheric Pressure Loading (APL) model of Technische Universität Wien used: Vienna-APL (see Wijaya et al. 2013).
Non-tidal atmosphere loading	Vienna-APL model (see Wijaya et al. 2013).
Pole tide	According to the IERS Conventions 2010 (see Petit and Luzum 2010).
Ocean pole tide	According to the IERS Conventions 2010 (see Petit and Luzum 2010).
Mean pole model	Cubic model according to the IERS Conventions 2010 (see Petit and Luzum 2010).
Thermal antenna deformation	According to Nothnagel (2009).

Table 6.5 (continued): A priori model settings common to all of the defined parameterizations 1 to 4.

Option	Setting
EOP	
A priori time series	IERS 08 C04 a priori EOP time series and inclusion of a priori celestial pole offsets.
Ocean tides and libration	Effects of the ocean tides and the libration on the Earth rotation parameters treated according to the IERS Conventions 2010 (see Petit and Luzum 2010).
Precession/Nutation model	IAU 2006/2000A (see Capitaine et al. 2003; Mathews et al. 2002). IAU is the International Astronomical Union.
Interpolation method	Lagrange.

In Table 6.6 the settings for the parameter estimation, which are common to all of the above defined parameterizations 1 to 4 used for the VLBI analysis with VieVS, are presented.

Table 6.6: Settings for the parameter estimation common to all of the defined parameterizations 1 to 4.

Parameter	Setting
Clock	First estimation solution per clock: quadratic polynomial. Main estimation solution per clock: one rate and one quadratic term plus PWL offsets in the interval of 60 min. with relative constraints of 1.3 cm after 60 min. Estimations are with respect to a reference clock.
ZWD	Interval of 30 min., relative constraints of 1.5 cm after 30 min., PWL offsets. Derived using wet mapping factors either from VMF1 or from the ray-tracing results (see Equation (5.9)).
EOP	Polar motion, precession/nutation parameters and $\Delta UT1$ estimated. Intervals of 1 day, relative constraints of $1 \cdot 10^{-4}$ mas after 1 day (very tight setting), PWL offsets.
Station coordinates	Offsets per session (1 day), application of NNT and NNR conditions.
Source coordinates	PWL offsets per day, relative constraints of $1 \cdot 10^{-4}$ mas after 1 day (very tight setting). Only coordinates of sources not contained in the chosen CRF are estimated.

The parameterizations 1 to 4 used for the investigation are based on the defined common settings for the a priori models and the parameter estimation, which have been presented in Tables 6.5 and 6.6. Amongst each other they differ partly in the a priori troposphere model settings and partly in the estimation part concerning the troposphere parameters. These differences are described in Table 6.7.

Table 6.7: Differences between the defined parameterizations 1 to 4.

Parameterization:	1	2	3	4
A priori tropospheric delay				
A priori slant delay determined from ZHD^S with the VMF1. Pressure for the ZHD^S calculation is taken from the NGS data file.	✓	✓		
Ray-traced slant total delay used as a priori slant delay.			✓	✓
Tropospheric gradient model and estimation				
No a priori gradient model used, but North- and East-gradients estimated as PWL offsets every 120 min. with relative constraints of 0.05 cm after 120 min.	✓		✓	
No a priori gradient model used and no tropospheric gradients estimated.		✓		✓

The VLBI analysis delivers individual results for each single session. These results from a specific parameterization will be used to calculate the BLR. In order to determine a new TRF from the results of each parameterization a global solution has to be determined after the single session analysis.

6.4.3 Impact of ray-traced delays from program RADIATE on the VLBI analysis

In this section the impact of the RADIATE ray-traced delays applied to the VLBI analysis shall be investigated through the comparison of the individual analysis results with respect to the BLR and the TRF solution.

6.4.3.1 Exclusion of analysed but unsuitable VLBI sessions

Since some sessions on the process list "pl_long-run" reveal with their analysis that they are not suitable for the following investigations, an optimization of the session set has to be done.

This task is handled by creating a so-called exclude list. On this list those sessions are put, which are unsuitable with respect to at least one of the three following aspects:

1. The solution of a session is close to singular.
2. The root mean square (RMS), i.e. the a posteriori standard deviation of the unit weight, of an analysed session is larger than 3.
3. The session results contain at least one baseline that has a formal error larger than 10 cm.

These criteria ensure that the later determinations of the BLR and the TRF are not affected by corrupt session results. The exclude list is created as a common list for all of the different analysis solutions from the different parameterizations 1 to 4. This means that if a session is rejected due to one above defined criterion in one of the solutions, it is rejected also from the other solutions, even if the criterion is not fulfilled in the other solutions. This ensures that all solutions share the same sessions.

Using the above defined criteria an exclude list with 121 sessions is created. These sessions are removed from the data set. Thus the following investigations will be carried out using the results of 2 340 sessions between 1999.0 and 2015.5.

6.4.3.2 Impact of the ray-traced delays on the baseline length repeatability

The first assessment of the impact of the ray-traced delays on the VLBI analysis is done by comparing the BLR results from the different analysis parameterizations.

Compared to Equation (5.10) presented in Section 5.3.3 the BLR used in the following investigation in this section is determined differently in two aspects. Firstly, it is necessary to subtract a trend term from each baseline length estimate due to the long time span covered by the set of sessions. This trend mainly comes from the plate tectonics, but it is also due to single events such as earthquakes or station relocations. Secondly, instead of the weighted mean baseline length, the unweighted mean baseline length is used to determine the BLR. Common to Equation (5.10) is that the BLR is determined also in this section as the unbiased[1] weighted estimate of the standard deviation. i.e. again determined as weighted BLR. The weights for the estimation of the BLR are again the inverses of the squared formal baseline length errors. These are derived in a calculation using the estimated coordinates and the according covariances of the baseline-forming stations. Equation (6.3) shows the formalism of the BLR calculation as used in the following investigation in this section, which is based on[2] the formalism described in Wikipedia (2016) and Galassi et al. (2015),

$$BLR = \sqrt{\frac{\sum_{i=1}^{n} w_i \left(b_i - \overline{b}\right)^2}{\sum_{i=1}^{n} w_i - \frac{\sum_{i=1}^{n} w_i^2}{\sum_{i=1}^{n} w_i}}} \tag{6.3}$$

[1] This means that the standard deviation is determined with a degree of freedom of $n-1$.

[2] Denoted as based on, because not the weighted mean but the normal mean is used here within the calculation in contrast to the formalism described in Wikipedia (2016) and Galassi et al. (2015).

with the weight w_i of each length estimate b_i of a specific baseline. The mean baseline length $\overline{b}$ is determined as

$$\overline{b} = \frac{1}{n} \sum_{i=1}^{n} b_i. \tag{6.4}$$

From each length estimate b_i a trend term has already been subtracted before the introduction to the BLR calculations with Equations (6.3) and (6.4). Since the baseline-forming stations may have multiple breaks in their observation time span, it is necessary to determine a different value for the subtracted baseline trend for each break interval. Subsequently Equation (6.3) is evaluated for each break interval of a baseline separately. The final BLR result is then calculated as weighted mean of all individual BLR values from the different break intervals. The weighting is done according to the number of observations, i.e. baseline estimates, of each break interval. In order to receive reliable trend values a minimum number of baseline estimates per break interval must be given, otherwise the resulting BLR for the interval might be far off a reliable value. Therefore a limit of at least 30 baseline estimates for each break interval is set. In case this minimum limit is not fulfilled no BLR is determined for the specific break interval.

For the investigation of the impact of the ray-traced delays on the VLBI analysis the differences ΔBLR between the results of the analysis solutions from different parameterizations are computed as described by Equations (6.5) and (6.6). In the two comparisons always a solution without applying the ray-traced delays is referred to a solution with applying the ray-traced delays. The subscripts to the individual BLR denote which parameterization has been used in the VLBI analysis. The parameterizations 1 to 4 are described on page 126. Positive ΔBLR indicate that the application of the ray-traced delays improves the BLR. The ΔBLR are computed as

$$\Delta BLR = BLR_{Param.\ 1} - BLR_{Param.\ 3} \tag{6.5}$$

or as

$$\Delta BLR = BLR_{Param.\ 2} - BLR_{Param.\ 4}. \tag{6.6}$$

Furthermore the change of the baseline length repeatability δBLR due to applying ray-traced delays to the analysis compared to not applying them is determined. This parameter reveals the relative amount of improvement or degradation of the BLR in percent and it is determined for the two comparisons as described by Equations (6.7) and (6.8). The subscripts to the individual BLR denote again which parameterization has been used in the VLBI analysis. A positive value reveals the relative amount of improvement of the BLR in case the ray-traced delays are applied to the analysis compared to not applying them. The δBLR are computed as

$$\delta BLR[\%] = \frac{BLR_{Param.\ 1} - BLR_{Param.\ 3}}{BLR_{Param.\ 1}} \cdot 100 \tag{6.7}$$

or as

$$\delta BLR[\%] = \frac{BLR_{Param.\ 2} - BLR_{Param.\ 4}}{BLR_{Param.\ 2}} \cdot 100. \tag{6.8}$$

Only reliable BLR are introduced to the comparisons. This means that those baselines, which have a weighted and unweighted BLR result of larger than 10 cm in both compared solutions, are excluded.

At first the results from the parameterizations 1 and 3 are compared in Figure 6.10. The absolute BLR results are shown in Figure 6.10a as determined by Equation (6.3). Figure 6.10b presents the ΔBLR as calculated by Equation (6.5) and Figure 6.10c shows the δBLR as determined by Equation (6.7).

Part of the comparison are 44 stations with a total of 374 different baselines. A look at the ΔBLR presented in Figure 6.10b reveals that the parameterization 3 with applied ray-traced delays delivers BLR, which are very similar to the typical VLBI analysis as represented by parameterization 1. The differences only reach up to a minimum/maximum of around ±1 mm and are 0.0 mm on average. From the 374 baselines 209, i.e. 55.9%, benefit from the application of the ray-traced delays at sub-mm level. The changes of the individual BLR (δBLR) as shown in Figure 6.10c indicate that those baselines, whose BLR is improved, benefit more from the application of the ray-traced delays than the deteriorated baselines are degraded in terms of their BLR. Nevertheless the maximum relative improvement is 6.1% and the maximum relative degradation is 7.6% as determined by the δBLR compared to the BLR from parameterization 1. The average of the δBLR is 0.2%.

Table 6.8 provides a statistical overview of the results for the ΔBLR and δBLR between the parameterizations 1 and 3.

Table 6.8: Statistics of the comparison of the BLR from parameterizations 1 and 3.

ΔBLR δBLR	Basel.	Mean [mm] [%]	Median [mm] [%]	St. dev. [mm] [%]	Min. [mm] [%]	Max. [mm] [%]	Nr. +	Nr. −	% +	% −
ΔBLR	374	0.0	0.0	0.2	-0.8	1.0	209	165	55.9	44.1
δBLR	374	0.2	0.2	1.8	-7.6	6.1				

A compilation of the ΔBLR of the described comparison of the results from the parameterizations 1 and 3 presented on a per-station basis, which provides a more detailed insight into the performance of individual stations, can be found in Appendix Section B.5 in Figure B.26 on page 245. The according statistics of the ΔBLR on a per-station basis can be found in Appendix Section A.4 in Table A.4 on page 192.

The compilation of the δBLR presented on a per-station basis is contained in Appendix Section B.5 in Figure B.27 on page 247. The according statistics of the δBLR on a per-station basis can be found in Appendix Section A.4 in Table A.5 on page 194.

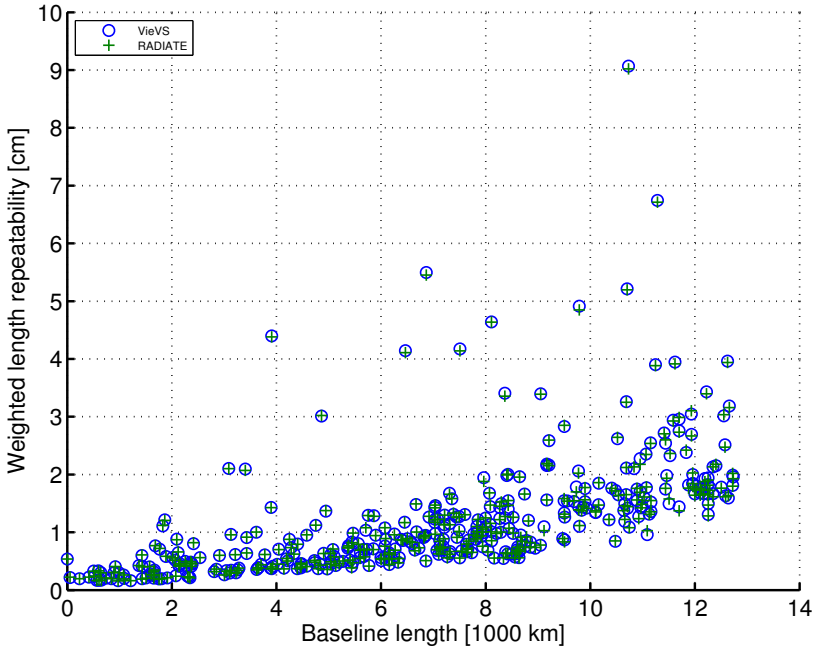

(a) BLR from the parameterizations 1 and 3.

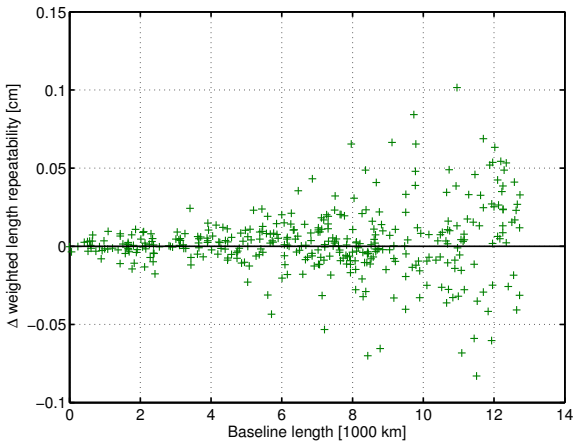

(b) ΔBLR between parameterizations 1 and 3 as determined by Equation (6.5). Positive differences indicate that the application of ray-traced delays improves the BLR.

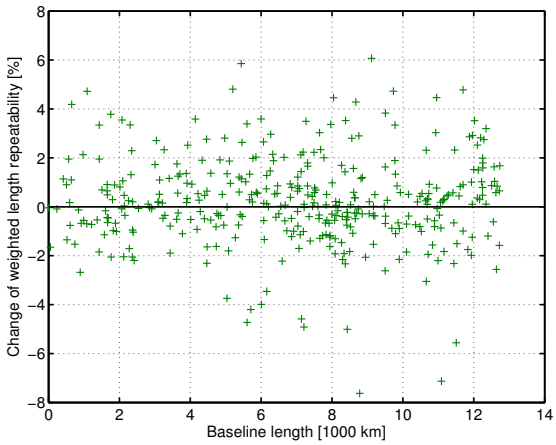

(c) Change of the BLR (δBLR) due to parameterization 3 compared to parameterization 1 as determined by Equation (6.7). Positive percentages indicate the relative amount of improvement of the BLR if ray-traced delays are applied compared to not applying them.

Figure 6.10: Comparison of the BLR of the analysis solutions with the parameterizations 1 and 3 as described on page 126. This comparison shows the impact if ray-traced delays are applied a priori in the VLBI analysis. Tropospheric gradients have been estimated for both analysis solutions.

A clear trend of the impact of the ray-traced delays on the baselines of individual stations, i.e. 100% improvement or degradation, can be found only for five stations. Nevertheless the trends at these stations are not significant since they have only a very limited number of baselines. Station

SC-VLBA seems to especially benefit from the application of ray-traced delays since 16 of the 17 baselines are improved, which are 94.1% of the baselines of this station, and the only negative baseline has a BLR of de facto 0 mm. The relative improvement in the BLR is on average 1.7% compared to the solution without ray-traced delays. This station is situated on the island St. Croix, which is part of the Virgin Islands of the United States in the Caribbean Sea. Also the stations LA-VLBA, NL-VLBA, SESHAN25 and WESTFORD seem to benefit from the application of ray-traced delays as the BLR of more than 70% of their baselines are positively influenced. Only station YARRA12M shows the opposite effect as more than 80% of its baselines, i.e. 13 of 16, are degraded.

The BLR results from the parameterizations 2 and 4 are compared in Figure 6.11. The absolute BLR results are shown in Figure 6.11a as determined by Equation (6.3). Figure 6.11b presents the ΔBLR as calculated by Equation (6.6) and Figure 6.11c shows the δBLR as determined by Equation (6.8).

Part of the comparison are again 44 stations with a total of 374 different baselines[1]. No tropospheric gradients have been estimated within the here compared analysis solutions. This change in the analysis setting reveals the potential of applying ray-traced delays to the VLBI analysis since the BLR is significantly better if the ray-traced delays from program RADIATE are applied compared to the solution from the typical analysis parameterization without applied ray-traced delays and without estimated tropospheric gradients. This fact also serves as a key assessment of the ray-traced delays, which provide the gradient information implicitly through the slant delays. In this respect, an additional estimation of tropospheric gradients is only necessary to possibly further improve the analysis results in case ray-traced delays are applied to the VLBI analysis. The ΔBLR between the solutions, visible in Figure 6.11b, have values in the range of -2.4 mm to 6.5 mm. The average difference is 1.0 mm, which emphasizes the positive impact of the ray-traced delays on the BLR. From the 374 different baselines 339, i.e. 90.6%, are improved through the application of ray-traced delays. The changes of the individual BLR (δBLR), visible in Figure 6.11c, show that the BLR of almost all baselines are significantly improved compared to the BLR from the parameterization without applied ray-traced delays. The maximum relative improvement is 42.8% whereas the maximum relative degradation is 21.0%, but the average of the δBLR is 9.3%, which states a clear relative improvement of the BLR compared to parameterization 2.

Table 6.9 provides a statistical overview of the results for the ΔBLR and δBLR between the parameterizations 2 and 4.

The compilation of the ΔBLR of the described comparison of the results from the parameterizations 2 and 4 presented on a per-station basis, which provides a more detailed insight into the performance of individual stations, can be found in Appendix Section B.5 in Figure B.28 on page 249. The according statistics of the ΔBLR on a per-station basis can be found in Appendix Section A.4 in Table A.6 on page 196.

The compilation of the δBLR presented on a per-station basis is contained in Appendix Sec-

[1]The exactly same baselines are compared as in the previous comparison.

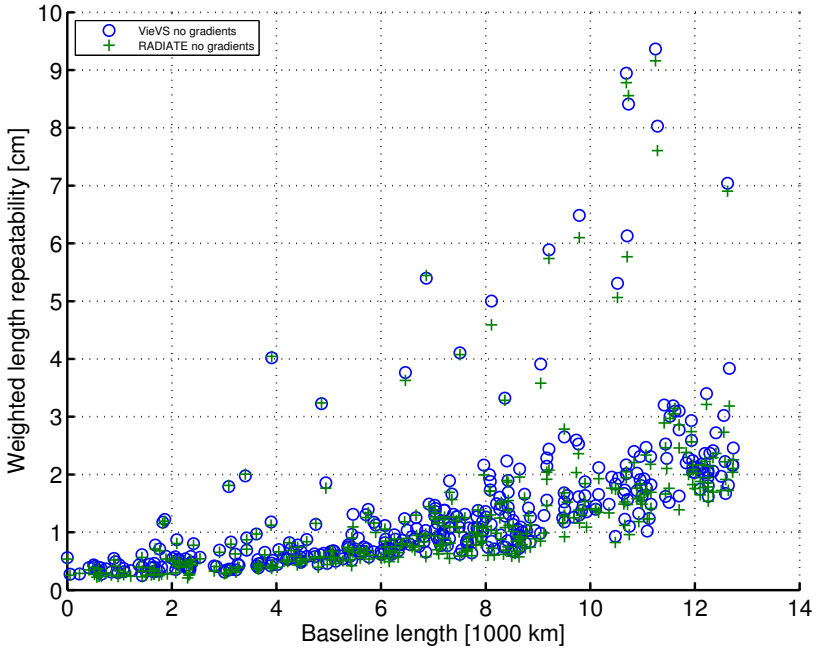

(a) BLR from the parameterizations 2 and 4.

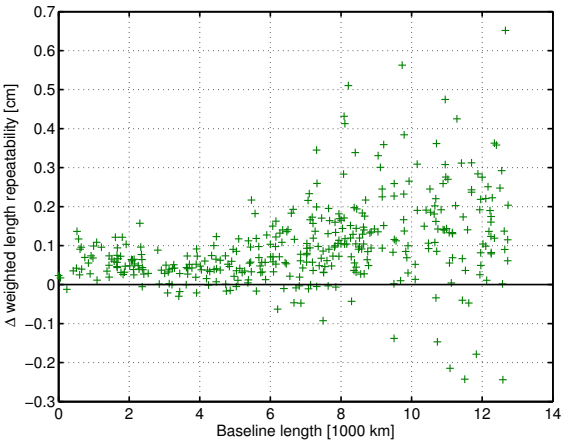

(b) ΔBLR between parameterizations 2 and 4 as determined by Equation (6.6). Positive differences indicate that the application of ray-traced delays improves the BLR.

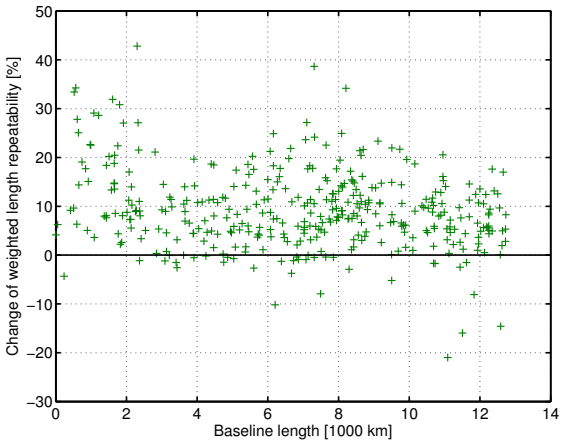

(c) Change of the BLR (δBLR) due to parameterization 4 compared to parameterization 2 as determined by Equation (6.8). Positive percentages indicate the relative amount of improvement of the BLR if ray-traced delays are applied compared to not applying them.

Figure 6.11: Comparison of the BLR of the analysis solutions with the parameterizations 2 and 4 as described on page 126. This comparison shows the impact if ray-traced delays are applied a priori in the VLBI analysis. Tropospheric gradients have not been estimated for the two analysis solutions.

tion B.5 in Figure B.29 on page 251. The according statistics of the δBLR on a per-station basis can be found in Appendix Section A.4 in Table A.7 on page 198.

Since only 35 of the 374 baselines are not improved through the application of the ray-traced

Table 6.9: Statistics of the comparison of the BLR from parameterizations 2 and 4.

ΔBLR / δBLR	Basel.	Mean [mm] [%]	Median [mm] [%]	St. dev. [mm] [%]	Min. [mm] [%]	Max. [mm] [%]	Nr. +	Nr. −	% +	% −
ΔBLR	374	1.0	0.8	1.1	-2.4	6.5	339	35	90.6	9.4
δBLR	374	9.3	8.5	8.1	-21.0	42.8				

delays, it is very clear that each station shows a clear trend of improvement. There is no station where a trend of degradation can be found. The stations SYOWA and OHIGGINS, which do not share the positive trend, are not significant due to the small number of baselines and the values of their baselines results.

As a final conclusion of the two different comparisons of analysis results from parameterizations with and without estimated tropospheric gradients, it can be stated that especially in case no tropospheric gradients are estimated, the application of ray-traced delays to the VLBI analysis is useful as the delays implicitly add the lacking tropospheric gradient information and thus significantly improve the BLR. In case the tropospheric gradients are estimated within the analysis, the application of ray-traced delays may not improve the average BLR of all baselines, but nevertheless more than half of the baselines benefit from the applied ray-traced delays at sub-mm level.

In the following short side note the BLR results of the VLBI analysis solutions from the parameterizations 1 and 4 are compared. This means that a typical VLBI solution, which includes the estimation of tropospheric gradients, but no application of ray-traced delays, is compared to a solution without the estimation of tropospheric gradients, but with applied ray-traced delays from program RADIATE. The interesting question here is, if the ray-traced delays can solely compensate the missing estimation of the tropospheric gradients just by the implicit introduction of the tropospheric gradient information through the ray-traced delays. Considering the differences in the weighted baseline length repeatability, which is used throughout this work as value for the BLR, only 41.4% of the 374 baselines[1] benefit in terms of their BLR if parameterization 4 with applied ray-traced delays but without tropospheric gradient estimation is used. On average the weighted baseline length repeatability is 0.7 mm larger with this parameterization. In contrast, if the unweighted baseline length repeatability is compared, parameterization 4 improves 54% of the baselines. Nevertheless parameterization 4 has also in terms of the unweighted baseline length repeatability values, which are on average larger by 0.9 mm. This apparent contradiction results from the fact that some baselines are degraded in terms of the unweighted baseline length repeatability by up to 12.7 cm, but the improvement reaches only 1.9 cm at the maximum. The median of the differences in the unweighted baseline length repeatability shows of course an improvement by a value of 1.3 mm. This comparison reveals that some baselines do not need the

[1] Again the exactly same baselines are compared as in the previous comparisons.

additional estimation of tropospheric gradients, but some do, in order to reach the optimal BLR.

6.4.3.3 Determination of TRF solutions

As described in Section 2.3 a global solution of the single session analysis results can be determined. The VLBI software VieVS has a separate module for the determination of global solutions including the estimation of a new TRF solution. Therefore VieVS is also used for the determination of global solutions within the presented research. A more detailed insight into the procedures of the global solution with respect to VieVS can be found in Krásná (2012).

For the research of the impact of applying ray-traced delays to the VLBI analysis global solutions of the station coordinates and velocities are estimated in order to determine new TRF solutions. For the global solutions of all different single session analysis results from the individual parameterizations 1 to 4 the same settings are used. These settings for the parameter estimation within the global solution are described in Table 6.10.

Table 6.10: Settings for the parameter estimation within the global solution as used together with each of the different single session analysis solutions.

Parameter	Setting
Clock	Reduced from the global solution.
ZWD	Reduced from the global solution.
Tropospheric gradients	Reduced from the global solution.
EOP	Reduced from the global solution.
Station coordinates	Estimated in the global solution. Reference epoch is 2000.0, i.e. mjd 51544, which is 01.01.2000 00:00:00 h UTC.
Station velocities	Estimated in the global solution. Reference epoch is 2000.0, i.e. mjd 51544, which is 01.01.2000 00:00:00 h UTC.
Station axis offsets	Fixed to a priori values.
Source coordinates	Fixed to a priori coordinates.

Within each global solution determination a new TRF solution is estimated based on the definitions described in Table 6.11. The definitions of the datum stations, the reduced stations, the station velocity treatment and the station velocity ties have been developed for the use within this research by enhancing and adapting basic definitions, which have been kindly provided by Sigrid Böhm.

Table 6.11: Settings for the TRF determination within the global solution as used together with each of the different single session analysis solutions.

Option	Setting
Datum definition	6 Helmert parameters with application of NNT and NNR conditions.
Datum stations	11 pre-selected stations, which have a good global distribution. All datum stations observed in sessions, which cover a large time span in the global solution. 10 of the 11 stations are part of sessions, which cover almost the complete time interval of the global solution. See Figure 6.12 for the datum station locations and Table 6.13 for more details on their observing interval and their mean coordinate error σ_{XYZ} as determined from Equation (6.9).
Reduced stations	Sessionwise reduction of all stations, which participated in less than 10 sessions or have observing time spans of less than 2 years in the global solution. Additionally, stations with unreliable a priori coordinates or large formal coordinate errors are reduced. Stations that remain in the TRF solution have an observation time span of more than 4 years. One exception to this rule is the station HART15M with an observation time span of only 2.7 years. See Figure 6.12 for the locations of all 46 stations, which are part of the TRF solution.
Station discontinuities	Discontinuities of stations are treated. As data source a VieVS internal version of the file *VLBI position discontinuities* from http://lupus.gsfc.nasa.gov/files_IVS-AC/discontinuities.txt is used (see Nothnagel and Ray 2011).
Station velocities	Velocities of stations with discontinuities, which were due to relocations or repair works, are kept constant.
Station velocity ties	Velocities of co-located stations are tied.

Each TRF solution is determined from the results of the same 2 340 sessions between 1999.0 and 2015.5, which have been defined in Section 6.4.3.1 to be the basis of the research and have already been used for the *BLR* investigation in Section 6.4.3.2.

For a clarification of the origin of the individual TRF solutions Table 6.12 describes, which analysis results have been used to create them. The presented nomenclature will be used in the following for the description of the impact of utilized ray-traced delays on the TRF.

Table 6.12: Nomenclature of the different TRF solutions emerging from the individual VLBI analysis results from the parameterizations 1 to 4 as described in Section 6.4.2 on page 126 and more detailed in Table 6.7 on page 129.

VLBI analysis parameterization:	1	2	3	4
Name of the TRF solution from the global solution	TRF 1	TRF 2	TRF 3	TRF 4

Figure 6.12 shows the locations of all 46 stations, which are part of each TRF solution. The 11 datum stations are highlighted and labelled. Table 6.13 gives more details on the individual

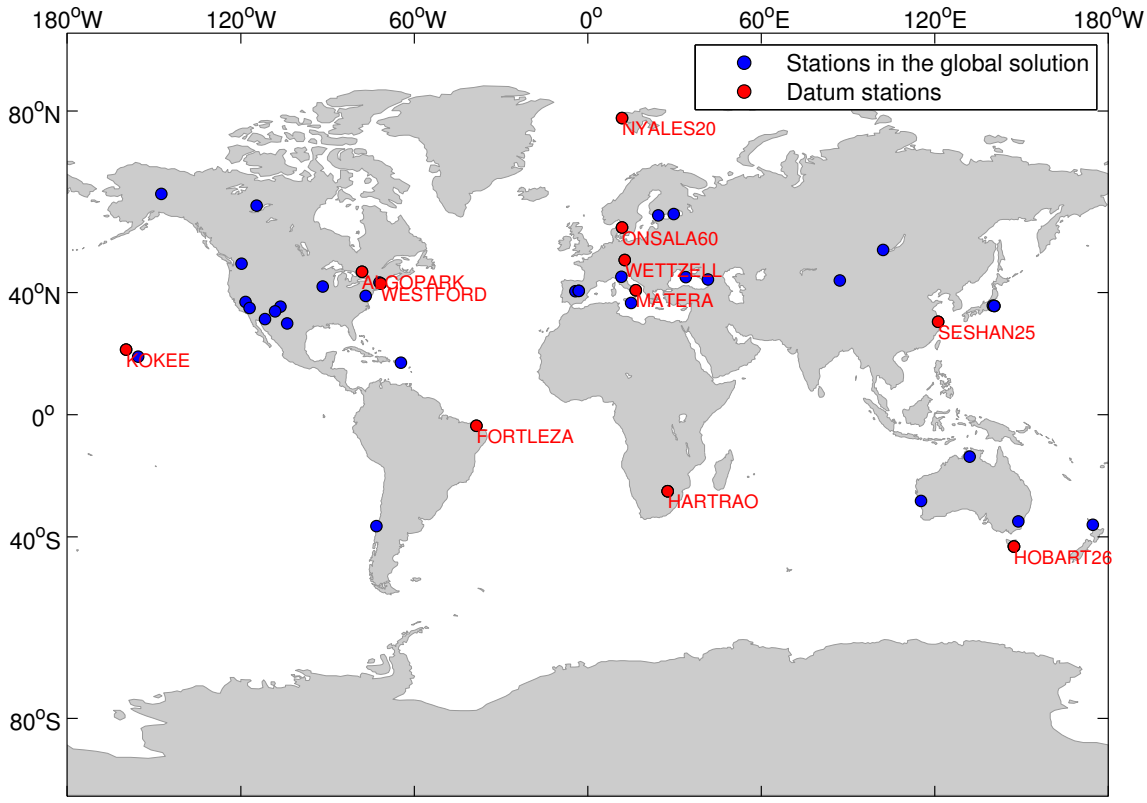

Figure 6.12: Locations of all 46 stations, which are part of each TRF solution. The datum stations are highlighted and labelled.

datum stations by describing their observation activity. Furthermore their mean coordinate error σ_{XYZ} as determined for each TRF solution within each global solution is reported. This parameter is calculated according to Equation (6.9) and serves as a quality assessment parameter of a station position:

$$\sigma_{XYZ} = \sqrt{\frac{\sigma_X^2 + \sigma_Y^2 + \sigma_Z^2}{3}} \tag{6.9}$$

with the formal errors σ_X, σ_Y and σ_Z of the Cartesian coordinates X, Y and Z of the station.

Table 6.13: Datum stations of all TRF solutions, their observing interval and their mean coordinate error σ_{XYZ} as determined from Equation (6.9) for each global solution.

Name	Nr. of sessions (max. 2 340)	Observing time span (max. 16.5 years)	σ_{XYZ} [mm] in TRF 1	TRF 2	TRF 3	TRF 4
ALGOPARK	487	7.6	0.4	0.4	0.4	0.4
FORTLEZA	1 040	16.5	0.5	0.5	0.4	0.4
HARTRAO	598	16.2	0.6	0.6	0.6	0.6
HOBART26	436	16.3	0.8	0.8	0.8	0.7
KOKEE	1 519	16.5	0.3	0.3	0.3	0.3
MATERA	683	16.4	0.3	0.3	0.3	0.3
NYALES20	1 334	16.5	0.2	0.2	0.2	0.2
ONSALA60	467	16.4	0.3	0.3	0.3	0.3
SESHAN25	204	16.4	0.6	0.6	0.6	0.6
WESTFORD	905	15.6	0.2	0.2	0.2	0.2
WETTZELL	1 824	16.5	0.2	0.2	0.2	0.2

6.4.3.4 Parameters for the assessment of the impact of the ray-traced delays on the TRF

The TRF solutions, which emerged from the different analysis parameterizations, are used for the research of the impact of the ray-traced delays on them. This assessment is carried out by comparing the different TRF solutions with respect to station coordinate differences and the Helmert transformation parameters between two different realizations.

The differences ΔX, ΔY and ΔZ in the Cartesian coordinates X, Y and Z of a specific station are determined between the TRF solutions TRF 1 and TRF 3 or between TRF 2 and TRF 4 in the form

$$\begin{bmatrix} \Delta X \\ \Delta Y \\ \Delta Z \end{bmatrix} = \begin{bmatrix} X_{TRF\ 3} \\ Y_{TRF\ 3} \\ Z_{TRF\ 3} \end{bmatrix} - \begin{bmatrix} X_{TRF\ 1} \\ Y_{TRF\ 1} \\ Z_{TRF\ 1} \end{bmatrix} \tag{6.10}$$

or

$$\begin{bmatrix} \Delta X \\ \Delta Y \\ \Delta Z \end{bmatrix} = \begin{bmatrix} X_{TRF\ 4} \\ Y_{TRF\ 4} \\ Z_{TRF\ 4} \end{bmatrix} - \begin{bmatrix} X_{TRF\ 2} \\ Y_{TRF\ 2} \\ Z_{TRF\ 2} \end{bmatrix}, \tag{6.11}$$

where the subscripts of the coordinates describe from which TRF solution they originate.

The differences ΔN, ΔE and ΔU in the local coordinate components North, East and up of a specific station can be determined by transforming the differences from the Cartesian coordinate system to the local topocentric coordinate system according to the transformation equation described by Tanir et al. (2009):

$$\begin{bmatrix} \Delta N \\ \Delta E \\ \Delta U \end{bmatrix} = \Omega \cdot \begin{bmatrix} \Delta X \\ \Delta Y \\ \Delta Z \end{bmatrix}, \tag{6.12}$$

where the ΔX, ΔY and ΔZ originate from Equation (6.10) or (6.11) depending on the considered comparison. The rotation matrix Ω is determined as (Tanir et al. 2009)

$$\Omega = \begin{bmatrix} -\sin\varphi\cos\lambda & -\sin\varphi\sin\lambda & \cos\varphi \\ -\sin\lambda & \cos\lambda & 0 \\ \cos\varphi\cos\lambda & \cos\varphi\sin\lambda & \sin\varphi \end{bmatrix}, \tag{6.13}$$

where φ and λ are the (ellipsoidal) latitude and longitude of the station as determined from its Cartesian coordinates in the TRF with respect to a reference ellipsoid. In case of the comparison with Equation (6.10) the coordinates in TRF 1 are used whereas for the comparison with Equation (6.11) those in TRF 2 are used for the determination of φ and λ of the station.

Additionally to the differences in the individual horizontal directions North and East a common value for the horizontal displacement ΔP can be determined as

$$\Delta P = \sqrt{\Delta N^2 + \Delta E^2}. \tag{6.14}$$

Besides the determination of the ΔN, ΔE, ΔU and ΔP as assessment parameters for the comparison between different TRF solutions, it is necessary to have information about the accuracy of these parameters in order to be able to classify their value. Therefore the formal errors of the coordinate differences are also determined. This can be done according to the findings presented in Hofmeister (2013), which are described in the following.

The coordinates of the stations in each TRF solution have formal errors. In order to determine the formal errors of the differences in the coordinates between two TRF solutions, the covariance matrices of the coordinate differences are needed. The covariances of the coordinate estimates of one station between two TRF solutions are not known since the coordinates have been estimated

in different least-squares adjustments. Thus the inter-solution covariances are set to 0 and the covariance matrix of the coordinate differences $Cov_{\Delta XYZ}$ of one station can then be built as

$$Cov_{\Delta XYZ} = Cov_1 + Cov_2, \tag{6.15}$$

where Cov_1 and Cov_2 are the covariance matrices of a specific station from two different TRF solutions. The covariance matrix of each station in a TRF solution has the form

$$Cov = \begin{bmatrix} \sigma_X^2 & \sigma_{XY} & \sigma_{XZ} \\ \sigma_{YX} & \sigma_Y^2 & \sigma_{YZ} \\ \sigma_{ZX} & \sigma_{ZY} & \sigma_Z^2 \end{bmatrix}, \tag{6.16}$$

which contains the individual covariances of the Cartesian station coordinates X, Y and Z.

In the main diagonal of $Cov_{\Delta XYZ}$ the variances of the coordinate differences can be found. Calculation of the square root of each of these elements delivers the desired formal errors of the coordinate differences $\sigma_{\Delta X}$, $\sigma_{\Delta Y}$ and $\sigma_{\Delta Z}$.

In order to receive the formal errors of the coordinate differences in the local topocentric coordinate system a transformation of the covariance matrix of the coordinate differences $Cov_{\Delta XYZ}$ has to be done according to the equation given by Tanir et al. (2009) to get the covariance matrix of the coordinate differences $Cov_{\Delta NEU}$ in the local topocentric coordinate system:

$$Cov_{\Delta NEU} = \Omega \cdot Cov_{\Delta XYZ} \cdot \Omega^T, \tag{6.17}$$

where Ω is the rotation matrix as determined by Equation (6.13). The formal errors of the local coordinate differences $\sigma_{\Delta N}$, $\sigma_{\Delta E}$ and $\sigma_{\Delta U}$ are then again obtained by calculating the square roots of the main diagonal entries of $Cov_{\Delta NEU}$.

The formal error $\sigma_{\Delta P}$ of the horizontal displacement ΔP is determined as

$$\sigma_{\Delta P} = \sqrt{\frac{\sigma_{\Delta N}^2 + \sigma_{\Delta E}^2}{2}}. \tag{6.18}$$

In order to receive a reduced set of parameter values for each TRF solution for a general comparison of the TRF, the individual ΔN, ΔE, ΔU and ΔP of the different stations are averaged to get the mean values $\overline{\Delta N}$, $\overline{\Delta E}$, $\overline{\Delta U}$ and $\overline{\Delta P}$. For the calculation of these mean values different station sets, i.e. tie point sets, are used:

1. *Datum stations*
   - This tie point set contains the 11 datum stations of the individual TRF solutions.
2. *$\sigma_{XYZ} < 4$ mm*
   - This tie point set contains only stations, which have a mean coordinate error

$\sigma_{XYZ} < 4$ mm in one specific TRF solution.

3. *All stations*

   - This tie point set contains all stations, which are part of the individual TRF solutions.

Furthermore the standard deviations of the local coordinate differences are calculated and denoted as[1] $s_{\overline{\Delta N}}$, $s_{\overline{\Delta E}}$, $s_{\overline{\Delta U}}$ and $s_{\overline{\Delta P}}$. In order to avoid outliers to be part of the results a simple outlier reduction is carried out. All stations with a ΔN, ΔE or ΔU outside the interval [-250 mm, 250 mm] are declared as outliers. In no TRF solution any station is recognized as an outlier and thus no station is excluded from the averaging due to being identified as an outlier.

A further assessment of the changes between individual TRF solutions can be done with respect to the transformation parameters between the frames. The approach of determining these parameters is again based on the findings presented in Hofmeister (2013), which are described in the following.

Based on specific transformation equations and a number of tie points, i.e. stations which are common to both TRF solutions, the transformation parameters can be determined in a least-squares adjustment.

According to Böckmann et al. (2010) it is necessary to check the robustness of the determined transformation parameters since the VLBI stations are typically not very well globally distributed. Therefore it is advisable to use different sets of tie points in order to determine individual solutions of the transformation parameters. In the optimum case the resulting parameters from the different tie point sets should be similar, which would correspond to a robust transformation solution.

For this research three different sets of tie points are used for the estimation of the transformation parameters. These sets are defined in the same way as described above for the calculation of the mean coordinate differences. Thus there is again the set containing the datum stations of the TRF, the set containing the stations with a mean coordinate error $\sigma_{XYZ} < 4$ mm in one of the TRF solutions and the set containing all stations, i.e. tie points, between the compared TRF solutions, which are all 46 stations since all TRF solutions in this research contain the same stations.

The fundamental concept of the transformation between two TRF solutions used in this research follows the concept and equations presented in the IERS Conventions 2010 (see Petit and Luzum 2010).

The used transformation is a 14 Helmert parameters transformation. Thus there are the seven conventional transformation parameters consisting of the three translations T_X, T_Y and T_Z, the three rotation angles ω_X, ω_Y and ω_Z and the scale m. Furthermore the temporal derivatives of the parameters are introduced, i.e. $\dot{T}_X$, $\dot{T}_Y$, $\dot{T}_Z$, $\dot{\omega}_X$, $\dot{\omega}_Y$, $\dot{\omega}_Z$ and $\dot{m}$.

In the following the transformation equations and the derivation of the parameter estimation are described based on the example of transforming a station from the TRF 1 to the TRF 2. By

[1] Please note that these are not the averaged formal errors of the differences in the local coordinate system, but the true standard deviations of the differences.

the numbers no specific TRF solution of this research is meant here in this context.

According to Hofmeister (2013) the 14 Helmert parameters transformation is divided into two parts. The first part is the static part that is constant in time and describes the transformation of the station positions through the parameters T_X, T_Y, T_Z, ω_X, ω_Y, ω_Z and m. The second part is variable in time and describes the transformation of the station velocities through the parameters $\dot{T}_X$, $\dot{T}_Y$, $\dot{T}_Z$, $\dot{\omega}_X$, $\dot{\omega}_Y$, $\dot{\omega}_Z$ and $\dot{m}$.

At first the transformation of the station positions is depicted. The transformation equation, i.e. the 7 Helmert parameters transformation of a station position (X, Y, Z) from frame 1 to frame 2 can be written as

$$\vec{X}_2 = \vec{T} + (1+m) \cdot \Omega \cdot \vec{X}_1 \tag{6.19}$$

with the scale m, the position vectors $\vec{X}_1$ and $\vec{X}_2$ containing the station coordinates in the two frames, the translation vector $\vec{T}$ containing the translations of the coordinates and the rotation matrix Ω containing the rotation angles around the coordinate axes.

$$\vec{X}_1 = \begin{bmatrix} X_1 \\ Y_1 \\ Z_1 \end{bmatrix}, \qquad \vec{X}_2 = \begin{bmatrix} X_2 \\ Y_2 \\ Z_2 \end{bmatrix}, \qquad \vec{T} = \begin{bmatrix} T_X \\ T_Y \\ T_Z \end{bmatrix}, \qquad \Omega = \begin{bmatrix} 1 & \omega_Z & -\omega_Y \\ -\omega_Z & 1 & \omega_X \\ \omega_Y & -\omega_X & 1 \end{bmatrix}. \tag{6.20}$$

Due to the fact that the rotation angles ω_X, ω_Y and ω_Z between the two frames are very small, which means that they are expected to be below 1 mas, it is sufficient to use for the rotation matrix Ω the linearized form as presented in Equation (6.20), which contains the rotation angles in radians (Hofmeister 2013).

The transformation of the station velocities[1] $\left(\dot{X}, \dot{Y}, \dot{Z}\right)$ from frame 1 to frame 2 can be formed by the temporal derivative $\frac{\mathrm{d}}{\mathrm{d}t}$ of the position transformation from Equation (6.19), which leads to (Hofmeister 2013)

$$\dot{\vec{X}}_2 = \dot{\vec{T}} + \dot{\Omega} \cdot \left(\vec{X}_1 + m \cdot \vec{X}_1\right) + \dot{m} \cdot \Omega \cdot \vec{X}_1 + (\Omega + m \cdot \Omega) \cdot \dot{\vec{X}}_1 \tag{6.21}$$

with the temporal derivative of the scale $\dot{m}$, the velocity vectors $\dot{\vec{X}}_1$ and $\dot{\vec{X}}_2$ containing the station velocities in the two frames, the temporal derivative of the translation vector $\dot{\vec{T}}$ containing the translations of the velocities and the temporal derivative of the rotation matrix $\dot{\Omega}$ containing the temporal derivatives of the rotation angles around the coordinate axes.

$$\dot{\vec{X}}_1 = \begin{bmatrix} \dot{X}_1 \\ \dot{Y}_1 \\ \dot{Z}_1 \end{bmatrix}, \qquad \dot{\vec{X}}_2 = \begin{bmatrix} \dot{X}_2 \\ \dot{Y}_2 \\ \dot{Z}_2 \end{bmatrix}, \qquad \dot{\vec{T}} = \begin{bmatrix} \dot{T}_X \\ \dot{T}_Y \\ \dot{T}_Z \end{bmatrix}, \qquad \dot{\Omega} = \begin{bmatrix} 0 & \dot{\omega}_Z & -\dot{\omega}_Y \\ -\dot{\omega}_Z & 0 & \dot{\omega}_X \\ \dot{\omega}_Y & -\dot{\omega}_X & 0 \end{bmatrix}. \tag{6.22}$$

[1] The station velocities are available since they have been estimated within the global solutions.

For a solution of the 14 Helmert parameters transformation accordingly at least 14 observation equations are needed. This means that coordinate and velocity information of at least 3 tie points needs to be known in both frames. In case more than the needed 14 observation equations are present, which is the case for the presented research, the transformation system is overdetermined and there is no unique solution. Therefore a least-squares adjustment can be carried out to solve for the unknown transformation parameters. For this task the non-linear observation equations, i.e. the transformation equations, need to be linearized (Hofmeister 2013).

Within the transformation equation of the static part for the station positions described by Equation (6.19) the product $(1+m)\cdot\Omega$ needs to be linearized. This can be reached by neglecting all products of m with Ω except for those of m with the main diagonal of Ω, which leads to

$$\begin{aligned}(1+m)\cdot\begin{bmatrix}1 & \omega_Z & -\omega_Y\\ -\omega_Z & 1 & \omega_X\\ \omega_Y & -\omega_X & 1\end{bmatrix} &\approx\\ \approx\begin{bmatrix}1+m & \omega_Z & -\omega_Y\\ -\omega_Z & 1+m & \omega_X\\ \omega_Y & -\omega_X & 1+m\end{bmatrix} &=\\ =\begin{bmatrix}1 & 0 & 0\\ 0 & 1 & 0\\ 0 & 0 & 1\end{bmatrix}+\begin{bmatrix}m & 0 & 0\\ 0 & m & 0\\ 0 & 0 & m\end{bmatrix}&+\begin{bmatrix}0 & \omega_Z & -\omega_Y\\ -\omega_Z & 0 & \omega_X\\ \omega_Y & -\omega_X & 0\end{bmatrix}.\end{aligned} \tag{6.23}$$

This approximation is applicable since the neglected products are small (Hofmeister 2013). The linearized form of Equation (6.19) can then be written as

$$\vec{X}_2 = \vec{T} + \vec{X}_1 + m\cdot\vec{X}_1 + \Omega_0\cdot\vec{X}_1 \tag{6.24}$$

with

$$\Omega_0 = \begin{bmatrix}0 & \omega_Z & -\omega_Y\\ -\omega_Z & 0 & \omega_X\\ \omega_Y & -\omega_X & 0\end{bmatrix}. \tag{6.25}$$

Also the transformation equation of the station velocities, described by Equation (6.21), needs to be linearized. For this task the temporal derivative of the linearized transformation equation of the station positions from Equation (6.24) is built and leads to

$$\dot{\vec{X}}_2 = \dot{\vec{T}} + \dot{\vec{X}}_1 + \dot{m}\cdot\vec{X}_1 + m\cdot\dot{\vec{X}}_1 + \dot{\Omega}_0\cdot\vec{X}_1 + \Omega_0\cdot\dot{\vec{X}}_1 \tag{6.26}$$

with

$$\dot{\Omega}_0 = \begin{bmatrix} 0 & \dot{\omega}_Z & -\dot{\omega}_Y \\ -\dot{\omega}_Z & 0 & \dot{\omega}_X \\ \dot{\omega}_Y & -\dot{\omega}_X & 0 \end{bmatrix}. \tag{6.27}$$

Equation (6.26) is the linearized transformation equation of the station velocities (Hofmeister 2013). According to the IERS Conventions 2010 (see Petit and Luzum 2010) Equation (6.26) could be simplified by neglecting the terms $m \cdot \vec{\dot{X}}_1$ and $\Omega_0 \cdot \vec{\dot{X}}_1$ since they lead to very small values of around only 0.1 mm per 100 years. Nevertheless these terms are not neglected in this research and remain in the transformation equation.

For the least-squares adjustment of the 14 transformation parameters the functional model can now be established by using Equations (6.24) and (6.26). The functional model D for a tie point between the frames 1 and 2 with the coordinates (X_1, Y_1, Z_1) or (X_2, Y_2, Z_2) and the velocities $\left(\dot{X}_1, \dot{Y}_1, \dot{Z}_1\right)$ or $\left(\dot{X}_2, \dot{Y}_2, \dot{Z}_2\right)$ is received from differentiating Equations (6.24) and (6.26) with respect to the unknown transformation parameters, which leads to

$$D = \begin{bmatrix} 1 & 0 & 0 & 0 & -Z_1 & Y_1 & X_1 & 0 & 0 & 0 & 0 & 0 & 0 & 0 \\ 0 & 1 & 0 & Z_1 & 0 & -X_1 & Y_1 & 0 & 0 & 0 & 0 & 0 & 0 & 0 \\ 0 & 0 & 1 & -Y_1 & X_1 & 0 & Z_1 & 0 & 0 & 0 & 0 & 0 & 0 & 0 \\ 0 & 0 & 0 & 0 & -\dot{Z}_1 & \dot{Y}_1 & \dot{X}_1 & 1 & 0 & 0 & 0 & -Z_1 & Y_1 & X_1 \\ 0 & 0 & 0 & \dot{Z}_1 & 0 & -\dot{X}_1 & \dot{Y}_1 & 0 & 1 & 0 & Z_1 & 0 & -X_1 & Y_1 \\ 0 & 0 & 0 & -\dot{Y}_1 & \dot{X}_1 & 0 & \dot{Z}_1 & 0 & 0 & 1 & -Y_1 & X_1 & 0 & Z_1 \end{bmatrix}. \tag{6.28}$$

With the functional model D the complete linearized equation system for the least-squares adjustment can be written as

$$\begin{bmatrix} X_2 - X_1 \\ Y_2 - Y_1 \\ Z_2 - Z_1 \\ \dot{X}_2 - \dot{X}_1 \\ \dot{Y}_2 - \dot{Y}_1 \\ \dot{Z}_2 - \dot{Z}_1 \end{bmatrix} = D \cdot \begin{bmatrix} T_X \\ T_Y \\ T_Z \\ \omega_X \\ \omega_Y \\ \omega_Z \\ m \\ \dot{T}_X \\ \dot{T}_Y \\ \dot{T}_Z \\ \dot{\omega}_X \\ \dot{\omega}_Y \\ \dot{\omega}_Z \\ \dot{m} \end{bmatrix}. \tag{6.29}$$

Accordingly the results of the least-squares adjustment are the 14 transformation parameters. Additionally the a posteriori standard deviations[1] of these parameters are determined. Please note that the term standard deviation is used to describe the formal error of a parameter determined in a least-squares adjustment. Within the least-squares adjustment a weighting of the observation equations of the station coordinates and velocities is done. The weights are the inverses of the respective squared coordinate or velocity formal errors from the global solution of the frame 2.

6.4.3.5 Impact of the ray-traced delays on the TRF

In this section the individual TRF solutions from the different global solutions of the differently parameterized single session analysis solutions are compared. To facilitate the nomenclature the TRF solutions are denoted according to Table 6.12.

The first investigation of the impact of the ray-traced delays on the TRF compares TRF 1 and TRF 3, i.e. the solution using a standard VLBI analysis parameterization and the solution using in principle the same parameterization but with a priori application of ray-traced delays instead of slant delays determined from ZHD^S with the VMF1. For the assessment of the changes in the resulting TRF solutions due to the different parameterizations, the coordinate differences and the transformation parameters between the two frames are determined as described in Section 6.4.3.4. Figure 6.13 presents the horizontal and height displacements of those stations, which have a mean coordinate error $\sigma_{XYZ} < 4$ mm in TRF 3. These are all stations in the TRF solutions except WARK12M and YARRA12M, i.e. a total of 44 stations. Considering the horizontal displacements, it seems that most of the stations are moved outwards, away from Central Europe, but since the values are below 1 mm, except for TIGOCONC and YARRA12M with horizontal displacements of also only 1.0 mm and 1.1 mm, this is not significant. Figure 6.14 displays the individual coordinate differences ΔN, ΔE and ΔU with respect to the stations' longitudes and latitudes of those stations, which have a mean coordinate error $\sigma_{XYZ} < 4$ mm in TRF 3, i.e. of the same stations as presented in Figure 6.13. There is no special trend of the differences with respect to the longitude or latitude of the stations derivable.

Considering the height displacements, the ΔU, most of the stations are not significantly affected by the application of the ray-traced delays to the VLBI analysis since also in the height-component the differences remain very small, mostly up to only ±2 mm. Furthermore it can be stated that the application of the ray-traced delays does not lead to a uniform uplift or subsidence of the station heights. There is only a tendency of an uplift since more stations have positive ΔU values.

A detailed look at the coordinate differences and their formal errors of all individual stations in the TRF solutions is given by Table A.8 in Appendix Section A.5 on page 200.

Table 6.14 presents the mean differences $\overline{\Delta N}$, $\overline{\Delta E}$, $\overline{\Delta U}$ and $\overline{\Delta P}$ and the according standard deviations $s_{\overline{\Delta N}}$, $s_{\overline{\Delta E}}$, $s_{\overline{\Delta U}}$ and $s_{\overline{\Delta P}}$ of the comparison of TRF 3 - TRF 1. The averaged differences

[1] They are denoted as σ_{T_X}, σ_{T_Y}, σ_{T_Z}, σ_{ω_X}, σ_{ω_Y}, σ_{ω_Z}, σ_m, $\sigma_{\dot{T}_X}$, $\sigma_{\dot{T}_Y}$, $\sigma_{\dot{T}_Z}$, $\sigma_{\dot{\omega}_X}$, $\sigma_{\dot{\omega}_Y}$, $\sigma_{\dot{\omega}_Z}$ and $\sigma_{\dot{m}}$.

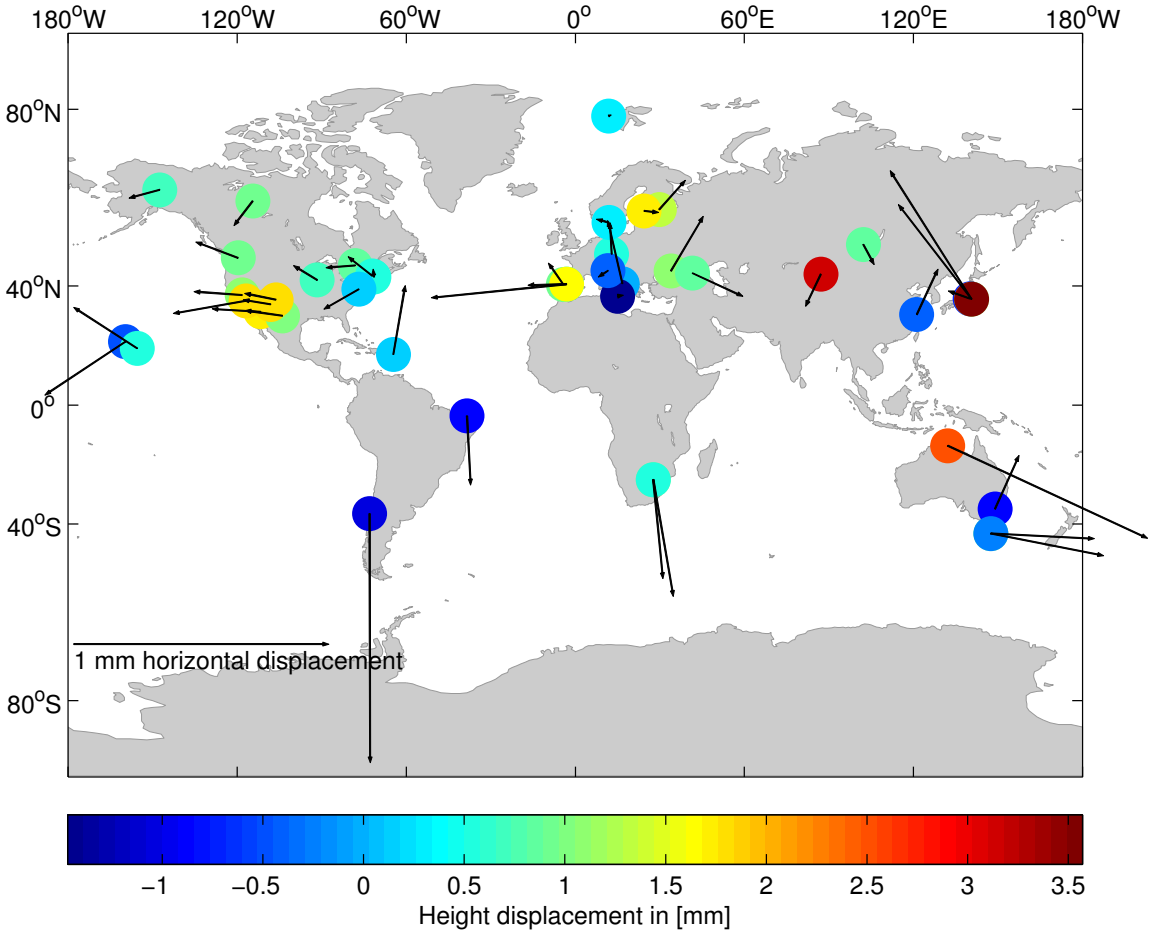

Figure 6.13: Horizontal and height displacements from TRF 3 - TRF 1 of those stations, which have a mean coordinate error $\sigma_{XYZ} < 4$ mm in TRF 3. Reference epoch of the TRF solutions is 2000.0.

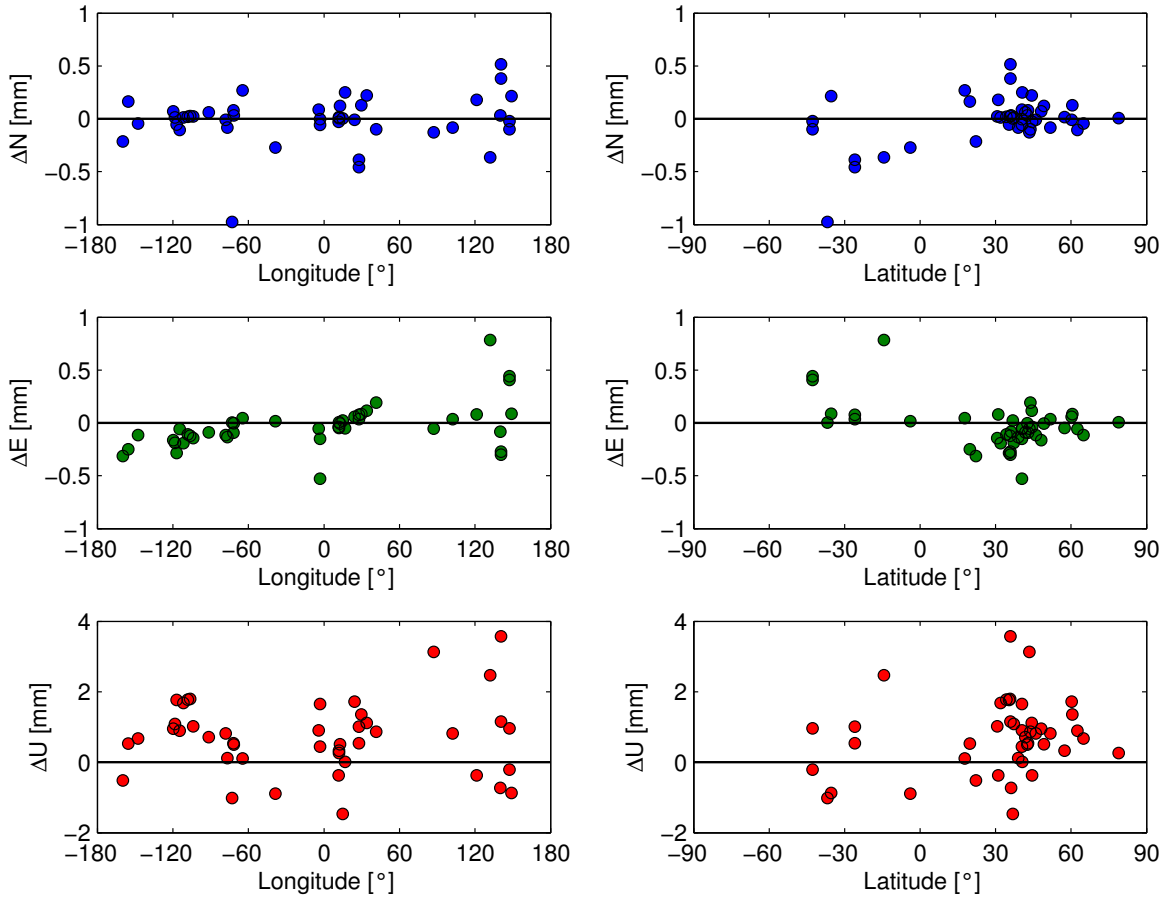

Figure 6.14: Coordinate differences ΔN, ΔE and ΔU from TRF 3 - TRF 1 of those stations, which have a mean coordinate error $\sigma_{XYZ} < 4$ mm in TRF 3. The plots on the left side present the differences with respect to the stations' longitudes and the ones on the right side show the differences with respect to the stations' latitudes. Reference epoch of the TRF solutions is 2000.0.

are built for different sets of tie points according to the definitions on page 142. The $\overline{\Delta N}$, $\overline{\Delta E}$

Table 6.14: Mean coordinate differences $\overline{\Delta N}$, $\overline{\Delta E}$, $\overline{\Delta U}$ and $\overline{\Delta P}$ and the according standard deviations $s_{\overline{\Delta N}}$, $s_{\overline{\Delta E}}$, $s_{\overline{\Delta U}}$ and $s_{\overline{\Delta P}}$ of the comparison TRF 3 - TRF 1 for different sets of tie points. The differences at each station are calculated according to Equations (6.10) and (6.12) to (6.14) and then averaged. Reference epoch of the TRF solutions is 2000.0.

Mean difference:	TRF 3 - TRF 1					
Tie point set	Datum stations		$\sigma_{XYZ} < 4$ mm in TRF 3		All stations	
Nr. of tie points	11		44		46	
Mean differences	Parameter	St. dev.	Parameter	St. dev.	Parameter	St. dev.
$\overline{\Delta N}$ [mm]	-0.0	0.2	-0.0	0.2	-0.0	0.3
$\overline{\Delta E}$ [mm]	0.0	0.2	-0.0	0.2	-0.0	0.3
$\overline{\Delta U}$ [mm]	0.2	0.6	0.7	1.0	1.1	2.3
$\overline{\Delta P}$ [mm]	0.2	0.2	0.2	0.2	0.3	0.3

and $\overline{\Delta P}$ of each tie point set show that the ray-traced delays do not impact the horizontal station positions as these differences are on average between 0.0 mm and 0.3 mm depending on the considered domain. In case of the $\overline{\Delta U}$ from the different tie point sets it can be seen that there is a small positive tendency of the impact. This small trend is increased from 0.2 mm to 0.7 mm and to 1.1 mm in case more than only the ΔU of the datum stations are averaged. The values of the ΔU at the stations WARK12M and YARRA12M, which are only part of the tie point set with all stations, are not reliable since the according formal errors are very large. Their values can be found in Table A.8 in Appendix Section A.5 on page 200. Thus, the $\overline{\Delta U}$ of the tie point set containing all stations is affected especially by the ΔU of 14.8 mm at station YARRA12M, leading to the not reliable $\overline{\Delta U}$ of 1.1 mm.

Table 6.15 presents the 14 Helmert parameters and the according standard deviations for the transformation from TRF 1 to TRF 3. The transformation parameters are determined for different sets of tie points according to the definitions on page 142. The received transformation parameters deliver similar values for the different sets of tie points, which means that the results are robust. The compared TRF solutions are almost equal due to the small absolute values of the transformation parameters. The temporal derivatives of the position transformation parameters are even zero or almost zero and therefore negligible. An impact of the applied ray-traced delays on the TRF would be visible in the scale m, but this has a maximum value of only 0.1 ppb and thus the TRF is not affected with respect to this parameter.

Considering all above described comparison results of TRF 3 against TRF 1, it can be concluded that the ray-traced delays do not significantly impact the TRF solution, neither positively nor negatively, in case they are applied to a standard VLBI analysis instead of using a priori slant delays determined from ZHD^S with the VMF1. Only with respect to the station heights a slight

Table 6.15: The 14 Helmert parameters and the according standard deviations for the transformation from TRF 1 to TRF 3 for different sets of tie points. Reference epoch of the TRF solutions is 2000.0.

Transformation:	TRF 1 → TRF 3					
Tie point set	Datum stations		$\sigma_{XYZ} < 4$ mm in TRF 3		All stations	
Nr. of tie points	11		44		46	
Helmert parameters	Parameter	St. dev.	Parameter	St. dev.	Parameter	St. dev.
T_X [mm]	0.1	0.1	-0.2	0.1	-0.2	0.1
T_Y [mm]	0.1	0.1	-0.2	0.1	-0.2	0.1
T_Z [mm]	-0.0	0.1	-0.0	0.1	-0.0	0.1
ω_X [µas]	-2.8	4.9	7.0	3.0	6.9	3.1
ω_Y [µas]	4.6	5.1	-2.6	3.0	-2.7	3.1
ω_Z [µas]	3.6	3.6	2.9	1.9	2.9	2.0
m [ppb]	0.0	0.0	0.1	0.0	0.1	0.0
$\dot{T}_X$ [mm/year]	0.0	0.0	0.0	0.0	0.0	0.0
$\dot{T}_Y$ [mm/year]	0.0	0.0	0.0	0.0	0.0	0.0
$\dot{T}_Z$ [mm/year]	0.0	0.0	0.0	0.0	0.0	0.0
$\dot{\omega}_X$ [µas/year]	-0.5	0.6	-0.1	0.3	-0.1	0.3
$\dot{\omega}_Y$ [µas/year]	0.5	0.6	0.4	0.3	0.4	0.3
$\dot{\omega}_Z$ [µas/year]	0.3	0.4	0.2	0.2	0.2	0.2
$\dot{m}$ [ppb/year]	-0.0	0.0	-0.0	0.0	-0.0	0.0

average uplift tendency is seen.

The second investigation of the impact of the ray-traced delays on the TRF compares TRF 2 and TRF 4, i.e. the solution using a standard VLBI analysis parameterization but without tropospheric gradient estimation and the solution using in principle the same parameterization but with a priori application of ray-traced delays instead of slant delays determined from ZHD^S with the VMF1. For the assessment of the changes in the resulting TRF solutions due to the different parameterizations, the coordinate differences and the transformation parameters between the two frames are again determined as described in Section 6.4.3.4. Figure 6.15 presents the horizontal and height displacements of those stations, which have a mean coordinate error $\sigma_{XYZ} < 4$ mm in TRF 4. These are also in this comparison all stations in the TRF solutions except WARK12M and YARRA12M, i.e. a total of 44 stations. There is a clear trend of the horizontal displacements vis-

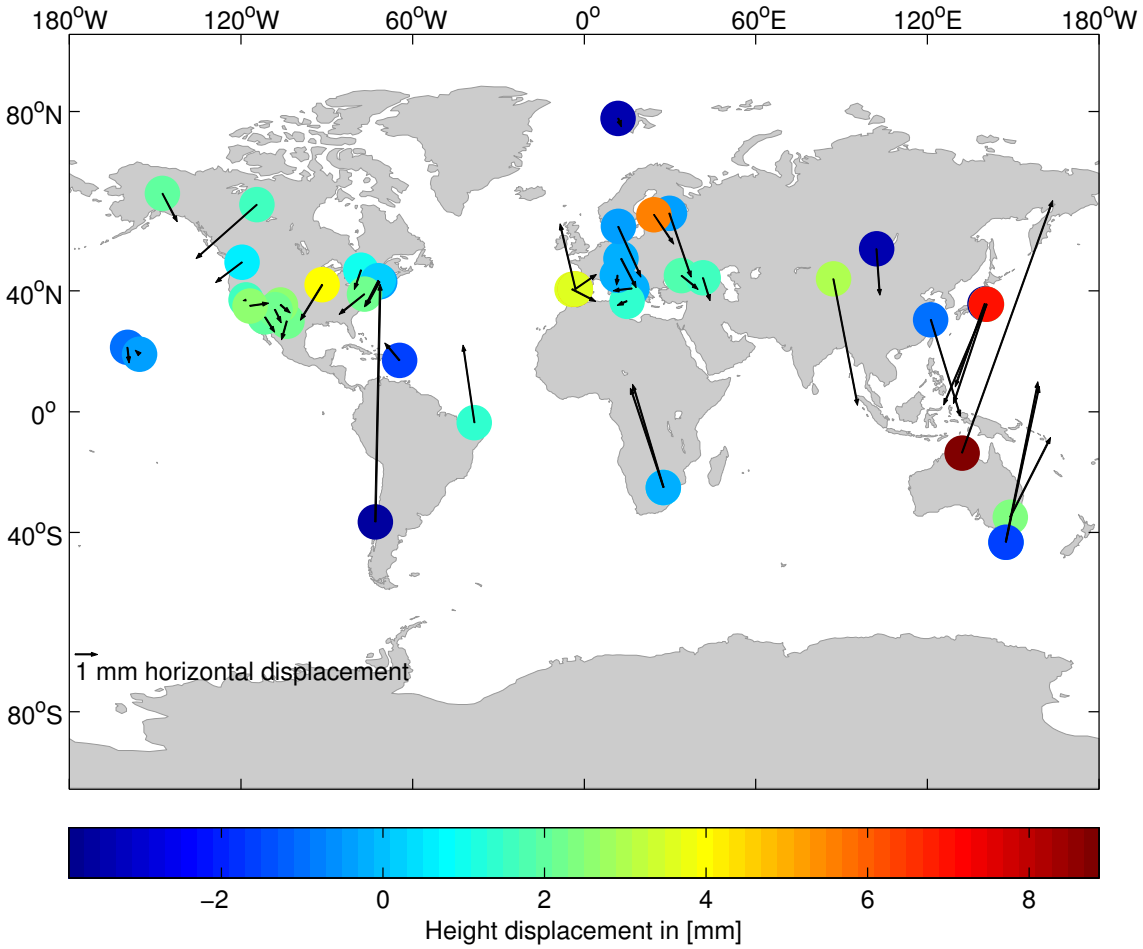

Figure 6.15: Horizontal and height displacements from TRF 4 - TRF 2 of those stations, which have a mean coordinate error $\sigma_{XYZ} < 4$ mm in TRF 4. Reference epoch of the TRF solutions is 2000.0.

ible. Almost all stations are horizontally displaced towards the equator. Stations on the northern hemisphere are moved towards the South and stations on the southern hemisphere are moved

towards the North in case ray-traced delays are applied to the VLBI analysis. This behaviour is reasonable since the analysis without ray-traced delays is lacking the tropospheric gradient information, which is implicitly contained in the ray-traced delays. Furthermore this trend is significant since most of the stations are displaced by 1 mm or more on the horizontal plane. Associated with the presented values in Figure 6.15 the individual coordinate differences ΔN, ΔE and ΔU of those stations, which have a mean coordinate error $\sigma_{XYZ} < 4$ mm in TRF 4 are shown in Figure 6.16 with respect to the stations' longitudes and latitudes. The observed effect

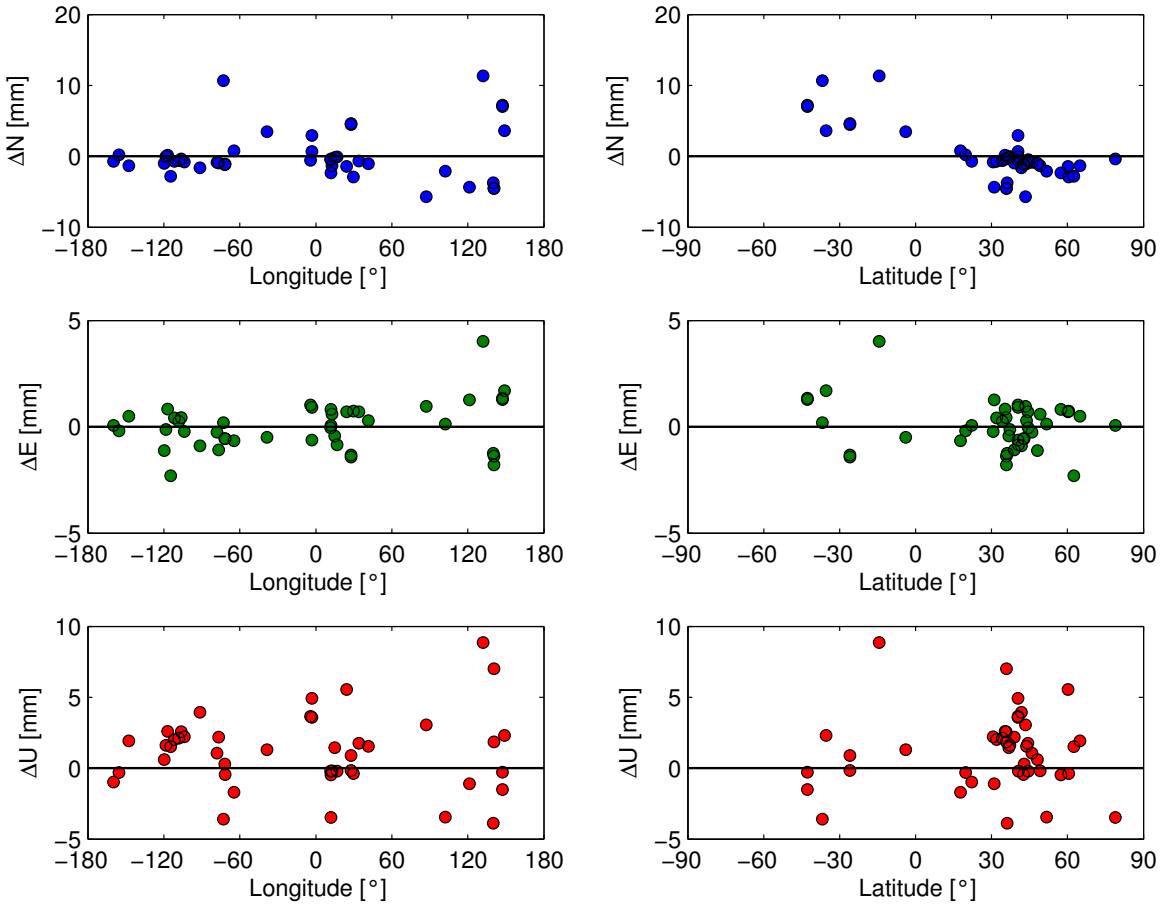

Figure 6.16: Coordinate differences ΔN, ΔE and ΔU from TRF 4 - TRF 2 of those stations, which have a mean coordinate error $\sigma_{XYZ} < 4$ mm in TRF 4. The plots on the left side present the differences with respect to the stations' longitudes and the ones on the right side show the differences with respect to the stations' latitudes. Reference epoch of the TRF solutions is 2000.0.

on the horizontal station positions can be seen in the uppermost right plot of Figure 6.16, which shows the ΔN with respect to the stations' latitudes. All stations on the southern hemisphere have positive ΔN and almost all stations on the northern hemisphere have negative ΔN.

Considering the height displacements, the ΔU, no trend with respect to the stations' longitudes or latitudes is derivable. Most ΔU are in the range of ±4 mm, i.e. the impact of the ray-traced delays on the station heights is increased compared to the previous comparison of TRF solutions from VLBI analysis with tropospheric gradient estimation. Again it can be stated that the

application of the ray-traced delays does not lead to a uniform uplift or subsidence of the station heights. Also this time there is only a tendency of an uplift since more stations have positive ΔU values.

A detailed look at the coordinate differences and their formal errors of all individual stations in the TRF solutions is given by Table A.9 in Appendix Section A.5 on page 202.

Table 6.16 presents the mean differences $\overline{\Delta N}$, $\overline{\Delta E}$, $\overline{\Delta U}$ and $\overline{\Delta P}$ and the according standard deviations $s_{\overline{\Delta N}}$, $s_{\overline{\Delta E}}$, $s_{\overline{\Delta U}}$ and $s_{\overline{\Delta P}}$ of the comparison of TRF 4 - TRF 2. The averaged differences are built for different sets of tie points, which are as always created according to the definitions on page 142. The $\overline{\Delta N}$ and $\overline{\Delta E}$ are between -0.2 mm and 0.4 mm from the different tie point sets,

Table 6.16: Mean coordinate differences $\overline{\Delta N}$, $\overline{\Delta E}$, $\overline{\Delta U}$ and $\overline{\Delta P}$ and the according standard deviations $s_{\overline{\Delta N}}$, $s_{\overline{\Delta E}}$, $s_{\overline{\Delta U}}$ and $s_{\overline{\Delta P}}$ of the comparison TRF 4 - TRF 2 for different sets of tie points. The differences at each station are calculated according to Equations (6.11) and (6.12) to (6.14) and then averaged. Reference epoch of the TRF solutions is 2000.0.

Mean difference:	TRF 4 - TRF 2					
Tie point set	Datum stations		$\sigma_{XYZ} < 4$ mm in TRF 4		All stations	
Nr. of tie points	11		44		46	
Mean differences	Parameter	St. dev.	Parameter	St. dev.	Parameter	St. dev.
$\overline{\Delta N}$ [mm]	0.4	3.4	0.1	3.6	0.2	3.8
$\overline{\Delta E}$ [mm]	0.1	0.9	0.0	1.1	-0.2	2.3
$\overline{\Delta U}$ [mm]	-0.4	1.3	1.1	2.6	1.6	3.7
$\overline{\Delta P}$ [mm]	2.6	2.2	2.7	2.7	3.0	3.2

which is not a significant range of average values, but these are only the averages for the separate coordinate directions. Combined to the average horizontal displacement the $\overline{\Delta P}$ of each tie point set shows that the ray-traced delays lead to an impact on the horizontal station position if no tropospheric gradients are estimated within the VLBI analysis. The obtained average values are 2.6 mm for the tie point set of the datum stations, 2.7 mm for the stations with a mean coordinate error $\sigma_{XYZ} < 4$ mm in TRF 4 and 3.0 mm for the tie point set of all stations. The $\overline{\Delta U}$ from the different tie point sets show that there is definitely an impact on the station heights in case the ray-traced delays are applied to the analysis. The $\overline{\Delta U}$ of the tie point set containing only the 11 datum stations of the TRF solutions is -0.4 mm, which means that the stations are subsided on average. Due to the small number of stations in the sample this result is not significant. The tie point set containing the stations with a mean coordinate error $\sigma_{XYZ} < 4$ mm in TRF 4 delivers a $\overline{\Delta U}$ of 1.1 mm, which means that the stations are uplifted on average. In case the mean of the individual ΔU is computed from all stations, the $\overline{\Delta U}$ increases to 1.6 mm. The values of the ΔU at the stations WARK12M and YARRA12M, which are only part of this tie point set with all stations, are also in this comparison not reliable since the according formal errors are very large.

Their values can be found in Table A.9 in Appendix Section A.5 on page 202. The increased $\overline{\Delta U}$ is this time, oppositely to the previous comparison of TRF 3 - TRF 1, mainly due to the large ΔU of 18.9 mm at station WARK12M and not due the value at YARRA12M. Thus, the $\overline{\Delta U}$ of 1.6 mm is not reliable.

Table 6.17 presents the 14 Helmert parameters and the according standard deviations for the transformation from TRF 2 to TRF 4. The transformation parameters are determined for different sets of tie points, which are as always created according to the definitions on page 142. Also in this

Table 6.17: The 14 Helmert parameters and the according standard deviations for the transformation from TRF 2 to TRF 4 for different sets of tie points. Reference epoch of the TRF solutions is 2000.0.

Transformation:	TRF 2 → TRF 4					
Tie point set	Datum stations		$\sigma_{XYZ} < 4$ mm in TRF 4		All stations	
Nr. of tie points	11		44		46	
Helmert parameters	Parameter	St. dev.	Parameter	St. dev.	Parameter	St. dev.
T_X [mm]	1.0	0.6	0.3	0.3	0.3	0.3
T_Y [mm]	-0.4	0.5	-0.8	0.3	-0.8	0.3
T_Z [mm]	-0.7	0.5	-0.9	0.3	-0.9	0.3
ω_X [µas]	28.9	20.1	38.4	10.7	37.7	10.5
ω_Y [µas]	36.2	20.2	26.4	10.6	26.0	10.5
ω_Z [µas]	2.7	14.9	3.0	6.9	3.0	6.8
m [ppb]	-0.1	0.1	0.1	0.0	0.1	0.0
$\dot{T}_X$ [mm/year]	0.0	0.1	-0.0	0.0	-0.0	0.0
$\dot{T}_Y$ [mm/year]	0.0	0.1	-0.0	0.0	-0.0	0.0
$\dot{T}_Z$ [mm/year]	0.0	0.1	0.0	0.0	0.0	0.0
$\dot{\omega}_X$ [µas/year]	-0.3	2.3	0.7	1.2	0.7	1.2
$\dot{\omega}_Y$ [µas/year]	0.3	2.3	0.1	1.2	0.1	1.2
$\dot{\omega}_Z$ [µas/year]	0.9	1.8	0.5	0.9	0.4	0.8
$\dot{m}$ [ppb/year]	0.0	0.0	0.0	0.0	0.0	0.0

comparison the received transformation parameters deliver similar values for the different sets of tie points, which means that the results are robust. Compared to the determined parameters for the transformation from TRF 1 to TRF 3, the ones for the transformation from TRF 2 to TRF 4 are slightly increased with respect to their absolute values. Especially the position transformation parameters are increased. The temporal derivatives of the position transformation parameters are also in this comparison negligible. Nevertheless it can in general be stated that these two frames are also very similar due to the still small absolute values of all transformation parameters. Again an impact of the applied ray-traced delays on the TRF would be visible in the scale m, but this has

also in this comparison a maximum value of only 0.1 ppb and thus the TRF is again not affected with respect to this parameter. The scale m of the datum station tie point set is negative and has a value of -0.1 ppb, but this is due to the fact that the $\overline{\Delta U}$ of this set is negative, which has been identified not to be significant since the sample size of this tie point set is small.

Considering all above described comparison results of TRF 4 against TRF 2, it can be concluded that the application of ray-traced delays to a VLBI analysis without tropospheric gradient estimation impacts the TRF solution with respect to the horizontal station positions since the ray-traced delays deliver implicitly the not estimated tropospheric gradient information. Furthermore the stations are uplifted on average by a small amount. Nevertheless the determined transformation parameters between the two compared frames show that the TRF solutions with and without applied ray-traced delays are very similar.

As a final conclusion of the impact of ray-traced delays on the estimated TRF solutions, it can be stated that in case tropospheric gradients are estimated within the VLBI analysis, the application of ray-traced delays shows no significant impact on the TRF neither with respect to the station coordinates nor with respect to the determined transformation parameters between the solutions without and with applied ray-traced delays. In case no tropospheric gradients are estimated within the analysis, the application of ray-traced delays influences the station coordinates of the TRF since the ray-traced delays implicitly introduce the lacking tropospheric gradient information and thus the TRF is improved compared to the solution without applied ray-traced delays. This is especially effective on the horizontal station positions. The station heights are also changed by small amounts in the low mm range. On average there is a small uplift of the stations due to the application of the ray-traced delays.

6.5 Comparison of VLBI analysis results from using RADIATE or NASA GSFC ray-traced delays for the years 2000.0 to 2015.1

In this section a comparison of the VLBI analysis results of solutions from applied ray-traced delays from program RADIATE or from the National Aeronautics and Space Administration Goddard Space Flight Center (NASA GSFC) is carried out. The differences are validated with respect to the BLR determined from the analysis solutions of VLBI sessions between January 2000 and the end of January 2015. This interval will be denoted as 2000.0 to 2015.1 in the following. This assessment reveals the performance of the ray-traced delays from program RADIATE in comparison to the ray-traced delays from NASA GSFC.

6.5.1 Data for the comparison

The ray-traced delays from program RADIATE used for this comparison are the same, which have already been described in Section 6.4.1. This means that program RADIATE has been executed with the settings and options according to the conclusions for the operational service of

the program, which have been described in Section 5.6. Accordingly, the PWL ray-tracing approach has been used to determine ray-traced delays at the exact observation times through time interpolation utilizing ECMWF NWM[1] data as specified in Table 4.2 on page 63 with a horizontal resolution of 1° x 1°. The vertical resolution of the meteorological data has been increased by applying the strict "profilewise" vertical interpolation approach. The ray-traced delays have been introduced to the VLBI analysis software VieVS again via the so-called ".trp" files, which have been created as an output by program RADIATE.

The ray-traced delays from NASA GSFC (see Eriksson and MacMillan 2016) have been obtained from their service on the web page http://lacerta.gsfc.nasa.gov/tropodelays in form of ".trp" files. A description, which data and approaches the NASA GSFC uses to determine its ray-traced delays, can be found in Eriksson et al. (2014). An important note should be made at this point regarding the NWM used for the determination of the NASA GSFC ray-traced delays. According to Eriksson et al. (2014) the NASA GSFC GMAO GEOS-5 FP-IT[2] NWM is used, which is a terrain following model. Since program RADIATE uses pressure level-based NWM data from the ECMWF certain differences in the ray-traced delay results are already introduced at the data level due to the different data origins and the different data types neglecting the differences at the processing level between the program of the NASA GSFC and RADIATE

Unfortunately ray-traced delays from NASA GSFC have not been available for the complete time span 1999.0 to 2015.5, which has been used in Section 6.4 for the VLBI analysis. Only the interval 2000.0 to 2015.1 is covered by the NASA GSFC ray-traced delays. Thus based on the process list "pl_long-run", used for the VLBI analysis in Section 6.4, a new process list called "pl_RADIATE_NASA GSFC" has been created for the VLBI analysis in this section. Due to the shorter time interval and missing ray-tracing data from NASA GSFC for some sessions in between the interval, the final process list "pl_RADIATE_NASA GSFC" contains instead of the former 2 461 the reduced number of 2 196 sessions. The VLBI observations cover a time span of approximately 15 years.

6.5.2 VLBI analysis with applied RADIATE or NASA GSFC ray-traced delays

In order to be able to calculate the *BLR* for a comparison of the performances of the ray-traced delays from RADIATE and from NASA GSFC, VLBI analysis solutions from two different parameterizations are determined. The analysis itself is again carried out with the software VieVS. The fundamental parameterization of each analysis is the same as presented in Section 6.4.2 in Tables 6.5 and 6.6 on page 126. The complete two parameterizations, used in this section, are received from these basic settings for the a priori models and the parameter estimation combined with the settings of either parameterization 3 or 4 as defined in Table 6.7 on page 129. In detail, the two parameterizations differ only in terms of estimating tropospheric gradients or not. Please

[1] The ERA-Interim NWM is used for observations before 01.01.2008 and the ECMWF operational NWM is used for later observations.

[2] Goddard Earth Observing System Model version 5.9.1 Forward Processing for Instrument Teams

note, that although in the short descriptions of the parameterizations 3 and 4 on page 126 it is written that ray-traced delays from program RADIATE are applied to the analysis, the paramterizations are used in this section in the way that ray-traced delays either from RADIATE or from NASA GSFC are used for determining the analysis results for the comparison.

Thus, from the determined four different analysis solutions the BLR are determined, which will be used for the comparison of the performance of RADIATE and NASA GSFC ray-traced delays in two cases: In the first case if tropospheric gradients are estimated within the VLBI analysis, in the second case if they are not.

6.5.3 Comparison of baseline length repeatability results from using RADIATE or NASA GSFC ray-traced delays

In this section the BLR results from using either ray-traced delays from RADIATE or from NASA GSFC are compared. This reveals the performance of the different ray-traced delays against each other and thus provides a further quality assessment of the RADIATE ray-traced delays.

6.5.3.1 Exclusion of analysed but unsuitable VLBI sessions

For the determination of the BLR only suitable analysis results shall be used. Thus, the results of some sessions on the process list "pl_RADIATE_NASA GSFC" need to be excluded from the BLR determination since they are not reliable. Therefore the exclude list defined in Section 6.4.3.1 is used as a starting point. Now, also the analysis solutions from the applied NASA GSFC ray-traced delays are checked with respect to the criteria 1 to 3 described in Section 6.4.3.1 on page 129. Furthermore there are sessions for which the according NASA GSFC data do not provide the needed ray-traced delays for every analysed observation in the session. Therefore these sessions, in total 13, are also put on the extended exclude list in order to use only such session analysis results in the BLR calculation for whose determination ray-traced delays have been used for every single observation within the analysis. The extended exclude list created for the comparison of the BLR results from using RADIATE or NASA GSFC ray-traced delays reduces the data set for the comparison from 2 196 to 2 085 sessions.

6.5.3.2 Differences in the baseline length repeatability results

For each of the four different analysis solutions the BLR are determined with Equation (6.3) as described in Section 6.4.3.2.

For the comparison of the results of the solutions from applied RADIATE or NASA GSFC ray-traced delays again the ΔBLR are calculated. Equations (6.30) and (6.31) describe the calculations, which use the respective BLR results of a specific analysis parameterization. The subscripts to the individual BLR denote the origin of the applied ray-traced delays and which parameterization has been used for the VLBI analysis. The parameterizations 3 and 4 are described in Table 6.7 on page 129. Positive ΔBLR indicate that the application of the ray-traced delays from RADIATE

improve the BLR compared to the results from applying the NASA GSFC ray-traced delays. The ΔBLR are computed as

$$\Delta BLR = BLR_{NASA\ GSFC,\ Param.\ 3} - BLR_{RADIATE,\ Param.\ 3} \tag{6.30}$$

or as

$$\Delta BLR = BLR_{NASA\ GSFC,\ Param.\ 4} - BLR_{RADIATE,\ Param.\ 4}. \tag{6.31}$$

Also the change of the baseline length repeatability δBLR is again determined as this parameter reveals the relative amount of improvement or degradation of the BLR in percent. It is determined for the two comparisons as described by Equations (6.32) and (6.33). The subscripts to the individual BLR denote again the origin of the applied ray-traced delays and which parameterization has been used for the VLBI analysis. A positive value reveals the relative amount of improvement of the BLR in the case RADIATE ray-traced delays are applied to the analysis instead of the NASA GSFC ray-traced delays. The δBLR are computed as

$$\delta BLR[\%] = \frac{BLR_{NASA\ GSFC,\ Param.\ 3} - BLR_{RADIATE,\ Param.\ 3}}{BLR_{NASA\ GSFC,\ Param.\ 3}} \cdot 100 \tag{6.32}$$

or as

$$\delta BLR[\%] = \frac{BLR_{NASA\ GSFC,\ Param.\ 4} - BLR_{RADIATE,\ Param.\ 4}}{BLR_{NASA\ GSFC,\ Param.\ 4}} \cdot 100. \tag{6.33}$$

Equal to the comparisons in Section 6.4.3.2, only reliable BLR are introduced to the comparisons in this section. This means that those baselines, which have a weighted and unweighted BLR result of larger than 10 cm in both compared solutions, are excluded.

The four analysis solutions, determined according to Section 6.5.2, are compared pairwise. At first the BLR from the solutions using parameterization 3 and then those using parameterization 4 are compared. The only difference between each compared VLBI analysis solution from the same analysis parameterization is the origin of the applied ray-traced delays, i.e. from RADIATE or from NASA GSFC.

Figure 6.17 compares the results of the BLR of the analysis solutions with applied ray-traced delays from NASA GSFC or from RADIATE using parameterization 3, described in Table 6.7 on page 129. Within the analysis of the solutions tropospheric gradients have been estimated. The absolute BLR results are shown in Figure 6.17a as determined by Equation (6.3). Figure 6.17b presents the ΔBLR as calculated by Equation (6.30) and Figure 6.17c shows the δBLR as determined by Equation (6.32).

The solutions contain 41 stations with a total of 341 different baselines. The ΔBLR, presented in Figure 6.17b, reveal that both solutions deliver BLR, which are quite similar as they mainly

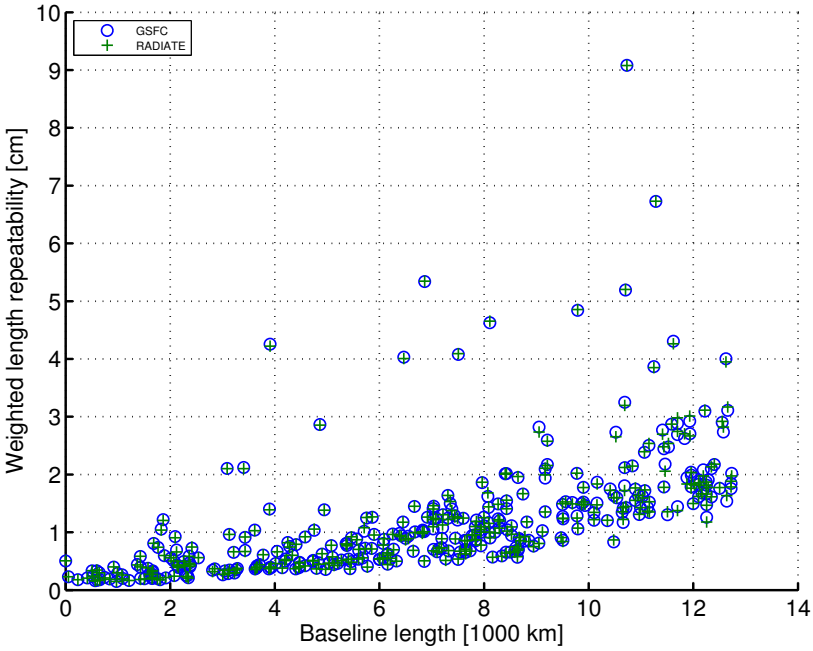

(a) BLR of the analysis solutions from parameterization 3 with applied ray-traced delays from NASA GSFC or from RADIATE.

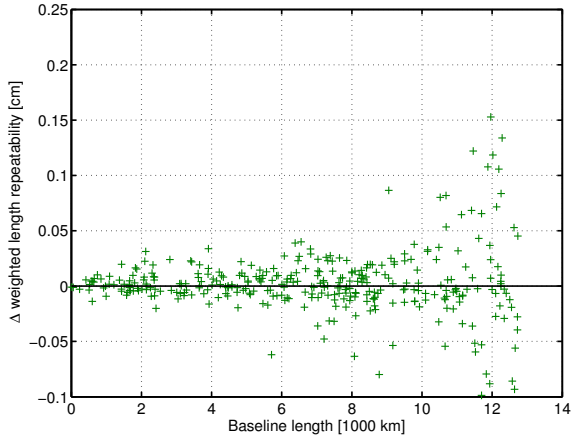

(b) ΔBLR as determined by Equation (6.30) between the results from applied ray-traced delays from NASA GSFC or from RADIATE using parameterization 3. Positive differences indicate that the application of ray-traced delays from RADIATE improves the BLR.

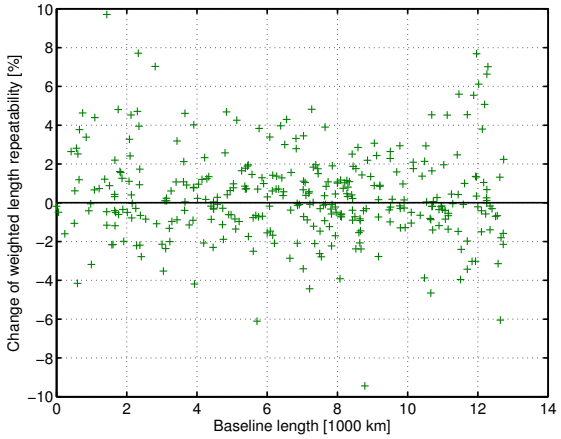

(c) Change of the BLR (δBLR) as determined by Equation (6.32) if ray-traced delays from RADIATE are applied instead of those from NASA GSFC using always the analysis parameterization 3. Positive percentages indicate the relative amount of improvement of the BLR if ray-traced delays from RADIATE are applied instead of those from NASA GSFC.

Figure 6.17: Comparison of the BLR of the analysis solutions with applied ray-traced delays from NASA GSFC or from RADIATE using parameterization 3 as described in Table 6.7 on page 129. Tropospheric gradients have been estimated for both analysis solutions.

differ by only ± 0.5 mm. A few baselines have a ΔBLR of down to -1 mm or up to +1.5 mm.

On average the ΔBLR is 0.0 mm, but looking at the individual baselines, slightly more than half of all baselines have a better BLR by sub-mm difference if the ray-traced delays from program RADIATE are applied to the VLBI analysis. From the 341 baselines 175, i.e. 51.3%, benefit from the application of the RADIATE ray-traced delays. The changes of the BLR (δBLR), shown in Figure 6.17c, indicate that all those baselines, which have a better BLR in case RADIATE ray-traced are applied to the analysis, benefit more from these ray-traced delays than the remaining baselines are degraded, i.e. improved by using the NASA GSFC ray-traced delays. This leads to an average relative improvement of the BLR of 0.3% if RADIATE ray-traced delays are used instead of NASA GSFC ray-traced delays. The maximum relative improvement is 9.7% and the maximum relative degradation is 9.4% when using RADIATE ray-traced delays.

Table 6.18 provides a statistical overview of the results for the ΔBLR and δBLR between the VLBI analysis solutions from parameterization 3, described in Table 6.7 on page 129, with applied ray-traced delays from NASA GSFC or from RADIATE.

Table 6.18: Statistics of the comparison of the BLR from the analysis solutions with applied ray-traced delays from NASA GSFC or from RADIATE using parameterization 3.

	Basel.	Mean	Median	St. dev.	Min.	Max.	Nr. +	Nr. −	% +	% −
ΔBLR		[mm]	[mm]	[mm]	[mm]	[mm]				
δBLR		[%]	[%]	[%]	[%]	[%]				
ΔBLR	341	0.0	0.0	0.3	-1.0	1.5	175	166	51.3	48.7
δBLR	341	0.3	0.1	2.3	-9.4	9.7				

A per-station compilation of the ΔBLR between the analysis solution with applied ray-traced delays from NASA GSFC and the analysis solution with applied ray-traced delays from RADIATE using parameterization 3 can be found in Appendix Section B.6 in Figure B.30 on page 254. The according statistics of the ΔBLR on a per-station basis can be found in Appendix Section A.6 in Table A.10 on page 204.

A per-station compilation of the δBLR is contained in Appendix Section B.6 in Figure B.31 on page 256. The according statistics of the δBLR on a per-station basis can be found in Appendix Section A.6 in Table A.11 on page 206.

A "significant station" denotes in the following a station with a sufficient total number of baselines for which a reliable statement about the impact of the different ray-traced delays can be given. There is no "significant station", whose baselines show that either the ray-traced delays from NASA GSFC or from RADIATE lead to uniform better BLR results. This behaviour can only be seen at the three stations KASHIM34, SYOWA and URUMQI, which have too few baselines as to be "significant". The six "significant stations" BADARY, BR-VLBA, FD-VLBA, NL-VLBA, SC-VLBA and SESHAN25 tend to reveal that they mainly benefit from the application of the ray-traced delays from RADIATE instead of those from NASA GSFC since more than 70% of their baselines benefit from the RADIATE ray-traced delays. Oppositely the four "significant stations" FORTLEZA, HN-VLBA, MATERA and WARK12M seem to benefit more from using NASA GSFC ray-traced delays as

more than 70% of their baselines are then improved. Due to the fact that the ΔBLR are mostly at the sub-mm level, the comparison of the number of positively or negatively influenced baselines may lead to the impression that the difference between the two compared analysis solutions is more drastic than it really is. Therefore also those stations with strong trends of the impact of ray-traced delays from a certain origin have very similar absolute BLR results as they differ mainly at the sub-mm level when using the NASA GSFC or the RADIATE ray-traced delays.

A short side note is made here. Interestingly Eriksson et al. (2014) found that the application of the NASA GSFC ray-traced delays to the VLBI analysis leads to an improvement of 71%[1] or 72%[2] of the baselines in terms of the BLR compared to the a priori use of the VMF1. These results seem to be contradictory to the results presented in this thesis at a first glance. The direct comparison of the performance of the ray-traced delays from RADIATE against the one of the ray-traced delays from NASA GSFC, which has been described above, shows a very similar performance of the different ray-traced delays with a slightly better performance of the RADIATE ray-traced delays in terms of the BLR. In Section 6.4.3.2 the RADIATE ray-traced delays have been applied to the VLBI analysis. In case the tropospheric gradients are estimated within the analysis every 2 hours[3] 55.9% of the baselines are improved in terms of the BLR by using the RADIATE ray-traced delays compared to a priori utilizing the VMF1. At a first glance the different improvement percentages of the analysis by using the RADIATE or the NASA GSFC ray-traced delays compared to the a priori utilization of the VMF1 seem not to fit with the results of the direct comparison if RADIATE or NASA GSFC ray-traced delays are applied to the analysis. The contradiction can be resolved by the fact that Eriksson et al. (2014) estimated the tropospheric gradients within the analysis only every 6 hours instead of every 2 hours. Thus the impact of the ray-traced delays on the analysis is significantly larger as the implicit tropospheric gradient information of the ray-traced delays is more important if there are fewer tropospheric gradient estimates. Also other analysis settings used by Eriksson et al. (2014) are different to those used in this thesis. Furthermore the observation data used by Eriksson et al. (2014) are significantly different compared to the research presented here, which also plays a role for the percentage of the baselines which are improved by the application of ray-traced delays.

The results of the BLR of the analysis solutions with applied ray-traced delays from NASA GSFC or from RADIATE using parameterization 4 are compared in Figure 6.18. The absolute BLR results are shown in Figure 6.18a as determined by Equation (6.3). Figure 6.18b presents the ΔBLR as calculated by Equation (6.31) and Figure 6.18c shows the δBLR as determined by Equation (6.33). The important difference to the last comparison of the solutions using parameterization 3 is that this time no tropospheric gradients have been estimated within the analysis. Thus, the tropospheric gradient information is introduced only implicitly by the applied ray-traced delays. Therefore it can be said that the better this information is introduced,

[1] In case of the analysis of specific VLBI sessions in the time period 2011.0 to 2013.5 (see Eriksson et al. 2014).

[2] In case of the analysis of the CONT11 sessions (see Eriksson et al. 2014).

[3] This is the comparison between the results of the parameterizations 1 and 3. The analysis parameterization details can be found in Section 6.4.2.

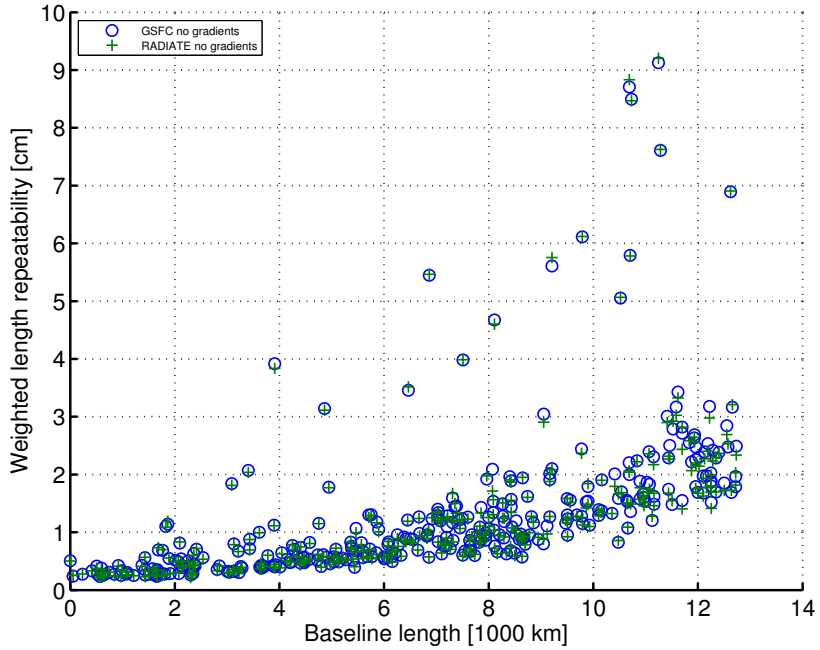

(a) BLR of the analysis solutions from parameterization 4 with applied ray-traced delays from NASA GSFC or from RADIATE.

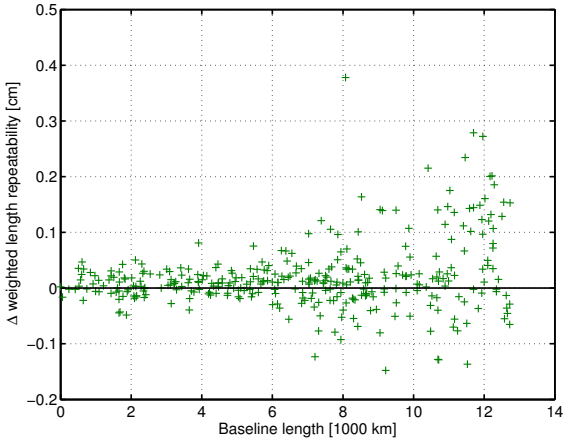

(b) ΔBLR as determined by Equation (6.31) between the results from applied ray-traced delays from NASA GSFC or from RADIATE using parameterization 4. Positive differences indicate that the application of ray-traced delays from RADIATE improves the BLR.

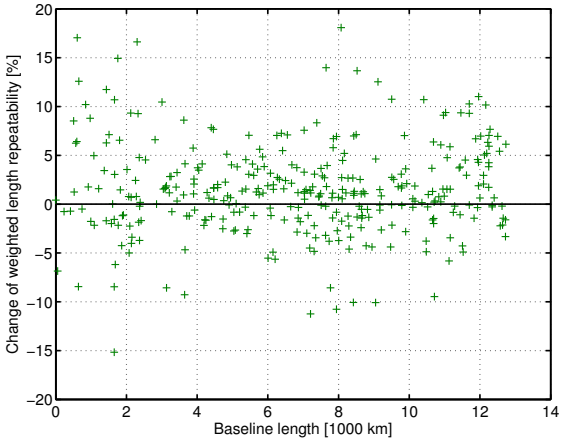

(c) Change of the BLR (δBLR) as determined by Equation (6.33) if ray-traced delays from RADIATE are applied instead of those from NASA GSFC using always the analysis parameterization 4. Positive percentages indicate the relative amount of improvement of the BLR if ray-traced delays from RADIATE are applied instead of those from NASA GSFC.

Figure 6.18: Comparison of the BLR of the analysis solutions with applied ray-traced delays from NASA GSFC or from RADIATE using parameterization 4 as described in Table 6.7 on page 129. Tropospheric gradients have not been estimated for the two analysis solutions.

the better the BLR results will be. The following comparison will reveal if the NASA GSFC or the RADIATE ray-traced delays are performing better in this respect.

Again 41 stations with a total of 341 different baselines[1] are contained in the comparison. Looking at the ΔBLR presented in Figure 6.18b, it is clearly visible that more baselines benefit from the application of the RADIATE ray-traced delays than from the NASA GSFC ray-traced delays. Especially at the shorter baselines on which the tropospheric gradients have a larger impact, the performance of the RADIATE ray-traced delays is better. In general most baselines have ΔBLR of around ± 1 mm, but for some baselines the BLR can be improved by using the RADIATE ray-traced delays by up to around 3 mm. On average the ΔBLR is 0.2 mm. 215 of the 341 baselines, i.e. 63% benefit from the application of the RADIATE ray-traced delays. In terms of the changes of the BLR (δBLR) Figure 6.18c reveals that also in this comparison those baselines, which benefit from applying the RADIATE ray-traced delays, benefit more from their application than the size of which the remaining baselines benefit from applying the NASA GSFC ray-traced delays. The changes in the BLR range from -15.2% to 18.1%. On average there is a relative improvement of the BLR of 1.5% if the RADIATE ray-traced delays are used instead of the NASA GSFC ray-traced delays.

Table 6.19 provides a statistical overview of the results for the ΔBLR and δBLR between the VLBI analysis solutions from parameterization 4, described in Table 6.7 on page 129, with applied ray-traced delays from NASA GSFC or from RADIATE.

Table 6.19: Statistics of the comparison of the BLR from the analysis solutions with applied ray-traced delays from NASA GSFC or from RADIATE using parameterization 4.

	Basel.	Mean	Median	St. dev.	Min.	Max.	Nr. +	Nr. −	% +	% −
ΔBLR		[mm]	[mm]	[mm]	[mm]	[mm]				
δBLR		[%]	[%]	[%]	[%]	[%]				
ΔBLR	341	0.2	0.1	0.6	-1.5	3.8	215	126	63.0	37.0
δBLR	341	1.5	1.2	4.7	-15.2	18.1				

A per-station compilation of the ΔBLR between the analysis solution with applied ray-traced delays from NASA GSFC and the analysis solution with applied ray-traced delays from RADIATE using parameterization 4 can be found in Appendix Section B.6 in Figure B.32 on page 258. The according statistics of the ΔBLR on a per-station basis can be found in Appendix Section A.6 in Table A.12 on page 208.

A per-station compilation of the δBLR is contained in Appendix Section B.6 in Figure B.33 on page 260. The according statistics of the δBLR on a per-station basis can be found in Appendix Section A.6 in Table A.13 on page 210.

Looking at the baseline results on a per-station basis, there are again no "significant stations"[2],

[1] The exactly same baselines are compared as in the previous comparison of the solutions from parameterization 3.

[2] This denotes stations with a sufficient total number of baselines for which a reliable statement about the impact of the different ray-traced delays can be given.

which show a uniform improvement if NASA GSFC or RADIATE ray-traced delays are applied to the analysis. Only the four stations KASHIM34, NOTO, SYOWA and URUMQI show this behaviour, but they have too few baselines in the solutions as to be "significant". Nevertheless ten "significant stations" have better *BLR* for more than 70% of their baselines if ray-traced delays from RADIATE are applied to the analysis instead of those from NASA GSFC. Only station WARK12M benefits at 75% of its baselines if the ray-traced delays from NASA GSFC are used instead of those from RADIATE. In general it is the case that more baselines of the individual stations have a better *BLR* if the ray-traced delays from RADIATE are applied to the VLBI analysis. This indicates that the implicit tropospheric gradient information from the RADIATE ray-traced delays tends to be better than the one from the NASA GSFC ray-traced delays. This is especially visible in terms of the relative improvement of the *BLR* in case the RADIATE ray-traced delays are applied instead of the NASA GSFC ray-traced delays. Please refer to Figure 6.18c or Figure B.33 in Appendix Section B.6 on page 260 for visual representations of this finding.

As final conclusions to the above findings of the comparisons between the analysis results using NASA GSFC or RADIATE ray-traced delays, it can be stated that the ray-traced delays from NASA GSFC and RADIATE deliver similar *BLR* results in case tropospheric gradients are estimated within the analysis. Nevertheless the ray-traced delays from RADIATE show a slightly better performance as more than half of the baselines have a better *BLR* by sub-mm level difference if they are applied to the analysis instead of those from NASA GSFC. Furthermore it seems that the RADIATE ray-traced delays provide a better implicit tropospheric gradient information since significantly more baselines, i.e. in total 63% of all baselines, benefit from their application to the analysis compared to the application of the NASA GSFC ray-traced delays if no tropospheric gradients are estimated within the analysis. Also the average amount of 1.5% relative improvement of the *BLR* by applying the RADIATE ray-traced delays instead of the NASA GSFC ray-traced delays is a substantial indicator of this aspect. In general the performance differences between the ray-traced delays from RADIATE and from NASA GSFC may mainly come from the different utilized NWM and not from the ray-tracing itself.

Chapter 7

Summary, conclusions and outlook

In terms of space geodetic observations the atmosphere plays an important role since it is a major error source, which needs to be treated in order to receive accurate and precise solutions for the investigated parameters. The signal paths as well as the signal propagation speeds are affected. In order to overcome the influences of the atmosphere, so-called path delays need to be considered in the analysis of the observations. For this task different approaches are available. This work has focussed on the application of ray-tracing for the delay determination since the ray-tracing approach stays closest to the true atmospheric conditions that act on the signals due to the direct use of meteorological data for the delay determination without the utilization of beforehand derived values from modelled and estimated zenith delays and mapping functions. As field of application the space geodetic technique of VLBI has been chosen since it is a well-established and important method within geodetic science. Due to the fact that VLBI uses microwave frequency signals the atmospheric influence can be restricted to the neutral atmosphere as the ionospheric effect can be determined very accurately by utilizing the dispersion effect on the signals in the ionosphere. Main targets of this works have been the determination of ray-traced delays and their application to the VLBI analysis in order to improve the analysis results.

7.1 Achieved goals and results of this thesis

Based on the theoretical fundamentals of the atmosphere and of the propagation of microwave frequency range signals in the neutral atmosphere, the concepts of ray-tracing and delay calculation have been depicted in this work in terms of theory as well as in terms of practical approaches. With these theoretical and practical backgrounds a professional ray-tracing program called RADIATE has been developed and tested in MATLAB® in different versions. For the operational application of ray-tracing a Fortran version of program RADIATE has been developed. A closer look on different important parts of the developed ray-tracing program has been taken.

Furthermore research on the best suitable operational ray-tracing strategy, which comprises the optimal compromise of accuracy of the delay results and processing speed, has been carried out. Based on the findings program RADIATE can be set up to deliver fast and accurate ray-

traced delays for VLBI observations. Important aspects for the best suitable operational ray-tracing strategy are the horizontal resolution of the utilized NWM, the used ray-tracing approach as well as the desired inner accuracy of the ray-traced delays. In terms of the horizontal resolution of the NWM, it has been found that for the application of the ray-traced delays to the VLBI analysis, which is the main purpose of this work, it is sufficient to use the lower horizontal resolution of 1° x 1° for the NWM since there is no significant benefit with respect to the analysis results if a higher resolution, e.g. 0.125° x 0.125°, is used, which would only lead to an increase of processing time and memory usage. In terms of direct effects on the ray-traced delays, observations at low elevations benefit from horizontally higher resolved NWM data. A compromise has also to be made with regard to the utilized ray-tracing approach. The 2D PWL approach is not the direct and thus not the strict solution of the Eikonal equation for reconstructing the signal path as different approximations are introduced, but compared to other practical approaches it is a fast-performing algorithm and in case vertically high resolved fields of refractive indices are provided, this method is still accurate enough and therefore suitable for operational ray-tracing at a high performance level. Program RADIATE is set up to reach an inner accuracy of the SHD of at least 0.1 mm at an elevation angle of 3°, which means that, not considering the general accuracy of the utilized ray-tracing approach, the ray path is determined very accurately, i.e. it is defined to reach the outgoing elevation angle from the observation with an accuracy of at least $1 \cdot 10^{-7}$ rad through iterative ray-tracing. This setup ensures that within a specific ray-tracing approach the delays are determined very accurately.

Through a validation of the results from program RADIATE against results of other ray-tracing packages a quality assessment has successfully been carried out. The results of program RADIATE agree very well with those from ray-tracing packages, which used the same NWM data for their calculations. Especially the STD_{mf}, i.e. the STD determined from the mapping factors, show a very good agreement both in terms of the trend across the range of azimuths as well as in terms of the value itself. The individual mean differences of the RADIATE PWL solution to the solutions of the other ray-tracing programs are less than 1 cm with standard deviations below 0.6 cm at station TSUKUB32 and less than 2.4 cm with standard deviations below 1 cm at station WETTZELL, always at an elevation angle of 5°, neglecting the results of those programs which used a different NWM. Thus this assessment shows the good performance of program RADIATE and is a valuable indicator that the program delivers accurate ray-traced delays.

In order to gain a detailed insight into ray-traced delay results from the operational Fortran version of program RADIATE and the needed processing time, delays have been estimated for simulated observations with elevation angles in the interval [0.5°:0.5°:90°] and at azimuths in the interval [0°:10°:360°[. From this test it can be concluded that program RADIATE is a fast-performing application, which is capable of executing the pure iterative ray-tracing and delay calculations of 1000 observations in an average time of only 0.8 seconds in case a wide range of elevation angles is used. The processing time is dependent on the value of the elevation angle since low elevation observations require more processing time. Furthermore the elevation and azimuth dependencies of the ray-traced delays have been presented.

A further step towards an integral validation of the ray-tracing program RADIATE has been made by investigating the performance of the zenith delays determined within the program compared to zenith delays estimated within a common VLBI analysis, which uses only the total pressure data at the station positions in order to a priori determine the zenith hydrostatic delays and which utilizes mapping functions, here the VMF1, in order to estimate the zenith wet delays. For the observational data set of CONT11, i.e. throughout 15 days, the ZTD, ZHD and ZWD have been investigated at the participating stations. This comparison shows that the zenith delays from ray-tracing have a good overall agreement with the values from the VLBI analysis. The ray-traced zenith delays have the advantage that they do not rely on meteorological data provided by the stations. Thus, in case the total pressure at the station is wrong due to problems with the sensor, the ZHD of the analysis, which is a priori determined through the zenith hydrostatic delay from Saastamoinen's equation ZHD^S (see Equation (3.28)), is affected and the ray-traced zenith delay shows a significantly better result as long as the NWM data are correct. In terms of the ZWD the analysis results show a higher variability since the estimation interval has been set to 30 minutes. Therefore not always all short-term effects can be caught by the 6 hourly used NWM data. Also the horizontal resolution may play a role here in terms of not covering local small scale effects. Nevertheless extreme variabilities in the analysis results of the ZWD at the beginning and at the end of individual sessions come from oscillations (Runge's phenomenon), which is only due to numerical solution effects and therefore such affected estimates can not be seen as reliable, i.e. the ray-traced zenith delays should be closer to the truth at such points. The standard deviations of the differences in the different zenith delays determined at the NWM epochs, thus time resolution related issues are not acting on the differences, prove the good overall agreement between the RADIATE zenith delays and those from a common VLBI analysis. The standard deviation of the differences in the ZTD is at almost all stations below 15 mm. The standard deviation of the differences in the ZHD is always below 5 mm and the standard deviation of the differences in the ZWD is at almost all stations below 15 mm.

After the detailed validation of program RADIATE and its ray-traced path delay results, the focus has been set on the application of the ray-traced delays to the VLBI analysis, which is the main target of the presented work. In order to assess the influence on the analysis, the solutions of analyses without and with applied ray-traced delays have been investigated in terms of comparisons of BLR results and TRF solutions. Through the research on different parameterizations, different impact aspects of the ray-traced delays on the analysis have been studied. The observational data used for the investigation comprise observations of 16.5 years from 1999.0 to 2015.5, which is therefore a well-founded basis for reliable comparison results.

In case tropospheric gradients are estimated within the analysis, there is no impact of the applied ray-traced delays on the BLR on average, but nevertheless 55.9% of all baselines benefit from their application at sub-mm level. A mean relative improvement of the BLR compared to the analysis without applying the ray-traced delays of 0.2% is found. The impact of the ray-traced delays on the analysis solution is clearly visible if the tropospheric gradients are not estimated within the analysis. Through the application of the ray-traced delays the missing tropospheric

gradient information is implicitly introduced to the analysis. Therefore the BLR is signficantly improved. 90.6% of all baselines benefit from the application of the ray-traced delays and a mean improvement of the BLR of 1.0 mm is achieved. Compared to the analysis without applying the ray-traced delays a mean relative improvment of the BLR of 9.3% is reached. The results of this comparison are important with respect to two aspects. Firstly, it confirms that the ray-traced delays from program RADIATE are correct. Secondly, the usability of the ray-traced delays is demonstrated as the analysis results are well-improved. A further comparison showed that it is dependent on the baseline if the solely application of ray-traced delays without an estimation of tropospheric gradients within the analysis already leads to the optimal BLR or if the tropospheric gradients need to be estimated additionally.

Looking at the impact of the ray-traced delays on the TRF, it can be stated that in case the tropospheric gradients are estimated within the analysis, the application of ray-traced delays to the analysis does not significantly impact the TRF solution. The transformation parameters show only sub-mm or low μas values and a scale effect of 0.0 ppb or only 0.1 ppb depending on the used set of tie points. The temporal derivatives of the position transformation parameters can be neglected at all. In terms of the station positions, the horizontal displacements are not significant as they are mostly below 1 mm and only 1.1 mm at the maximum. Only with respect to the station heights a slight average uplift tendency is seen. Depending on the tie point set the average uplift varies. In case of the most reliable set of points, i.e. the one using the stations which have a mean coordinate error $\sigma_{XYZ} < 4$ mm in TRF 3, it is 0.7 mm. Thus, in general the frame stays almost the same. In case no tropospheric gradients are estimated within the analysis the impact of the ray-traced delays on the TRF solution is increased. Although the transformation parameters between the solution with and the one without applied ray-traced delays still have very small absolute values, they are slightly larger than in the previous comparison. The temporal derivatives of the position transformation parameters are still too small to be significant, but the translation and rotation parameters display the impact of the application of the ray-traced delays. Nevertheless it can be concluded that the two compared TRF solutions are very similar. The scale parameter is again not significantly affected, having values in the range of ±0.1 ppb depending on the tie point set. In terms of the actual station positions an increased impact of the applied ray-traced delays can be seen. Since the ray-traced delays introduce the missing tropospheric gradient information to the analysis, most of the stations are displaced horizontally by 1 mm or more. Stations on the northern hemisphere are displaced towards the South and stations on the southern hemisphere are displaced towards the North. This is a significant impact of the ray-traced delays as the average horizontal displacement reaches values of 2.6 mm to 3.0 mm depending on the tie point set. Also the effect on the station heights is clearer than in the previous comparison as the average uplift of the stations is 1.1 mm in case only those stations are used, which have a mean coordinate error $\sigma_{XYZ} < 4$ mm in TRF 4. Thus, the effect on the TRF is in general small, but there is an impact on the individual station coordinates. With all the above mentioned results it can be stated that the ray-traced delays from program RADIATE can improve the VLBI analysis.

Another validation of the ray-traced delays from program RADIATE has been carried out: The

performance of the RADIATE ray-traced delays, if applied to the analysis, is compared to the performance of the ray-traced delays from the National Aeronautics and Space Administration Goddard Space Flight Center (NASA GSFC), if these are applied to the analysis. In this comparison the impact of the different ray-traced delays has been assessed in terms of the *BLR*. Again different analysis parameterizations have been used to test the performance of the ray-traced delays from program RADIATE against the one of the ray-traced delays from NASA GSFC. Approximately 15 years of VLBI observations from 2000.0 to 2015.1 have been analysed for this task. The results reveal that in case of an analysis with estimation of tropospheric gradients there is on average no difference in the *BLR* results if either the one or the other ray-tracing solution is applied. Nevertheless 51.3% of the baselines are better at sub-mm level if the ray-traced delays from RADIATE are applied instead of those from NASA GSFC. Furthermore a mean relative improvement of the *BLR* of 0.3% compared to the results from applied NASA GSFC ray-traced delays is seen. In terms of an analysis solution without estimation of tropospheric gradients the difference in the performance between the ray-traced delays from RADIATE and those from NASA GSFC is more evident. 63.0% of all baselines have in this case an improved *BLR* if the ray-traced delays from RADIATE are applied to the analysis instead of those from NASA GSFC. On average this leads to an improvement of 0.2 mm in the *BLR*. A mean relative improvement of the *BLR* of 1.5% is reached if the RADIATE ray-traced delays are applied instead of the NASA GSFC ray-traced delays. From these findings it can be concluded that the RADIATE ray-traced delays provide a better implicit tropospheric gradient information, which is introduced to the analysis. The RADIATE ray-traced delays perform better especially at shorter baselines. This may be due to the fact, that on these the tropospheric gradients have an increased impact. In general the performance differences between the ray-traced delays from RADIATE and from NASA GSFC may mainly come from the different utilized NWM and not from the ray-tracing itself. With the comparison of the performance of the RADIATE ray-traced delays to the one of the NASA GSFC ray-traced delays in case of their application to the analysis, it has been shown that the RADIATE ray-traced delays are correct and have a good performance. Through this validation it has been further indicated that the ray-traced delays from program RADIATE are very accurate and are suitable for the VLBI analysis.

In this thesis an extensive research on tropospheric path delays in the atmosphere for geodetic VLBI determined by means of ray-tracing has been carried out. It has been shown that ray-tracing is a useful approach for providing the essential tropospheric delay information needed for the correction of the VLBI observations in order to derive accurate geodetic target parameters.

With the achievements of this thesis it is possible to derive tropospheric zenith and slant delays for all VLBI observations of the past and also for all future observations. Thus, using the developed ray-tracing program RADIATE tropospheric delays can be determined for every VLBI session since 1979.

7.2 Outlook

Based on the achievements presented within this thesis there are numerous possibilities to further enhance the analysis of VLBI observations or even that of other space geodetic techniques by direct or indirect use of ray-traced delays from the developed program RADIATE.

With program RADIATE it is possible to probe the atmosphere through globally distributed and sky-covering simulated observations. The derived global knowledge of the zenith and slant path delays and of the total pressures, temperatures and water vapour pressures at the station positions can be used to contribute valuable atmospheric information to different space geodetic techniques.

These values derived from ray-tracing can be used to develop new improved mapping functions for tropospheric delay modelling or new tropospheric gradient models, which enable a further improvement of the analysis of space geodetic observations. These are examples of the indirect use of the ray-traced delays. At the research group of Advanced Geodesy at the Department of Geodesy and Geoinformation at the Technische Universität Wien new mapping functions and gradient models have already been developed using ray-traced delays from program RADIATE and further models are currently under development, which are based again on ray-traced delays from program RADIATE.

Besides this indirect application of the ray-traced delays, it is possible to enhance GNSS analysis by using ray-traced delays. Due to the amount of observations it will not be feasible to calculate ray-traced delays for every single observation, but for limited data sets this may be possible. With respect to this target a further increase of the processing speed may be needed. According strategies have been described in Section 5.6. Hence, the application of parallel processing on multiple CPU-cores or the step from a CPU processing to a GPU processing may therefore be needed.

Furthermore the application of ray-traced delays to the observations of the techniques Satellite Laser Ranging (SLR) and Lunar Laser Ranging (LLR) is also possible by adaptation of the signal path and delay calculations according to the requirements and frequency ranges of these techniques.

With respect to the forced upcoming near real-time application of VLBI analysis, which is already state of the art for selected intensive sessions, also the provision of ray-traced delays will be needed in near real-time. In order to conquer this task, the utilization of NWM, which provide forecast data, will be needed as to be able to provide the tropospheric delays in due time for the use within the analysis.

The described outlooks are only a small selection from the wide field of atmospheric ray-tracing applications for which this thesis provides a profound basis.

In the near future the operational Fortran version of program RADIATE will be set up to run on the ECMWF supercomputers for the operational determination of ray-traced tropospheric path delays. Furthermore the determined ray-traced tropospheric delays and provided additional ray-tracing results will be made available for interested institutions and users.

Appendix A

Additional tables

A.1 Structure and implemented subroutines of program RADIATE

In Table A.1 the structure and the implemented subroutines of the operational Fortran version of program RADIATE are presented including a short description of the main task of each subroutine.

Table A.1: Structure and implemented subroutines of program RADIATE. The structure of program RADIATE is presented on the basis of the implemented subroutines of the operational version written in Fortran. Additionally the main task of each subroutine is described.

Program section	*Subroutine*/Task	Nr.
Program start		
	RADIATE_Fortran_start	1
	The entry point of the program. Main settings are defined and user defined settings are recognized. The program is started.	
Main program part		
	RayTrace_main_global	2
	Main program subroutine for the coordination and execution of the workflow starting with data loading across data preparation and processing until the output of the final results.	
Data loading and data preparation		
	import_station_data	3
	Loading of all station data, i.e. names and ellipsoidal coordinates, from a specific station catalogue. These data will be needed for the ray-tracing of the observations at the individual stations.	
	create_session_index_and_epologs_single	4

Table A.1 (continued): Structure and implemented subroutines of program RADIATE.

Program section	*Subroutine*/Task	Nr.
	Loading of all observation data from the input observation data file. Assignment of each observation to one specific, i.e. the closest, epoch of the NWM according to the observation time. Writing of so-called "epolog" text files. Each "epolog" contains the observations assigned to one specific epoch. Furthermore a so-called "session index" text file is written, which contains the names of all "epolog" text files that have been created on the basis of the input observations to the program. This subroutine is used in case there is no need to calculate the ray-traced delays at the exact observation times. See Section 4.2.6 for more information.	
	create_session_index_and_epologs_dual	5
	This subroutine is very similar to the previous one. The important difference is the method of the assignments of the input observations to the epochs of the NWM. Each observation is assigned to two epochs instead of to only one. These are the last epoch of the NWM before the observation time (or the epoch exactly at the observation time) and the first epoch after the observation time. Thus, each observation will be assigned to two "epologs" and the observational data are duplicated. Accordingly "epolog" text files are written. The created "session index" text file contains the names of all produced "epolog" text files. This subroutine is needed in case the ray-traced delays should be calculated at the exact observation times. See Section 4.2.6 for more information.	
	load_session_index	6
	Loading of the file names of all "epolog" text files contained in the "session index" text file. These will be needed for the processing of the respective session for which ray-traced delays will be determined.	
	load_epologs	7
	Loading of the content of a specific "epolog" text file, i.e. loading of the observational data assigned to a specific epoch of the NWM, whose meteorological data will be used to determine ray-traced delays for the observations loaded from the "epolog" text file.	

Table A.1 (continued): Structure and implemented subroutines of program RADIATE.

Program section	*Subroutine*/Task	Nr.
	get_observing_stations Determination of the unique observing station names based on the input of a set of observation data, e.g. from a specific "epolog" text file. Additionally the number of observations per unique station is reported.	8
	get_coord_observing_stations For each observing station, e.g. derived from a specific "epolog" text file, the ellipsoidal coordinates, which are not part of the observation data, are determined using the information from the station catalogue, which has been loaded by subroutine nr. 3 *import_station_data*.	9
Meteorological data loading, processing and vertical interpolation		
	get_meteo_undulation_refr_glob Main calling subroutine for preparing and providing meteorological data needed for the ray-tracing section of the program. Determination of different meteorological parameters mainly needed for the calculation of vertically high resolved refractive index profiles at the global scale, which is the major goal of the subroutine. There are two different versions of this subroutine. One version calls a subroutine that loads the NWM data from a so-called "grib" file, which is a binary file provided by the ECMWF. The second version calls a subroutine that loads the NWM data from a text file, which has been created from the data of the original "grib" file of the ECMWF in a preparation step before the call of program RADIATE.	10
	get_gribdata_gribex Loading of the meteorological parameters geopotential, temperature and humidity, which are provided at discrete total pressure levels on the global scale in a grid with a specific horizontal resolution. The subroutine loads the data from the binary "grib" file provided by the ECMWF using subroutines of the program "gribex" from the ECMWF.	11

Table A.1 (continued): Structure and implemented subroutines of program RADIATE.

Program section	*Subroutine*/Task	Nr.
	get_gribdata_txt	12
	This subroutine is similar to subroutine nr. 11. The only difference is that the meteorological parameters are loaded from a text file that has been created using the original binary "grib" file from the ECMWF. Again geopotential, temperature and humidity, which are provided at discrete total pressure levels on the global scale in a grid with a specific horizontal resolution, are loaded.	
	get_global_undulation	13
	Loading of global geoid undulations from a text file. Determined through the horizontal resolution of the meteorological data the according text file, which provides the geoid undulations in the same horizontal resolution, is loaded.	
	profilewise_refrHD_ECMWFmin	14
	This subroutine vertically interpolates the meteorological parameters in order to increase the vertical resolution. For each horizontal grid point on the global scale a vertical profile of refractive indices is determined. The calculations are done according to the strategy and the equations presented in Section 4.2.2. The vertical interpolation is done using the "profilewise" and thus strict approach as described in Section 4.2.2.1.	
	gridwise_refrHD_ECMWFmin	15
	This subroutine is similar to subroutine nr. 14. The meteorological parameters are vertically interpolated in order to increase the vertical resolution. For each horizontal grid point on the global scale a vertical profile of refractive indices is determined. The calculations are done according to the strategy and the equations presented in Section 4.2.2. The difference to subroutine nr. 14 is due to the utilized "gridwise" vertical interpolation mode, which is described in Section 4.2.2.1.	
	standard_atm	16

Table A.1 (continued): Structure and implemented subroutines of program RADIATE.

Program section	*Subroutine*/Task	Nr.
	Temperature and total pressure are determined at a specific height using the U.S. Standard Atmosphere 1976 (see COESA 1976). The Fortran version of this subroutine has been created using the algorithm of a MATLAB® function developed by Richard Rieber which implements the U.S. Standard Atmosphere 1976 model.	
	gph2horth	17
	Transformation of geopotential heights to orthometric heights using Equation (4.59). The transformation equation uses the gravity as calculated according to Kraus (2001) (see Equation (4.58)).	
	calc_refr_ind_at_stations	18
	This subroutine determines the meteorological parameters at the exact horizontal and vertical positions of individual stations. Temperature, total pressure and water vapour pressure as well as the for the ray-tracing needed total, hydrostatic and wet refractive indices are determined at each station as described in Section 4.2.2.	
Ray-tracing and delay calculation		
	get_RayTrace2D_pwl_global	19
	Implementation of the PWL ray-tracing approach. The details on the approach and the theoretical background used for the implementation are described in Section 4.1.1.	
	get_RayTrace2D_ref_pwl_global	20
	Implementation of the refined PWL ray-tracing approach. The details on the approach and the theoretical background used for the implementation are presented in Section 4.1.2	
	get_RayTrace2D_Thayer_global	21
	Implementation of the Thayer ray-tracing approach. The details on the approach and the theoretical background used for the implementation are presented in Section 4.1.3	

Table A.1 (continued): Structure and implemented subroutines of program RADIATE.

Program section	*Subroutine*/Task	Nr.
	R_earth_euler This subroutine determines the Earth radius by using the Euler radius of curvature. See Section 4.2.3 for more details on the determination of the Earth radius and the calculation of the Euler radius of curvature.	22
	R_earth_gaussian This subroutine determines the Earth radius by using the Gaussian curvature radius. See Section 4.2.3 for more details on the determination of the Earth radius and the calculation of the Gaussian curvature radius. This subroutine was used only in former versions of program RADIATE and has been replaced by subroutine nr. 22 *R_earth_euler*.	23
	determine_lat_lon With this subroutine the latitude and longitude of a specific point along the ray path are determined using the latitude and longitude of the station position, the geocentric angles of the desired point and the station point and the azimuth. A detailed description of the determination can be found in Section 4.2.4.	24
	adapt_lat_lon_to_interval The determination of the latitude and longitude of a ray point with the equations implemented in subroutine nr. 24 can lead to results, which lie outside the allowed intervals of [90°, -90°] in latitude and [0°, 360°[in longitude. Therefore this subroutine checks the resulting latitude and longitude values and adapts them in such a way that they are lying in the allowed intervals.	25
	get_ref_pwl_delay Auxiliary subroutine for the ref. PWL ray-tracing approach. For a single linear segment along the path the refractive indices used for the path determination and those used for the delay determination as well as the slant delay itself are calculated.	26
	get_ref_pwl_delay_zenith	27

Table A.1 (continued): Structure and implemented subroutines of program RADIATE.

Program section	*Subroutine*/Task	Nr.
	Auxiliary subroutine for the ref. PWL ray-tracing approach. For a single linear segment in zenith direction the according refractive indices and utilizing them the zenith total, hydrostatic and wet delays are calculated.	
Time interpolation of the delays		
	combine_and_sort_rd	28
	In this subroutine the observations and the according determined delays from each "epolog", i.e. the observations and the delays calculated at a specific epoch of the NWM, are combined to one data set. Furthermore the observations and the according delays become sorted.	
	time_interpolation	29
	In case a time interpolation shall be done in order to get ray-traced delays at the exact observation times (see Section 4.2.6 for more details), this subroutine identifies those delays, which are valid at different epochs of the NWM, but which belong to the same observation. These delays are the input to subroutine nr. 30 *lagrange_int* for calculating the time interpolated delay. By using the determined Lagrange basis polynomials it is possible to carry out the time interpolation for more than one parameter. In this way e.g. the zenith and slant delays in the total, hydrostatic and wet domains and the meteorological parameters at the station are interpolated.	
	lagrange_int	30
	This subroutine carries out a Lagrange interpolation using the input data. In program RADIATE the Lagrange interpolation is used to do the time interpolation of the delays determined at specific epochs of the NWM in order to get a delay at the exact observation time. See Section 4.2.6 for more details. The subroutine provides also the Lagrange basis polynomials as output in order to interpolate further parameters.	
Creating the output		

Table A.1 (continued): Structure and implemented subroutines of program RADIATE.

Program section	*Subroutine*/Task	Nr.
	create_radiate_global	31
	All final results of the ray-tracing program RADIATE are written to a so-called ".radiate" text file. For each observation, which is reported with all information from the original input, slant and zenith delays in the total, hydrostatic and wet domains are written to the file as determined within the program. Furthermore the geometric bending effect, the total, hydrostatic and wet mapping factors as well as the total pressure, temperature and water vapour pressure at the station derived from the vertically interpolated NWM data are reported. Additionally the elevation angle at the station as well as the outgoing elevation angle, which have been both derived or reconstructed by ray-tracing, are written to the file. The file also contains general information about the settings and input data, which have been used for the processing.	
	get_unique_stations_with_coord	32
	The subroutine determines from the input of the station data of the observations in the session the unique station names with the according ellipsoidal coordinates. Furthermore the total number of observations per observing station is determined and if ray-tracing has been skipped for the station. This subroutine is based on subroutine nr. 8 *get_observing_stations*. The important difference is that the according station coordinates are this time part of the input. Therefore a later coordinate determination with subroutine nr. 9 *get_coord_observing_stations* can be omitted since the coordinates are already assigned to the unique stations in this subroutine.	
	create_trp_global	33

Table A.1 (continued): Structure and implemented subroutines of program RADIATE.

Program section	*Subroutine*/Task	Nr.
	This subroutine creates, unless the program has been set not to do so, an additional output text file called ".trp", which reports only the most important ray-tracing results in a more standardized format, i.e. in accordance to the format by the NASA GSFC. This ".trp" file can be applied directly to the VLBI analysis in case of using the analysis software VieVS since it contains for each observation the slant total delay and the zenith hydrostatic and wet delays converted to seconds as well as the wet mapping factor. Additionally all observing stations of the session are reported with their ellipsoidal and geocentric Cartesian coordinates. The file also contains general information about the settings and input data, which have been used for the processing.	
	ell2xyz	34
	Ellipsoidal coordinates are transformed to geocentric Cartesian coordinates. This is needed for the creation of the ".trp" text file, where the observing stations of the session are written including their ellipsoidal and geocentric Cartesian coordinates.	
	create_errorlog	35

Table A.1 (continued): Structure and implemented subroutines of program RADIATE.

Program section	*Subroutine*/Task	Nr.
	This subroutine creates a so-called ".err" text file, which contains all errors that have occurred within the execution of program RADIATE. The term error used here only addresses such errors, which are not that severe that the program needs to be aborted instantaneously. Reported errors address missing station coordinates or duplicate station data in the catalogue, the need of skipping the ray-tracing for the observations of a specific station and problems with reaching the desired accuracy of the ray-traced path due to exceeding the maximum allowed number of iterations, which is a sign for a non-convergence of the ray-tracing iteration. During the program run occurred errors have been stored in a so-called "errorlog" structure, which contains a number, a type and a description for each error. The ".err" text file is only created if any error has occurred at all and the program option for saving the errors in a file has been set. Besides the individual occurred errors basic information about the processing is additionally written to the ".err" text file. These are the session name, the total number of occurred errors and general information about the settings and input data, which have been used for the processing.	
Auxiliary subroutines used in different/various parts of the program		
	get_elapsed_time	36
	The elapsed time with respect to a specific reference time is determined using the system clock.	
	upper	37
	This subroutine converts all characters of input strings to upper case. The code of the subroutine is taken from http://rosettacode.org/wiki/String_case, Rosetta Code (2014c).	
	mjd2date	38
	Provided modified Julian dates (mjd) are converted to civil date representations reporting year, month, day, hour, minute and second including fractions of a second. The algorithm is based on equations according to Hofmann-Wellenhof et al. (1992).	

Table A.1 (continued): Structure and implemented subroutines of program RADIATE.

Program section	*Subroutine*/Task	Nr.
	date2mjd	39
	Provided civil date representations are converted to modified Julian dates (mjd). The algorithm is based on equations according to Hofmann-Wellenhof et al. (1992).	
	qsort	40
	Subroutine for the sorting of input data, depending on the data type either in ascending or alphabetical order. The sorting is done according to the quicksort algorithm, which is a so-called unstable sorting method, which does not preserve a previous sorting order in case this would be possible, but in turn it is a very fast method. The code of the subroutine is based on code from http://rosettacode.org/wiki/Sorting_algorithms/Quicksort, Rosetta Code (2014b).	
	msort	41
	Subroutine for the sorting of input data, depending on the data type either in ascending or alphabetical order. The sorting is done according to the merge sort algorithm, which is a so-called stable sorting method, which preserves a previous sorting order in case this is possible. The code of the subroutine is based on code from http://rosettacode.org/wiki/Sorting_algorithms/Merge_sort, Rosetta Code (2014a).	
	meshgrid2D	42
	Rectangular grids in two coordinate domains are created on the basis of the input of two coordinate vectors, e.g. a vector with latitude and a vector with longitude values.	
	test_start_values_and_global_coverage	43
	This subroutine tests if a 2D grid is starting at a desired latitude and longitude value and if the grid is providing a global coverage of latitude and longitude nodes according to the grid resolution. This test serves as a check if meteorological data are provided on a global grid with the first node being a specific desired node.	

Table A.1 (continued): Structure and implemented subroutines of program RADIATE.

Program section	*Subroutine*/Task	Nr.
	mean_total2D	44
	From the input of a variable, which can be a scalar, a vector or any array, the scalar mean value of all data entries is calculated. This subroutine is called within subroutine nr. 15 *gridwise_refrHD_ECMWFmin* for the determination of the mean height value of all heights present in a specific NWM total pressure level, i.e. of a 2D grid of different heights. This mean value is needed for the decision of the change of the total pressure levels within the vertical interpolation scheme of the "gridwise" approach. See Section 4.2.2.1 for more details on the "gridwise" vertical interpolation approach.	
	get_bilint_value	45
	This is the main subroutine for the determination of bilinear interpolated values. The bilinear interpolation is used for the horizontal interpolation of parameters, which are available in a gridded form. See Section 4.2.5 for a description of the bilinear interpolation scheme.	
	determine_grid_points	46
	In case the positions, i.e. the indices, of the grid nodes needed for the bilinear interpolation are not known, this subroutine is used to derive them according to the position at which the bilinear interpolation shall be done. See Section 4.2.5 for a description of the bilinear interpolation scheme.	
	bilinear_interpolation	47
	Implementation of the bilinear interpolation method. See Section 4.2.5 for a description.	
	resize_errorlog	48

Table A.1 (continued): Structure and implemented subroutines of program RADIATE.

Program section	*Subroutine*/Task	Nr.
	In case a specific error, which is not a severe error that needs an instant program abortion, occurs within program RADIATE, this subroutine resizes the so-called "errorlog" structure, where all errors are stored, according to the number of new occurred errors. At the end of the program subroutine nr. 35 *create_errorlog* stores the errors in a so-called ".err" text file if the program option for saving the errors has been set.	
Modules for the definition of structures, derived types and global variables in Fortran		
	module_type_definitions	49
	Module for the definition of various structures and derived types, which are needed within program RADIATE in order to structure, facilitate and improve the data assignments and data transfers within or between the individual subroutines.	
	module_date_type_definition	50
	Module for the definition of a structure, which is used to store a civil date as needed e.g. for the calls of the subroutines nr. 38 *mjd2date* and nr. 39 *date2mjd*.	
	module_sort_type_definitions	51
	Module for the definition of a structure, which is used for executing sorting operations with the subroutines nr. 40 *qsort* and nr. 41 *msort*.	
	module_global_var	52
	Module for the definition of global variables, which are needed throughout the program, e.g. information about the elapsed time and auxiliary variables for its determination.	
Modules for the definition of constants		
	module_constants	53

Table A.1 (continued): Structure and implemented subroutines of program RADIATE.

Program section	*Subroutine*/Task	Nr.
	Module for the definition of various constants, which are needed within program RADIATE, e.g. the normal gravity, the reference ellipsoid, conversion factors, programming-related constants, etc.	
	module_meteo_constants	54
	Module for the definition of various meteorological constants, e.g. the universal gas constant and the refractivity coefficients for the microwave frequency range.	

Besides the above described operational Fortran version of program RADIATE also a number of different stand-alone versions have been created in the programming language MATLAB® during the development phase. A short side note on them shall be made here. On the one hand there is a version, in two slightly different realizations[1], which extracts subgrids around the individual observing stations from the global NWM data and uses them for the determination of the ray-traced delays as described in Section 4.2.2.2. On the other hand there are two different versions, again each in two slightly different realizations[2], which use the complete globally provided NWM data for the ray-tracing just like the operational Fortran version. The main difference between the two "global" versions is the method of horizontally interpolating the refractive index during the ray-tracing. As described in Section 4.2.5 the operational Fortran version of program RADIATE and the according MATLAB® development version directly horizontally interpolate the refractive index. The alternative method, which at first horizontally interpolates the total pressure, the water vapour pressure and the temperature and then calculates the refractive index from these values, is implemented in an own standalone MATLAB® version of program RADIATE.

From the previous short descriptions of the stand-alone MATLAB® versions of program RADIATE it follows that sometimes also their implemented functions differ in some parts significantly from those of the operational Fortran version, described in Table A.1, due to the differences of the program versions compared to the operational version. Nevertheless the main structure of all MATLAB® versions is the same as the one of the operational Fortran version and also the main tasks of the implemented functions are equal. Due to programming facilitations in MATLAB® compared to Fortran some Fortran subroutines are not explicitly needed since they are already provided by MATLAB®. However, the utilization of special intrinsic MATLAB® functions has been avoided during the development due to the goal of establishing a Fortran version.

[1] The difference in the realizations is due to the treatment of cases if the ray path crosses the horizontal grid boundary.

[2] See footnote 1.

A.2 Structure and implemented subroutines of the auxiliary program Epochs_RADIATE

In Table A.2 the structure and subroutines of the auxiliary program Epochs_RADIATE, written in Fortran, are described. The main purpose of this program is the determination of the NWM epochs, which are covered by the observations in a specific user-defined session. The epoch information is needed in order to be able to provide the according NWM data later to program RADIATE for the calculation of ray-traced delays for the specific session using a certain time interpolation mode (see Section 4.2.6). Within program Epochs_RADIATE different modi for the epoch determination are available. All modi have in common that they deliver the dates of the 6 hourly epochs of the ECMWF NWM data. Depending on the chosen mode only the according to the observations and chosen time interpolation mode really needed epochs are determined or all epochs, starting with the last epoch before the first observation until the first epoch after the last observation, are reported.

Table A.2: Structure and implemented subroutines of the auxiliary program Epochs_RADIATE. The structure of the program is presented on the basis of the implemented subroutines written in Fortran. Additionally the main task of each subroutine is described.

Program section	*Subroutine*/Task	Nr.
Program start		
	Epochs_RADIATE	1
	The entry point of the auxiliary program. Main settings are defined and user defined settings, i.e. the file name of the observation data and the optional setting of the epoch determination mode, are recognized. The program is started. The 6 hourly epochs of the ECMWF NWM are determined according to the chosen or the default mode and written to a text file.	
Determination of the epochs		
	epochs6h_one_epoch_per_obs	2

Table A.2 (continued): Structure and implemented subroutines of the auxiliary program Epochs_RADIATE.

Program section	*Subroutine*/Task	Nr.
	This subroutine is used in case only those 6 hourly epochs of the ECMWF NWM shall be determined, which are needed if no time interpolation of the ray-traced delays will be done in the later call of program RADIATE, i.e. ray-traced delays will then be determined in such a way that they are valid at the time of the epoch closest to the true observation time. Therefore only those epochs are reported by this subroutine which are closest to at least one of the input observations and each observation is assigned to only one epoch. See Section 4.2.6 for more details on the time dependency of the ray-traced delays from program RADIATE.	
	epochs6h_two_epochs_per_obs	3
	This subroutine is used in case only those 6 hourly epochs of the ECMWF NWM shall be determined, which are needed if a time interpolation of the ray-traced delays will be done in the later call of program RADIATE, i.e. ray-traced delays will then be determined in such a way that they are valid at the exact observation time. Therefore those epochs are reported by this subroutine to which at least one of the input observations is assigned and each observation is assigned to two epochs, the last epoch before and the first epoch after the observation time. The last epoch before the observation time can also be exactly at the observation time if the epoch time coincides with the observation time. See Section 4.2.6 for more details on the time dependency of the ray-traced delays from program RADIATE.	
	epochs6h_complete	4
	This subroutine is the default case for the determination of the 6 hourly epochs of the ECMWF NWM in program Epochs_RADIATE. The subroutine determines all epochs covered by the time span of the input observations, starting with the last epoch before the first observation until the first epoch after the last observation.	
Auxiliary subroutine		
	mjd2date	5

Table A.2 (continued): Structure and implemented subroutines of the auxiliary program Epochs_RADIATE.

Program section	*Subroutine*/Task	Nr.
	This subroutine is the same as subroutine nr. 38 *mjd2date* of program RADIATE described in Table A.1 in Appendix Section A.1.	
Module for the definition of a structure, i.e. a derived type, in Fortran		
	module_date_type_definition	6
	This module is the same as subroutine nr. 50 *module_date_type_definition* of program RADIATE described in Table A.1 in Appendix Section A.1.	
Module for the definition of constants		
	module_epochs_constants	7
	Module for the definition of different constants needed within program Epochs_RADIATE.	

A.3 IVS CONT11 stations

Table A.3 contains general information on all observing stations in the IVS CONT11 campaign.

Table A.3: Stations of the IVS CONT11 campaign (IVS 2015).

Name	Code	Observatory name and location
BADARY	Bd	Badary Radio Astronomical Observatory, Russia
FORTLEZA	Ft	Space Radio Observatory of the Northeast (ROEN), Fortaleza, Brazil
HARTRAO	Hh	Hartebeesthoek Radio Astronomy Observatory, South Africa
HOBART12	Hb	Mt. Pleasant Radio Astronomy Observatory, Hobart, Tasmania, Australia
KOKEE	Kk	Kokee Park Geophysical Observatory, Kauai, Hawaii, USA
NYALES20	Ny	Ny Ålesund Geodetic Observatory, Spitsbergen, Norway
ONSALA60	On	Onsala Space Observatory, Sweden
TIGOCONC	Tc	Transportable Integrated Geodetic Observatory (TIGO), Concepción, Chile
TSUKUB32	Ts	Tsukuba VLBI Station, Japan
WARK12M	Ww	Warkworth VLBI Station, New Zealand
WESTFORD	Wf	Westford Antenna, Haystack Observatory, Massachusetts, USA
WETTZELL	Wz	Fundamentalstation Wettzell, Germany
YEBES40M	Ys	Astronomical Center at Yebes, Spain
ZELENCHK	Zc	Radioastronomical Observatory Zelenchukskaya, Russia

A.4 Additional tables of the impact of the ray-traced delays on the baseline length repeatability from VLBI analysis of the years 1999.0 to 2015.5

The upcoming tables provide statistical overviews of the ΔBLR or δBLR results of Section 6.4.3.2 from the comparisons of analysis solutions using different parameterizations. The statistics are determined separately for all baselines of a specific station, which delivers an insight into the ΔBLR or δBLR on a per-station basis. The ΔBLR are determined from Equation (6.5) or (6.6) and the δBLR are determined from Equation (6.7) or (6.8) as described in Section 6.4.3.2. The use of the equations depends on the used VLBI analysis results from the parameterizations 1 to 4, described in Section 6.4.2 on page 126 or more detailed in Table 6.7 on page 129.

Table A.4: Per-station statistics of the ΔBLR, determined using Equation (6.5), from the comparison of the BLR results from the parameterizations 1 and 3. Positive ΔBLR indicate that the application of the ray-traced delays improves the BLR. The description of the parameterizations is given in Section 6.4.2 on page 126 and more detailed in Table 6.7 on page 129. Tropospheric gradients have been estimated for both analysis solutions.

ΔBLR	Basel.	Mean [mm]	Median [mm]	St. dev. [mm]	Min. [mm]	Max. [mm]	Nr. +	Nr. −	% +	% −
AIRA	1	-0.3	-0.3	0.0	-0.3	-0.3	0	1	0.0	100.0
ALGOPARK	14	0.1	0.0	0.2	-0.1	0.7	8	6	57.1	42.9
BADARY	18	0.0	0.0	0.2	-0.3	0.4	10	8	55.6	44.4
BR-VLBA	17	0.1	0.0	0.2	-0.1	0.5	11	6	64.7	35.3
CRIMEA	5	0.0	0.0	0.1	-0.1	0.1	3	2	60.0	40.0
FD-VLBA	17	0.0	0.0	0.1	-0.1	0.5	11	6	64.7	35.3
FORTLEZA	26	0.0	-0.0	0.2	-0.6	0.5	13	13	50.0	50.0
GILCREEK	15	0.1	-0.0	0.3	-0.3	1.0	7	8	46.7	53.3
HART15M	15	-0.1	0.0	0.3	-0.7	0.2	9	6	60.0	40.0
HARTRAO	30	0.2	0.1	0.3	-0.3	0.8	19	11	63.3	36.7
HN-VLBA	17	-0.0	-0.0	0.1	-0.3	0.1	7	10	41.2	58.8
HOBART12	18	-0.1	-0.1	0.2	-0.6	0.2	7	11	38.9	61.1
HOBART26	19	0.2	0.1	0.3	-0.2	1.0	12	7	63.2	36.8
KASHIM34	2	-0.3	-0.3	0.2	-0.4	-0.1	0	2	0.0	100.0
KATH12M	18	0.1	-0.0	0.2	-0.2	0.7	8	10	44.4	55.6
KOKEE	39	0.0	0.0	0.2	-0.4	0.7	23	16	59.0	41.0
KP-VLBA	17	0.0	0.0	0.1	-0.1	0.3	9	8	52.9	47.1

Table A.4 (continued): Per-station statistics of the ΔBLR, determined using Equation (6.5), from the comparison of the BLR results from the parameterizations 1 and 3. Positive ΔBLR indicate that the application of the ray-traced delays improves the BLR.

ΔBLR	Basel.	Mean [mm]	Median [mm]	St. dev. [mm]	Min. [mm]	Max. [mm]	Nr. +	Nr. −	% +	% −
LA-VLBA	17	0.1	0.1	0.1	-0.0	0.5	12	5	70.6	29.4
MATERA	22	0.0	0.0	0.1	-0.3	0.4	12	10	54.5	45.5
MEDICINA	27	-0.0	0.0	0.2	-0.7	0.3	15	12	55.6	44.4
METSAHOV	3	0.0	0.1	0.1	-0.1	0.1	2	1	66.7	33.3
MK-VLBA	17	0.0	0.0	0.1	-0.1	0.3	11	6	64.7	35.3
NL-VLBA	17	0.0	0.0	0.1	-0.2	0.5	13	4	76.5	23.5
NOTO	4	-0.1	-0.1	0.0	-0.1	-0.0	0	4	0.0	100.0
NRAO20	5	-0.1	-0.1	0.1	-0.2	0.0	2	3	40.0	60.0
NYALES20	38	-0.0	0.0	0.1	-0.4	0.3	21	17	55.3	44.7
OHIGGINS	6	0.3	0.3	0.2	0.0	0.5	6	0	100.0	0.0
ONSALA60	34	-0.0	-0.0	0.2	-0.7	0.4	12	22	35.3	64.7
OV-VLBA	17	0.0	0.0	0.1	-0.1	0.5	10	7	58.8	41.2
PIETOWN	17	0.1	0.0	0.2	-0.1	0.6	11	6	64.7	35.3
SC-VLBA	17	0.1	0.1	0.2	-0.0	0.8	16	1	94.1	5.9
SESHAN25	11	0.1	0.1	0.2	-0.1	0.7	9	2	81.8	18.2
SVETLOE	17	0.0	0.0	0.1	-0.3	0.3	11	6	64.7	35.3
SYOWA	3	0.3	0.3	0.2	0.1	0.5	3	0	100.0	0.0
TIGOCONC	22	0.0	0.1	0.3	-0.7	0.7	13	9	59.1	40.9
TSUKUB32	32	-0.0	-0.0	0.3	-0.7	0.7	13	19	40.6	59.4
URUMQI	2	-0.0	-0.0	0.1	-0.1	0.1	1	1	50.0	50.0
WARK12M	9	-0.1	-0.1	0.3	-0.4	0.4	3	6	33.3	66.7
WESTFORD	32	0.1	0.1	0.2	-0.4	0.5	28	4	87.5	12.5
WETTZELL	38	-0.0	-0.0	0.1	-0.3	0.4	13	25	34.2	65.8
YARRA12M	16	-0.3	-0.3	0.3	-0.8	0.1	3	13	18.8	81.3
YEBES40M	17	0.0	0.0	0.3	-0.8	0.7	10	7	58.8	41.2
YLOW7296	2	0.0	0.0	0.1	-0.0	0.1	1	1	50.0	50.0
ZELENCHK	18	0.0	0.0	0.2	-0.6	0.5	10	8	55.6	44.4

Table A.5: Per-station statistics of the δBLR, determined using Equation (6.7), from the comparison of the BLR results from the parameterizations 1 and 3. Positive δBLR indicate the relative amount of improvement of the BLR if ray-traced delays are applied compared to not applying them. The description of the parameterizations is given in Section 6.4.2 on page 126 and more detailed in Table 6.7 on page 129. Tropospheric gradients have been estimated for both analysis solutions.

δBLR	Basel.	Mean [%]	Median [%]	St. dev. [%]	Min. [%]	Max. [%]	Nr. +	Nr. −	% +	% −
AIRA	1	-2.3	-2.3	0.0	-2.3	-2.3	0	1	0.0	100.0
ALGOPARK	14	0.7	0.3	1.8	-1.6	6.1	8	6	57.1	42.9
BADARY	18	0.1	0.2	1.6	-2.2	4.3	10	8	55.6	44.4
BR-VLBA	17	1.0	0.6	1.9	-1.7	4.5	11	6	64.7	35.3
CRIMEA	5	-0.1	0.2	1.3	-2.1	1.1	3	2	60.0	40.0
FD-VLBA	17	0.7	0.6	1.4	-1.5	3.6	11	6	64.7	35.3
FORTLEZA	26	-0.0	-0.0	0.9	-2.0	2.0	13	13	50.0	50.0
GILCREEK	15	0.7	-0.0	2.6	-3.7	5.9	7	8	46.7	53.3
HART15M	15	-0.4	0.1	1.9	-5.0	2.2	9	6	60.0	40.0
HARTRAO	30	0.8	0.4	1.6	-1.8	4.7	19	11	63.3	36.7
HN-VLBA	17	-0.7	-0.2	1.9	-4.7	1.8	7	10	41.2	58.8
HOBART12	18	-0.6	-0.6	1.2	-2.3	1.6	7	11	38.9	61.1
HOBART26	19	0.8	0.8	1.7	-1.9	4.5	12	7	63.2	36.8
KASHIM34	2	-2.4	-2.4	2.6	-4.2	-0.6	0	2	0.0	100.0
KATH12M	18	0.3	-0.3	1.8	-2.1	4.8	8	10	44.4	55.6
KOKEE	39	0.1	0.2	1.5	-4.2	4.8	23	16	59.0	41.0
KP-VLBA	17	0.5	0.4	1.8	-2.3	4.2	9	8	52.9	47.1
LA-VLBA	17	2.1	2.8	2.0	-0.8	4.8	12	5	70.6	29.4
MATERA	22	0.1	0.2	1.1	-1.9	2.5	12	10	54.5	45.5
MEDICINA	27	0.0	0.0	2.5	-7.6	4.5	15	12	55.6	44.4
METSAHOV	3	0.3	0.9	2.1	-2.0	1.9	2	1	66.7	33.3
MK-VLBA	17	0.4	0.6	1.1	-2.3	2.8	11	6	64.7	35.3
NL-VLBA	17	1.0	1.0	1.7	-2.2	3.5	13	4	76.5	23.5
NOTO	4	-1.4	-1.1	1.0	-2.7	-0.5	0	4	0.0	100.0
NRAO20	5	-1.0	-0.6	1.6	-3.7	0.3	2	3	40.0	60.0
NYALES20	38	-0.0	0.1	1.0	-2.0	1.9	21	17	55.3	44.7

Table A.5 (continued): Per-station statistics of the δBLR, determined using Equation (6.7), from the comparison of the BLR results from the parameterizations 1 and 3. Positive δBLR indicate the relative amount of improvement of the BLR if ray-traced delays are applied compared to not applying them.

δBLR	Basel.	Mean [%]	Median [%]	St. dev. [%]	Min. [%]	Max. [%]	Nr. +	Nr. −	% +	% −
OHIGGINS	6	0.6	0.7	0.3	0.2	0.9	6	0	100.0	0.0
ONSALA60	34	-0.3	-0.7	2.1	-7.1	3.4	12	22	35.3	64.7
OV-VLBA	17	0.9	0.7	1.8	-1.8	4.7	10	7	58.8	41.2
PIETOWN	17	0.8	0.5	1.4	-1.9	3.5	11	6	64.7	35.3
SC-VLBA	17	1.7	1.7	1.3	-0.0	4.7	16	1	94.1	5.9
SESHAN25	11	0.9	0.8	1.3	-1.0	3.4	9	2	81.8	18.2
SVETLOE	17	0.2	0.3	1.6	-4.6	3.0	11	6	64.7	35.3
SYOWA	3	0.9	0.8	0.5	0.3	1.4	3	0	100.0	0.0
TIGOCONC	22	-0.2	0.3	1.4	-5.0	1.9	13	9	59.1	40.9
TSUKUB32	32	-0.3	-0.3	2.6	-7.6	6.1	13	19	40.6	59.4
URUMQI	2	-0.1	-0.1	0.4	-0.4	0.2	1	1	50.0	50.0
WARK12M	9	-0.4	-0.6	1.3	-2.2	1.6	3	6	33.3	66.7
WESTFORD	32	1.3	1.2	1.7	-3.1	4.3	28	4	87.5	12.5
WETTZELL	38	-0.4	-0.4	1.4	-4.0	3.6	13	25	34.2	65.8
YARRA12M	16	-2.2	-2.0	2.1	-7.1	0.5	3	13	18.8	81.3
YEBES40M	17	0.2	0.3	2.0	-5.6	4.8	10	7	58.8	41.2
YLOW7296	2	0.5	0.5	0.9	-0.1	1.1	1	1	50.0	50.0
ZELENCHK	18	0.2	0.3	1.2	-2.3	3.3	10	8	55.6	44.4

Table A.6: Per-station statistics of the ΔBLR, determined using Equation (6.6), from the comparison of the BLR results from the parameterizations 2 and 4. Positive ΔBLR indicate that the application of the ray-traced delays improves the BLR. The description of the parameterizations is given in Section 6.4.2 on page 126 and more detailed in Table 6.7 on page 129. Tropospheric gradients have not been estimated for the two analysis solutions.

ΔBLR	Basel.	Mean [mm]	Median [mm]	St. dev. [mm]	Min. [mm]	Max. [mm]	Nr. +	Nr. −	% +	% −
AIRA	1	2.0	2.0	0.0	2.0	2.0	1	0	100.0	0.0
ALGOPARK	14	1.2	0.7	1.1	0.4	3.4	14	0	100.0	0.0
BADARY	18	0.6	0.4	0.6	-0.4	1.8	15	3	83.3	16.7
BR-VLBA	17	1.1	1.0	0.6	0.3	2.6	17	0	100.0	0.0
CRIMEA	5	0.5	0.5	0.2	0.3	0.7	5	0	100.0	0.0
FD-VLBA	17	0.9	0.7	0.7	0.0	2.8	17	0	100.0	0.0
FORTLEZA	26	1.1	0.9	0.8	0.1	3.1	26	0	100.0	0.0
GILCREEK	15	1.3	0.9	1.2	-0.0	4.7	14	1	93.3	6.7
HART15M	15	0.9	0.9	0.5	0.1	2.3	15	0	100.0	0.0
HARTRAO	30	1.5	1.5	1.3	-1.4	5.6	27	3	90.0	10.0
HN-VLBA	17	0.5	0.3	0.6	-0.2	2.2	15	2	88.2	11.8
HOBART12	18	1.2	1.1	0.8	-0.0	2.5	17	1	94.4	5.6
HOBART26	19	1.8	1.6	1.6	-0.4	4.7	17	2	89.5	10.5
KASHIM34	2	1.7	1.7	1.7	0.5	2.8	2	0	100.0	0.0
KATH12M	18	1.4	2.0	1.3	-1.4	3.1	14	4	77.8	22.2
KOKEE	39	0.9	0.7	1.0	-1.5	3.8	33	6	84.6	15.4
KP-VLBA	17	0.6	0.5	0.4	-0.0	1.5	16	1	94.1	5.9
LA-VLBA	17	0.5	0.4	0.4	-0.1	1.3	15	2	88.2	11.8
MATERA	22	1.1	0.9	1.3	-2.4	5.1	21	1	95.5	4.5
MEDICINA	27	1.0	0.9	0.8	-0.1	3.5	26	1	96.3	3.7
METSAHOV	3	0.5	0.4	0.2	0.3	0.7	3	0	100.0	0.0
MK-VLBA	17	0.8	0.5	0.8	-0.6	2.7	16	1	94.1	5.9
NL-VLBA	17	1.3	1.2	0.8	0.2	3.5	17	0	100.0	0.0
NOTO	4	0.3	0.4	0.1	0.3	0.4	4	0	100.0	0.0
NRAO20	5	0.4	0.4	0.4	-0.1	1.0	3	2	60.0	40.0
NYALES20	38	0.7	0.5	0.9	-1.8	4.3	32	6	84.2	15.8
OHIGGINS	6	-0.1	-0.2	0.9	-1.5	1.4	2	4	33.3	66.7

Table A.6 (continued): Per-station statistics of the ΔBLR, determined using Equation (6.6), from the comparison of the BLR results from the parameterizations 2 and 4. Positive ΔBLR indicate that the application of the ray-traced delays improves the BLR.

ΔBLR	Basel.	Mean [mm]	Median [mm]	St. dev. [mm]	Min. [mm]	Max. [mm]	Nr. +	Nr. −	% +	% −
ONSALA60	34	0.9	1.0	0.8	-2.1	2.7	32	2	94.1	5.9
OV-VLBA	17	0.8	0.7	0.5	0.1	2.2	17	0	100.0	0.0
PIETOWN	17	0.6	0.5	0.4	-0.1	1.3	16	1	94.1	5.9
SC-VLBA	17	1.0	0.7	1.3	-0.1	5.6	16	1	94.1	5.9
SESHAN25	11	2.5	1.9	1.8	0.3	6.5	11	0	100.0	0.0
SVETLOE	17	0.8	0.6	0.8	-0.0	3.1	16	1	94.1	5.9
SYOWA	3	-0.1	-0.2	0.4	-0.5	0.4	1	2	33.3	66.7
TIGOCONC	22	2.5	2.2	1.5	-0.2	6.5	21	1	95.5	4.5
TSUKUB32	32	1.3	1.2	1.1	-0.6	4.3	29	3	90.6	9.4
URUMQI	2	1.6	1.6	2.4	-0.2	3.3	1	1	50.0	50.0
WARK12M	9	-0.4	0.0	1.1	-2.4	0.9	5	4	55.6	44.4
WESTFORD	32	1.3	1.0	1.0	0.0	4.1	32	0	100.0	0.0
WETTZELL	38	1.1	1.0	0.7	-0.1	3.6	37	1	97.4	2.6
YARRA12M	16	0.4	0.6	1.2	-2.4	1.9	12	4	75.0	25.0
YEBES40M	17	0.4	0.4	1.2	-2.4	2.5	11	6	64.7	35.3
YLOW7296	2	0.5	0.5	0.1	0.4	0.6	2	0	100.0	0.0
ZELENCHK	18	0.7	0.6	0.7	-0.4	2.3	15	3	83.3	16.7

Table A.7: Per-station statistics of the δBLR, determined using Equation (6.8), from the comparison of the BLR results from the parameterizations 2 and 4. Positive δBLR indicate the relative amount of improvement of the BLR if ray-traced delays are applied compared to not applying them. The description of the parameterizations is given in Section 6.4.2 on page 126 and more detailed in Table 6.7 on page 129. Tropospheric gradients have not been estimated for the two analysis solutions.

δBLR	Basel.	Mean [%]	Median [%]	St. dev. [%]	Min. [%]	Max. [%]	Nr. +	Nr. −	% +	% −
AIRA	1	15.4	15.4	0.0	15.4	15.4	1	0	100.0	0.0
ALGOPARK	14	11.5	8.7	6.7	4.3	25.1	14	0	100.0	0.0
BADARY	18	4.9	4.8	4.6	-2.9	16.1	15	3	83.3	16.7
BR-VLBA	17	19.3	19.4	10.1	5.7	42.8	17	0	100.0	0.0
CRIMEA	5	5.4	4.4	2.4	2.6	8.5	5	0	100.0	0.0
FD-VLBA	17	14.4	12.4	8.8	0.7	34.3	17	0	100.0	0.0
FORTLEZA	26	5.5	5.2	2.8	1.1	11.3	26	0	100.0	0.0
GILCREEK	15	12.6	11.8	6.3	-0.7	21.2	14	1	93.3	6.7
HART15M	15	7.0	6.2	3.8	1.0	14.9	15	0	100.0	0.0
HARTRAO	30	8.0	8.4	6.5	-7.9	21.7	27	3	90.0	10.0
HN-VLBA	17	8.3	7.0	8.0	-2.7	31.9	15	2	88.2	11.8
HOBART12	18	5.8	5.5	3.3	-0.0	12.6	17	1	94.4	5.6
HOBART26	19	8.7	8.2	7.6	-2.6	24.9	17	2	89.5	10.5
KASHIM34	2	8.9	8.9	7.4	3.7	14.2	2	0	100.0	0.0
KATH12M	18	8.0	10.2	7.2	-5.2	16.5	14	4	77.8	22.2
KOKEE	39	6.5	6.9	5.2	-3.7	18.5	33	6	84.6	15.4
KP-VLBA	17	11.1	10.5	7.8	-0.4	27.0	16	1	94.1	5.9
LA-VLBA	17	9.3	7.6	8.3	-4.3	27.8	15	2	88.2	11.8
MATERA	22	10.3	8.9	9.2	-14.6	34.2	21	1	95.5	4.5
MEDICINA	27	12.1	10.8	9.1	-1.1	38.7	26	1	96.3	3.7
METSAHOV	3	9.4	7.3	8.1	2.6	18.4	3	0	100.0	0.0
MK-VLBA	17	9.6	9.6	7.7	-10.2	24.9	16	1	94.1	5.9
NL-VLBA	17	20.9	18.8	10.0	7.6	42.8	17	0	100.0	0.0
NOTO	4	6.6	6.5	2.3	4.3	9.2	4	0	100.0	0.0
NRAO20	5	3.9	3.1	5.8	-1.1	13.1	3	2	60.0	40.0
NYALES20	38	6.4	5.5	6.0	-8.1	20.3	32	6	84.2	15.8

Table A.7 (continued): Per-station statistics of the δBLR, determined using Equation (6.8), from the comparison of the BLR results from the parameterizations 2 and 4. Positive δBLR indicate the relative amount of improvement of the BLR if ray-traced delays are applied compared to not applying them.

δBLR	Basel.	Mean [%]	Median [%]	St. dev. [%]	Min. [%]	Max. [%]	Nr. +	Nr. −	% +	% −
OHIGGINS	6	-0.0	-0.7	2.0	-1.7	3.6	2	4	33.3	66.7
ONSALA60	34	10.7	10.5	8.6	-21.0	29.1	32	2	94.1	5.9
OV-VLBA	17	13.5	11.4	7.8	3.6	28.6	17	0	100.0	0.0
PIETOWN	17	12.3	11.0	9.7	-4.3	34.3	16	1	94.1	5.9
SC-VLBA	17	10.5	10.7	6.9	-0.5	21.7	16	1	94.1	5.9
SESHAN25	11	13.8	10.9	9.0	2.2	34.2	11	0	100.0	0.0
SVETLOE	17	9.5	8.6	7.5	-0.0	29.1	16	1	94.1	5.9
SYOWA	3	-0.3	-0.5	1.3	-1.5	1.1	1	2	33.3	66.7
TIGOCONC	22	7.1	5.9	4.9	-1.2	17.0	21	1	95.5	4.5
TSUKUB32	32	10.0	9.4	8.0	-10.2	24.9	29	3	90.6	9.4
URUMQI	2	4.0	4.0	6.3	-0.5	8.5	1	1	50.0	50.0
WARK12M	9	-2.0	0.1	6.1	-14.6	5.0	5	4	55.6	44.4
WESTFORD	32	12.9	13.7	6.0	0.7	25.1	32	0	100.0	0.0
WETTZELL	38	12.4	12.0	6.6	-1.1	33.4	37	1	97.4	2.6
YARRA12M	16	1.7	2.5	9.1	-21.0	12.5	12	4	75.0	25.0
YEBES40M	17	4.4	4.6	8.9	-16.0	20.5	11	6	64.7	35.3
YLOW7296	2	5.7	5.7	0.4	5.4	6.0	2	0	100.0	0.0
ZELENCHK	18	5.4	5.4	4.4	-2.5	14.4	15	3	83.3	16.7

A.5 Additional tables of the impact of the ray-traced delays on the TRF from VLBI analysis of the years 1999.0 to 2015.5

The upcoming tables belong to the comparisons in Section 6.4.3.5 and provide the coordinate differences ΔN, ΔE, ΔU and ΔP between two different TRF solutions including the formal errors of the coordinate differences $\sigma_{\Delta N}$, $\sigma_{\Delta E}$, $\sigma_{\Delta U}$ and $\sigma_{\Delta P}$ for each station contained in the TRF solutions. The coordinate differences are determined from Equation (6.10) or (6.11) with subsequent estimation of Equations (6.12) to (6.14). The formal errors are determined according to Equations (6.15) to (6.18). All equations are described in Section 6.4.3.4. The nomenclature of the TRF solutions and thereby also their differences are explained in Table 6.12 on page 139.

Table A.8: Coordinate differences ΔN, ΔE, ΔU and ΔP and the according formal errors $\sigma_{\Delta N}$, $\sigma_{\Delta E}$, $\sigma_{\Delta U}$ and $\sigma_{\Delta P}$ of the comparison TRF 3 - TRF 1 for all stations in the TRF solutions. The differences at each station are calculated according to Equations (6.10) and (6.12) to (6.14). The formal errors are calculated according to Equations (6.15) to (6.18). Reference epoch of the TRF solutions is 2000.0.

Difference:	TRF 3 - TRF 1							
Units are [mm]	ΔN	$\sigma_{\Delta N}$	ΔE	$\sigma_{\Delta E}$	ΔU	$\sigma_{\Delta U}$	ΔP	$\sigma_{\Delta P}$
ALGOPARK	-0.0	0.3	-0.1	0.3	0.8	0.9	0.1	0.3
BADARY	-0.1	1.1	0.0	1.1	0.8	3.5	0.1	1.1
BR-VLBA	0.1	0.3	-0.2	0.3	1.0	0.8	0.2	0.3
CRIMEA	0.2	1.8	0.1	1.6	1.1	7.3	0.2	1.7
DSS15	-0.1	1.4	-0.3	1.3	1.8	4.0	0.3	1.4
DSS45	0.2	3.0	0.1	2.9	-0.9	5.9	0.2	3.0
DSS65	0.1	1.0	-0.1	0.9	0.9	3.3	0.1	1.0
FD-VLBA	0.0	0.4	-0.1	0.4	1.0	0.8	0.1	0.4
FORTLEZA	-0.3	0.5	0.0	0.4	-0.9	1.0	0.3	0.4
GGAO7108	-0.1	2.1	-0.1	2.3	0.1	8.3	0.2	2.2
GILCREEK	-0.0	0.3	-0.1	0.3	0.7	0.8	0.1	0.3
HART15M	-0.5	1.1	0.1	0.9	0.5	2.6	0.5	1.0
HARTRAO	-0.4	0.6	0.0	0.5	1.0	1.4	0.4	0.6
HN-VLBA	0.1	0.3	-0.1	0.4	0.5	1.0	0.1	0.3
HOBART12	-0.0	0.9	0.4	0.8	-0.2	2.4	0.4	0.8
HOBART26	-0.1	0.7	0.4	0.6	1.0	1.8	0.5	0.7
KASHIM11	0.5	2.3	-0.3	2.2	3.6	6.9	0.6	2.3
KASHIM34	0.4	1.4	-0.3	1.4	1.2	4.2	0.5	1.4

Table A.8 (continued): Coordinate differences and the according formal errors of the comparison TRF 3 - TRF 1 for all stations in the TRF solutions. Reference epoch of the TRF solutions is 2000.0.

Difference:	TRF 3 - TRF 1							
Units are [mm]	ΔN	$\sigma_{\Delta N}$	ΔE	$\sigma_{\Delta E}$	ΔU	$\sigma_{\Delta U}$	ΔP	$\sigma_{\Delta P}$
KATH12M	-0.4	3.2	0.8	2.8	2.5	8.3	0.9	3.0
KOKEE	-0.2	0.4	-0.3	0.4	-0.5	0.6	0.4	0.4
KP-VLBA	0.0	0.4	-0.2	0.4	1.7	0.8	0.2	0.4
LA-VLBA	0.0	0.4	-0.1	0.4	1.8	0.8	0.1	0.4
MATERA	0.2	0.2	-0.1	0.2	0.0	0.6	0.3	0.2
MEDICINA	-0.0	0.3	-0.0	0.3	-0.4	0.8	0.0	0.3
METSAHOV	-0.0	1.8	0.1	1.7	1.7	6.9	0.1	1.8
MK-VLBA	0.2	0.5	-0.2	0.5	0.5	1.1	0.3	0.5
NL-VLBA	0.1	0.3	-0.1	0.4	0.7	0.9	0.1	0.3
NOTO	0.0	0.6	0.0	0.7	-1.5	2.3	0.0	0.7
NYALES20	0.0	0.2	0.0	0.2	0.3	0.4	0.0	0.2
ONSALA60	0.0	0.2	-0.0	0.2	0.3	0.6	0.1	0.2
OV-VLBA	0.0	0.4	-0.2	0.4	1.1	0.9	0.2	0.4
PIETOWN	0.0	0.4	-0.1	0.4	1.8	0.8	0.1	0.4
SC-VLBA	0.3	0.5	0.0	0.5	0.1	1.3	0.3	0.5
SESHAN25	0.2	0.5	0.1	0.5	-0.4	1.4	0.2	0.5
SVETLOE	0.1	0.4	0.1	0.4	1.4	1.3	0.2	0.4
TIGOCONC	-1.0	1.5	0.0	1.2	-1.0	3.4	1.0	1.4
TSUKUB32	0.0	0.4	-0.1	0.4	-0.7	0.8	0.1	0.4
URUMQI	-0.1	1.2	-0.1	1.3	3.1	3.3	0.1	1.2
WARK12M	0.7	7.2	0.4	6.7	2.4	22.7	0.8	6.9
WESTFORD	0.0	0.2	-0.0	0.2	0.5	0.5	0.0	0.2
WETTZELL	0.1	0.2	-0.0	0.2	0.5	0.4	0.1	0.2
YARRA12M	-0.6	3.8	1.0	3.5	14.8	11.1	1.1	3.7
YEBES	-0.0	1.1	-0.2	1.0	0.4	4.3	0.2	1.1
YEBES40M	-0.1	1.3	-0.5	1.3	1.7	4.2	0.5	1.3
YLOW7296	-0.1	1.4	-0.1	1.2	0.9	4.2	0.1	1.3
ZELENCHK	-0.1	0.6	0.2	0.6	0.9	2.4	0.2	0.6

Table A.9: Coordinate differences ΔN, ΔE, ΔU and ΔP and the according formal errors $\sigma_{\Delta N}$, $\sigma_{\Delta E}$, $\sigma_{\Delta U}$ and $\sigma_{\Delta P}$ of the comparison TRF 4 - TRF 2 for all stations in the TRF solutions. The differences at each station are calculated according to Equations (6.11) and (6.12) to (6.14). The formal errors are calculated according to Equations (6.15) to (6.18). Reference epoch of the TRF solutions is 2000.0.

Difference:	TRF 4 - TRF 2							
Units are [mm]	ΔN	$\sigma_{\Delta N}$	ΔE	$\sigma_{\Delta E}$	ΔU	$\sigma_{\Delta U}$	ΔP	$\sigma_{\Delta P}$
ALGOPARK	-0.9	0.2	-0.3	0.3	1.1	0.9	0.9	0.2
BADARY	-2.1	0.8	0.1	0.8	-3.4	3.5	2.1	0.8
BR-VLBA	-1.0	0.3	-1.1	0.3	0.6	0.8	1.5	0.3
CRIMEA	-0.7	1.2	0.7	1.1	1.7	6.7	1.0	1.2
DSS15	0.1	1.1	0.8	1.1	2.6	4.0	0.8	1.1
DSS45	3.6	2.6	1.7	2.4	2.3	5.9	4.0	2.5
DSS65	-0.6	0.8	1.0	0.7	3.7	3.3	1.2	0.8
FD-VLBA	-0.8	0.3	-0.2	0.3	2.2	0.8	0.9	0.3
FORTLEZA	3.5	0.4	-0.5	0.3	1.3	0.9	3.5	0.4
GGAO7108	-1.0	1.8	-1.1	1.7	2.2	7.9	1.5	1.7
GILCREEK	-1.4	0.2	0.5	0.3	1.9	0.7	1.4	0.3
HART15M	4.5	0.8	-1.4	0.7	-0.2	2.3	4.7	0.7
HARTRAO	4.6	0.4	-1.3	0.4	0.9	1.3	4.8	0.4
HN-VLBA	-1.2	0.3	-0.6	0.3	0.3	1.0	1.3	0.3
HOBART12	7.0	0.7	1.3	0.6	-1.5	2.3	7.1	0.7
HOBART26	7.2	0.6	1.3	0.5	-0.3	1.6	7.3	0.5
KASHIM11	-4.6	1.9	-1.8	1.8	7.0	6.9	4.9	1.9
KASHIM34	-4.5	1.2	-1.4	1.1	1.9	4.2	4.7	1.2
KATH12M	11.3	2.6	4.0	2.3	8.9	7.9	12.0	2.5
KOKEE	-0.7	0.3	0.1	0.3	-1.0	0.5	0.7	0.3
KP-VLBA	-0.7	0.3	0.4	0.3	2.0	0.8	0.8	0.3
LA-VLBA	-0.4	0.3	0.4	0.3	2.6	0.8	0.6	0.3
MATERA	-0.1	0.2	-0.8	0.2	-0.2	0.6	0.8	0.2
MEDICINA	-0.4	0.2	-0.0	0.2	-0.2	0.7	0.4	0.2
METSAHOV	-1.4	1.4	0.7	1.4	5.5	6.4	1.6	1.4
MK-VLBA	0.2	0.4	-0.2	0.4	-0.3	1.0	0.3	0.4

Table A.9 (continued): Coordinate differences and the according formal errors of the comparison TRF 4 - TRF 2 for all stations in the TRF solutions. Reference epoch of the TRF solutions is 2000.0.

Difference:	TRF 4 - TRF 2							
Units are [mm]	ΔN	$\sigma_{\Delta N}$	ΔE	$\sigma_{\Delta E}$	ΔU	$\sigma_{\Delta U}$	ΔP	$\sigma_{\Delta P}$
NL-VLBA	-1.6	0.3	-0.9	0.3	3.9	0.8	1.9	0.3
NOTO	-0.2	0.5	-0.4	0.6	1.4	2.2	0.5	0.5
NYALES20	-0.4	0.2	0.1	0.2	-3.5	0.4	0.4	0.2
ONSALA60	-2.3	0.2	0.8	0.2	-0.5	0.6	2.5	0.2
OV-VLBA	-0.0	0.3	-0.1	0.3	1.6	0.8	0.1	0.3
PIETOWN	-0.6	0.3	0.3	0.3	2.1	0.8	0.7	0.3
SC-VLBA	0.8	0.4	-0.7	0.4	-1.7	1.0	1.0	0.4
SESHAN25	-4.4	0.4	1.3	0.4	-1.1	1.3	4.5	0.4
SVETLOE	-2.9	0.3	0.7	0.3	-0.4	1.3	3.0	0.3
TIGOCONC	10.7	1.2	0.2	0.9	-3.6	3.1	10.7	1.1
TSUKUB32	-3.8	0.4	-1.2	0.3	-3.9	0.8	4.0	0.4
URUMQI	-5.7	1.0	1.0	1.0	3.0	3.2	5.8	1.0
WARK12M	-5.1	5.7	-13.5	5.7	18.9	21.3	14.5	5.7
WESTFORD	-1.1	0.2	-0.6	0.2	-0.5	0.5	1.2	0.2
WETTZELL	-1.3	0.1	0.6	0.1	-0.2	0.4	1.5	0.1
YARRA12M	6.0	3.1	3.5	2.9	3.1	10.0	7.0	3.0
YEBES	0.7	0.9	0.9	0.8	4.9	4.3	1.1	0.8
YEBES40M	2.9	1.1	-0.6	1.1	3.6	3.9	3.0	1.1
YLOW7296	-2.8	1.0	-2.3	1.0	1.5	4.2	3.6	1.0
ZELENCHK	-1.0	0.4	0.3	0.4	1.5	2.3	1.1	0.4

A.6 Additional tables of the comparison of VLBI analysis results from using RADIATE or NASA GSFC ray-traced delays for the years 2000.0 to 2015.1

The upcoming tables provide statistical overviews of the ΔBLR or δBLR results of Section 6.5.3.2 from the comparison of VLBI analysis results from using RADIATE or NASA GSFC ray-traced delays. The statistical values are determined separately for all baselines of a specific station, which delivers an insight into the ΔBLR or δBLR on a per-station basis.

The ΔBLR are determined from Equation (6.30) or (6.31) and the δBLR are determined from Equation (6.32) or (6.33), which are all described in Section 6.5.3.2. The use of the equations depends on the used parameterization for determining the VLBI analysis results, which is parameterization 3 for the first comparison and parameterization 4 for the second comparison. They are described in Section 6.4.2 in Table 6.7 on page 129.

Table A.10: Per-station statistics of the ΔBLR, determined using Equation (6.30), between the analysis solution with applied ray-traced delays from NASA GSFC and the analysis solution with applied ray-traced delays from RADIATE using parameterization 3. Positive ΔBLR indicate that the application of the RADIATE ray-traced delays improves the BLR. The description of the parameterization is given in Section 6.4.2 in Table 6.7 on page 129. Tropospheric gradients have been estimated for both analysis solutions.

ΔBLR	Basel.	Mean [mm]	Median [mm]	St. dev. [mm]	Min. [mm]	Max. [mm]	Nr. +	Nr. −	% +	% −
ALGOPARK	12	0.0	0.0	0.1	-0.1	0.3	6	6	50.0	50.0
BADARY	17	0.1	0.1	0.2	-0.3	0.5	12	5	70.6	29.4
BR-VLBA	15	0.1	0.0	0.3	-0.1	1.1	12	3	80.0	20.0
CRIMEA	5	0.1	0.1	0.1	-0.0	0.2	3	2	60.0	40.0
FD-VLBA	16	0.1	0.0	0.3	-0.1	1.1	14	2	87.5	12.5
FORTLEZA	24	-0.2	-0.1	0.3	-1.0	0.2	6	18	25.0	75.0
GILCREEK	13	0.0	0.0	0.1	-0.1	0.3	7	6	53.8	46.2
HART15M	13	-0.0	-0.0	0.3	-0.5	0.3	6	7	46.2	53.8
HARTRAO	28	0.3	0.0	0.6	-0.5	1.5	14	14	50.0	50.0
HN-VLBA	16	0.0	-0.0	0.2	-0.2	0.8	4	12	25.0	75.0
HOBART12	18	-0.1	-0.1	0.3	-1.0	0.2	6	12	33.3	66.7
HOBART26	18	0.0	0.0	0.3	-0.6	0.8	10	8	55.6	44.4
KASHIM34	2	-0.6	-0.6	0.0	-0.6	-0.6	0	2	0.0	100.0
KATH12M	16	0.1	0.2	0.2	-0.2	0.7	11	5	68.8	31.3
KOKEE	37	0.0	-0.0	0.2	-0.6	0.9	18	19	48.6	51.4

Table A.10 (continued): Per-station statistics of the ΔBLR, determined using Equation (6.30), between the analysis solution with applied ray-traced delays from NASA GSFC and the analysis solution with applied ray-traced delays from RADIATE using parameterization 3. Positive ΔBLR indicate that the application of the RADIATE ray-traced delays improves the BLR.

ΔBLR	Basel.	Mean [mm]	Median [mm]	St. dev. [mm]	Min. [mm]	Max. [mm]	Nr. +	Nr. −	% +	% −
KP-VLBA	16	0.1	0.1	0.2	-0.1	0.7	11	5	68.8	31.3
LA-VLBA	16	0.1	0.0	0.4	-0.1	1.5	9	7	56.3	43.8
MATERA	21	-0.0	-0.0	0.1	-0.3	0.3	5	16	23.8	76.2
MEDICINA	15	-0.0	-0.0	0.3	-0.8	0.8	6	9	40.0	60.0
METSAHOV	3	0.1	0.2	0.2	-0.0	0.3	2	1	66.7	33.3
MK-VLBA	16	-0.0	-0.0	0.2	-0.3	0.5	6	10	37.5	62.5
NL-VLBA	15	0.1	0.1	0.3	-0.1	1.2	13	2	86.7	13.3
NOTO	3	-0.0	-0.0	0.1	-0.1	0.1	1	2	33.3	66.7
NYALES20	37	0.1	0.1	0.2	-0.8	0.4	22	15	59.5	40.5
OHIGGINS	6	0.1	0.0	0.2	-0.1	0.3	4	2	66.7	33.3
ONSALA60	28	0.0	-0.0	0.2	-0.2	0.8	9	19	32.1	67.9
OV-VLBA	15	0.1	0.0	0.4	-0.2	1.3	10	5	66.7	33.3
PIETOWN	16	0.1	0.0	0.3	-0.1	1.2	11	5	68.8	31.3
SC-VLBA	14	0.1	0.1	0.2	-0.1	0.6	10	4	71.4	28.6
SESHAN25	11	0.1	0.1	0.3	-0.6	0.3	8	3	72.7	27.3
SVETLOE	17	0.1	0.0	0.2	-0.1	0.7	11	6	64.7	35.3
SYOWA	2	0.4	0.4	0.1	0.3	0.4	2	0	100.0	0.0
TIGOCONC	22	0.1	0.0	0.3	-0.6	0.8	12	10	54.5	45.5
TSUKUB32	32	0.0	-0.0	0.2	-0.8	0.6	14	18	43.8	56.3
URUMQI	2	0.5	0.5	0.5	0.1	0.9	2	0	100.0	0.0
WARK12M	8	-0.3	-0.2	0.4	-0.9	0.3	2	6	25.0	75.0
WESTFORD	32	-0.1	-0.0	0.2	-0.9	0.3	16	16	50.0	50.0
WETTZELL	36	-0.0	-0.0	0.2	-0.9	0.3	15	21	41.7	58.3
YARRA12M	15	-0.2	-0.1	0.4	-0.9	0.5	5	10	33.3	66.7
YEBES40M	16	-0.0	-0.0	0.2	-0.5	0.7	6	10	37.5	62.5
ZELENCHK	18	0.0	-0.0	0.2	-0.4	0.4	9	9	50.0	50.0

Table A.11: Per-station statistics of the δBLR, determined using Equation (6.32), between the analysis solution with applied ray-traced delays from NASA GSFC and the analysis solution with applied ray-traced delays from RADIATE using parameterization 3. Positive δBLR indicate the relative amount of improvement of the BLR if RADIATE ray-traced delays are applied instead of NASA GSFC ray-traced delays. The description of the parameterization is given in Section 6.4.2 in Table 6.7 on page 129. Tropospheric gradients have been estimated for both analysis solutions.

δBLR	Basel.	Mean [%]	Median [%]	St. dev. [%]	Min. [%]	Max. [%]	Nr. +	Nr. −	% +	% −
ALGOPARK	12	0.2	0.2	1.0	-1.7	2.4	6	6	50.0	50.0
BADARY	17	0.6	1.0	1.4	-2.4	3.4	12	5	70.6	29.4
BR-VLBA	15	1.7	1.1	2.3	-2.0	5.1	12	3	80.0	20.0
CRIMEA	5	0.7	0.8	1.3	-0.6	2.4	3	2	60.0	40.0
FD-VLBA	16	1.9	1.9	2.1	-2.4	5.5	14	2	87.5	12.5
FORTLEZA	24	-0.7	-0.4	1.3	-3.4	1.0	6	18	25.0	75.0
GILCREEK	13	0.8	0.3	1.9	-2.1	4.8	7	6	53.8	46.2
HART15M	13	-0.3	-0.1	2.4	-4.7	3.5	6	7	46.2	53.8
HARTRAO	28	1.4	0.3	3.1	-2.8	7.7	14	14	50.0	50.0
HN-VLBA	16	-0.6	-0.9	1.8	-2.5	4.5	4	12	25.0	75.0
HOBART12	18	-0.8	-0.7	1.2	-3.4	0.8	6	12	33.3	66.7
HOBART26	18	0.5	0.2	2.1	-3.9	6.6	10	8	55.6	44.4
KASHIM34	2	-5.0	-5.0	1.5	-6.1	-3.9	0	2	0.0	100.0
KATH12M	16	1.1	1.2	1.8	-1.9	4.5	11	5	68.8	31.3
KOKEE	37	-0.1	-0.2	1.5	-6.1	3.1	18	19	48.6	51.4
KP-VLBA	16	2.1	3.1	2.4	-2.1	4.7	11	5	68.8	31.3
LA-VLBA	16	1.6	0.6	3.8	-3.5	9.7	9	7	56.3	43.8
MATERA	21	-0.5	-0.3	1.9	-4.2	3.5	5	16	23.8	76.2
MEDICINA	15	-0.4	-0.5	3.2	-9.4	4.8	6	9	40.0	60.0
METSAHOV	3	1.5	1.3	2.9	-1.2	4.5	2	1	66.7	33.3
MK-VLBA	16	-0.3	-0.4	2.1	-3.9	4.3	6	10	37.5	62.5
NL-VLBA	15	2.5	1.4	3.2	-2.1	9.7	13	2	86.7	13.3
NOTO	3	-0.4	-0.1	1.7	-2.2	1.2	1	2	33.3	66.7
NYALES20	37	0.7	0.4	1.8	-3.0	4.5	22	15	59.5	40.5
OHIGGINS	6	0.2	0.1	0.4	-0.3	0.8	4	2	66.7	33.3
ONSALA60	28	0.1	-0.3	1.9	-2.5	6.6	9	19	32.1	67.9

Table A.11 (continued): Per-station statistics of the δBLR, determined using Equation (6.32), between the analysis solution with applied ray-traced delays from NASA GSFC and the analysis solution with applied ray-traced delays from RADIATE using parameterization 3. Positive δBLR indicate the relative amount of improvement of the BLR if RADIATE ray-traced delays are applied instead of NASA GSFC ray-traced delays.

δBLR	Basel.	Mean [%]	Median [%]	St. dev. [%]	Min. [%]	Max. [%]	Nr. +	Nr. −	% +	% −
OV-VLBA	15	1.5	0.9	3.2	-4.2	7.7	10	5	66.7	33.3
PIETOWN	16	1.3	0.9	2.1	-2.0	6.1	11	5	68.8	31.3
SC-VLBA	14	1.6	1.5	2.7	-2.3	7.0	10	4	71.4	28.6
SESHAN25	11	0.9	1.1	1.6	-1.8	3.9	8	3	72.7	27.3
SVETLOE	17	0.4	0.4	1.1	-2.2	2.5	11	6	64.7	35.3
SYOWA	2	0.9	0.9	0.1	0.8	1.0	2	0	100.0	0.0
TIGOCONC	22	0.3	0.2	1.1	-1.8	2.9	12	10	54.5	45.5
TSUKUB32	32	-0.0	-0.3	2.5	-9.4	4.5	14	18	43.8	56.3
URUMQI	2	1.7	1.7	1.9	0.4	3.1	2	0	100.0	0.0
WARK12M	8	-1.3	-2.1	2.0	-3.1	2.1	2	6	25.0	75.0
WESTFORD	32	-0.3	-0.0	2.6	-6.1	7.0	16	16	50.0	50.0
WETTZELL	36	-0.4	-0.3	1.5	-3.9	2.5	15	21	41.7	58.3
YARRA12M	15	-1.1	-0.8	2.3	-6.1	1.6	5	10	33.3	66.7
YEBES40M	16	-0.3	-0.2	1.9	-4.0	4.5	6	10	37.5	62.5
ZELENCHK	18	0.2	-0.0	1.3	-2.1	2.9	9	9	50.0	50.0

Table A.12: Per-station statistics of the ΔBLR, determined using Equation (6.31), between the analysis solution with applied ray-traced delays from NASA GSFC and the analysis solution with applied ray-traced delays from RADIATE using parameterization 4. Positive ΔBLR indicate that the application of the RADIATE ray-traced delays improves the BLR. The description of the parameterization is given in Section 6.4.2 in Table 6.7 on page 129. Tropospheric gradients have not been estimated for the two analysis solutions.

ΔBLR	Basel.	Mean [mm]	Median [mm]	St. dev. [mm]	Min. [mm]	Max. [mm]	Nr. +	Nr. −	% +	% −
ALGOPARK	12	0.4	0.1	0.5	-0.2	1.5	10	2	83.3	16.7
BADARY	17	0.2	0.1	0.5	-0.5	1.4	11	6	64.7	35.3
BR-VLBA	15	0.2	0.2	0.4	-0.2	1.3	11	4	73.3	26.7
CRIMEA	5	-0.2	-0.2	0.2	-0.5	0.1	1	4	20.0	80.0
FD-VLBA	16	-0.0	-0.0	0.6	-0.9	1.5	7	9	43.8	56.3
FORTLEZA	24	0.5	0.2	0.9	-1.4	2.8	18	6	75.0	25.0
GILCREEK	13	0.1	0.1	0.3	-0.1	1.1	8	5	61.5	38.5
HART15M	13	0.4	0.1	0.7	-0.8	1.6	9	4	69.2	30.8
HARTRAO	28	0.6	0.2	0.9	-0.7	2.7	20	8	71.4	28.6
HN-VLBA	16	0.1	0.0	0.4	-0.5	1.4	10	6	62.5	37.5
HOBART12	18	0.1	0.0	0.6	-1.5	1.3	9	9	50.0	50.0
HOBART26	18	0.6	0.3	1.1	-0.5	3.8	14	4	77.8	22.2
KASHIM34	2	2.1	2.1	2.3	0.5	3.8	2	0	100.0	0.0
KATH12M	16	0.8	0.9	0.8	-0.8	2.2	15	1	93.8	6.3
KOKEE	37	0.1	0.1	0.4	-0.8	1.4	22	15	59.5	40.5
KP-VLBA	16	0.2	0.0	0.3	-0.2	1.2	8	8	50.0	50.0
LA-VLBA	16	0.4	0.3	0.7	-0.2	2.7	11	5	68.8	31.3
MATERA	21	0.0	0.1	0.3	-1.3	0.5	14	7	66.7	33.3
MEDICINA	15	-0.0	-0.1	0.2	-0.4	0.6	5	10	33.3	66.7
METSAHOV	3	0.1	0.2	0.5	-0.5	0.5	2	1	66.7	33.3
MK-VLBA	16	0.2	0.2	0.4	-0.4	1.5	13	3	81.3	18.8
NL-VLBA	15	0.2	0.1	0.7	-0.4	2.3	9	6	60.0	40.0
NOTO	3	0.1	0.1	0.1	0.0	0.2	3	0	100.0	0.0
NYALES20	37	0.2	0.1	0.5	-0.4	2.2	25	12	67.6	32.4
OHIGGINS	6	0.1	0.1	0.5	-0.6	0.8	3	3	50.0	50.0
ONSALA60	28	0.2	0.1	0.5	-0.9	1.6	18	10	64.3	35.7

Table A.12 (continued): Per-station statistics of the ΔBLR, determined using Equation (6.31), between the analysis solution with applied ray-traced delays from NASA GSFC and the analysis solution with applied ray-traced delays from RADIATE using parameterization 4. Positive ΔBLR indicate that the application of the RADIATE ray-traced delays improves the BLR.

ΔBLR	Basel.	Mean [mm]	Median [mm]	St. dev. [mm]	Min. [mm]	Max. [mm]	Nr. +	Nr. −	% +	% −
OV-VLBA	15	0.3	0.2	0.5	-0.1	1.9	12	3	80.0	20.0
PIETOWN	16	0.2	0.1	0.4	-0.2	1.6	12	4	75.0	25.0
SC-VLBA	14	0.0	0.1	0.3	-0.7	0.4	9	5	64.3	35.7
SESHAN25	11	0.2	0.1	0.8	-0.8	2.0	7	4	63.6	36.4
SVETLOE	17	0.3	0.2	0.4	-0.2	1.2	13	4	76.5	23.5
SYOWA	2	0.9	0.9	0.1	0.8	1.0	2	0	100.0	0.0
TIGOCONC	22	0.2	0.1	0.7	-1.5	1.4	14	8	63.6	36.4
TSUKUB32	32	0.0	0.0	0.5	-1.2	1.4	16	16	50.0	50.0
URUMQI	2	0.8	0.8	0.8	0.3	1.4	2	0	100.0	0.0
WARK12M	8	-0.4	-0.2	0.5	-1.4	0.3	2	6	25.0	75.0
WESTFORD	32	0.1	-0.0	0.5	-0.8	2.0	16	16	50.0	50.0
WETTZELL	36	0.0	0.0	0.4	-0.7	1.8	19	17	52.8	47.2
YARRA12M	15	-0.2	-0.0	0.7	-1.3	0.9	6	9	40.0	60.0
YEBES40M	16	0.2	0.1	0.6	-0.6	1.4	10	6	62.5	37.5
ZELENCHK	18	0.1	0.1	0.5	-0.8	1.4	12	6	66.7	33.3

Table A.13: Per-station statistics of the δBLR, determined using Equation (6.33), between the analysis solution with applied ray-traced delays from NASA GSFC and the analysis solution with applied ray-traced delays from RADIATE using parameterization 4. Positive δBLR indicate the relative amount of improvement of the BLR if RADIATE ray-traced delays are applied instead of NASA GSFC ray-traced delays. The description of the parameterization is given in Section 6.4.2 in Table 6.7 on page 129. Trop. gradients have not been estimated for the two analysis solutions.

δBLR	Basel.	Mean [%]	Median [%]	St. dev. [%]	Min. [%]	Max. [%]	Nr. +	Nr. −	% +	% −
ALGOPARK	12	2.5	1.5	5.2	-8.4	12.5	10	2	83.3	16.7
BADARY	17	1.1	1.2	3.1	-4.6	8.3	11	6	64.7	35.3
BR-VLBA	15	4.3	4.1	5.8	-3.8	16.6	11	4	73.3	26.7
CRIMEA	5	-2.8	-2.2	2.7	-6.2	1.1	1	4	20.0	80.0
FD-VLBA	16	-0.6	-1.2	7.9	-10.8	17.0	7	9	43.8	56.3
FORTLEZA	24	2.3	1.3	3.5	-4.9	10.3	18	6	75.0	25.0
GILCREEK	13	0.9	0.6	2.8	-2.6	7.0	8	5	61.5	38.5
HART15M	13	3.1	1.1	5.4	-4.9	13.7	9	4	69.2	30.8
HARTRAO	28	2.6	1.3	4.1	-3.4	11.0	20	8	71.4	28.6
HN-VLBA	16	1.4	0.9	5.0	-6.9	10.5	10	6	62.5	37.5
HOBART12	18	0.9	0.1	2.7	-2.6	6.9	9	9	50.0	50.0
HOBART26	18	3.2	2.7	4.9	-2.8	18.1	14	4	77.8	22.2
KASHIM34	2	10.8	10.8	10.2	3.6	18.1	2	0	100.0	0.0
KATH12M	16	5.6	6.1	4.1	-0.8	10.8	15	1	93.8	6.3
KOKEE	37	0.7	0.6	2.8	-4.8	8.5	22	15	59.5	40.5
KP-VLBA	16	2.2	0.7	5.2	-5.0	12.6	8	8	50.0	50.0
LA-VLBA	16	5.9	6.2	6.6	-3.2	17.0	11	5	68.8	31.3
MATERA	21	0.6	1.1	3.0	-9.5	6.4	14	7	66.7	33.3
MEDICINA	15	-0.8	-1.2	3.1	-4.9	6.4	5	10	33.3	66.7
METSAHOV	3	3.8	6.3	7.1	-4.2	9.3	2	1	66.7	33.3
MK-VLBA	16	2.5	2.7	3.8	-5.6	8.5	13	3	81.3	18.8
NL-VLBA	15	1.4	2.0	9.0	-15.2	16.6	9	6	60.0	40.0
NOTO	3	2.1	2.0	1.3	0.8	3.4	3	0	100.0	0.0
NYALES20	37	1.8	0.9	3.3	-2.9	10.7	25	12	67.6	32.4
OHIGGINS	6	0.3	0.1	1.3	-1.6	2.1	3	3	50.0	50.0
ONSALA60	28	1.8	1.3	5.0	-10.8	14.0	18	10	64.3	35.7

Table A.13 (continued): Per-station statistics of the δBLR, determined using Equation (6.33), between the analysis solution with applied ray-traced delays from NASA GSFC and the analysis solution with applied ray-traced delays from RADIATE using parameterization 4. Positive δBLR indicate the relative amount of improvement of the BLR if RADIATE ray-traced delays are applied instead of NASA GSFC ray-traced delays.

δBLR	Basel.	Mean [%]	Median [%]	St. dev. [%]	Min. [%]	Max. [%]	Nr. +	Nr. −	% +	% −
OV-VLBA	15	4.8	5.7	4.0	-2.2	10.2	12	3	80.0	20.0
PIETOWN	16	3.1	2.5	4.2	-3.4	10.7	12	4	75.0	25.0
SC-VLBA	14	1.0	2.1	5.0	-9.3	7.7	9	5	64.3	35.7
SESHAN25	11	1.5	1.1	5.3	-4.8	14.0	7	4	63.6	36.4
SVETLOE	17	2.0	1.9	2.8	-4.0	7.0	13	4	76.5	23.5
SYOWA	2	2.5	2.5	0.6	2.1	3.0	2	0	100.0	0.0
TIGOCONC	22	1.2	0.7	2.4	-2.6	7.0	14	8	63.6	36.4
TSUKUB32	32	-0.3	0.2	4.7	-11.2	12.5	16	16	50.0	50.0
URUMQI	2	2.7	2.7	2.7	0.9	4.6	2	0	100.0	0.0
WARK12M	8	-1.6	-1.6	2.4	-4.9	2.1	2	6	25.0	75.0
WESTFORD	32	-0.5	-0.0	5.0	-15.2	10.2	16	16	50.0	50.0
WETTZELL	36	-0.1	0.2	3.9	-10.1	9.4	19	17	52.8	47.2
YARRA12M	15	-1.0	-0.3	4.9	-11.2	5.8	6	9	40.0	60.0
YEBES40M	16	0.9	1.1	3.6	-4.3	9.3	10	6	62.5	37.5
ZELENCHK	18	0.6	1.0	3.4	-8.6	4.5	12	6	66.7	33.3

Appendix B

Additional figures

B.1 Additional meteorological profiles resulting from the vertical interpolation

This section contains further examples of results of the vertical interpolation, which is described in Section 4.2.2, in terms of vertical profiles of total pressure, temperature, water vapour pressure and refractivity. Note that the strict approach of the vertical interpolation, denoted as "profilewise", of program RADIATE has been used to derive the values. A description of the different modi of the vertical interpolation within program RADIATE is given in Section 4.2.2.1.

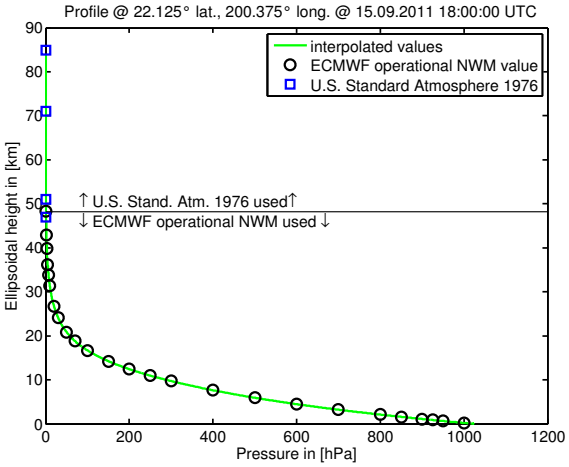

(a) Vertical profile of the pressure.

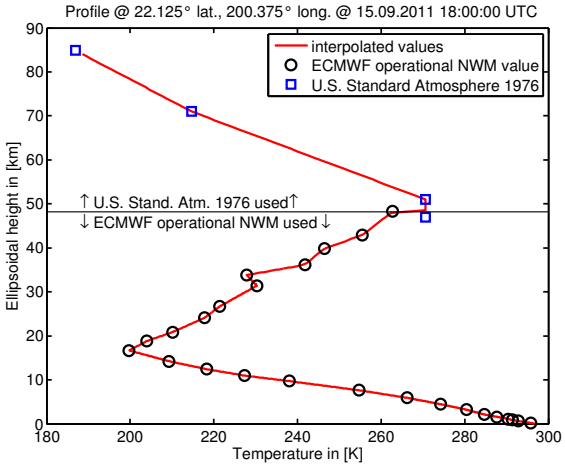

(b) Vertical profile of the temperature.

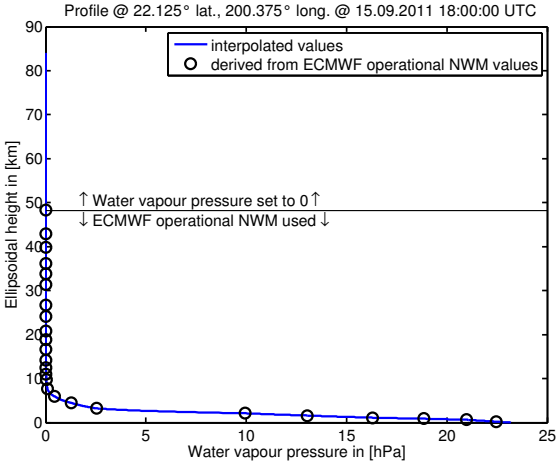

(c) Vertical profile of the water vapour pressure.

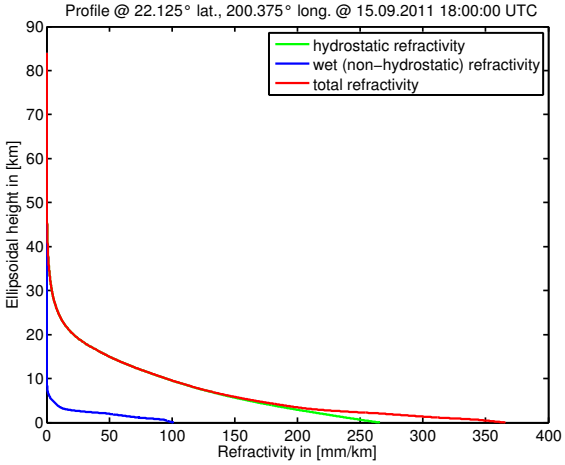

(d) Vertical profiles of the hydrostatic, wet and total refractivity.

Figure B.1: Vertical profiles of pressure, temperature, water vapour pressure and refractivity. The horizontal position of the profiles ($\varphi = 22.1250°, \lambda = 200.3750°$) is the nearest grid point of the NWM to the station KOKEE ($\varphi = 22.1266°, \lambda = 200.3349°$). The epoch of the NWM is 15.09.2011 18:00:00 h UTC. The defined NWM limit is represented by a horizontal line. Up to this point the ECMWF operational NWM data from 25 pressure levels, which are delivered in a horizontal resolution of 0.125° x 0.125°, have been used to interpolate the pressure, the temperature and the derived water vapour pressure. Above this limit the U.S. Standard Atmosphere 1976 has been used to interpolate the pressure and the temperature. The water vapour pressure has been set to 0 for these heights. For a better readability the refractivities are presented instead of the refractive indices. These values have been calculated according to Equations (4.61) to (4.63) using the interpolated pressure, temperature and water vapour pressure.

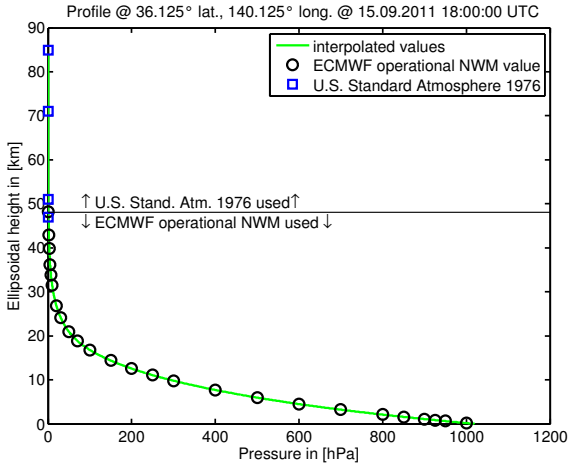

(a) Vertical profile of the pressure.

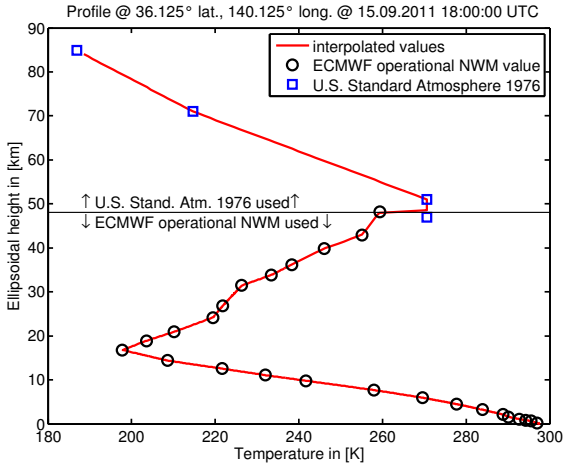

(b) Vertical profile of the temperature.

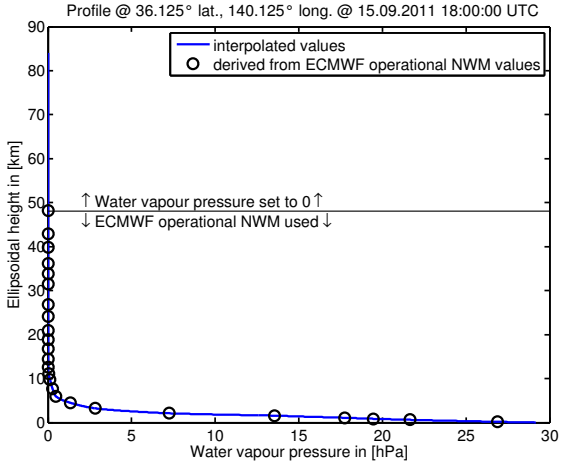

(c) Vertical profile of the water vapour pressure.

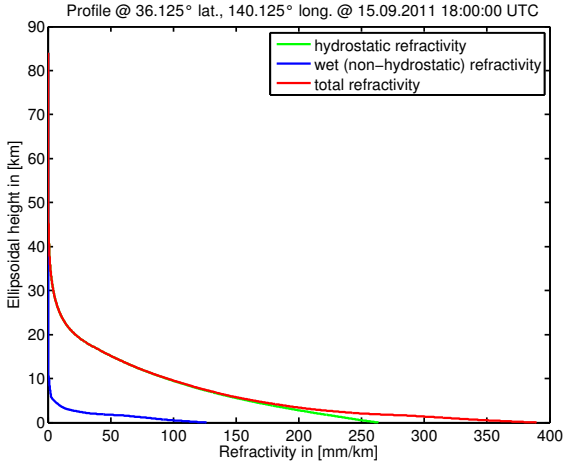

(d) Vertical profiles of the hydrostatic, wet and total refractivity.

Figure B.2: Vertical profiles of pressure, temperature, water vapour pressure and refractivity. The horizontal position of the profiles ($\varphi = 36.1250°, \lambda = 140.1250°$) is the nearest grid point of the NWM to the station TSUKUB32 ($\varphi = 36.1031°, \lambda = 140.0887°$). The epoch of the NWM is 15.09.2011 18:00:00 h UTC. The defined NWM limit is represented by a horizontal line. Up to this point the ECMWF operational NWM data from 25 pressure levels, which are delivered in a horizontal resolution of 0.125° x 0.125°, have been used to interpolate the pressure, the temperature and the derived water vapour pressure. Above this limit the U.S. Standard Atmosphere 1976 has been used to interpolate the pressure and the temperature. The water vapour pressure has been set to 0 for these heights. For a better readability the refractivities are presented instead of the refractive indices. These values have been calculated according to Equations (4.61) to (4.63) using the interpolated pressure, temperature and water vapour pressure.

B.2 Additional results of the impact of the horizontal resolution of the NWM on ray-traced delays for selected stations

All upcoming figures show the differences between the solutions RD(0.125°) and RD(1°) as described in Section 5.3.2 on page 89. The differences are built in the form $RD(0.125°) - RD(1°)$ with respect to the specific domain of the differences, i.e. ΔSTD, ΔSHD, ΔSWD or those differences using the mapping factor. The observation data are described in Section 5.3.1.2 on page 88.

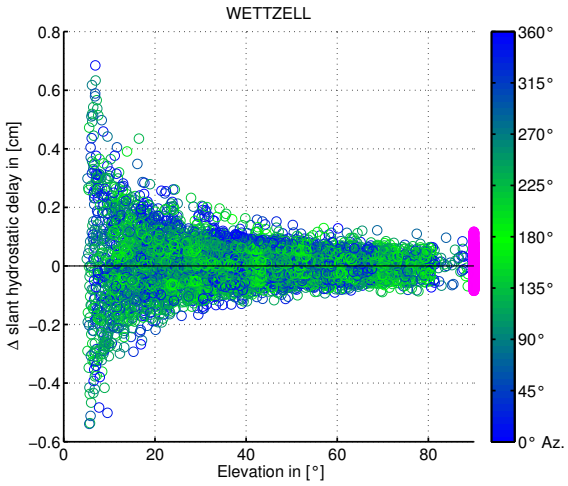

(a) ΔSHD are plotted with respect to the elevation angles, the respective azimuths are shown colour-coded.

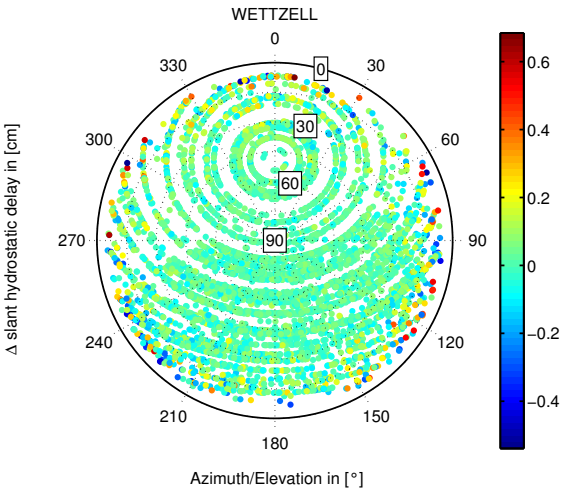

(b) ΔSHD are colour-coded in a skyplot of the observations.

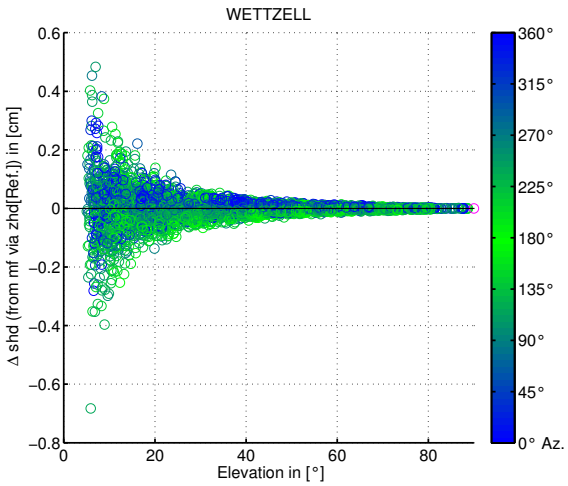

(c) ΔSHD_{mf} are plotted with respect to the elevation angles, the respective azimuths are shown colour-coded.

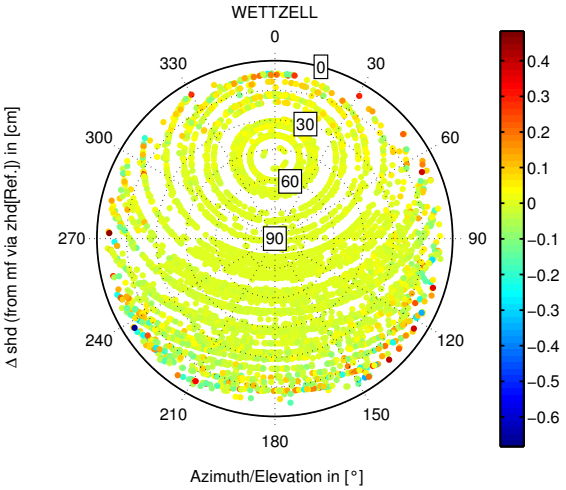

(d) ΔSHD_{mf} are colour-coded in a skyplot of the observations.

Figure B.3: ΔSHD and ΔSHD_{mf} for the CONT11 observations of station WETTZELL.

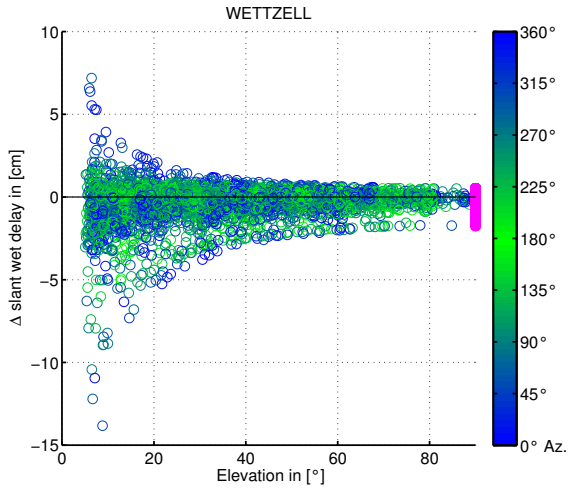

(a) ΔSWD are plotted with respect to the elevation angles, the respective azimuths are shown colour-coded.

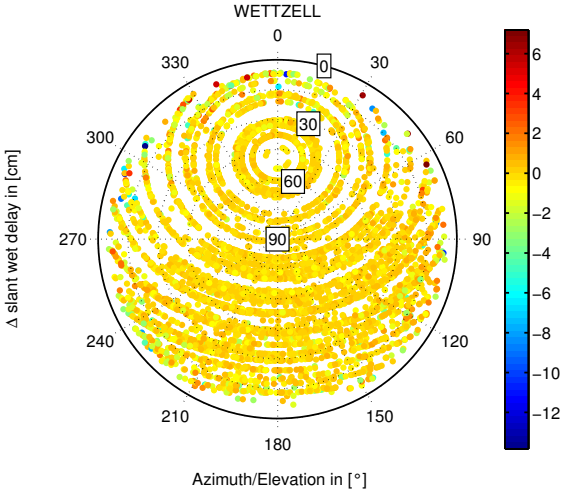

(b) ΔSWD are colour-coded in a skyplot of the observations.

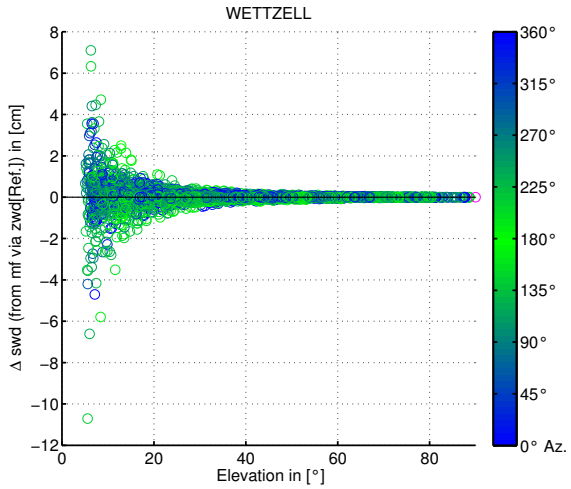

(c) ΔSWD_{mf} are plotted with respect to the elevation angles, the respective azimuths are shown colour-coded.

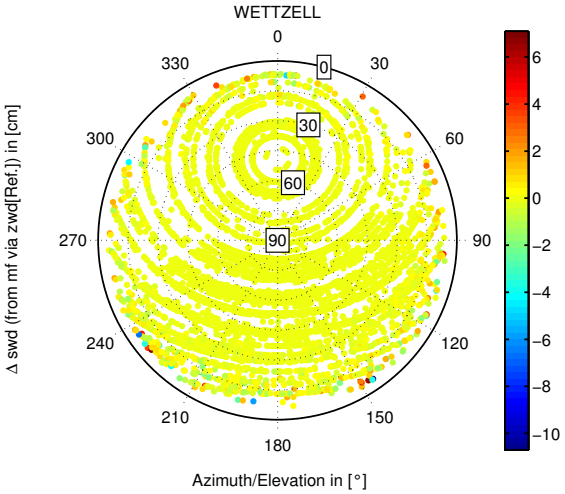

(d) ΔSWD_{mf} are colour-coded in a skyplot of the observations.

Figure B.4: ΔSWD and ΔSWD_{mf} for the CONT11 observations of station WETTZELL.

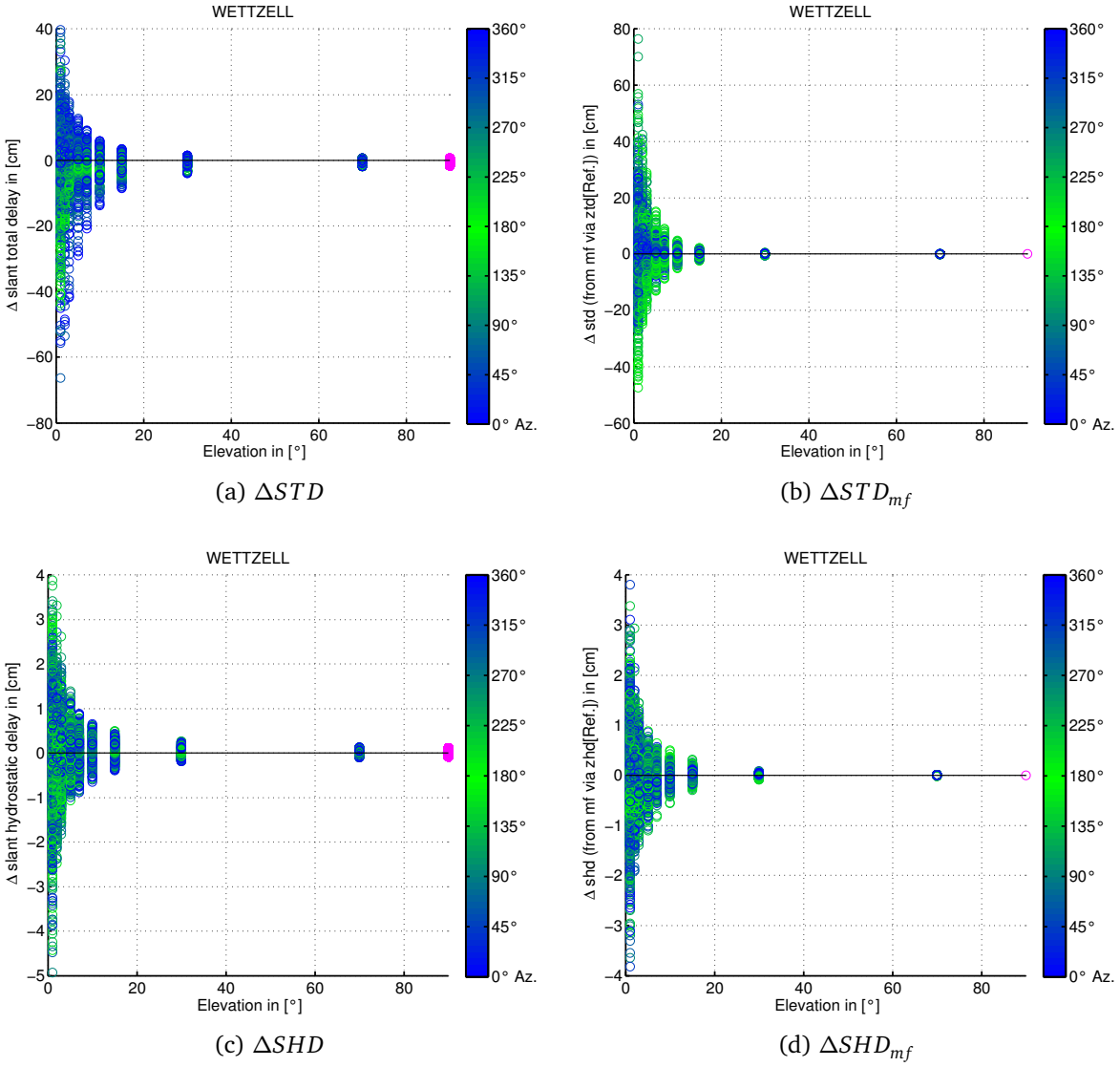

(a) ΔSTD (b) ΔSTD_{mf}

(c) ΔSHD (d) ΔSHD_{mf}

Figure B.5: Differences for the simulated observations of station WETTZELL. The differences are plotted with respect to the elevation angles, the respective azimuths are shown colour-coded.

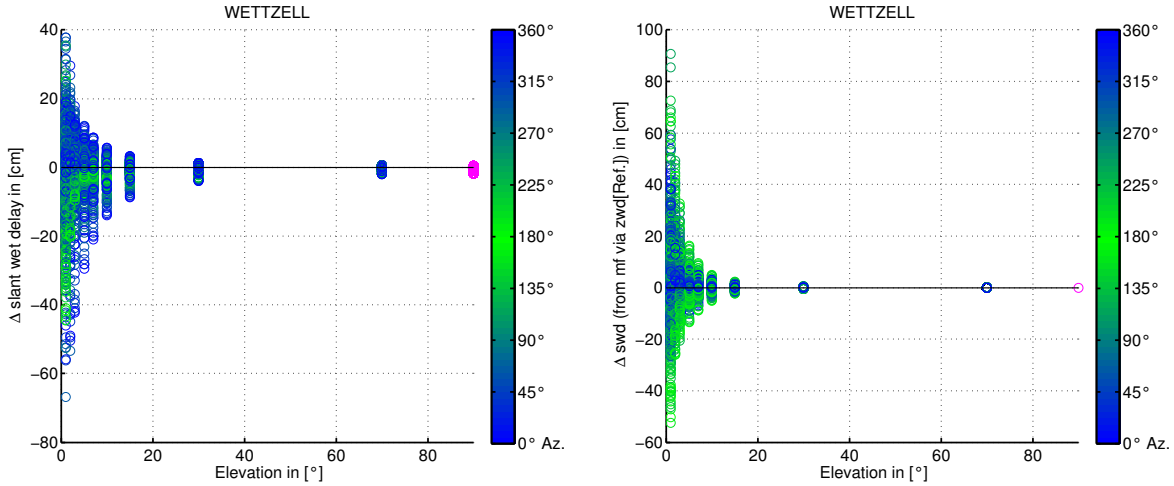

(e) ΔSWD (f) ΔSWD_{mf}

Figure B.5 (continued): Differences for the simulated observations of station WETTZELL. The differences are plotted with respect to the elevation angles, the respective azimuths are shown colour-coded.

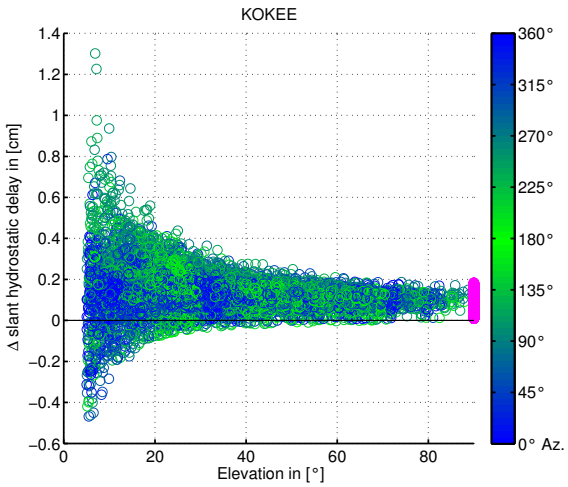

(a) ΔSHD are plotted with respect to the elevation angles, the respective azimuths are shown colour-coded.

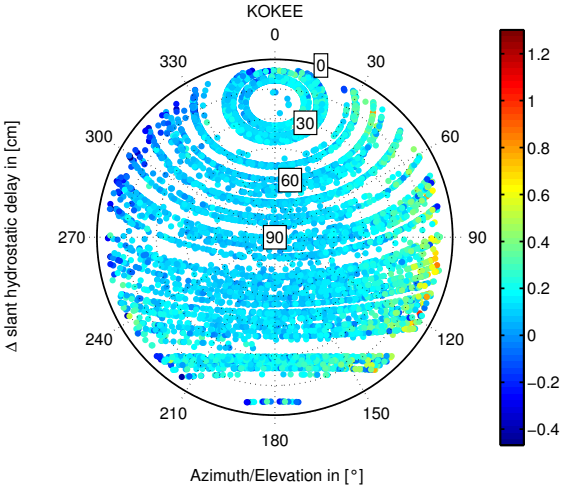

(b) ΔSHD are colour-coded in a skyplot of the observations.

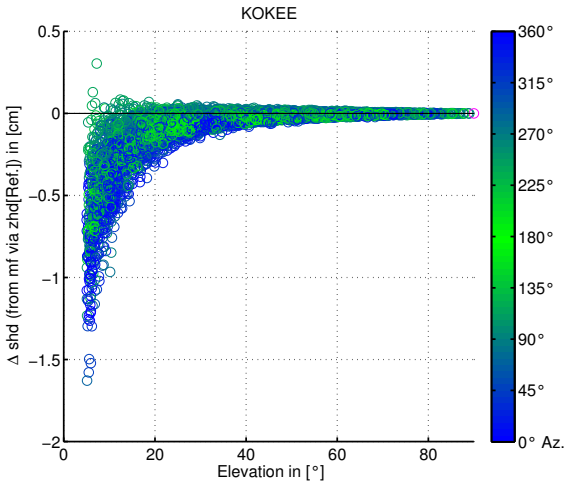

(c) ΔSHD_{mf} are plotted with respect to the elevation angles, the respective azimuths are shown colour-coded.

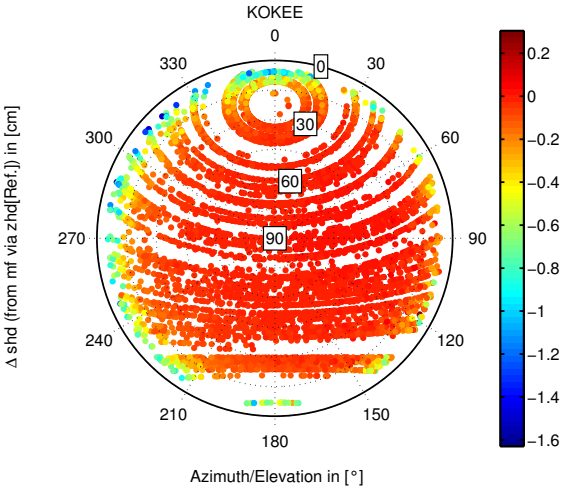

(d) ΔSHD_{mf} are colour-coded in a skyplot of the observations.

Figure B.6: ΔSHD and ΔSHD_{mf} for the CONT11 observations of station KOKEE.

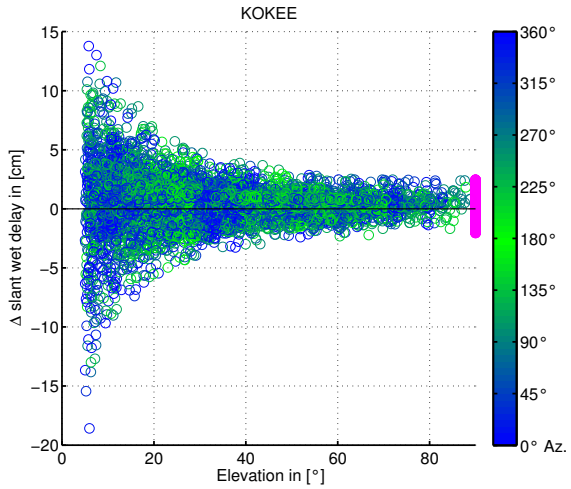

(a) ΔSWD are plotted with respect to the elevation angles, the respective azimuths are shown colour-coded.

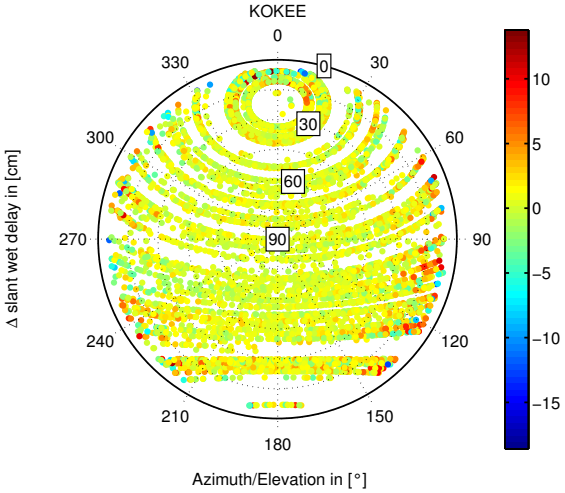

(b) ΔSWD are colour-coded in a skyplot of the observations.

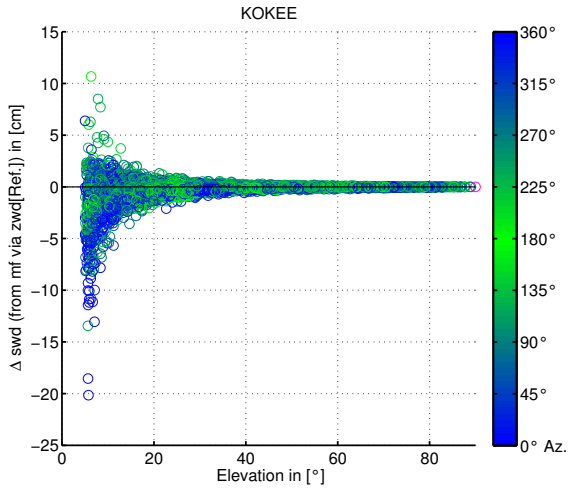

(c) ΔSWD_{mf} are plotted with respect to the elevation angles, the respective azimuths are shown colour-coded.

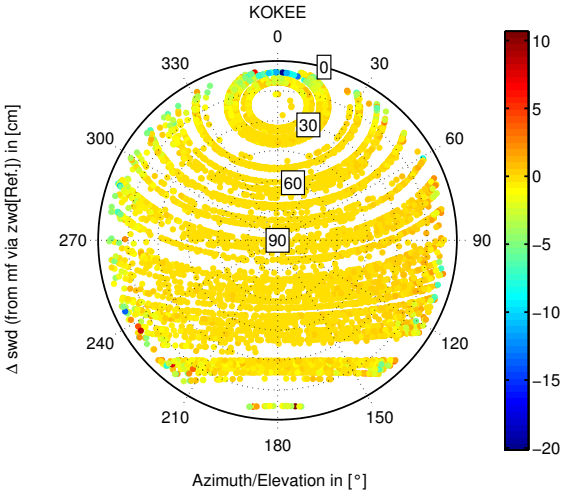

(d) ΔSWD_{mf} are colour-coded in a skyplot of the observations.

Figure B.7: ΔSWD and ΔSWD_{mf} for the CONT11 observations of station KOKEE.

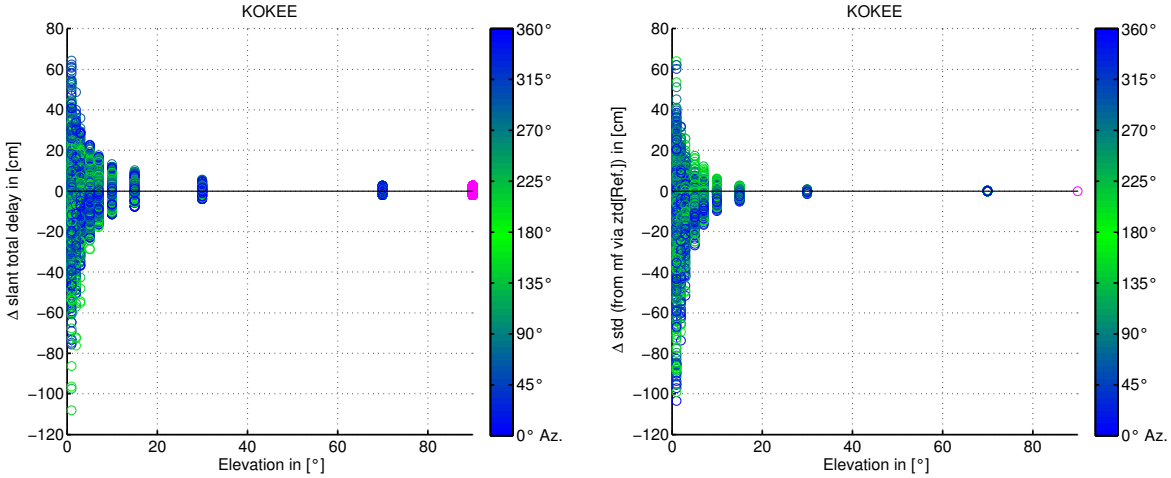

(a) ΔSTD (b) ΔSTD_{mf}

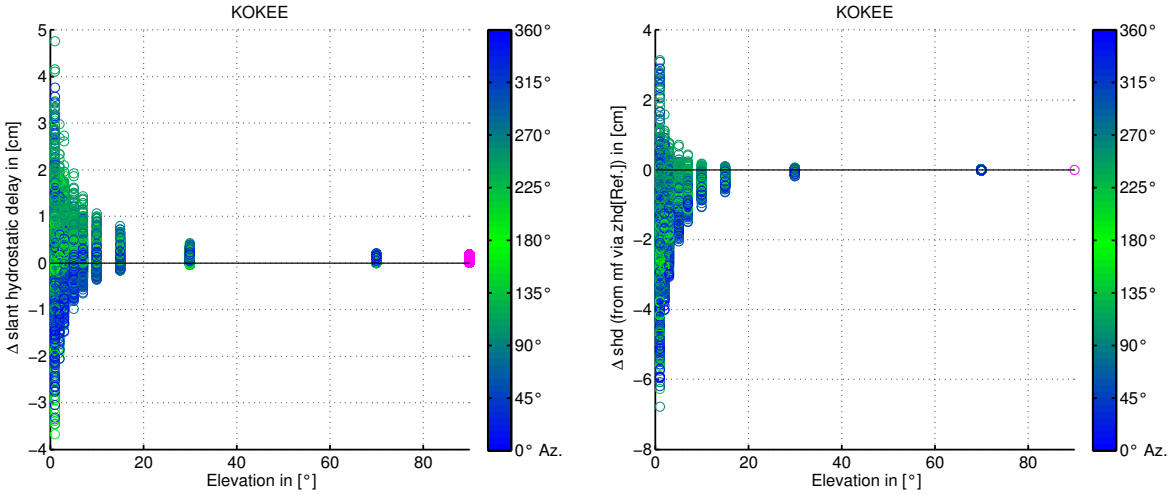

(c) ΔSHD (d) ΔSHD_{mf}

Figure B.8: Differences for the simulated observations of station KOKEE. The differences are plotted with respect to the elevation angles, the respective azimuths are shown colour-coded.

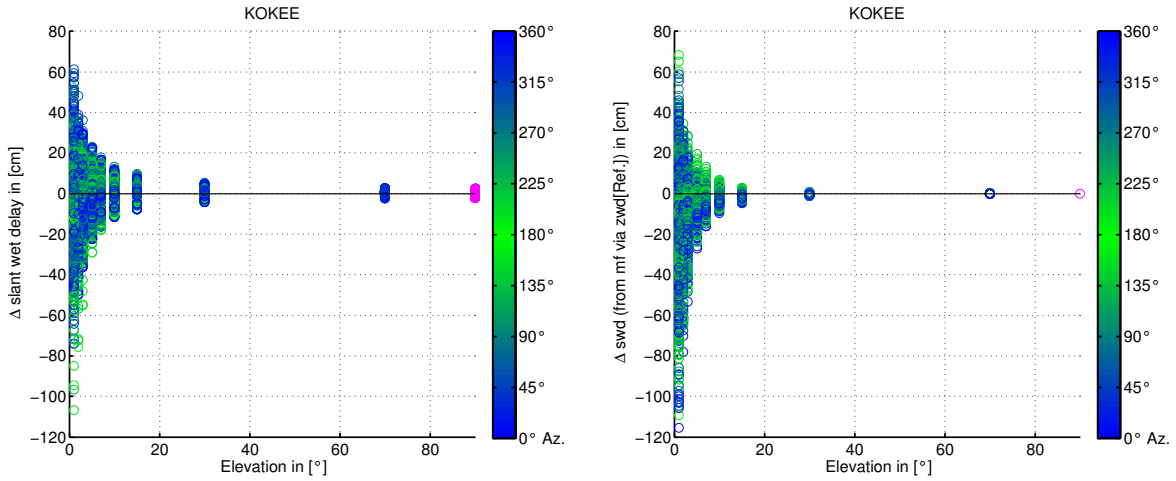

(e) ΔSWD (f) ΔSWD_{mf}

Figure B.8 (continued): Differences for the simulated observations of station KOKEE. The differences are plotted with respect to the elevation angles, the respective azimuths are shown colour-coded.

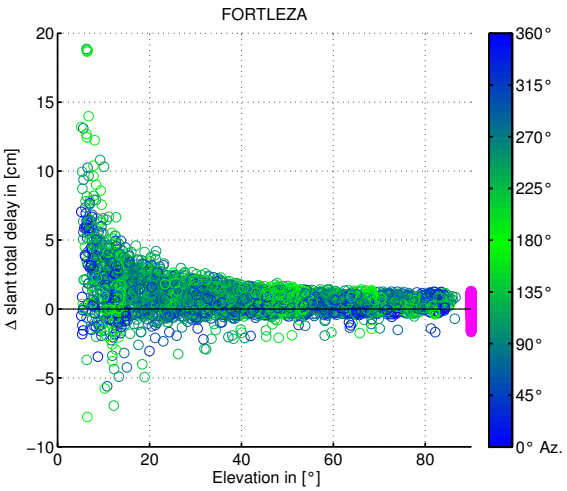

(a) ΔSTD are plotted with respect to the elevation angles, the respective azimuths are shown colour-coded.

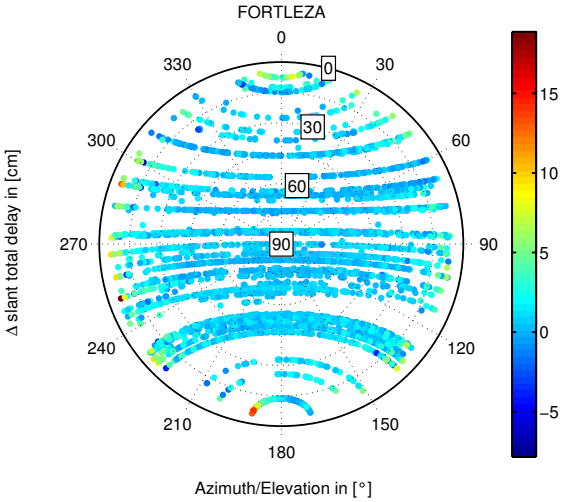

(b) ΔSTD are colour-coded in a skyplot of the observations.

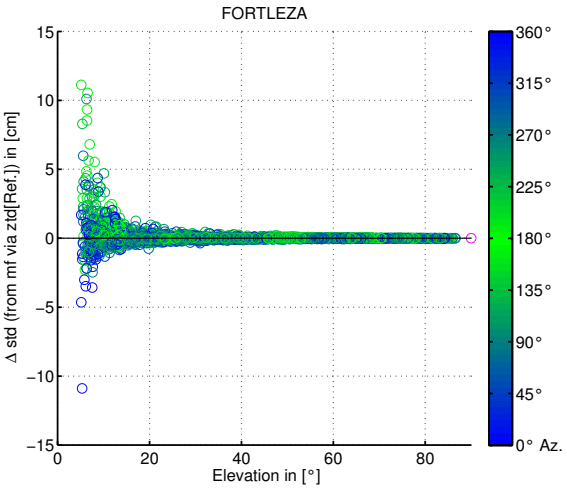

(c) ΔSTD_{mf} are plotted with respect to the elevation angles, the respective azimuths are shown colour-coded.

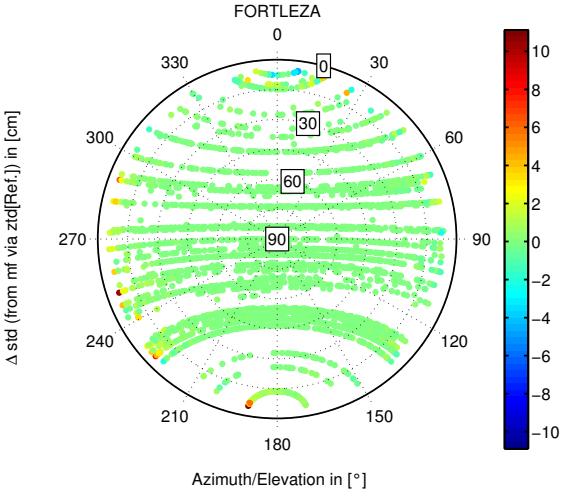

(d) ΔSTD_{mf} are colour-coded in a skyplot of the observations.

Figure B.9: ΔSTD and ΔSTD_{mf} for the CONT11 observations of station FORTLEZA.

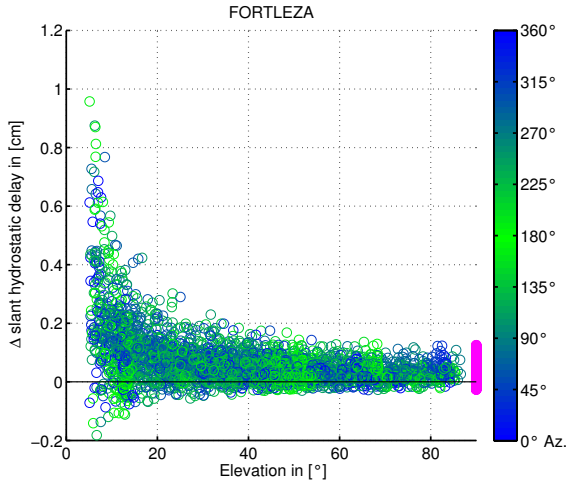

(a) ΔSHD are plotted with respect to the elevation angles, the respective azimuths are shown colour-coded.

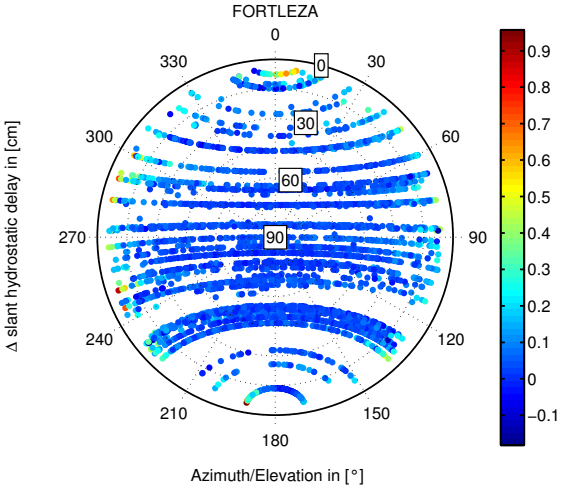

(b) ΔSHD are colour-coded in a skyplot of the observations.

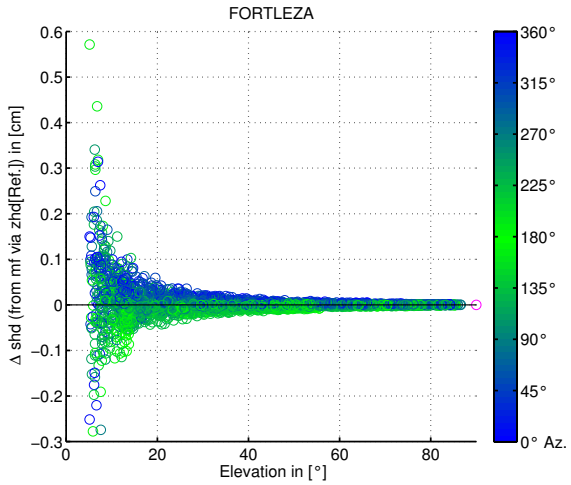

(c) ΔSHD_{mf} are plotted with respect to the elevation angles, the respective azimuths are shown colour-coded.

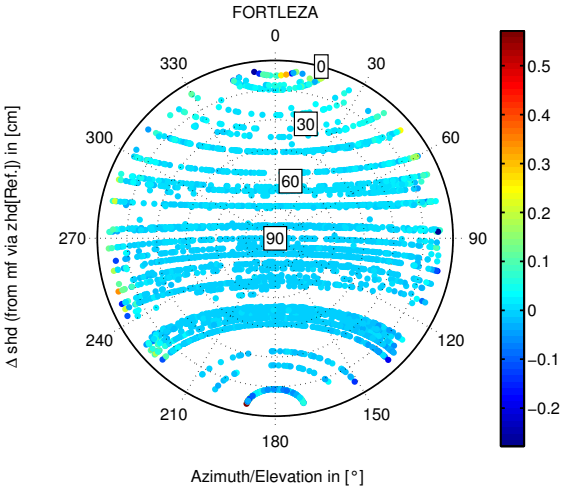

(d) ΔSHD_{mf} are colour-coded in a skyplot of the observations.

Figure B.10: ΔSHD and ΔSHD_{mf} for the CONT11 observations of station FORTLEZA.

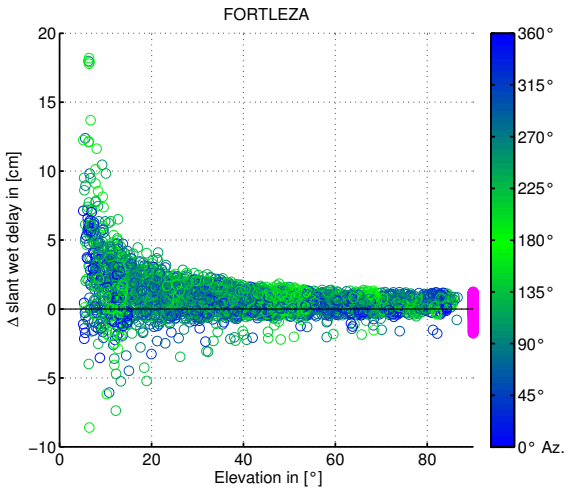

(a) ΔSWD are plotted with respect to the elevation angles, the respective azimuths are shown colour-coded.

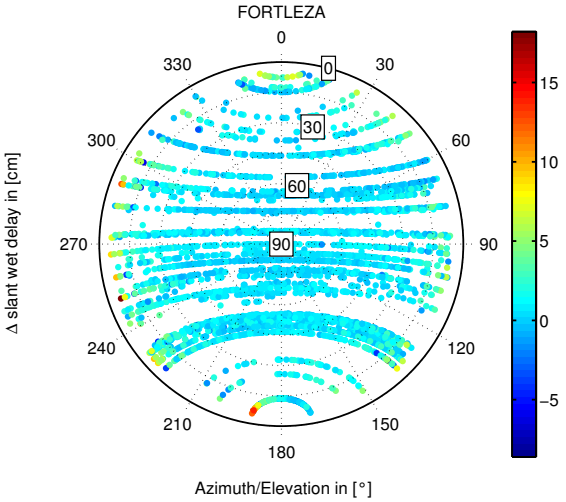

(b) ΔSWD are colour-coded in a skyplot of the observations.

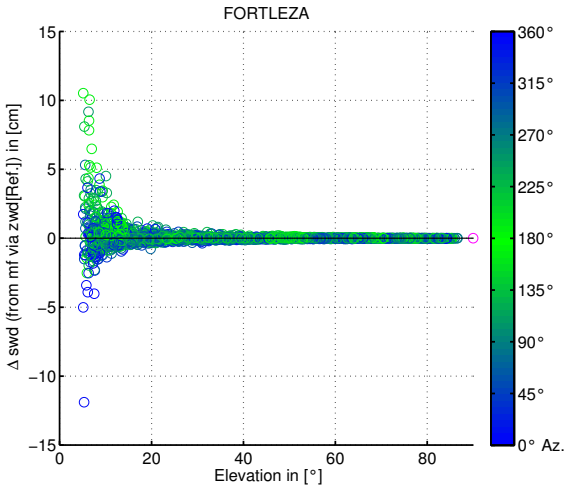

(c) ΔSWD_{mf} are plotted with respect to the elevation angles, the respective azimuths are shown colour-coded.

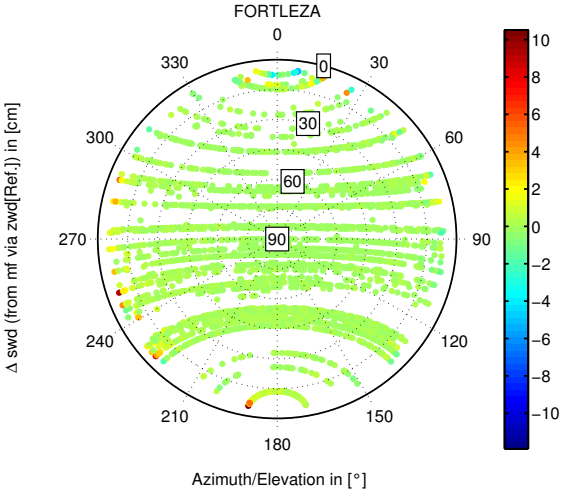

(d) ΔSWD_{mf} are colour-coded in a skyplot of the observations.

Figure B.11: ΔSWD and ΔSWD_{mf} for the CONT11 observations of station FORTLEZA.

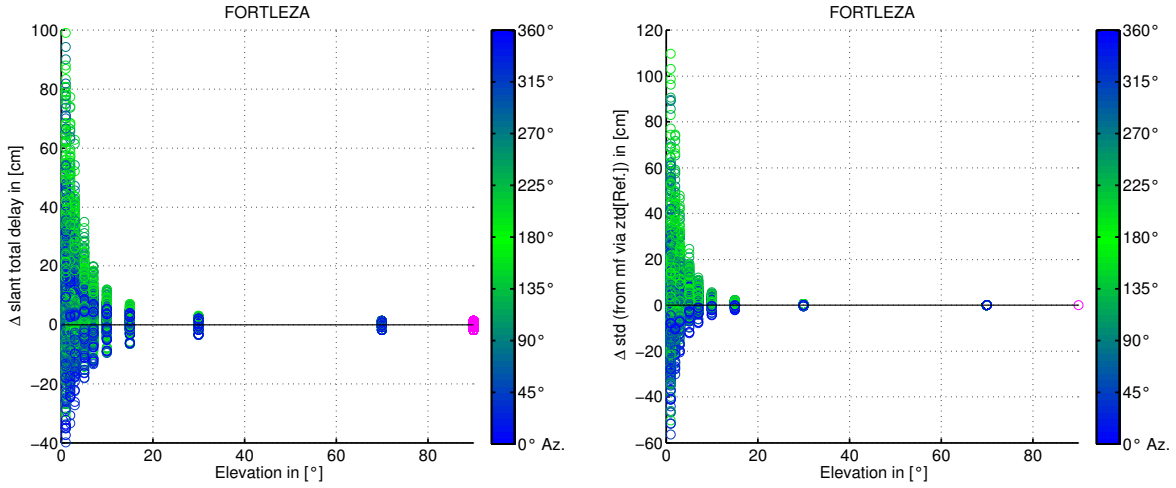

(a) ΔSTD

(b) ΔSTD_{mf}

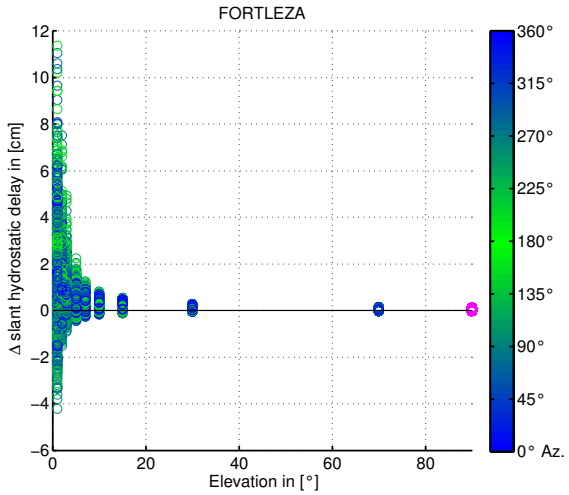

(c) ΔSHD

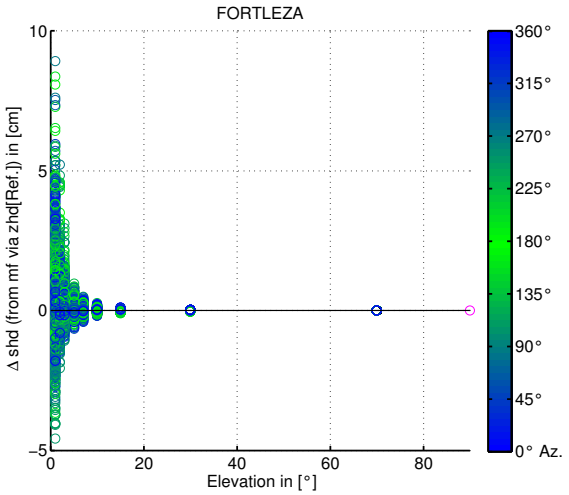

(d) ΔSHD_{mf}

Figure B.12: Differences for the simulated observations of station FORTLEZA. The differences are plotted with respect to the elevation angles, the respective azimuths are shown colour-coded.

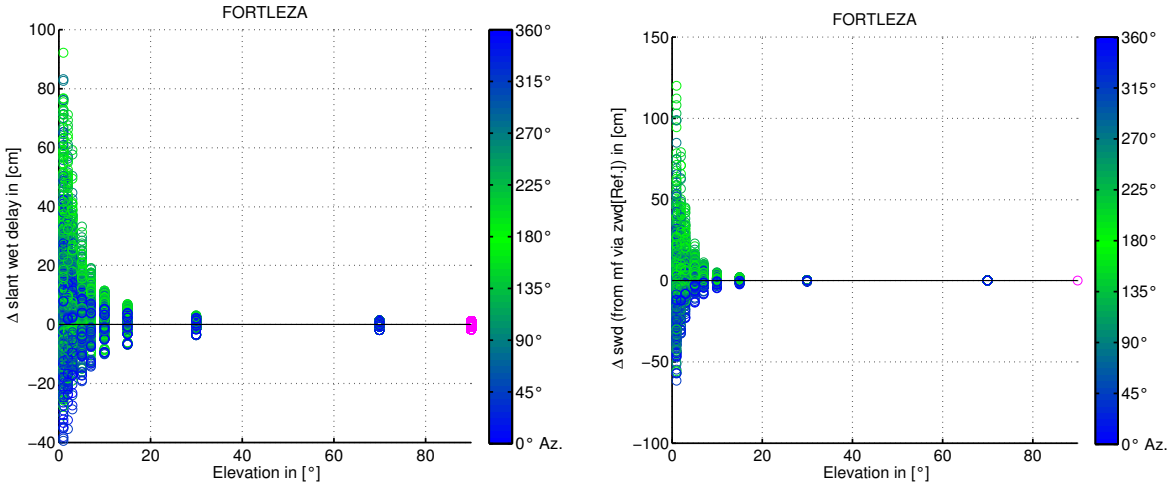

(e) ΔSWD (f) ΔSWD_{mf}

Figure B.12 (continued): Differences for the simulated observations of station FORTLEZA. The differences are plotted with respect to the elevation angles, the respective azimuths are shown colour-coded.

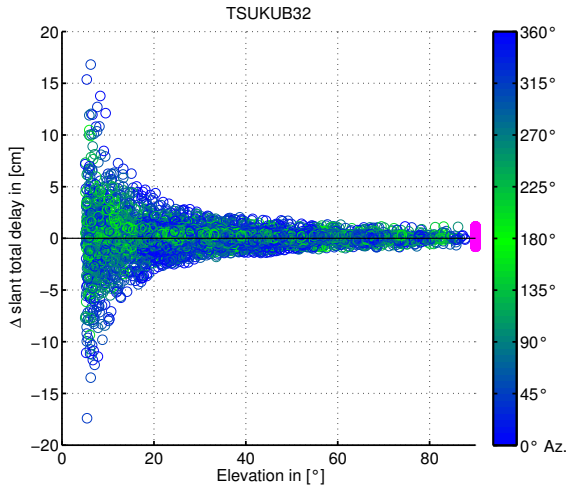

(a) ΔSTD are plotted with respect to the elevation angles, the respective azimuths are shown colour-coded.

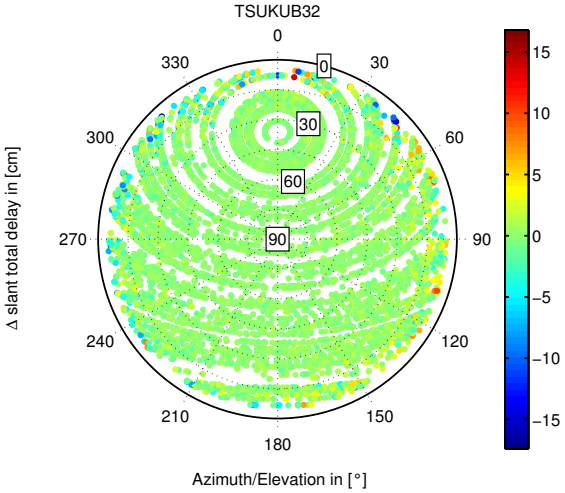

(b) ΔSTD are colour-coded in a skyplot of the observations.

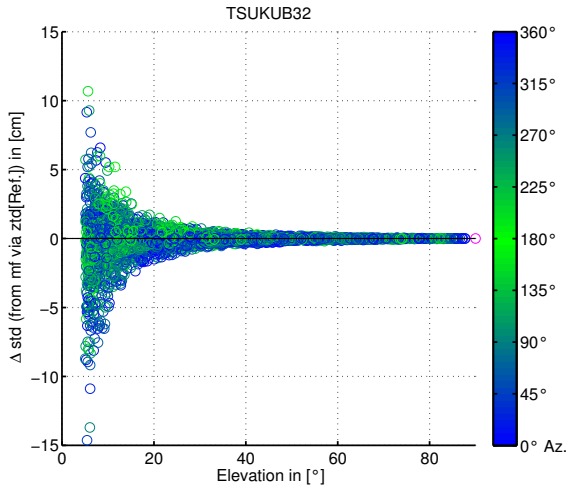

(c) ΔSTD_{mf} are plotted with respect to the elevation angles, the respective azimuths are shown colour-coded.

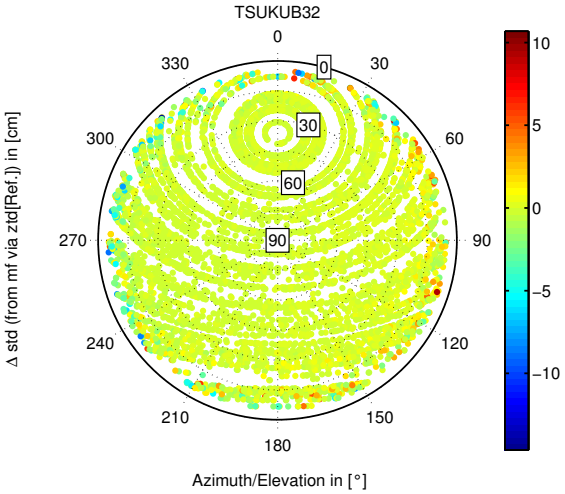

(d) ΔSTD_{mf} are colour-coded in a skyplot of the observations.

Figure B.13: ΔSTD and ΔSTD_{mf} for the CONT11 observations of station TSUKUB32.

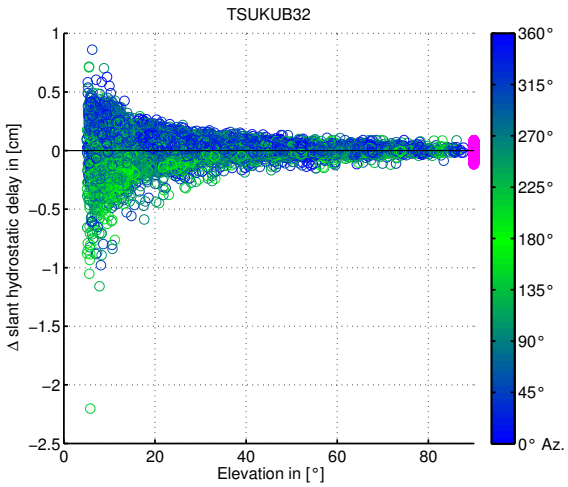

(a) ΔSHD are plotted with respect to the elevation angles, the respective azimuths are shown colour-coded.

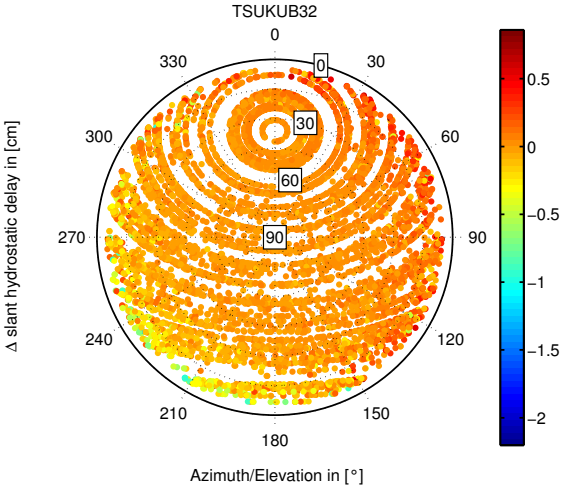

(b) ΔSHD are colour-coded in a skyplot of the observations.

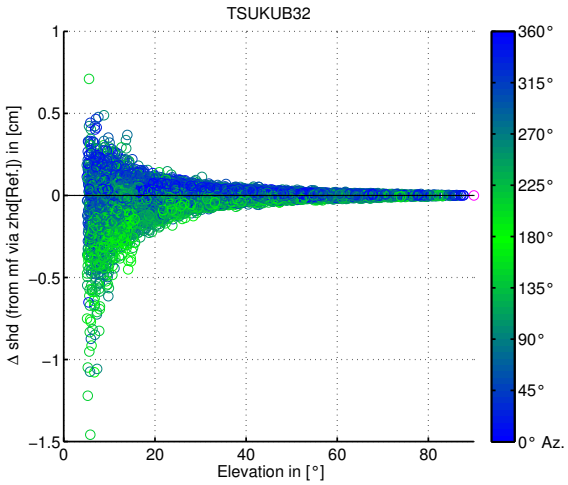

(c) ΔSHD_{mf} are plotted with respect to the elevation angles, the respective azimuths are shown colour-coded.

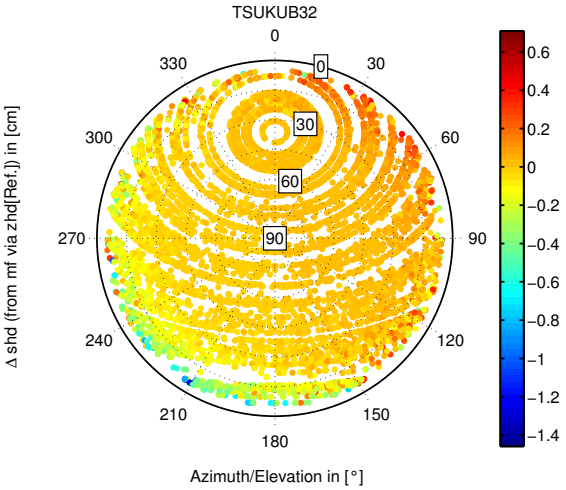

(d) ΔSHD_{mf} are colour-coded in a skyplot of the observations.

Figure B.14: ΔSHD and ΔSHD_{mf} for the CONT11 observations of station TSUKUB32.

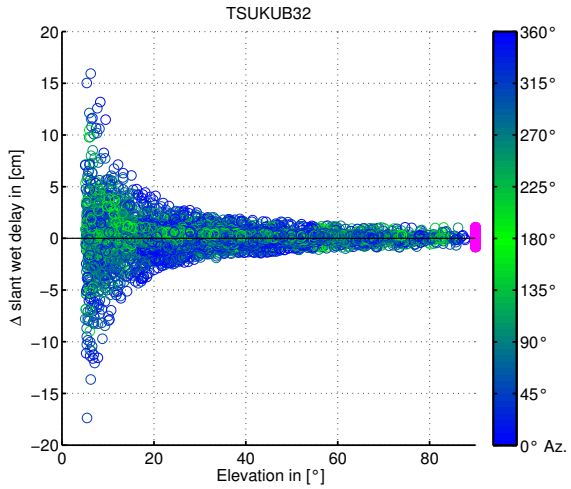

(a) ΔSWD are plotted with respect to the elevation angles, the respective azimuths are shown colour-coded.

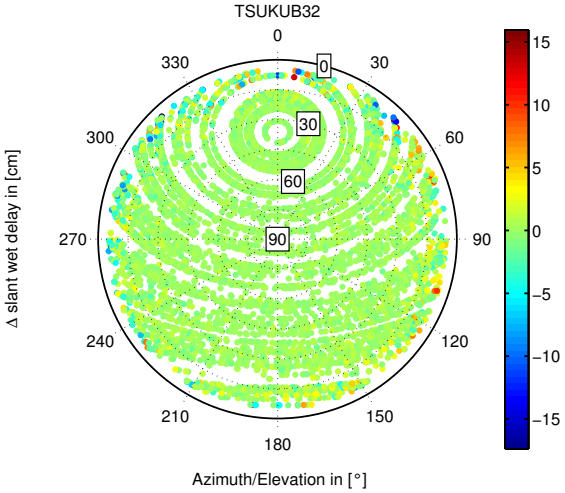

(b) ΔSWD are colour-coded in a skyplot of the observations.

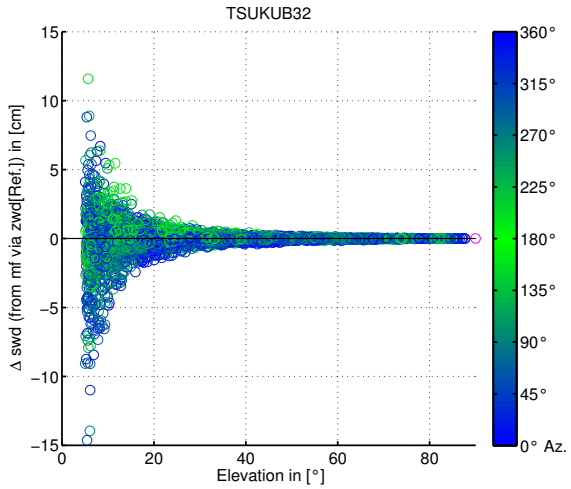

(c) ΔSWD_{mf} are plotted with respect to the elevation angles, the respective azimuths are shown colour-coded.

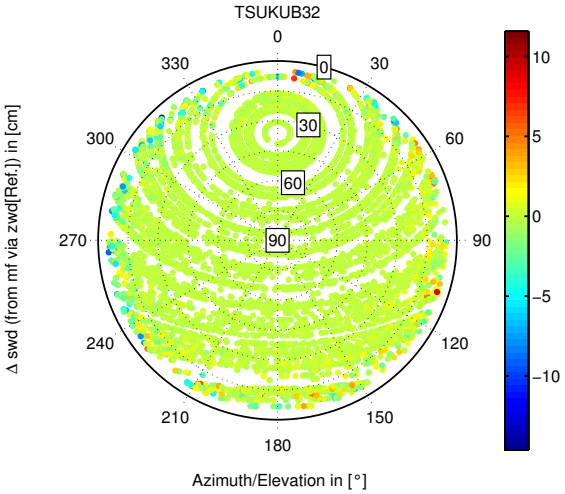

(d) ΔSWD_{mf} are colour-coded in a skyplot of the observations.

Figure B.15: ΔSWD and ΔSWD_{mf} for the CONT11 observations of station TSUKUB32.

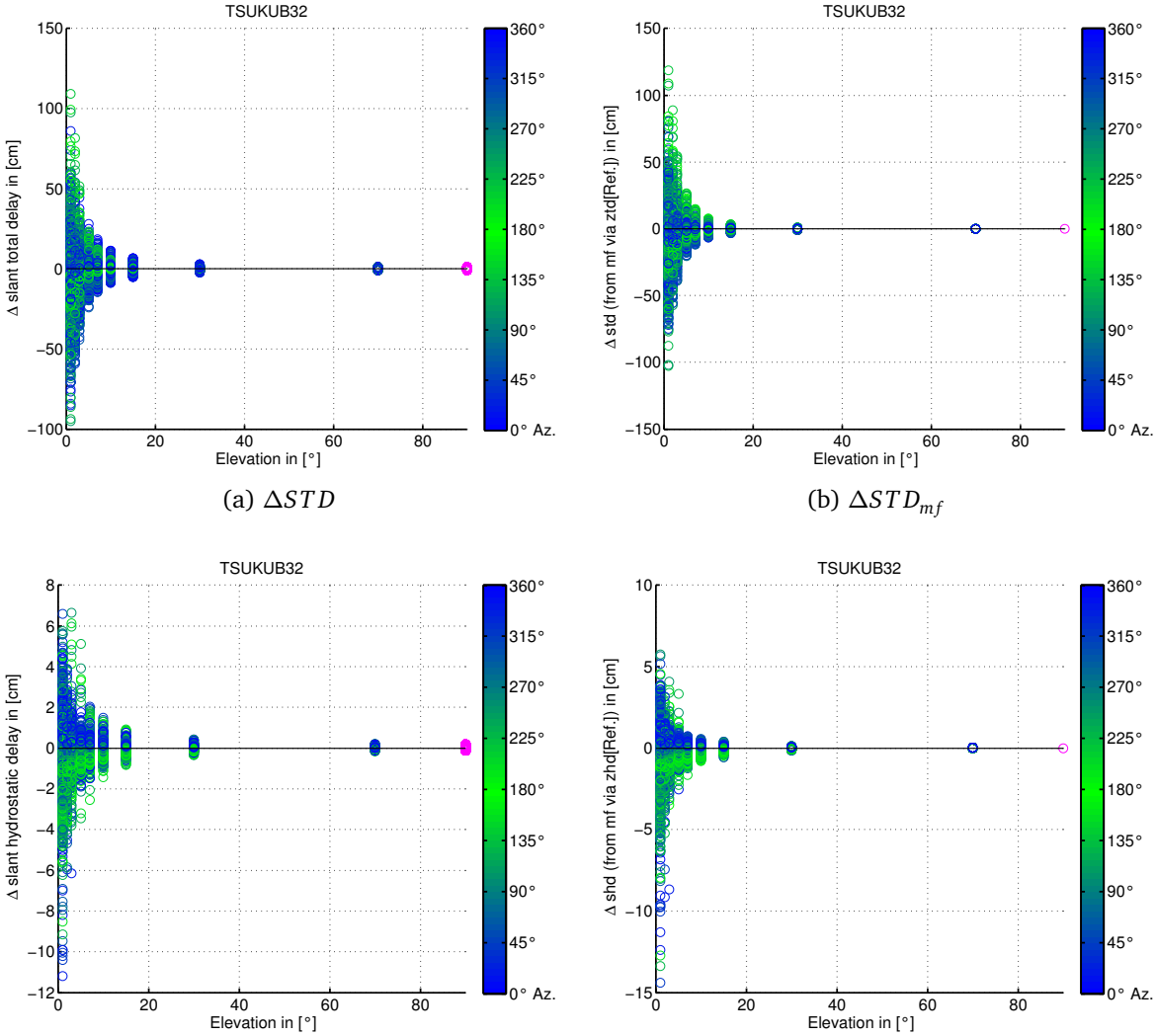

(a) ΔSTD (b) ΔSTD_{mf}

(c) ΔSHD (d) ΔSHD_{mf}

Figure B.16: Differences for the simulated observations of station TSUKUB32. The differences are plotted with respect to the elevation angles, the respective azimuths are shown colour-coded.

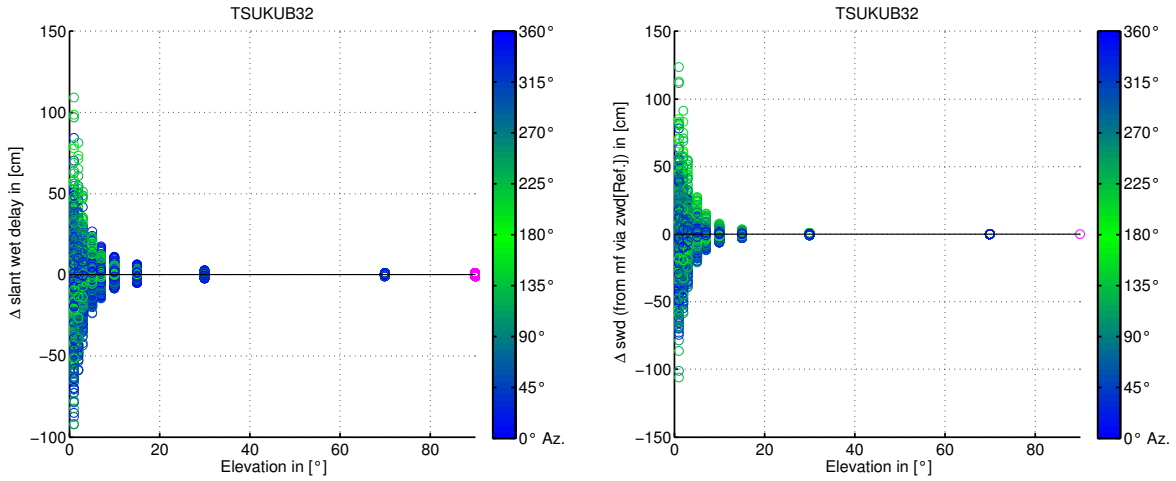

(e) ΔSWD (f) ΔSWD_{mf}

Figure B.16 (continued): Differences for the simulated observations of station TSUKUB32. The differences are plotted with respect to the elevation angles, the respective azimuths are shown colour-coded.

B.3 Additional sample ray-traced tropospheric path delay results determined with the operational Fortran version of program RADIATE

Additional to the results presented in Section 6.2.3, the following figures provide more sample results of the STD, SHD, SWD and the geometric bending effect g_{bend} at further stations for simulated observations at different elevation angles at 0° azimuth at 15.09.2011 18:00:00 h UTC. The geometric bending effect is already added to the STD and SHD according to common practice. Also plots of the azimuthal dependence of the SWD at the stations are shown.

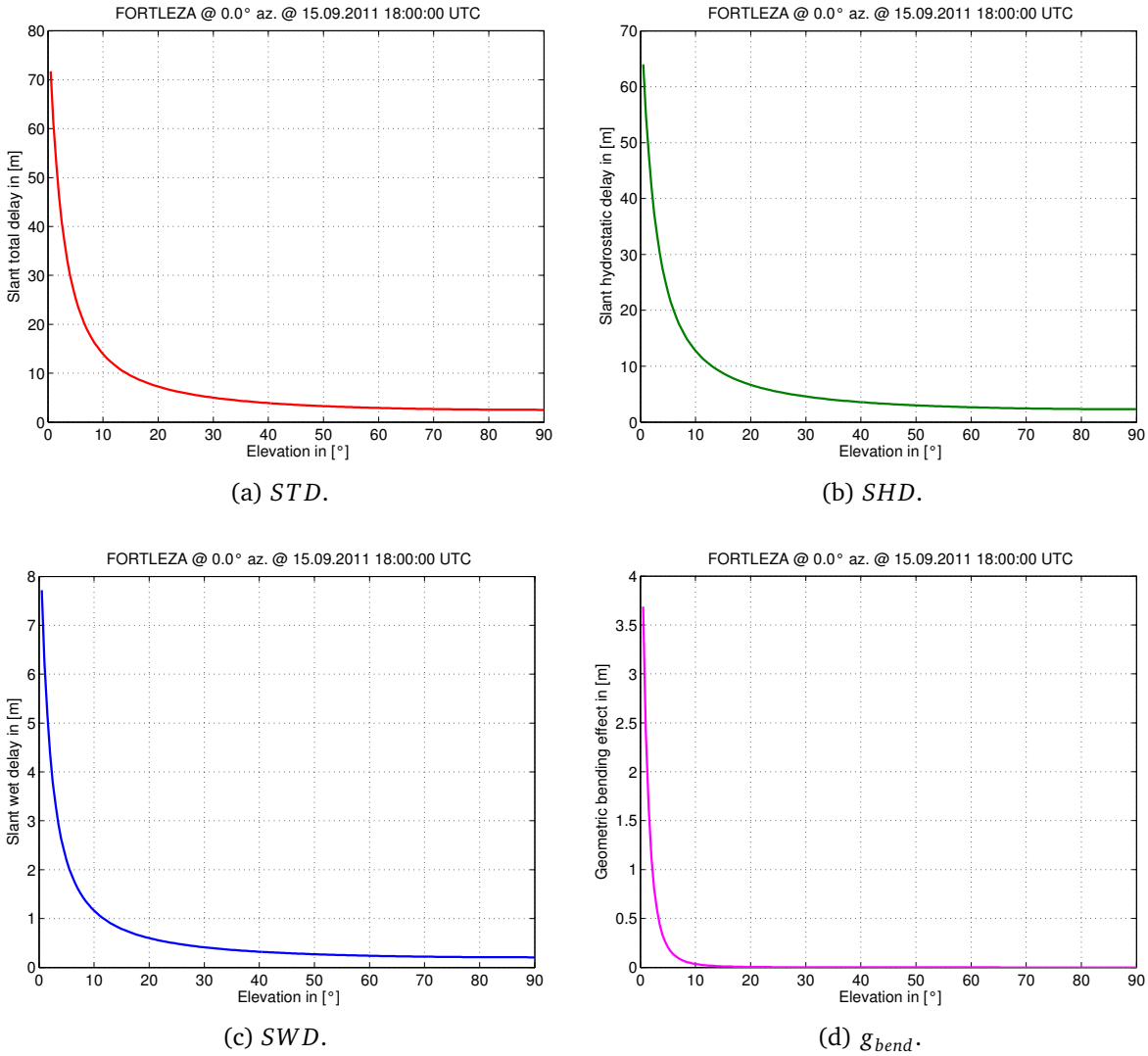

(a) STD. (b) SHD.

(c) SWD. (d) g_{bend}.

Figure B.17: STD, SHD, SWD and g_{bend} at station FORTLEZA for simulated observations at different elevation angles at 0° azimuth at 15.09.2011 18:00:00 h UTC. The geometric bending effect is already added to the STD and SHD.

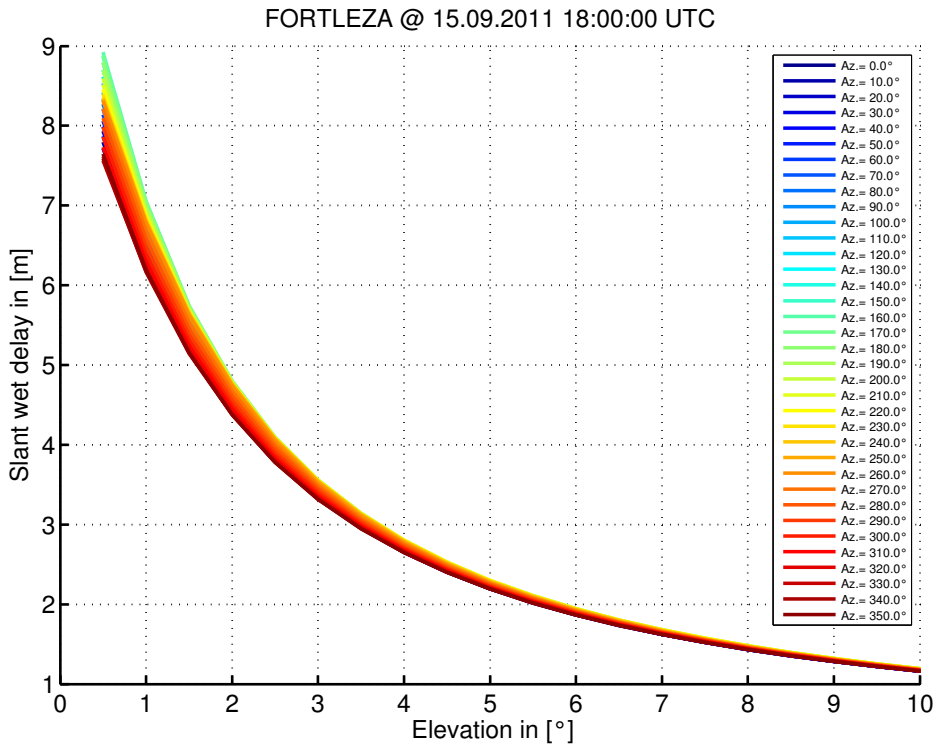

Figure B.18: Azimuthal dependence of the SWD at small elevation angles at 15.09.2011 18:00:00 h UTC at station FORTLEZA.

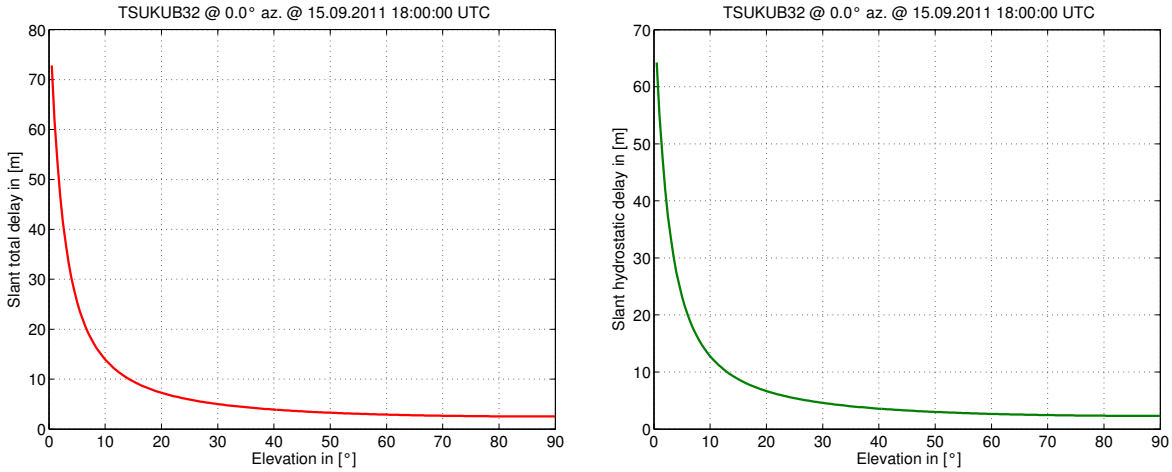

(a) STD. (b) SHD.

(c) SWD. (d) g_{bend}.

Figure B.19: STD, SHD, SWD and g_{bend} at station TSUKUB32 for simulated observations at different elevation angles at 0° azimuth at 15.09.2011 18:00:00 h UTC. The geometric bending effect is already added to the STD and SHD.

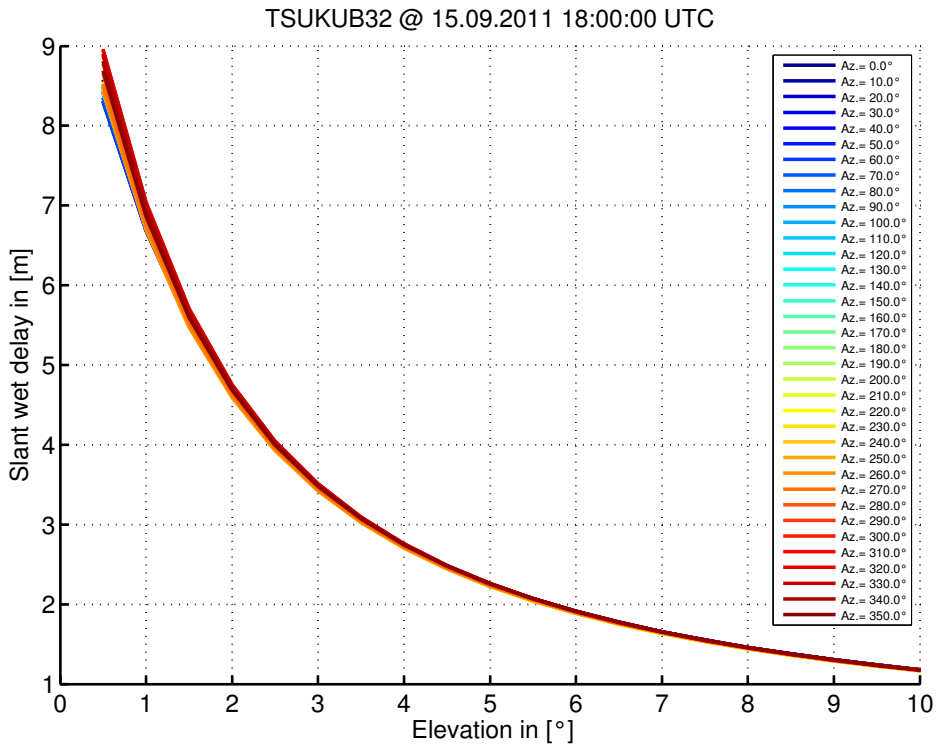

Figure B.20: Azimuthal dependence of the SWD at small elevation angles at 15.09.2011 18:00:00 h UTC at station TSUKUB32.

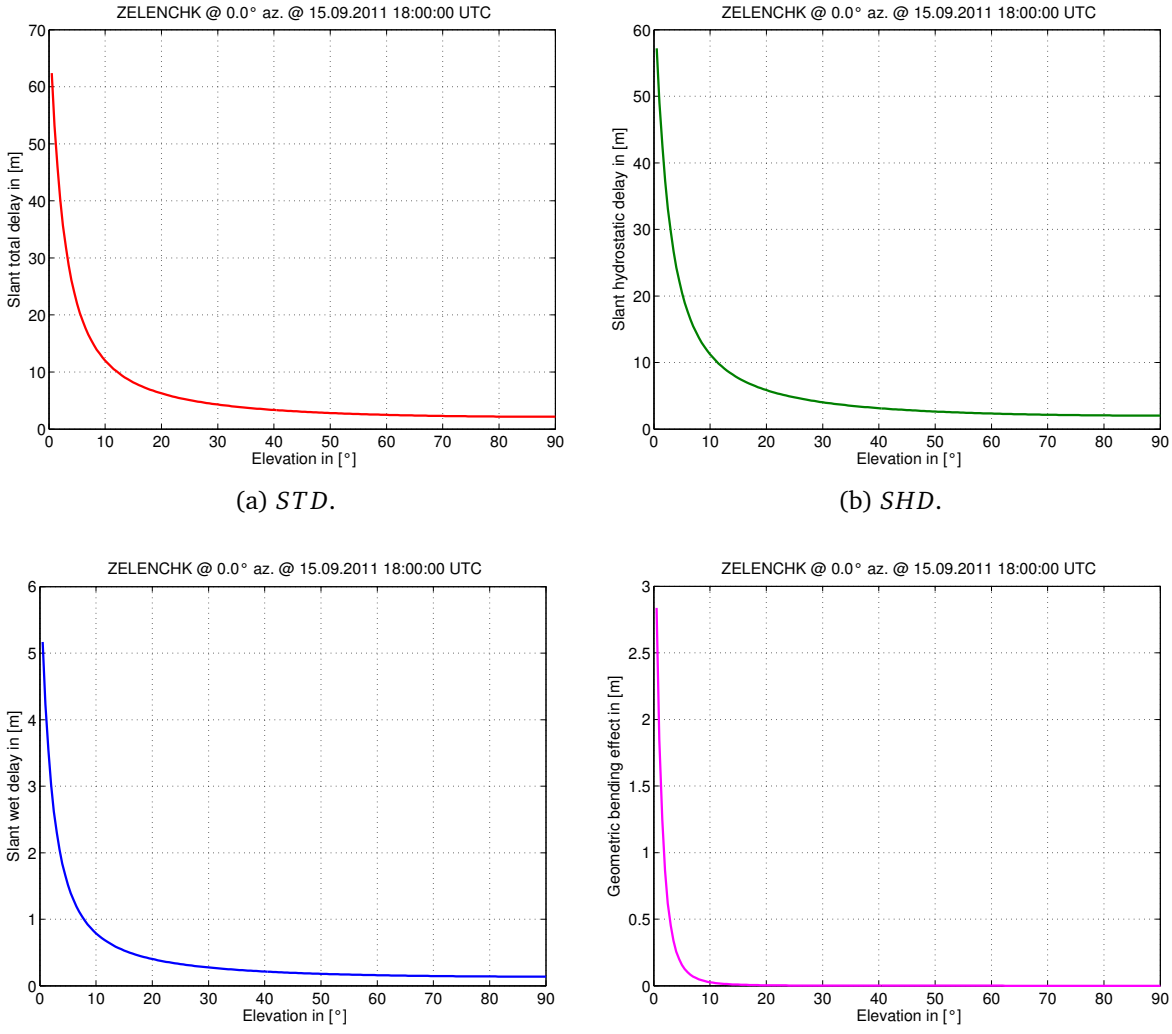

(a) STD. (b) SHD.

(c) SWD. (d) g_{bend}.

Figure B.21: STD, SHD, SWD and g_{bend} at station ZELENCHK for simulated observations at different elevation angles at 0° azimuth at 15.09.2011 18:00:00 h UTC. The geometric bending effect is already added to the STD and SHD.

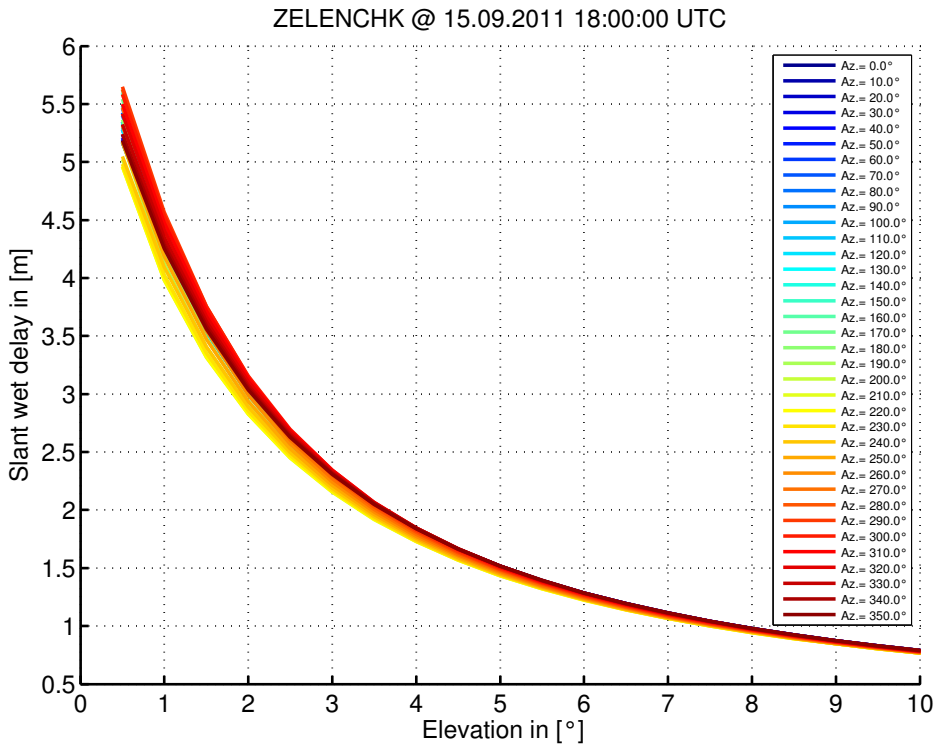

Figure B.22: Azimuthal dependence of the SWD at small elevation angles at 15.09.2011 18:00:00 h UTC at station ZELENCHK.

B.4 Additional figures of the comparison of zenith delays from RADIATE and from VLBI analysis on the example of CONT11

All upcoming figures show additional station results from Section 6.3 for the comparison of the ZTD, ZHD and ZWD determined by a pure VLBI analysis and determined by program RADIATE for the observations of the IVS CONT11 campaign.

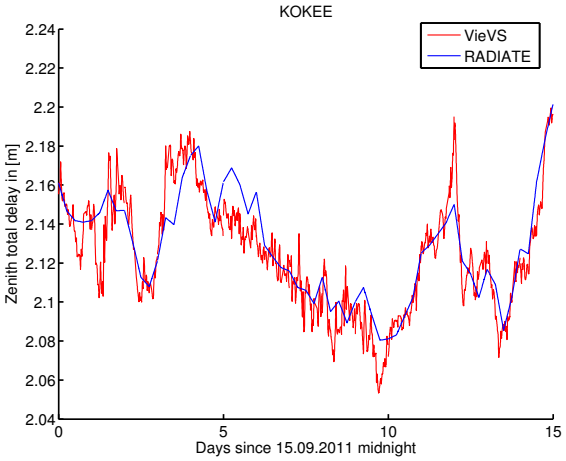

(a) ZTD.

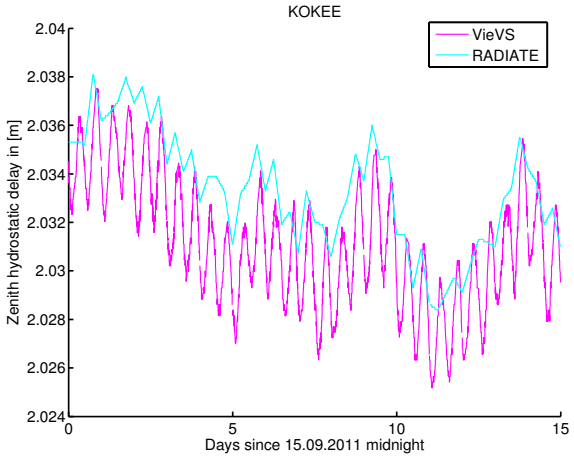

(b) ZHD.

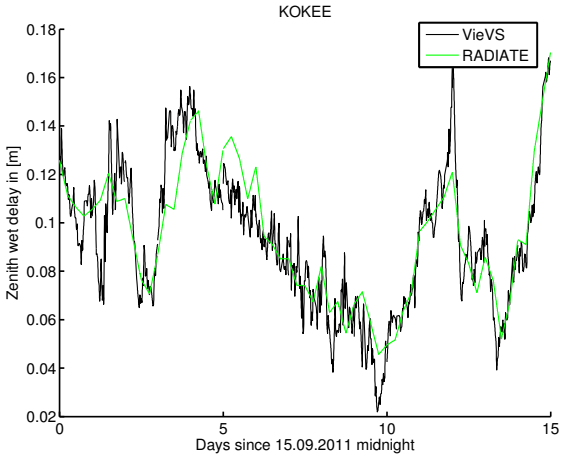

(c) ZWD.

Figure B.23: Comparison of the ZTD, ZHD and ZWD at station KOKEE for the observations of CONT11 from a VLBI analysis with VieVS and from ray-tracing with program RADIATE. Breaks in the plotted lines may be visible after the last observation of the station in a specific session of CONT11.

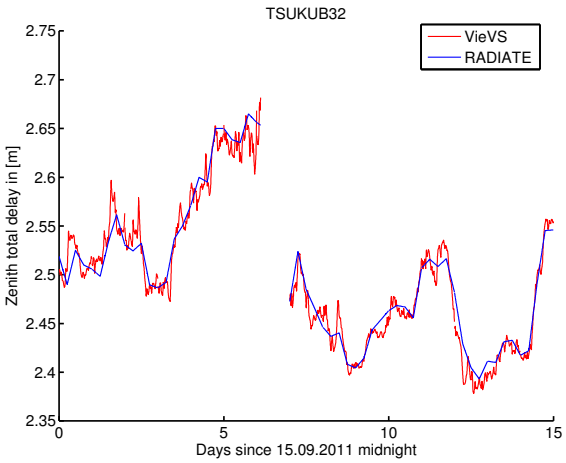

(a) ZTD.

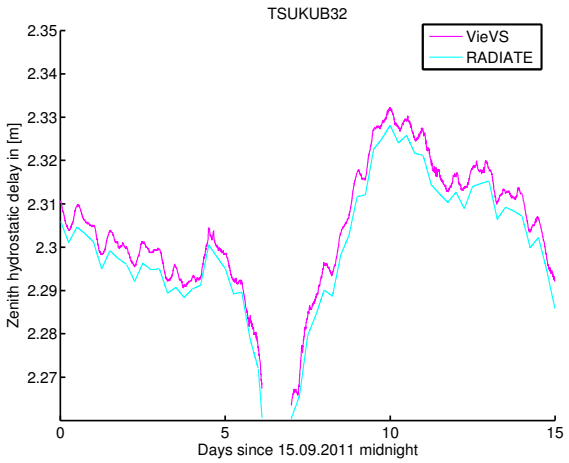

(b) ZHD.

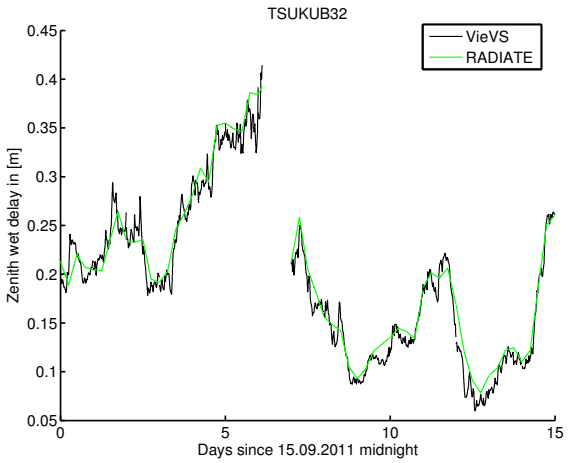

(c) ZWD.

Figure B.24: Comparison of the ZTD, ZHD and ZWD at station TSUKUB32 for the observations of CONT11 from a VLBI analysis with VieVS and from ray-tracing with program RADIATE. Breaks in the plotted lines may be visible after the last observation of the station in a specific session of CONT11.

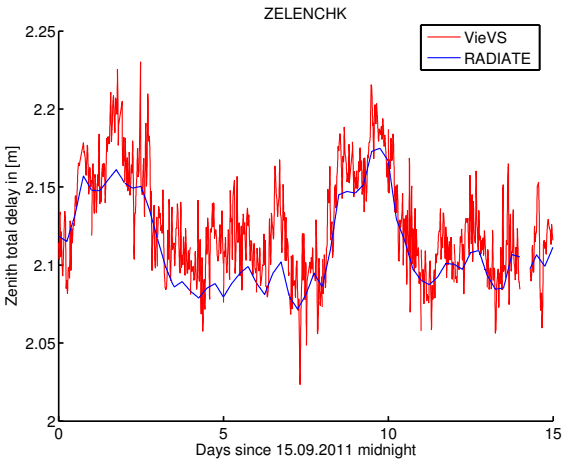

(a) ZTD.

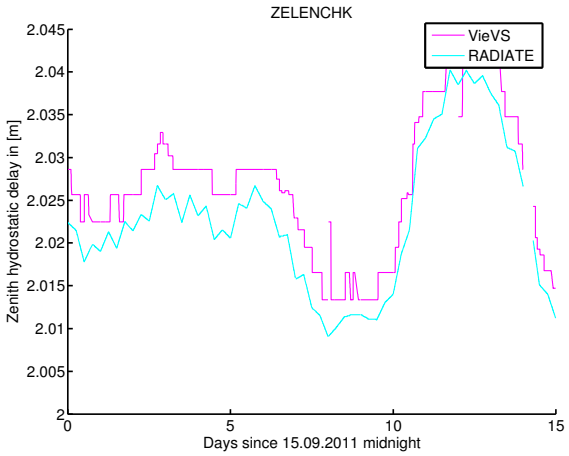

(b) ZHD.

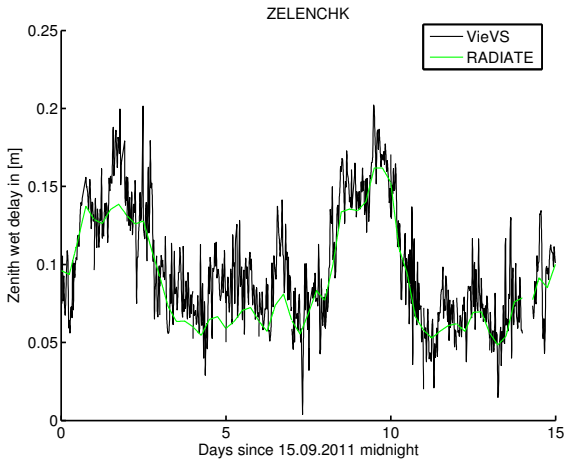

(c) ZWD.

Figure B.25: Comparison of the ZTD, ZHD and ZWD at station ZELENCHK for the observations of CONT11 from a VLBI analysis with VieVS and from ray-tracing with program RADIATE. Breaks in the plotted lines may be visible after the last observation of the station in a specific session of CONT11.

B.5 Additional figures of the impact of the ray-traced delays on the baseline length repeatability from VLBI analysis of the years 1999.0 to 2015.5

The upcoming figures show the ΔBLR as determined from Equation (6.5) or (6.6) and the δBLR as determined from Equation (6.7) or (6.8), which are all described in Section 6.4.3.2 to which also the presented results belong. The use of the equations depends on the used VLBI analysis results from the parameterizations 1 to 4, described in Section 6.4.2 on page 126 or more detailed in Table 6.7 on page 129.

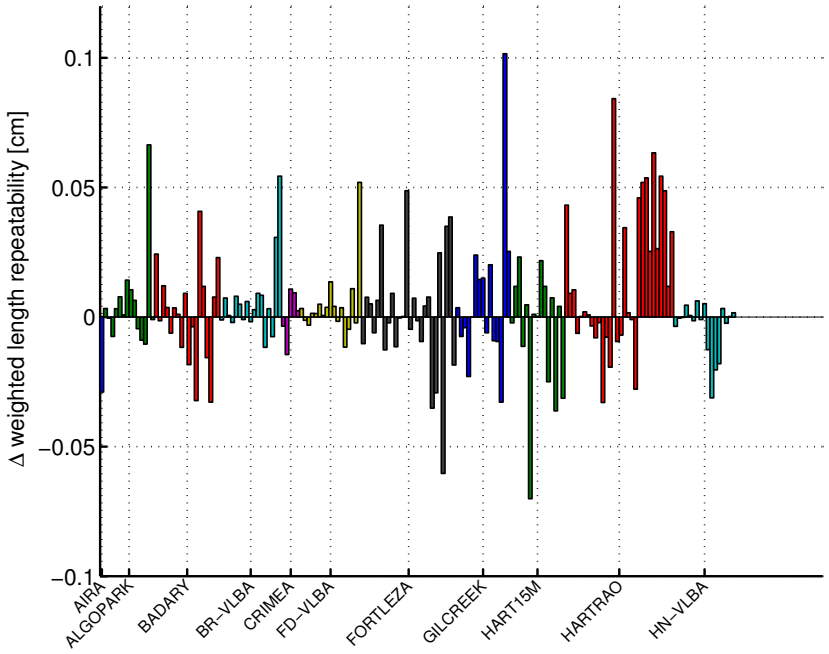

(a) ΔBLR of the baselines of the stations 1 to 11.

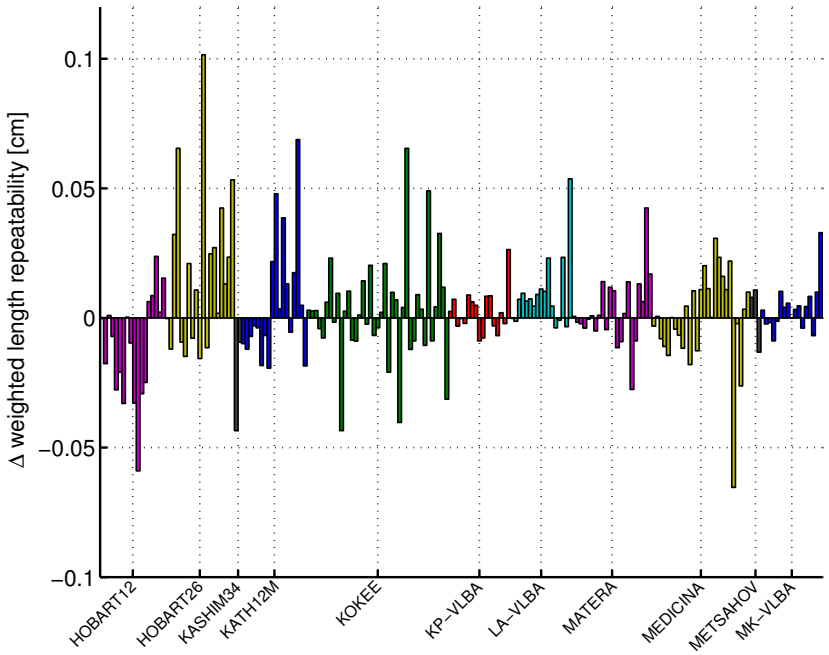

(b) ΔBLR of the baselines of the stations 12 to 22.

Figure B.26: ΔBLR as determined by Equation (6.5) between the BLR from the parameterizations 1 and 3, described on page 126, presented on a per-station basis. The baselines of each station are sorted by the mean baseline length. The ΔBLR show the impact if ray-traced delays are applied a priori in the VLBI analysis. Tropospheric gradients have been estimated for both analysis solutions. Positive differences indicate that the application of ray-traced delays improves the BLR.

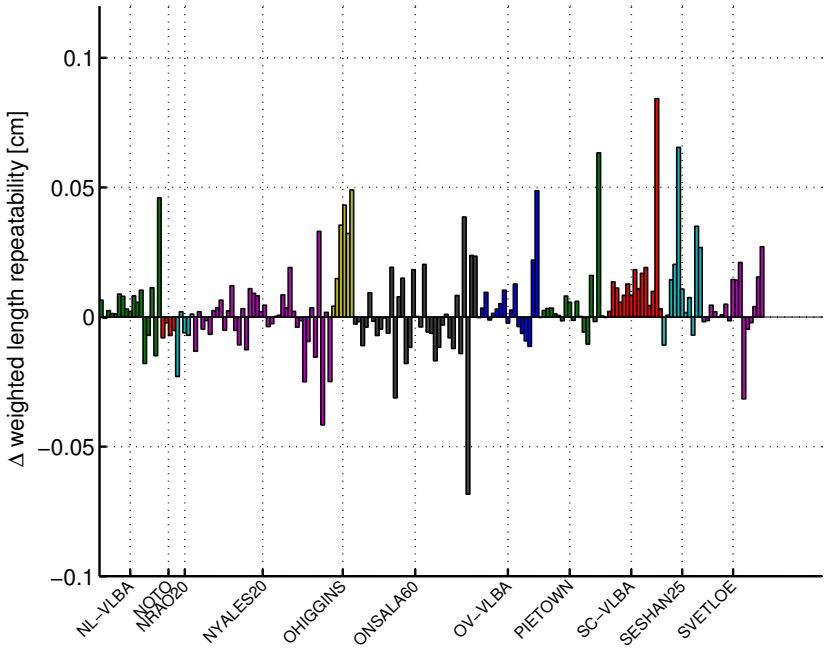

(c) ΔBLR of the baselines of the stations 23 to 33.

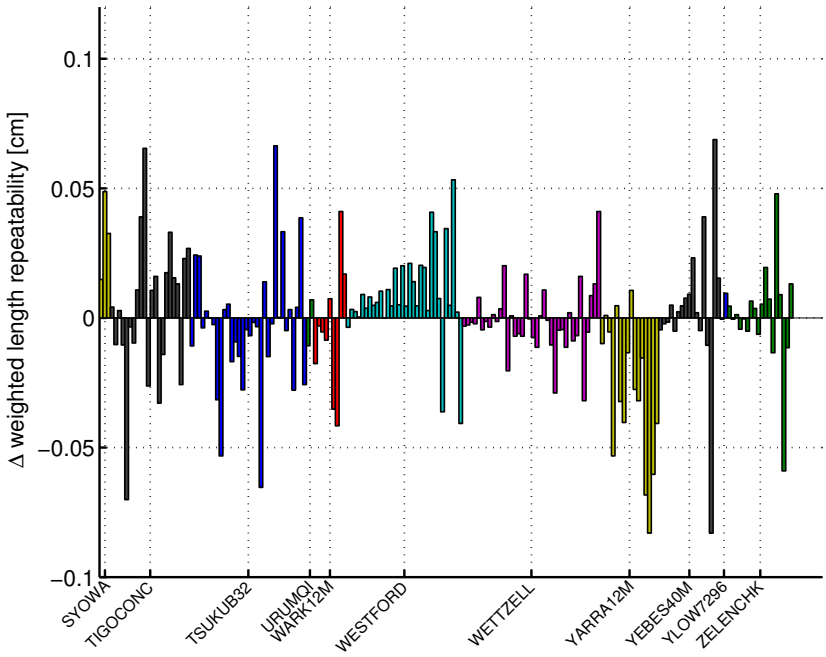

(d) ΔBLR of the baselines of the stations 34 to 44.

Figure B.26 (continued): ΔBLR as determined by Equation (6.5) between the BLR from the parameterizations 1 and 3, described on page 126, presented on a per-station basis. The baselines of each station are sorted by the mean baseline length. The ΔBLR show the impact if ray-traced delays are applied a priori in the VLBI analysis. Tropospheric gradients have been estimated for both analysis solutions. Positive differences indicate that the application of ray-traced delays improves the BLR.

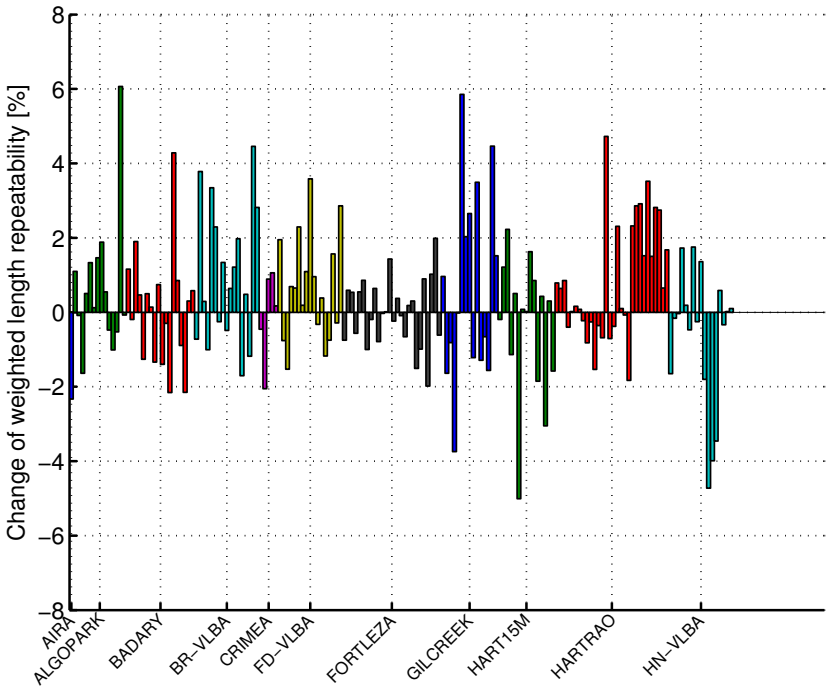

(a) δBLR of the baselines of the stations 1 to 11.

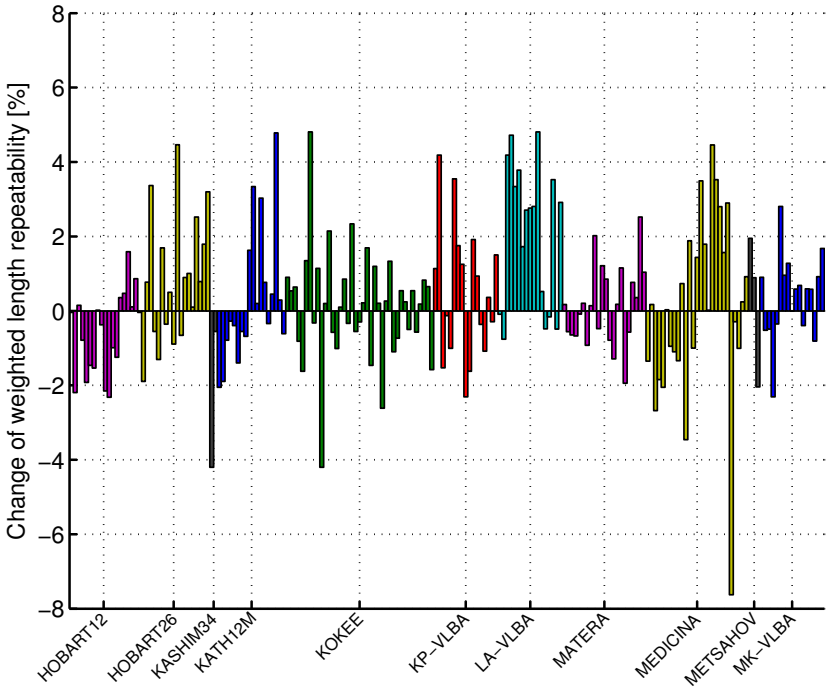

(b) δBLR of the baselines of the stations 12 to 22.

Figure B.27: Change of the BLR (δBLR) as determined by Equation (6.7) between the BLR from the parameterizations 1 and 3, described on page 126, presented on a per-station basis. The baselines of each station are sorted by the mean baseline length. Positive percentages indicate the relative amount of improvement of the BLR if ray-traced delays are applied compared to not applying them. In both cases tropospheric gradients have been estimated.

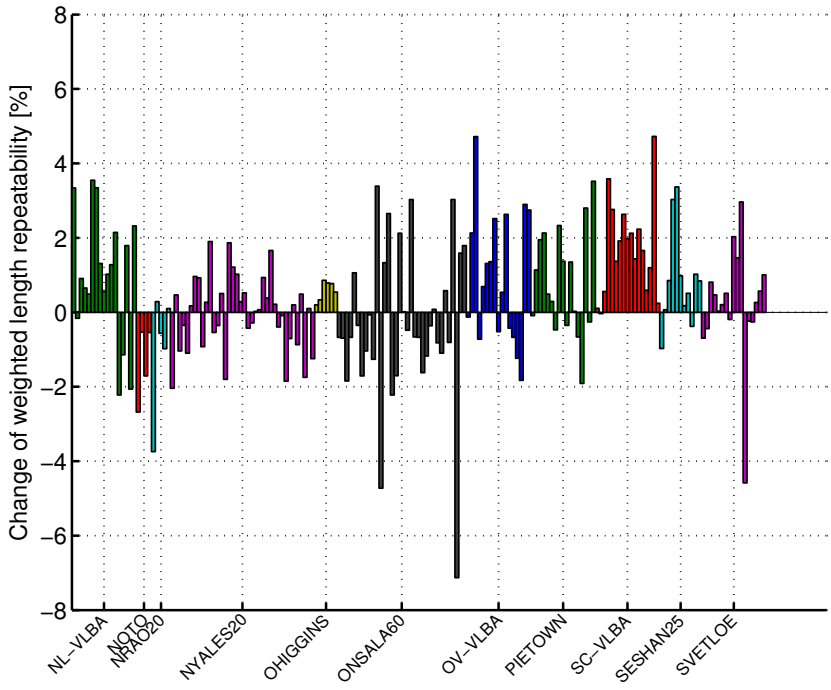

(c) δBLR of the baselines of the stations 23 to 33.

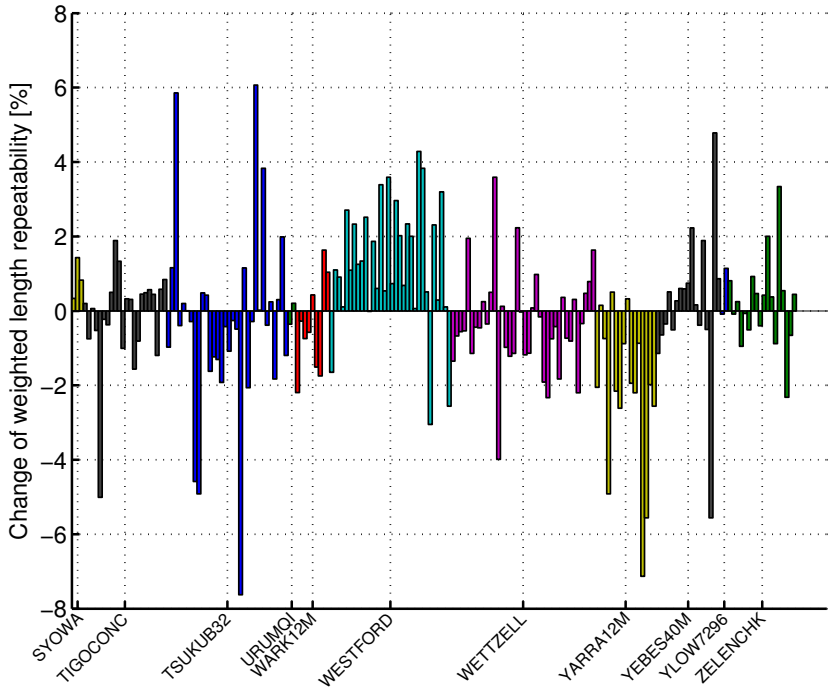

(d) δBLR of the baselines of the stations 34 to 44.

Figure B.27 (continued): Change of the BLR (δBLR) as determined by Equation (6.7) between the BLR from the parameterizations 1 and 3, described on page 126, presented on a per-station basis. The baselines of each station are sorted by the mean baseline length. Positive percentages indicate the relative amount of improvement of the BLR if ray-traced delays are applied compared to not applying them. In both cases tropospheric gradients have been estimated.

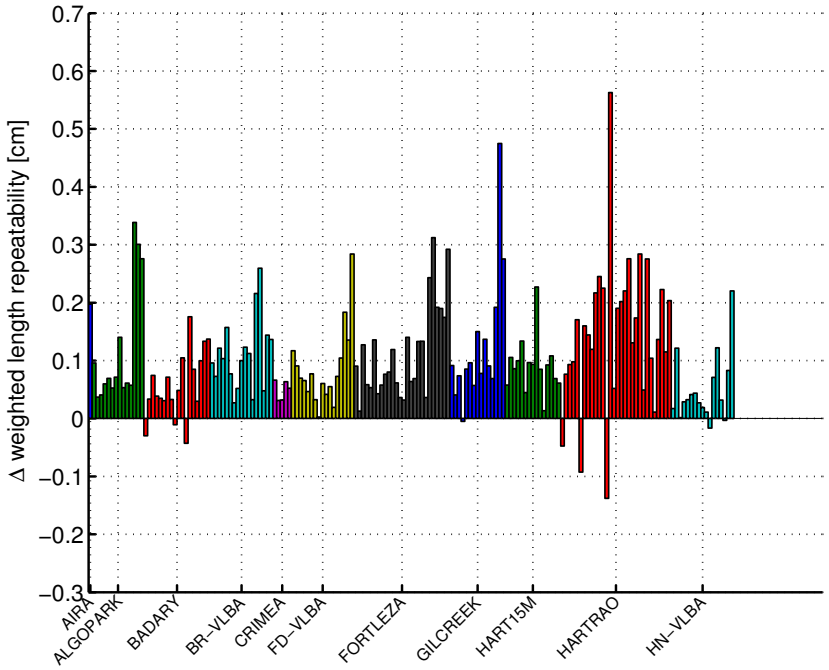

(a) ΔBLR of the baselines of the stations 1 to 11.

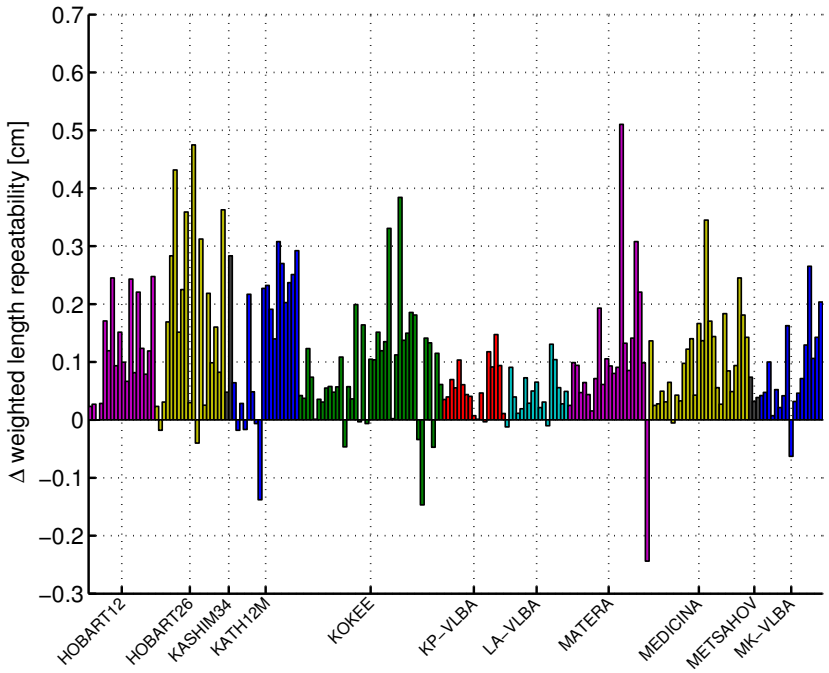

(b) ΔBLR of the baselines of the stations 12 to 22.

Figure B.28: ΔBLR as determined by Equation (6.6) between the BLR from the parameterizations 2 and 4, described on page 126, presented on a per-station basis. The baselines of each station are sorted by the mean baseline length. The ΔBLR show the impact if ray-traced delays are applied a priori in the VLBI analysis. Tropospheric gradients have not been estimated for the two analysis solutions. Positive differences indicate that the application of ray-traced delays improves the BLR.

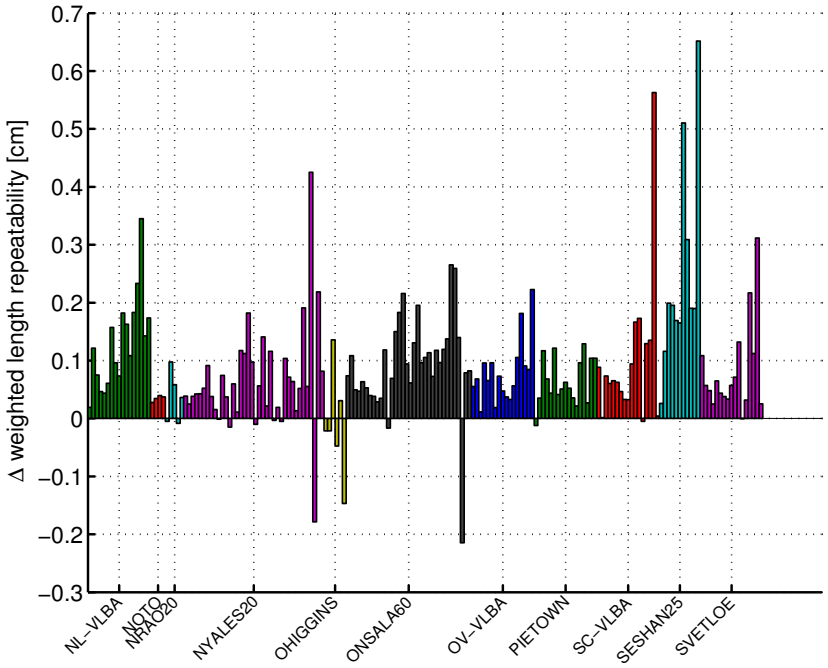

(c) ΔBLR of the baselines of the stations 23 to 33.

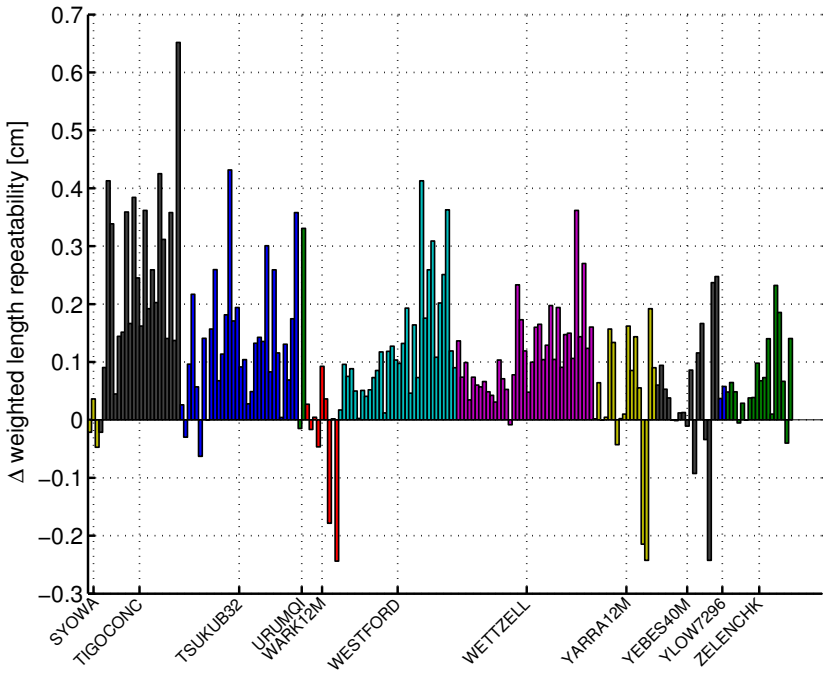

(d) ΔBLR of the baselines of the stations 34 to 44.

Figure B.28 (continued): ΔBLR as determined by Equation (6.6) between the BLR from the parameterizations 2 and 4, described on page 126, presented on a per-station basis. The baselines of each station are sorted by the mean baseline length. The ΔBLR show the impact if ray-traced delays are applied a priori in the VLBI analysis. Tropospheric gradients have not been estimated for the two analysis solutions. Positive differences indicate that the application of ray-traced delays improves the BLR.

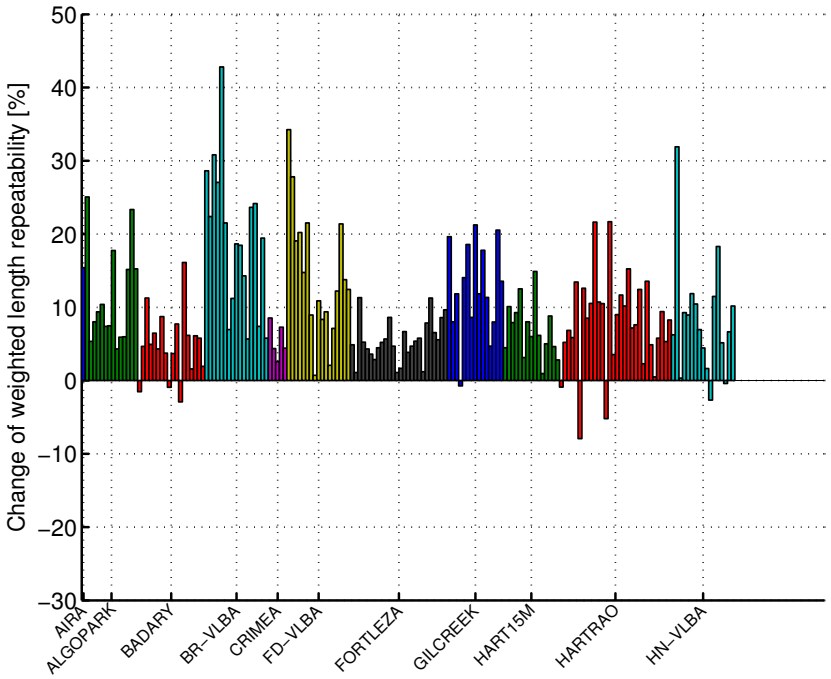

(a) δBLR of the baselines of the stations 1 to 11.

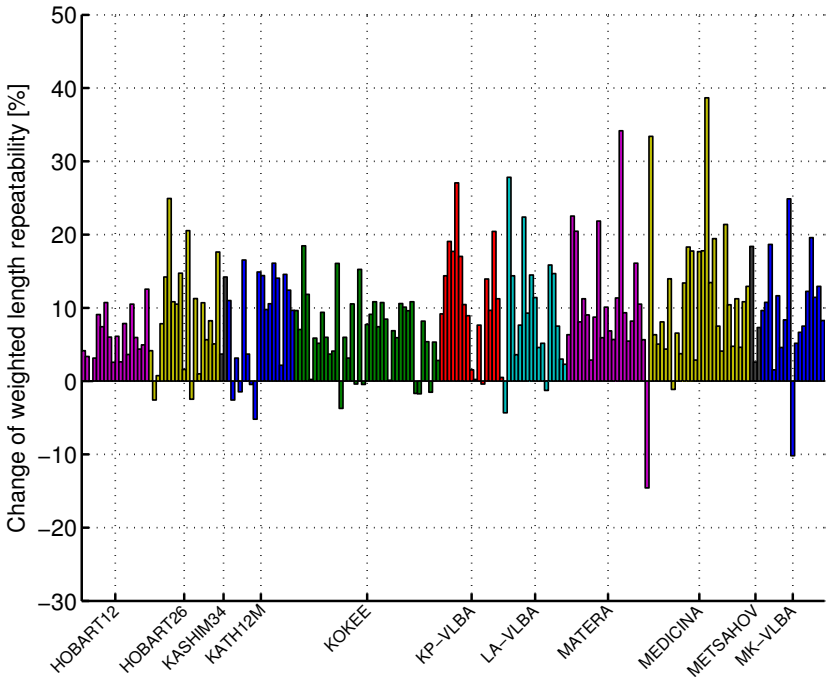

(b) δBLR of the baselines of the stations 12 to 22.

Figure B.29: Change of the BLR (δBLR) as determined by Equation (6.8) between the BLR from the parameterizations 2 and 4, described on page 126, presented on a per-station basis. The baselines of each station are sorted by the mean baseline length. Positive percentages indicate the relative amount of improvement of the BLR if ray-traced delays are applied compared to not applying them. In both cases no tropospheric gradients have been estimated.

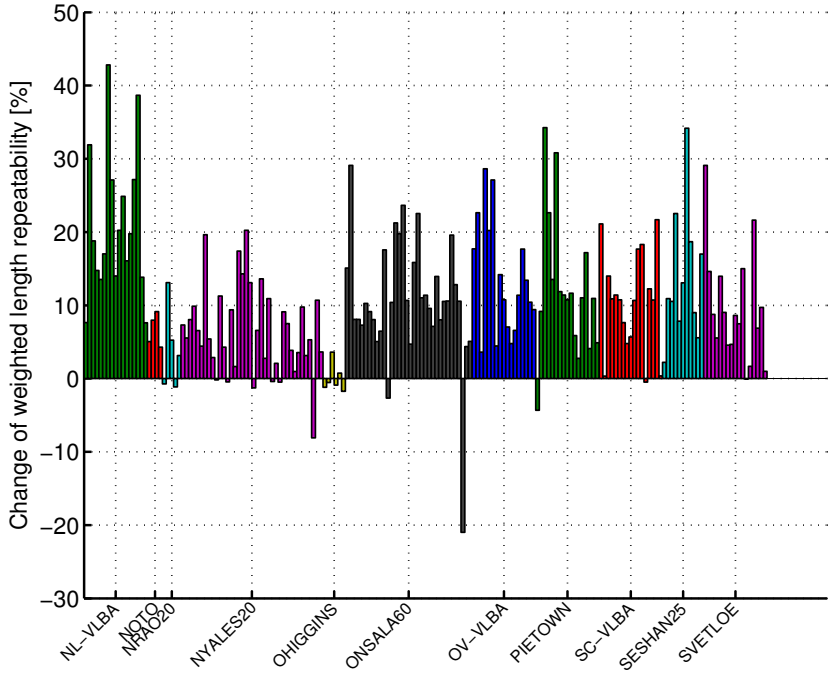

(c) δBLR of the baselines of the stations 23 to 33.

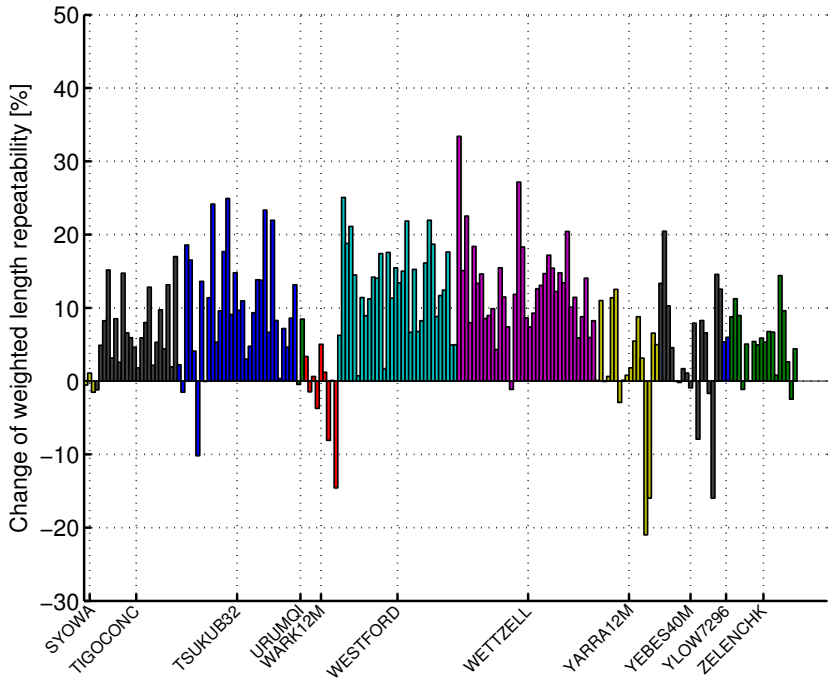

(d) δBLR of the baselines of the stations 34 to 44.

Figure B.29 (continued): Change of the BLR (δBLR) as determined by Equation (6.8) between the BLR from the parameterizations 2 and 4, described on page 126, presented on a per-station basis. The baselines of each station are sorted by the mean baseline length. Positive percentages indicate the relative amount of improvement of the BLR if ray-traced delays are applied compared to not applying them. In both cases no tropospheric gradients have been estimated.

B.6 Additional figures of the comparison of VLBI analysis results from using RADIATE or NASA GSFC ray-traced delays for the years 2000.0 to 2015.1

The upcoming figures show the ΔBLR as determined from Equation (6.30) or (6.31) and the δBLR as determined from Equation (6.32) or (6.33), which are all described in Section 6.5.3.2 to which also the presented results belong. The use of the equations depends on the used parameterization for determining the VLBI analysis results, which is parameterization 3 for the first comparison and parameterization 4 for the second comparison. They are described in Section 6.4.2 in Table 6.7 on page 129.

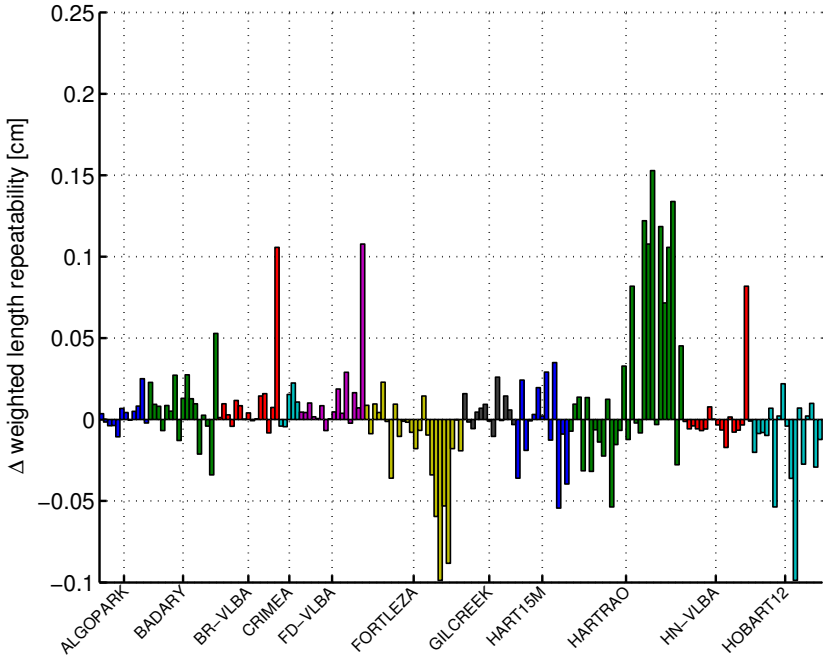

(a) ΔBLR of the baselines of the stations 1 to 11.

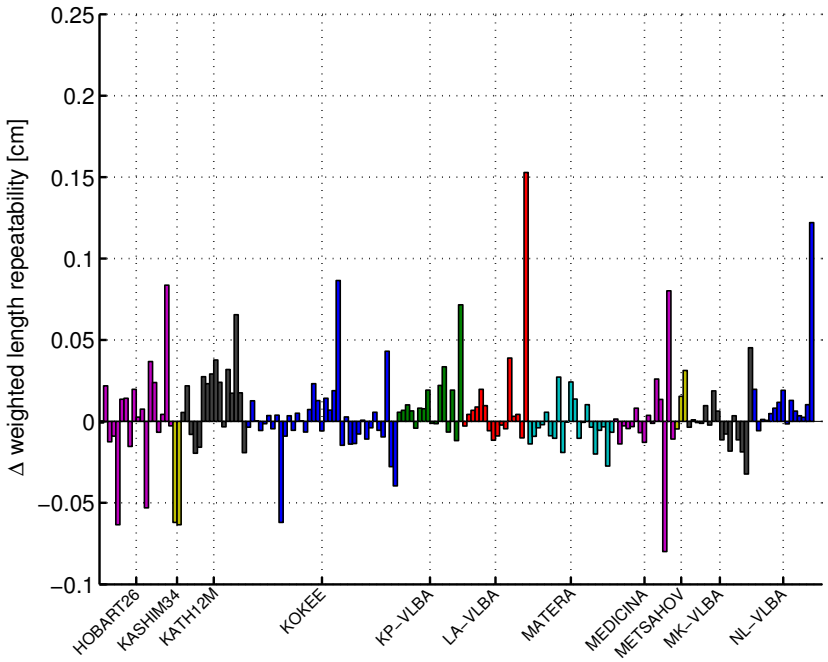

(b) ΔBLR of the baselines of the stations 12 to 22.

Figure B.30: ΔBLR as determined by Equation (6.30) between the VLBI analysis solutions from parameterization 3, described in Table 6.7 on page 129, with applied ray-traced delays from NASA GSFC or from RADIATE presented on a per-station basis. The baselines of each station are sorted by the mean baseline length. Tropospheric gradients have been estimated for both analysis solutions. Positive differences indicate that the application of ray-traced delays from RADIATE improves the BLR.

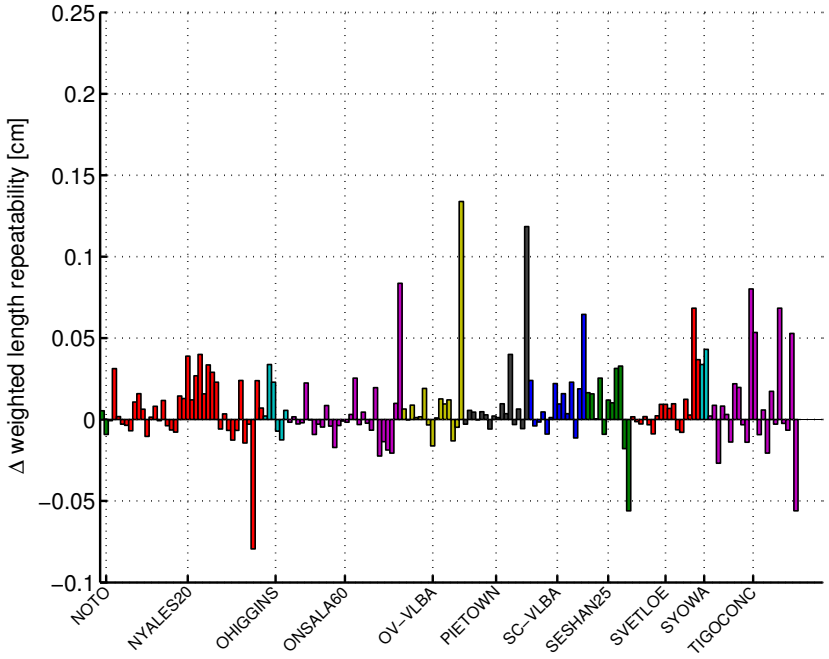

(c) ΔBLR of the baselines of the stations 23 to 33.

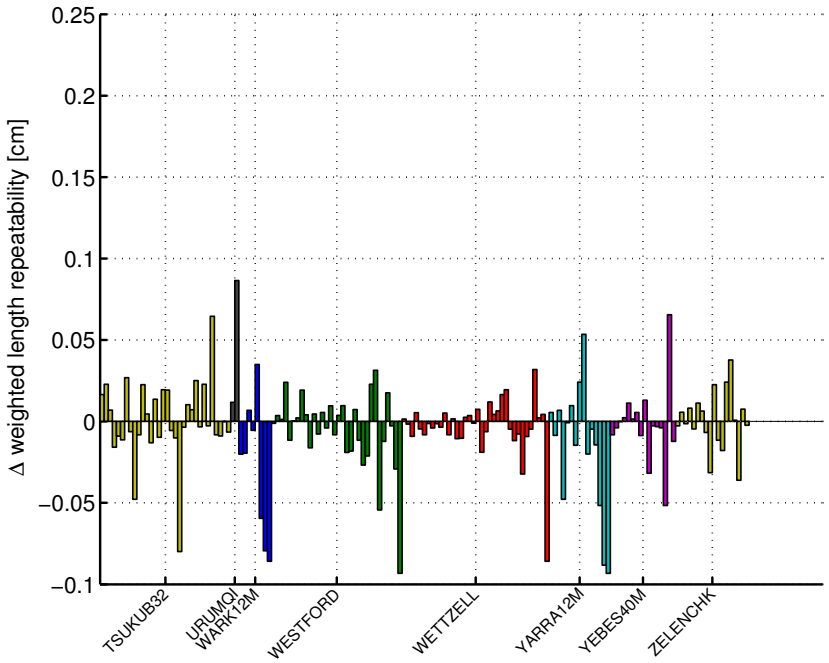

(d) ΔBLR of the baselines of the stations 34 to 41.

Figure B.30 (continued): ΔBLR as determined by Equation (6.30) between the VLBI analysis solutions from parameterization 3, described in Table 6.7 on page 129, with applied ray-traced delays from NASA GSFC or from RADIATE presented on a per-station basis. The baselines of each station are sorted by the mean baseline length. Tropospheric gradients have been estimated for both analysis solutions. Positive differences indicate that the application of ray-traced delays from RADIATE improves the BLR.

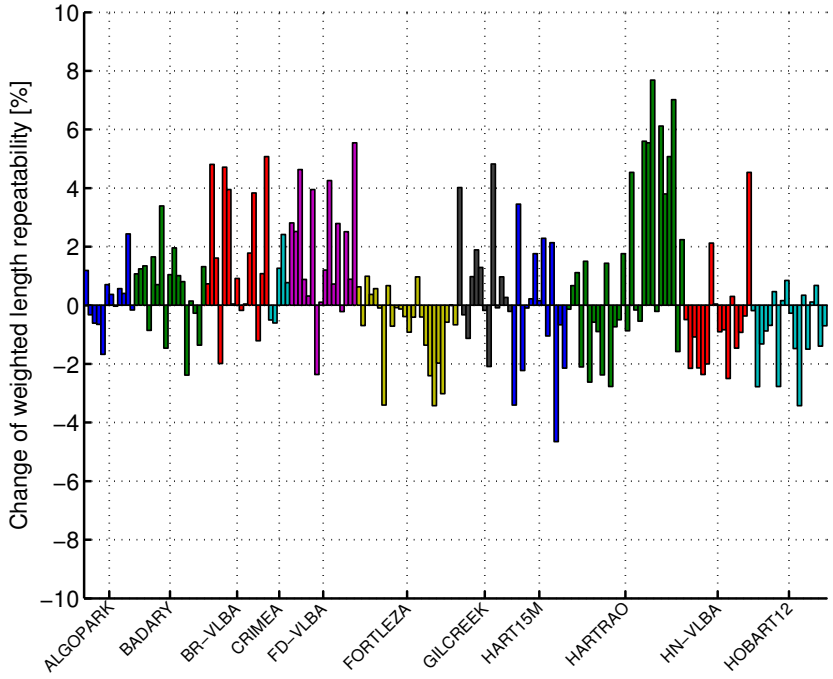

(a) δBLR of the baselines of the stations 1 to 11.

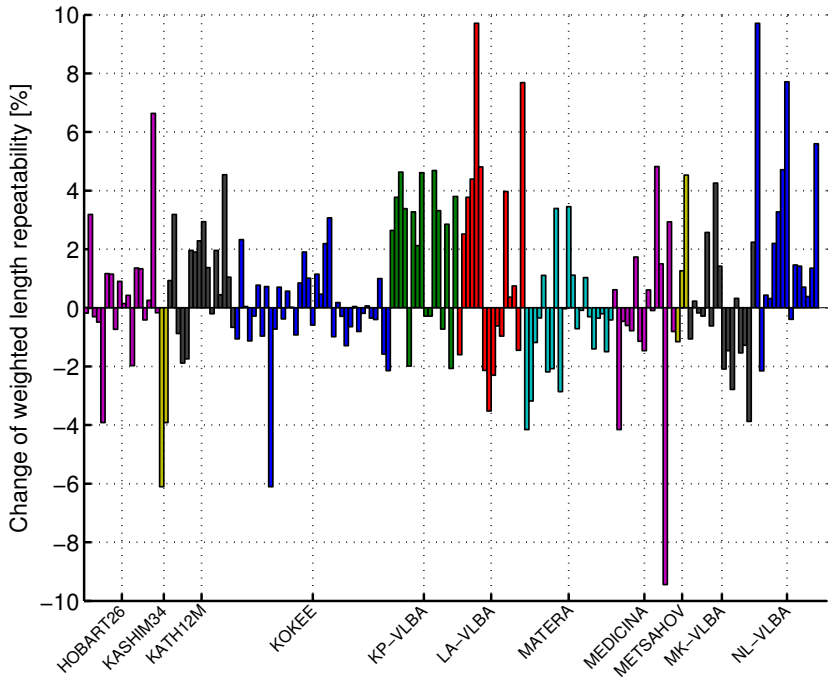

(b) δBLR of the baselines of the stations 12 to 22.

Figure B.31: Per-station representation of the δBLR as determined by Equation (6.32) if ray-traced delays from RADIATE are applied instead of those from NASA GSFC using always parameterization 3, described in Table 6.7 on page 129. The baselines of each station are sorted by the mean baseline length. Positive percentages indicate the relative amount of improvement of the BLR if ray-traced delays from RADIATE are applied. Tropospheric gradients have been estimated.

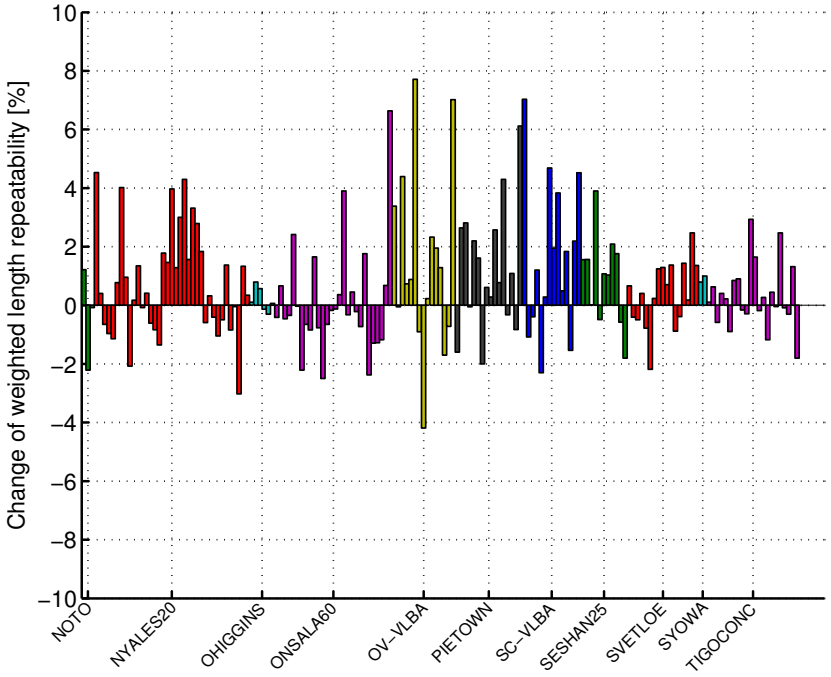

(c) δBLR of the baselines of the stations 23 to 33.

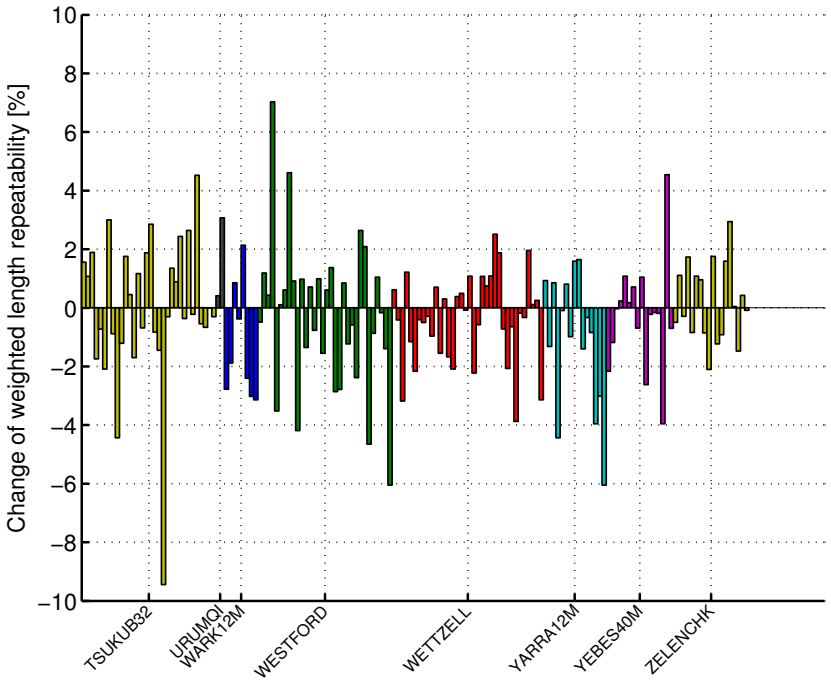

(d) δBLR of the baselines of the stations 34 to 41.

Figure B.31 (continued): Per-station representation of the δBLR as determined by Equation (6.32) if ray-traced delays from RADIATE are applied instead of those from NASA GSFC using always parameterization 3, described in Table 6.7 on page 129. The baselines of each station are sorted by the mean baseline length. Positive percentages indicate the relative amount of improvement of the BLR if ray-traced delays from RADIATE are applied.

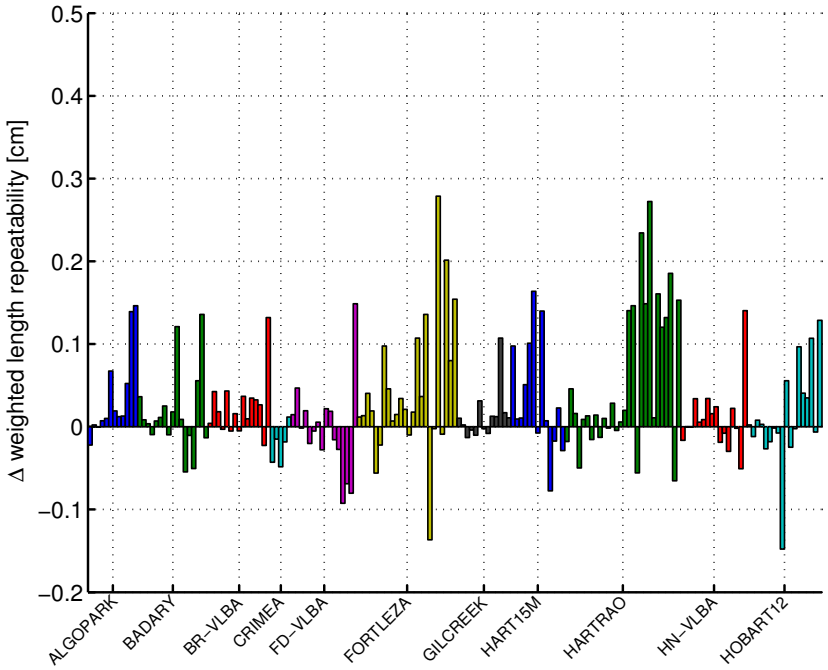

(a) ΔBLR of the baselines of the stations 1 to 11.

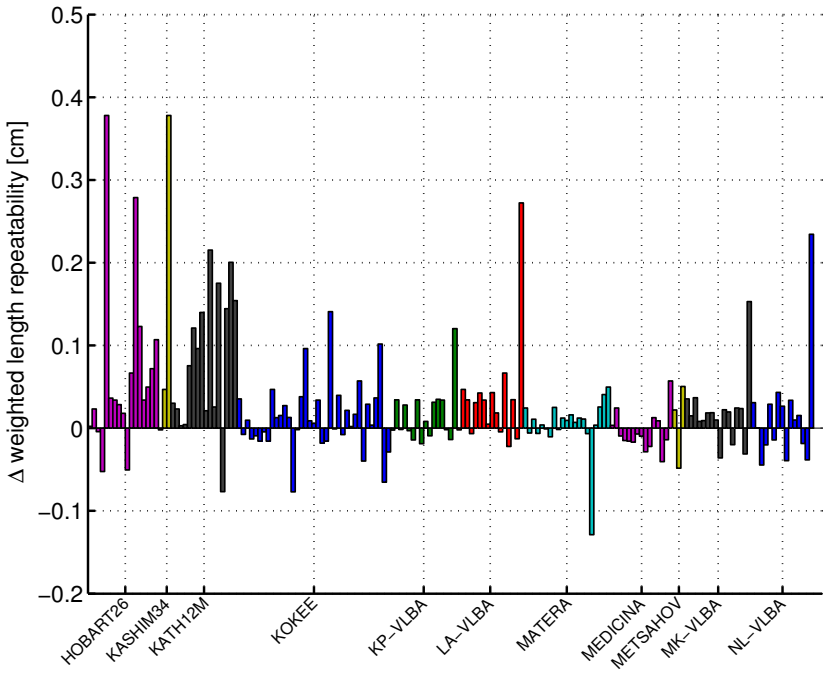

(b) ΔBLR of the baselines of the stations 12 to 22.

Figure B.32: ΔBLR as determined by Equation (6.31) between the VLBI analysis solutions from parameterization 4, described in Table 6.7 on page 129, with applied ray-traced delays from NASA GSFC or from RADIATE presented on a per-station basis. The baselines of each station are sorted by the mean baseline length. Tropospheric gradients have not been estimated for the two analysis solutions. Positive differences indicate that the application of ray-traced delays from RADIATE improves the BLR.

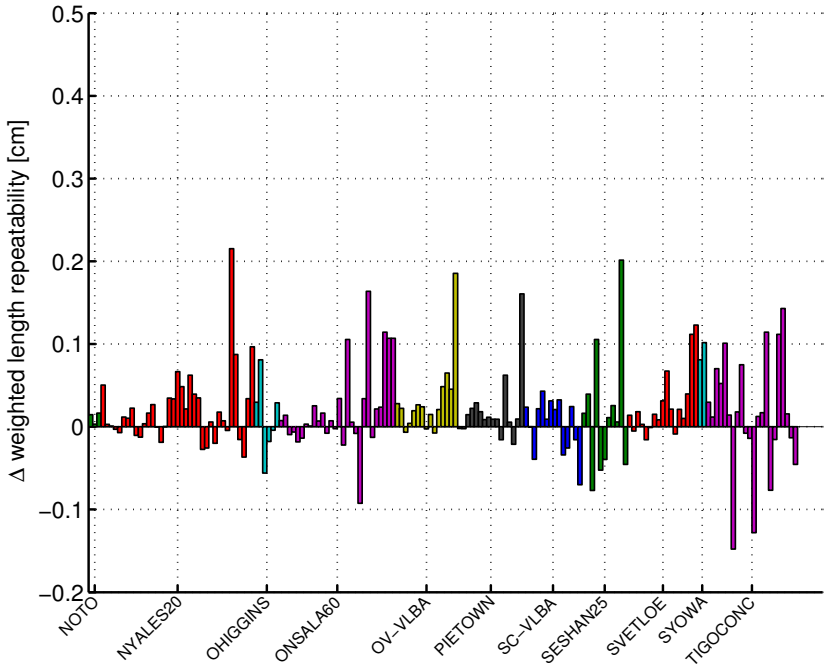

(c) ΔBLR of the baselines of the stations 23 to 33.

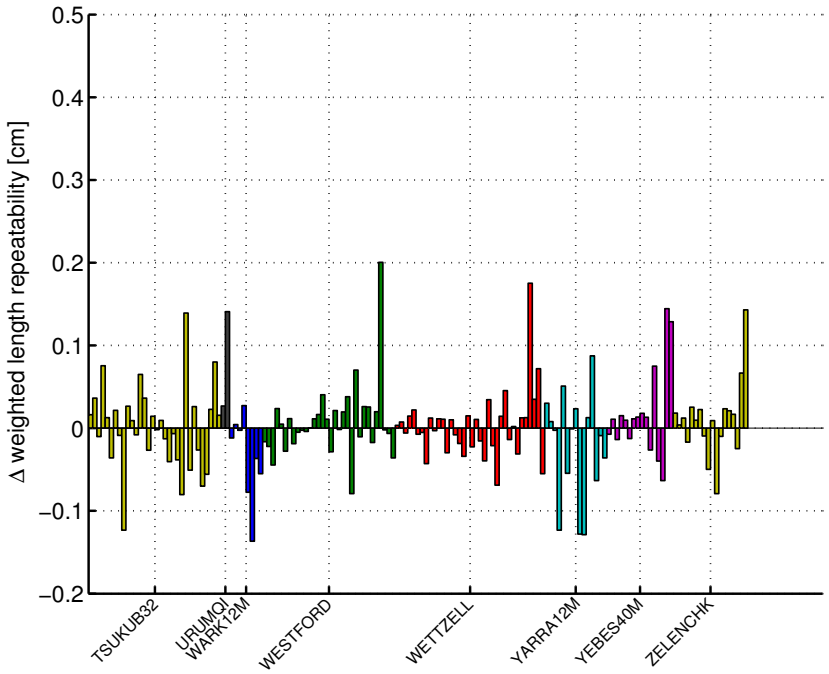

(d) ΔBLR of the baselines of the stations 34 to 41.

Figure B.32 (continued): ΔBLR as determined by Equation (6.31) between the VLBI analysis solutions from parameterization 4, described in Table 6.7 on page 129, with applied ray-traced delays from NASA GSFC or from RADIATE presented on a per-station basis. The baselines of each station are sorted by the mean baseline length. Tropospheric gradients have not been estimated for the two analysis solutions. Positive differences indicate that the application of ray-traced delays from RADIATE improves the BLR.

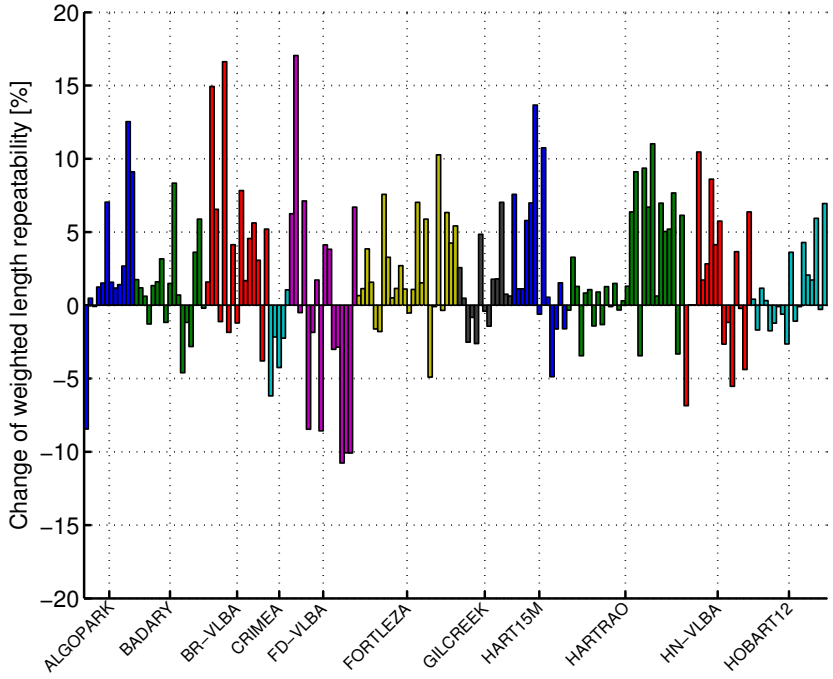

(a) δBLR of the baselines of the stations 1 to 11.

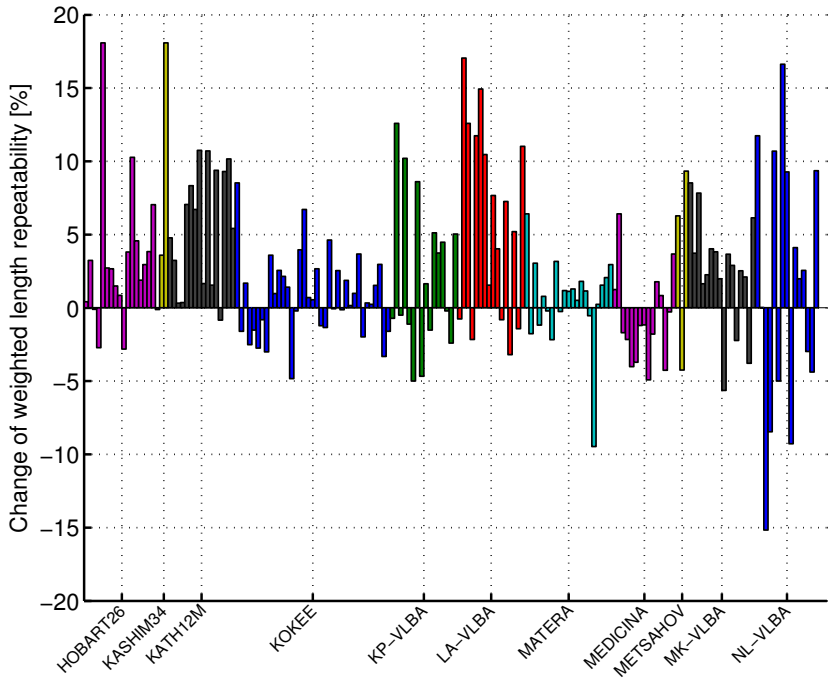

(b) δBLR of the baselines of the stations 12 to 22.

Figure B.33: Per-station representation of the δBLR as determined by Equation (6.33) if ray-traced delays from RADIATE are applied instead of those from NASA GSFC using always parameterization 4, described in Table 6.7 on page 129. The baselines of each station are sorted by the mean baseline length. Positive percentages indicate the relative amount of improvement of the BLR if ray-traced delays from RADIATE are applied. No trop. gradients have been estimated.

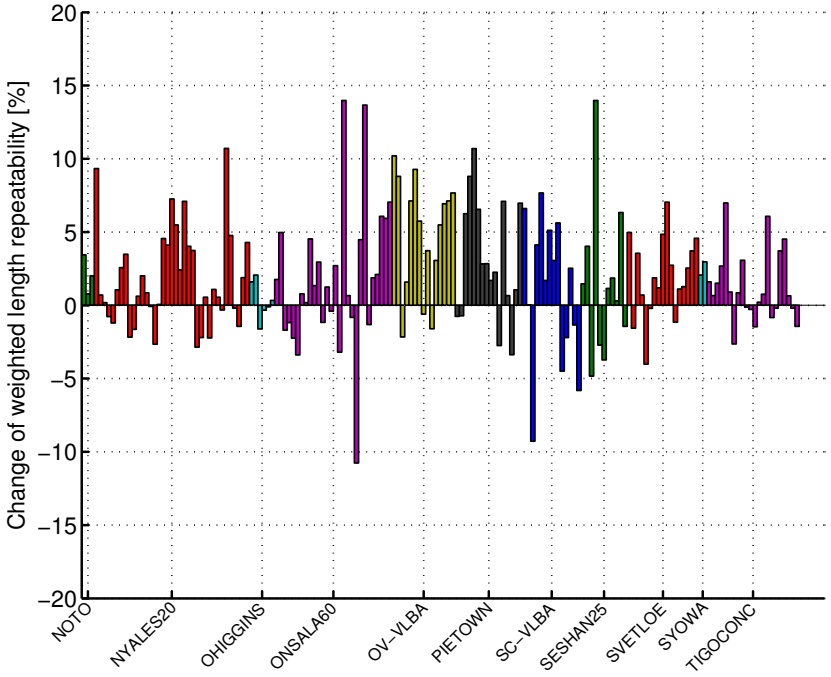

(c) δBLR of the baselines of the stations 23 to 33.

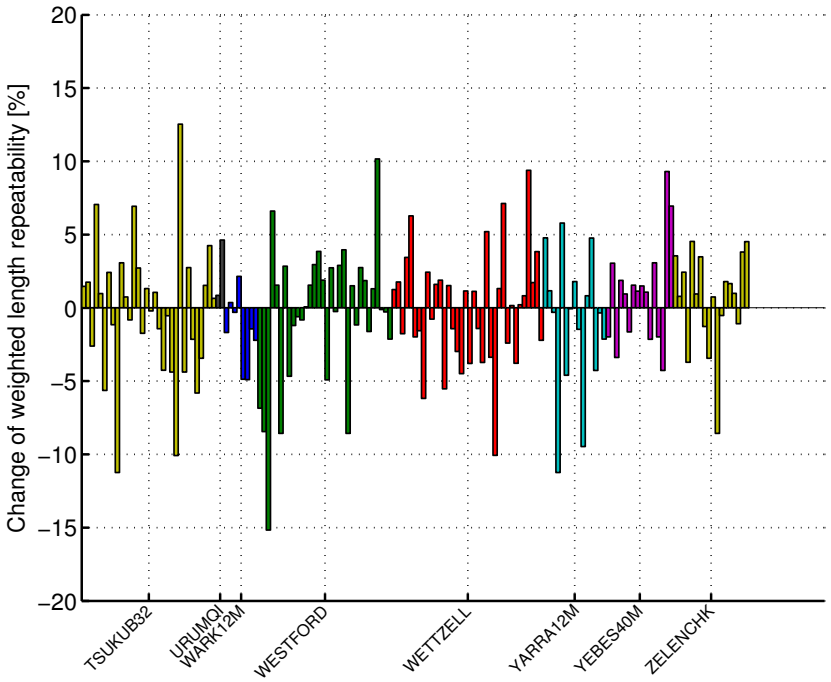

(d) δBLR of the baselines of the stations 34 to 41.

Figure B.33 (continued): Per-station representation of the δBLR as determined by Equation (6.33) if ray-traced delays from RADIATE are applied instead of those from NASA GSFC using always parameterization 4, described in Table 6.7 on page 129. The baselines of each station are sorted by the mean baseline length. Positive percentages indicate the relative amount of improvement of the BLR if ray-traced delays from RADIATE are applied.

List of Figures

List of Tables

Acronyms

Numbers

1D one-dimensional

2D two-dimensional

3D three-dimensional

A

APL Atmospheric Pressure Loading

C

CONT11 Continuous VLBI Campaign 2011

CPU Central Processing Unit

CRF Celestial Reference Frame

E

ECMWF European Centre for Medium-Range Weather Forecasts

EGM2008 Earth Gravitational Model 2008

EGM96 Earth Gravitational Model 1996

EOP Earth Orientation Parameter

ERA-40 ECMWF 40 years re-analysis

ERA-Interim ECMWF Re-Analyis-Interim

F

FWF Austrian Science Fund - Fonds zur Förderung der wissenschaftlichen Forschung

G

GEOS Goddard Earth Observing System Model

GMAO Global Modeling and Assimilation Office

GMF Global Mapping Function

GNSS Global Navigation Satellite Systems

GPU Graphics Processing Unit

I

IAU International Astronomical Union

ICRF International Celestial Reference Frame

ICRF2 International Celestial Reference Frame 2nd realization

IERS International Earth Rotation and Reference Systems Service

InSAR Interferometric Synthetic Aperture Radar

ITRF International Terrestrial Reference Frame

IVS International VLBI Service for Geodesy and Astrometry

L

LLR Lunar Laser Ranging

M

MPM Millimeter-wave Propagation Model

MTT Massachusetts Institute of Technology Temperature

N

NASA GSFC National Aeronautics and Space Administration Goddard Space Flight Center

NASA JPL National Aeronautics and Space Administration Jet Propulsion Laboratory

NGS National Geodetic Survey

NMF New or also called Niell Mapping Functions

NNR No-Net-Rotation

NNT No-Net-Translation

NWM Numerical Weather Model

P

PPP Precise Point Positioning

PWL piecewise-linear

R

RADIATE Ray-traced Delays in the Atmosphere

RAM Random Access Memory

RD Ray-traced Delays

S

SI Système International d'Unités (International System of Units)

SLR Satellite Laser Ranging

T

TRF Terrestrial Reference Frame

U

UTC Universal Time Coordinated

V

VGOS VLBI Global Observing System

VieVS Vienna VLBI Software

VLBI Very Long Baseline Interferometry

VMF Vienna Mapping Functions

VMF1 Vienna Mapping Functions 1

W

WGS84 World Geodetic System 1984

WVR Water Vapour Radiometer

Symbols

Notation	Description
A	exponential coefficient for the relation of radial distances to refractive indices in the Thayer ray-tracing approach
a	scalar in Hamiltonian formalism
a_{ell}	semi-major axis of the reference ellipsoid
α	azimuth angle
α_0	initial geodetic azimuth angle
b	baseline length
b_{ell}	semi-minor axis of the reference ellipsoid
$\overline{b}$	mean baseline length
$\vec{B}$	magnetic field vector
$\vec{b}$	baseline vector
$\overline{b}_w$	weighted mean baseline length
β	tilting angle of the mapping function
BLR	baseline length repeatability
BW	recorded bandwidth
BW_{eff}	effective bandwidth
c	speed of light in vacuum
C_A	effective antenna signal collection area
c'	speed of light in medium
C_b	empirical constant for the a priori geometric bending effect correction model
C_{grad}	coefficient for the gradient mapping function
C_n	coefficient for the exponential decrease of the refractive index with height

Notation	Description
C_p	geopotential
C_{p_w}	coefficient for the exponential decrease of the water vapour pressure with height
χ	auxiliary parameter for latitude dependent weighting in bilinear interpolation
$Cov_{\Delta NEU}$	covariance matrix of the differences in the North-, East- and up-component
$Cov_{\Delta XYZ}$	covariance matrix of the differences in XYZ
Cov	covariance matrix in XYZ
D	functional model of the least-squares adjustment
Δ	difference
δ	difference between the geocentric angles
ΔBLR	difference in the baseline length repeatability
δBLR	change of the baseline length repeatability
ΔE	difference in the East-component
Δe	difference in the elevation angle
$\overline{\Delta E}$	mean difference in the East-component
Δe_{out}	difference in the outgoing elevation angle
Δh	height difference
ΔL	atmospheric delay
ΔL_h	slant hydrostatic delay
$\Delta L_{t_{ep1}}$	atmospheric delay at the time of epoch 1
$\Delta L_{t_{ep2}}$	atmospheric delay at the time of epoch 2
$\Delta L_{t_{obs}}$	atmospheric delay at the time of the observation
ΔL_w	slant wet delay
ΔL^z	zenith total delay
ΔL_h^z	zenith hydrostatic delay
ΔL_w^z	zenith wet delay
ΔN	difference in the North-component
$\overline{\Delta N}$	mean difference in the North-component
ΔP	horizontal displacement
$\overline{\Delta P}$	mean horizontal displacement
ΔSCR	difference in the station coordinate repeatability

Notation	Description
ΔSHD	difference in the slant hydrostatic delay
ΔSHD_{mf}	difference in the slant hydrostatic delay from mapping factors
ΔSTD	difference in the slant total delay
ΔSTD_{mf}	difference in the slant total delay from mapping factors
ΔSWD	difference in the slant wet delay
ΔSWD_{mf}	difference in the slant wet delay from mapping factors
ΔU	difference in the up-component
$\overline{\Delta U}$	mean difference in the up-component
$\Delta UT1$	difference between UT1 and UTC
ΔX	difference in the X-coordinate
ΔY	difference in the Y-coordinate
ΔZ	difference in the Z-coordinate
ΔZHD	difference in the zenith hydrostatic delay
ΔZHD^S	difference in the zenith hydrostatic delay from Saastamoinen's equation
ΔZTD	difference in the zenith total delay
ΔZWD	difference in the zenith wet delay
e	elevation angle
e_{cc}^2	squared first numerical eccentricity of the reference ellipsoid
e_{out}	outgoing elevation angle
e_{outrt}	outgoing elevation angle from ray-tracing
$\vec{E}$	electric field vector
ε	electric permittivity
ε_0	vacuum permittivity or electric constant
η	geocentric angle
F_d	flux density of the source
G	geometric path in vacuum
g	gravity

Notation	Description
g_{apbend}	a priori geometric bending effect correction
G_{atm}	atmospheric gradient
g_{bend}	geometric bending effect
G_E	atmospheric gradient in East-direction
$\overline{g}$	mean acceleration due to the gravity between the geoid and the position of the point
G_N	atmospheric gradient in North-direction
g_n	normal gravity constant
γ	post-Newtonian parameter of space curvature due to gravity
Γ_i	constant Γ for gas i
Γ_w	constant Γ for wet air
gmf_h	hydrostatic global mapping factor
$H(\vec{r}, \nabla L)$	Hamiltonian function
h	height
h_0	(ellipsoidal) height of the station
h_d	geopotential (dynamic) height
h_{ell}	ellipsoidal height
h_L	Love number of the solid Earth tide model
h_N	geoid undulation
h_{orth}	orthometric (geometric) height
h_{scale}	scale height of the neutral atmosphere
k_1	refractivity coefficient k_1
k_2	refractivity coefficient k_2
k_2'	refractivity coefficient k_2'
k_3	refractivity coefficient k_3
k_4	refractivity coefficient k_4
k_B	Boltzmann constant
L	electric path length
L_λ	component of the electric path length in longitude direction

Notation	Description
L_{λ_0}	initial component of the electric path length in longitude direction
L_r	component of the electric path length in radial direction
L_{r_0}	initial component of the electric path length in radial direction
l_S	Shida number of the solid Earth tide model
L_ϑ	component of the electric path length in co-latitude direction
L_{ϑ_0}	initial component of the electric path length in co-latitude direction
λ	longitude
λ_0	initial longitude
Λ_i	constant Λ for gas i
Λ_{lw}	constant Λ for liqid water
Λ_w	constant Λ for wet air
m	scale
M_d	molar mass of dry air
$\dot{m}$	temporal derivative of the scale
M_w	molar mass of water vapour
mf	total mapping function or total mapping factor
mf_g	gradient mapping function
mf_h	hydrostatic mapping function or hydrostatic mapping factor
mf_w	wet mapping function or wet mapping factor
mjd	modified Julian date
μ	magnetic permeability
μ_0	vacuum permeability or magnetic constant
N	refractivity
n	refractive index
n^*	refractive index at the discrete height level
n_0	initial refractive index
N_d	dry refractivity

Notation	Description
N_h	hydrostatic refractivity
n_h	hydrostatic refractive index
n_h^*	hydrostatic refractive index at the discrete height level
n_h^z	hydrostatic refractive index in zenith direction
$\hat{n}$	refined calculated mean refractive index for Snell's law of refraction
$\overline{n}$	refined refractive index at the ray point
$\overline{n}^z$	refined refractive index in zenith direction
N_v	wet refractivity
N_w	non-hydrostatic (wet) refractivity
n_w	non-hydrostatic (wet) refractive index
n_w^*	non-hydrostatic (wet) refractive index at the discrete height level
n_w^z	non-hydrostatic (wet) refractive index in zenith direction
n^z	refractive index in zenith direction
$\nabla n(r, \vartheta, \lambda)$	gradient of the refractive index
∇n_λ	gradient component of the refractive index in longitude direction
∇n_r	gradient component of the refractive index in radial direction
∇n_ϑ	gradient component of the refractive index in co-latitude direction
ν	frequency
Ω	rotation matrix
ω	auxiliary parameter
$\dot{\Omega}$	temporal derivative of the rotation matrix
$\dot{\omega}_X$	temporal derivative of the rotation angle around the X-axis
$\dot{\omega}_Y$	temporal derivative of the rotation angle around the Y-axis
$\dot{\omega}_Z$	temporal derivative of the rotation angle around the Z-axis

Notation	Description
ω_X	rotation angle around the X-axis
ω_Y	rotation angle around the Y-axis
ω_Z	rotation angle around the Z-axis
P	point on the ray trajectory
p	total pressure
p_0	total pressure at the station
p_d	partial pressure of dry air
p_w	partial pressure of water vapour
p_{w0}	water vapour pressure at the station
φ	latitude
φ_0	(ellipsoidal) latitude of the station
ψ	auxiliary parameter for water vapour pressure calculation
Q	point on the surface
q	specific humidity
R	universal gas constant
r	radial distance
r_0	initial radial distance
R_α	Euler radius of curvature
R_{corr}	cross-correlation function
R_d	specific gas constant of dry air
R_E	Earth radius
R_G	Gaussian curvature radius
R_M	meridian radius of curvature
RMS	root mean square
$\overline{r}$	mean radial distance
R_N	polar radius of curvature
$\vec{r}$	position vector
R_w	specific gas constant of wet air
ρ	total density of moist air
ρ_d	density of dry air
ρ_i	density of gas i

Notation	Description
ρ_{lw}	density of liqid water
ρ_w	density of wet air
S	geometric signal path
s	arc length along the ray
$\vec{s}_0$	direction to the source
$s_{\overline{\Delta E}}$	standard deviation of the differences in the East-component
$s_{\overline{\Delta N}}$	standard deviation of the differences in the North-component
$s_{\overline{\Delta P}}$	standard deviation of the horizontal displacements
$s_{\overline{\Delta U}}$	standard deviation of the differences in the up-component
SCR	station coordinate repeatability
SHD	slant hydrostatic delay
SHD_{mf}	slant hydrostatic delay from mapping factor
σ_{coor}	mean coordinate accuracy
$\sigma_{\Delta E}$	formal error of the difference in the East-component
$\sigma_{\Delta N}$	formal error of the difference in the North-component
$\sigma_{\Delta P}$	formal error of the horizontal displacement
$\sigma_{\Delta U}$	formal error of the difference in the up-component
$\sigma_{\Delta X}$	formal error of the difference in the X-coordinate
$\sigma_{\Delta Y}$	formal error of the difference in the Y-coordinate
$\sigma_{\Delta Z}$	formal error of the difference in the Z-coordinate
σ_m	standard deviation of the scale
$\sigma_{\dot{m}}$	standard deviation of the temporal derivative of the scale
$\sigma_{\dot{\omega}_X}$	standard deviation of the temporal derivative of the rotation angle around the X-axis

Notation	Description
$\sigma_{\dot{\omega}_Y}$	standard deviation of the temporal derivative of the rotation angle around the Y-axis
$\sigma_{\dot{\omega}_Z}$	standard deviation of the temporal derivative of the rotation angle around the Z-axis
σ_{ω_X}	standard deviation of the rotation angle around the X-axis
σ_{ω_Y}	standard deviation of the rotation angle around the Y-axis
σ_{ω_Z}	standard deviation of the rotation angle around the Z-axis
$\sigma_{\dot{T}_X}$	standard deviation of the temporal derivative of the translation in the X-component
$\sigma_{\dot{T}_Y}$	standard deviation of the temporal derivative of the translation in the Y-component
$\sigma_{\dot{T}_Z}$	standard deviation of the temporal derivative of the translation in the Z-component
σ_{T_X}	standard deviation of the translation in the X-component
σ_{T_Y}	standard deviation of the translation in the Y-component
σ_{T_Z}	standard deviation of the translation in the Z-component
σ_τ	resolution of the (group-)delay
σ_X	formal error of the X-coordinate
σ_{XYZ}	mean coordinate error in XYZ
σ_Y	formal error of the Y-coordinate
σ_Z	formal error of the Z-coordinate
SNR	signal-to-noise ratio
STD	slant total delay
STD_{mf}	slant total delay from mapping factor
SWD	slant wet delay
SWD_{mf}	slant wet delay from mapping factor
T	temperature
t	time
T_0	temperature at the station

Notation	Description
t_1	reception time at station 1
t_2	reception time at station 2
$\dot{\vec{T}}$	temporal derivative of the translation vector
$\dot{T}_X$	temporal derivative of the translation in the X-component
$\dot{T}_Y$	temporal derivative of the translation in the Y-component
$\dot{T}_Z$	temporal derivative of the translation in the Z-component
t_{ep1}	time of epoch 1
t_{ep2}	time of epoch 2
T_{int}	averaging or integration interval
t_{obs}	observation time
T_S	system temperature of the receiver
t_{signal}	propagation time of the signal
T_v	virtual temperature
$\vec{T}$	translation vector
T_X	translation in the X-component
T_Y	translation in the Y-component
T_Z	translation in the Z-component
τ	delay
θ	position dependent elevation angle
ϑ	co-latitude
ϑ_0	initial co-latitude
u	parameter of interest in Hamiltonian formalism
υ	digital loss factor
$UT1$	Universal Time 1
UTC	Universal Time Coordinated
V	antenna voltage
w	weight
X	Cartesian X-coordinate

Notation	Description
$\dot{X}$	velocity in X-direction
$\dot{\vec{X}}$	velocity vector
x_i	constant factor of contribution of gas i to the total dry pressure
$\vec{X}$	position vector
$\overline{X}_w$	weighted mean X-coordinate
ξ	auxiliary parameter for longitude dependent weighting in bilinear interpolation
Y	Cartesian Y-coordinate
y	parameter within a continued fraction for a mapping function
$\dot{Y}$	velocity in Y-direction
Z	Cartesian Z-coordinate
Z_d	compressibility factor of dry air
$\dot{Z}$	velocity in Z-direction
Z_w	compressibility factor of water vapour
ζ_0	initial geodetic zenith angle
ZHD	zenith hydrostatic delay
ZHD^S	zenith hydrostatic delay from Saastamoinen's equation
ZTD	zenith total delay
ZWD	zenith wet delay
ZWD^S	zenith wet delay from Saastamoinen's equation

Bibliography

ADAMS, J. C., W. S. BRAINERD, R. A. HENDRICKSON, R. E. MAINE, J. T. MARTIN and B. T. SMITH (2009). *The Fortran 2003 Handbook. The Complete Syntax, Features and Procedures*. Springer-Verlag London. ISBN: 978-1-84628-746-6. DOI: 10.1007/978-1-84628-746-6.

BÖCKMANN, S., T. ARTZ and A. NOTHNAGEL (2010). 'VLBI terrestrial reference frame contributions to ITRF2008'. In: *Journal of Geodesy* 84 (3), pp. 201–219. ISSN: 1432-1394. DOI: 10.1007/s00190-009-0357-7.

BÖHM, J. (2004). 'Troposphärische Laufzeitverzögerungen in der VLBI'. PhD thesis. Institut für Geodäsie und Geophysik, Fakultät für Mathematik und Geoinformation, Technische Universität Wien.

BÖHM, J., S. BÖHM, T. NILSSON, A. PANY, L. PLANK, H. SPICAKOVA, K. TEKE and H. SCHUH (2012). 'The new Vienna VLBI Software VieVS'. In: *Geodesy for Planet Earth. Proceedings of the 2009 IAG Symposium*. Ed. by S. C. KENYON, M. C. PACINO and U. J. MARTI. Vol. 136. International Association of Geodesy Symposia Series. Springer-Verlag Berlin Heidelberg, pp. 1007–1011. ISBN: 978-3-642-20337-4. DOI: 10.1007/978-3-642-20338-1_126.

BÖHM, J., G. MÖLLER, M. SCHINDELEGGER, G. PAIN and R. WEBER (2015). 'Development of an improved empirical model for slant delays in the troposphere (GPT2w)'. In: *GPS Solutions* 19 (3), pp. 433–441. ISSN: 1080-5370. DOI: 10.1007/s10291-014-0403-7.

BÖHM, J., A. NIELL, P. TREGONING and H. SCHUH (2006a). 'Global Mapping Function (GMF): A new empirical mapping function based on numerical weather model data'. In: *Geophysical Research Letters* 33.7. L07304. ISSN: 1944-8007. DOI: 10.1029/2005GL025546.

BÖHM, J., D. SALSTEIN, M. M. ALIZADEH and D. D. WIJAYA (2013). 'Geodetic and Atmospheric Background'. In: *Atmospheric Effects in Space Geodesy*. Ed. by J. BÖHM and H. SCHUH. Springer Atmospheric Sciences. Springer-Verlag Berlin Heidelberg, pp. 1–33. ISBN: 978-3-642-36931-5. DOI: 10.1007/978-3-642-36932-2_1.

BÖHM, J. and H. SCHUH (2004). 'Vienna mapping functions in VLBI analyses'. In: *Geophysical Research Letters* 31.1. L01603. ISSN: 1944-8007. DOI: 10.1029/2003GL018984.

BÖHM, J., B. WERL and H. SCHUH (2006b). 'Troposphere mapping functions for GPS and very long baseline interferometry from European Centre for Medium-Range Weather Forecasts operational analysis data'. In: *Journal of Geophysical Research: Solid Earth* 111.B2. B02406. ISSN: 2156-2202. DOI: 10.1029/2005JB003629.

BORN, M. and E. WOLF (1999). *Principles of optics. Electromagnetic theory of propagation, interference and diffraction of light*. 7th ed. Cambridge University Press. 952 pp. ISBN: 0 521 642221.

CAMPBELL, J. (2000). 'From Quasars to Benchmarks: VLBI Links Heaven and Earth'. In: *International VLBI Service for Geodesy and Astrometry 2000 General Meeting Proceedings*. Ed. by N. R. VANDENBERG and K. D. BAVER. NASA/CP-2000-209893, pp. 19–34.

CAPITAINE, N., P. T. WALLACE and J. CHAPRONT (2003). 'Expressions for IAU 2000 precession quantities'. In: *Astronomy & Astrophysics* 412.2, pp. 567–586. DOI: 10.1051/0004-6361:20031539.

ČERVENÝ, V. (2005). *Seismic ray theory*. Cambridge University Press. 713 pp. ISBN: 978-0-521-01822-7.

CHEN, G. and T. A. HERRING (1997). 'Effects of atmospheric azimuthal asymmetry on the analysis of space geodetic data'. In: *Journal of Geophysical Research: Solid Earth* 102.B9, pp. 20489–20502. ISSN: 2156-2202. DOI: 10.1029/97JB01739.

CHOI, J. (1996). 'Tropospheric Effects of Time Delays and Angle of Arrivals in the Low Elevation Angle for Radiowave Propagation'. In: *Military Communications Conference, 1996. MILCOM '96, Conference Proceedings, IEEE*. Vol. 3, pp. 1041–1044. DOI: 10.1109/MILCOM.1996.571440.

COESA (1976). *U.S. Standard Atmosphere, 1976*. NASA-TM-X-74335, NOAA-S/T 76-1562. Washington, D.C.: U.S. Committee Extension Standard Atmosphere (COESA), National Oceanic and Atmospheric Administration (NOAA), National Aeronautics and Space Administration (NASA), United States Air Force (USAF). 241 pp. U.S. Government Printing Office Washington D.C. 20402.

DABBERDT, W. F., R. SHELLHORN, H. COLE, A. PAUKKUNEN, J. HÖRHAMMER and V. ANTIKAINEN (2003). *Radiosondes*. In: *Encyclopedia of Atmospheric Sciences*. Ed. by J. R. HOLTON. Oxford Academic Press, pp. 1900–1913. ISBN: 978-0-12-227090-1. DOI: 10.1016/B0-12-227090-8/00344-4.

DAVIS, J. L., T. A. HERRING, I. I. SHAPIRO, A. E. E. ROGERS and G. ELGERED (1985). 'Geodesy by radio interferometry: Effects of atmospheric modeling errors on estimates of baseline length'. In: *Radio Science* 20.6, pp. 1593–1607. ISSN: 1944-799X. DOI: 10.1029/RS020i006p01593.

DAVIS, J. L., G. ELGERED, A. E. NIELL and C. E. KUEHN (1993). 'Ground-based measurement of gradients in the "wet" radio refractivity of air'. In: *Radio Science* 28.6, pp. 1003–1018. ISSN: 1944-799X. DOI: 10.1029/93RS01917.

DEBYE, P. J. W. (1929). *Polar Molecules*. Chemical Catalog Company, Inc., New York. 172 pp.

DEMTRÖDER, W. (2013a). 'Elektromagnetische Wellen im Vakuum'. In: *Experimentalphysik 2. Elektrizität und Optik*. Springer-Lehrbuch. Springer-Verlag Berlin Heidelberg. Chap. 7, pp. 191–217. ISBN: 978-3-642-29943-8. DOI: 10.1007/978-3-642-29944-5_7.

— (2013b). 'Elektromagnetische Wellen in Materie'. In: *Experimentalphysik 2. Elektrizität und Optik*. Springer-Lehrbuch. Springer-Verlag Berlin Heidelberg. Chap. 8, pp. 219–259. ISBN: 978-3-642-29943-8. DOI: 10.1007/978-3-642-29944-5_8.

ERIKSSON, D. and D. S. MACMILLAN (2016). *Tropospheric ray traced delays provided by the NASA GSFC VLBI group*. Tropospheric ray traced delays provided by the NASA GSFC VLBI group which are available at http://lacerta.gsfc.nasa.gov/tropodelays (Eriksson & MacMillan). The computations were based on a numerical weather model provided by the NASA Global Modeling and Assimilation Office (GMAO). NASA GSFC. URL: http://lacerta.gsfc.nasa.gov/tropodelays (visited on 18/02/2016).

ERIKSSON, D., D. S. MACMILLAN and J. M. GIPSON (2014). 'Tropospheric delay ray tracing applied in VLBI analysis'. In: *Journal of Geophysical Research: Solid Earth* 119 (12), pp. 9156–9170. ISSN: 2169-9356. DOI: 10.1002/2014JB011552.

ESSEN, L. and K. D. FROOME (1951). 'The Refractive Indices and Dielectric Constants of Air and its Principal Constituents at 24,000 Mc/s'. In: *Proceedings of the Physical Society*. Section B 64.10, pp. 862–875. DOI: 10.1088/0370-1301/64/10/303.

FEY, A. L., D. GORDON and C. S. JACOBS, eds. (2009). *The Second Realization of the International Celestial Reference Frame by Very Long Baseline Interferometry*. Presented on behalf of the IERS/IVS Working Group. IERS Technical Note No. 35. Frankfurt am Main: Verlag des Bundesamts für Kartographie und Geodäsie. 204 pp. ISBN: 3-89888-918-6.

FOLKNER, W. M., J. G. WILLIAMS and D. H. BOGGS (2009). 'The Planetary and Lunar Ephemeris DE 421'. In: *Interplanetary Network Progress Report* 42-178, pp. 1–34.

GALASSI, M., J. DAVIES, J. THEILER, B. GOUGH, G. JUNGMANN, P. ALKEN, M. BOOTH, F. ROSSI and R. ULERICH (2015). *GNU Scientific Library. Reference Manual*. Version 2.1.

GARDNER, C. S. (1976). 'Effects of horizontal refractivity gradients on the accuracy of laser ranging to satellites'. In: *Radio Science* 11.12, pp. 1037–1044. ISSN: 1944-799X. DOI: 10.1029/RS011i012p01037.

GEGOUT, P., R. BIANCALE and L. SOUDARIN (2011). 'Adaptive mapping functions to the azimuthal anisotropy of the neutral atmosphere'. In: *Journal of Geodesy* 85 (10), pp. 661–677. ISSN: 1432-1394. DOI: 10.1007/s00190-011-0474-y.

HARGREAVES, J. K. (1995). *The Solar-Terrestrial Environment. An Introduction to Geospace - the Science of the Terrestrial Upper Atmosphere, Ionosphere, and Magnetosphere*. Cambridge Atmospheric and Space Science Series. Cambridge University Press. 436 pp. ISBN: 9780521427371.

HERRING, T. A. (1992). 'Modeling atmospheric delays in the analysis of space geodetic data'. In: *Refraction of transatmospheric signals in geodesy. Proceedings of the symposium*. Ed. by J. C. DE MUNCK and T. A. T. SPOELSTRA. Publications on Geodesy 36. Delft, the Netherlands: Netherlands Geodetic Commission, pp. 157–164. ISBN: 978 90 6132 243 6.

HOBIGER, T., R. ICHIKAWA, Y. KOYAMA and T. KONDO (2008a). 'Fast and accurate ray-tracing algorithms for real-time space geodetic applications using numerical weather models'. In: *Journal of Geophysical Research: Atmospheres* 113 (D20302). ISSN: 2156-2202. DOI: 10.1029/2008JD010503.

HOBIGER, T., R. ICHIKAWA, Y. KOYAMA and T. KONDO (2009). 'Computation of Troposphere Slant Delays on a GPU'. In: *IEEE Transactions on Geoscience and Remote Sensing* 47.10, pp. 3313–3318. ISSN: 0196-2892. DOI: 10.1109/TGRS.2009.2022168.

HOBIGER, T., R. ICHIKAWA, T. TAKASU, Y. KOYAMA and T. KONDO (2008b). 'Ray-traced troposphere slant delays for precise point positioning'. In: *Earth, Planets and Space* 60 (5), e1–e4. ISSN: 1880-5981. DOI: 10.1186/BF03352809.

HOBIGER, T., Y. KINOSHITA, S. SHIMIZU, R. ICHIKAWA, M. FURUYA, T. KONDO and Y. KOYAMA (2010a). 'On the importance of accurately ray-traced troposphere corrections for Interferometric SAR data'. In: *Journal of Geodesy* 84 (9), pp. 537–546. ISSN: 1432-1394. DOI: 10.1007/s00190-010-0393-3.

HOBIGER, T., S. SHIMADA, S. SHIMIZU, R. ICHIKAWA, Y. KOYAMA and T. KONDO (2010b). 'Improving GPS positioning estimates during extreme weather situations by the help of fine-mesh numerical weather models'. In: *Journal of Atmospheric and Solar-Terrestrial Physics* 72 (2-3), pp. 262–270. ISSN: 1364-6826. DOI: 10.1016/j.jastp.2009.11.018.

HOFMANN-WELLENHOF, B., H. LICHTENEGGER and J. COLLINS (1992). *Global Positioning System. Theory and Practice*. Springer-Verlag Wien New York. 326 pp. ISBN: 0-387-82364-6.

HOFMEISTER, A. (2013). 'Bestimmung von himmelsfesten Referenzrahmen mit VLBI'. Master thesis. Research Group Advanced Geodesy, Department of Geodesy and Geophysics, Faculty of Mathematics and Geoinformation, Technische Universität Wien.

HOFMEISTER, A. and J. BÖHM (2014). 'Ray-traced Delays in the Atmosphere for Geodetic VLBI'. In: *IVS 2014 General Meeting Proceedings*. Ed. by D. BEHREND, K. D. BAVER and K. L. ARMSTRONG, pp. 283–287. ISBN: 978-7-03-042974-2.

HOFMEISTER, A., D. LANDSKRON and J. BÖHM (2015). 'Influence of the horizontal resolution of numerical weather models on ray-traced delays for VLBI analysis'. In: *Proceedings of the 22nd European VLBI Group for Geodesy and Astronomy Working Meeting*. Ed. by R. HAAS and F. COLOMER, pp. 162–166. ISBN: 978-989-20-6191-7.

HOPFIELD, H. S. (1969). 'Two-quartic tropospheric refractivity profile for correcting satellite data'. In: *Journal of Geophysical Research* 74 (18), pp. 4487–4499. ISSN: 2156-2202. DOI: 10.1029/JC074i018p04487.

HUNSUCKER, R. D. and J. K. HARGREAVES (2002). *The High-Latitude Ionosphere and its Effects on Radio Propagation*. Cambridge Atmospheric and Space Science Series. Cambridge University Press. ISBN: 9780521330831.

IFADIS, I. (1986). *The atmospheric delay of radio waves: Modeling the elevation dependence on a global scale*. Technical Report No. 38L. School of Electrical Computer Engineering, Chalmers University of Technology, Göteborg, Sweden. 115 pp.

IIZUKA, K. (2008). 'Geometrical Optics'. In: *Engineering Optics*. 3rd ed. Vol. 35. Springer Series in Optical Sciences. Springer New York, pp. 101–138. ISBN: 978-0-387-75723-0. DOI: 10.1007/978-0-387-75724-7_5.

IVS (2015). *Observing Program CONT11*. International VLBI Service for Geodesy and Astrometry. URL: http://ivscc.gsfc.nasa.gov/program/cont11/ (visited on 22/07/2015).

JACKSON, J. D. (1998). *Classical Electrodynamics*. 3rd ed. John Wiley & Sons, Inc. 832 pp. ISBN: 978-0-471-30932-1.

KLEIJER, F. (2004). *Troposphere Modeling and Filtering for Precise GPS Leveling*. Publications on Geodesy 56. NCG, Nederlandse Commissie voor Geodesie, Netherlands Geodetic Commission, Delft, The Netherlands. 282 pp. ISBN: 90 6132 284 7.

KLOSE, B. and H. KLOSE (2015). 'Die Erdatmosphäre: Ihre chemische Zusammensetzung, vertikale Struktur und Physik'. In: *Meteorologie*. Springer-Lehrbuch. Springer-Verlag Berlin Heidelberg. Chap. 2, pp. 15–84. ISBN: 978-3-662-43577-9. DOI: 10.1007/978-3-662-43578-6_2.

KRÁSNÁ, H. (2012). 'Estimation of solid Earth tidal parameters and FCN with VLBI'. PhD thesis. Department für Geodäsie und Geoinformation, Fakultät für Mathematik und Geoinformation, Technische Universität Wien.

KRÁSNÁ, H., J. BÖHM and H. SCHUH (2013). 'Tidal Love and Shida numbers estimated by geodetic VLBI'. In: *Journal of Geodynamics* 70, pp. 21–27. ISSN: 0264-3707. DOI: 10.1016/j.jog.2013.05.001.

KRAUS, H. (2001). *Die Atmosphäre der Erde. Eine Einführung in die Meteorologie*. 2nd ed. Springer-Verlag Berlin Heidelberg. 470 pp. ISBN: 3-540-41844-X.

LEMOINE, F. G., S. C. KENYON, J. K. FACTOR, R. G. TRIMMER, N. K. PAVLIS, D. S. CHINN, C. M. COX, S. M. KLOSKO, S. B. LUTHCKE, M. H. TORRENCE, Y. M. WANG, R. G. WILLIAMSON, E. C. PAVLIS, R. H. RAPP and T. R. OLSON (1998). *The Development of the Joint NASA GSFC and the National Imagery and Mapping Agency (NIMA) Geopotential Model EGM96*. NASA/TP-1998-206861. NASA Goddard Space Flight Center, Greenbelt, Maryland, 20771 USA.

LIDE, D. R., ed. (1997). *CRC Handbook of Chemistry and Physics*. 78th ed. Boca Raton, Florida: CRC Press.

LIEBE, H. J., G. A. HUFFORD and M. G. COTTON (1993). 'Propagation modeling of moist air and suspended water/ice particles at frequencies below 1000 GHz'. In: *Proceedings of the AGARD 52nd Specialists Meeting of the Electromagnetic Wave Propagation Panel, Palma de Mallorca, Spain*. AGARD, pp. 3.1–3.10.

LIEBE, H. J. (1985). 'An updated model for millimeter wave propagation in moist air'. In: *Radio Science* 20 (5), pp. 1069–1089. DOI: 10.1029/RS020i005p01069.

— (1989). 'MPM - An atmospheric millimeter-wave propagation model'. In: *International Journal of Infrared and Millimeter Waves* 10 (6), pp. 631–650. ISSN: 0195-9271. DOI: 10.1007/BF01009565.

LYARD, F., F. LEFEVRE, T. LETELLIER and O. FRANCIS (2006). 'Modelling the global ocean tides: modern insights from FES2004'. In: *Ocean Dynamics* 56 (5-6), pp. 394–415. ISSN: 1616-7228. DOI: 10.1007/s10236-006-0086-x.

MACMILLAN, D. S. (1995). 'Atmospheric gradients from very long baseline interferometry observations'. In: *Geophysical Research Letters* 22.9, pp. 1041–1044. ISSN: 1944-8007. DOI: 10.1029/95GL00887.

MARINI, J. W. (1972). 'Correction of satellite tracking data for an arbitrary tropospheric profile'. In: *Radio Science* 7.2, pp. 223–231. ISSN: 1944-799X. DOI: 10.1029/RS007i002p00223.

MATHEWS, P. M., T. A. HERRING and B. A. BUFFETT (2002). 'Modeling of nutation and precession: New nutation series for nonrigid Earth and insights into the Earth's interior'. In: *Journal of Geophysical Research: Solid Earth* 107.B4, ETG 3-1–ETG 3-26. ISSN: 2156-2202. DOI: 10.1029/2001JB000390.

MENDES, V. B. (1999). 'Modeling the neutral-atmospheric propagation delay in radiometric space techniques'. Technical Report No. 199. Ph.D. dissertation. Department of Geodesy and Geomatics Engineering, University of New Brunswick, Fredericton, New Brunswick, Canada. 353 pp.

MENDES, V. B. and R. B. LANGLEY (1998). 'Tropospheric Zenith Delay Prediction Accuracy for Airborne GPS High-Precision Positioning'. In: *Proceedings of the 54th Annual Meeting of The Institute of Navigation*. Denver, Colorado, USA, pp. 337–347.

NAFISI, V., M. MADZAK, J. BÖHM, A. A. ARDALAN and H. SCHUH (2012a). 'Ray-traced tropospheric delays in VLBI analysis'. In: *Radio Science* 47 (R2020). ISSN: 00486604. DOI: 10.1029/2011RS004918.

NAFISI, V., L. URQUHART, M. C. SANTOS, F. G. NIEVINSKI, J. BÖHM, D. D. WIJAYA, H. SCHUH, A. A. ARDALAN, T. HOBIGER, R. ICHIKAWA, F. ZUS, J. WICKERT and P. GEGOUT (2012b). 'Comparison of ray-tracing packages for troposphere delays'. In: *IEEE Transactions on Geoscience and Remote Sensing* 50.2, pp. 469–481. ISSN: 01962892. DOI: 10.1109/TGRS.2011.2160952.

NIELL, A. E. (1996). 'Global mapping functions for the atmosphere delay at radio wavelengths'. In: *Journal of Geophysical Research: Solid Earth* 101.B2, pp. 3227–3246. ISSN: 2156-2202. DOI: 10.1029/95JB03048.

NIELL, A. E. (2001). 'Preliminary Evaluation of Atmospheric Mapping Functions Based on Numerical Weather Models'. In: *Physics and Chemistry of the Earth, Part A: Solid Earth and Geodesy* 26.6-8. Proceedings of the First COST Action 716 Workshop Towards Operational GPS Meteorology and the Second Network Workshop of the International GPS Service (IGS), pp. 475–480. ISSN: 1464-1895. DOI: 10.1016/S1464-1895(01)00087-4.

NIEVINSKI, F. G. (2009). 'Ray-tracing Options to Mitigate the Neutral Atmosphere Delay in GPS'. Technical Report No. 262. M.Sc.E. thesis. Department of Geodesy and Geomatics Engineering, University of New Brunswick, Fredericton, New Brunswick, Canada. 232 pp.

NILSSON, T., J. BÖHM, D. D. WIJAYA, A. TRESCH, V. NAFISI and H. SCHUH (2013). 'Path Delays in the Neutral Atmosphere'. In: *Atmospheric Effects in Space Geodesy*. Ed. by J. BÖHM and H. SCHUH. Springer Atmospheric Sciences. Springer-Verlag Berlin Heidelberg, pp. 73–136. ISBN: 978-3-642-36931-5. DOI: 10.1007/978-3-642-36932-2_3.

NOTHNAGEL, A. (2009). 'Conventions on thermal expansion modelling of radio telescopes for geodetic and astrometric VLBI'. In: *Journal of Geodesy* 83 (8), pp. 787–792. ISSN: 1432-1394. DOI: 10.1007/s00190-008-0284-z.

NOTHNAGEL, A. and J. RAY (2011). *VLBI position discontinuities*. URL: http://lupus.gsfc.nasa.gov/files_IVS-AC/discontinuities.txt (visited on 02/05/2016).

NOTHNAGEL, A., M. VENNEBUSCH and J. CAMPBELL (2002). 'On Correlations Between Parameters in Geodetic VLBI Data Analysis'. In: *IVS 2002 General Meeting Proceeedings*. Ed. by N. R. VANDENBERG and K. D. BAVER, pp. 260–264.

OWENS, J. C. (1967). 'Optical Refractive Index of Air: Dependence on Pressure, Temperature and Composition'. In: *Applied Optics* 6 (1), pp. 51–59. DOI: 10.1364/AO.6.000051.

PAVLIS, N. K., S. A. HOLMES, S. C. KENYON and J. K. FACTOR (2012). 'The development and evaluation of the Earth Gravitational Model 2008 (EGM2008)'. In: *Journal of Geophysical Research: Solid Earth* 117 (B04406). ISSN: 2156-2202. DOI: 10.1029/2011JB008916.

PETIT, G. and B. LUZUM, eds. (2010). *IERS Conventions (2010)*. IERS Technical Note No. 36. Frankfurt am Main: Verlag des Bundesamts für Kartographie und Geodäsie. 179 pp. ISBN: 3-89888-989-6.

PETRACHENKO, B., A. NIELL, D. BEHREND, B. COREY, J. BÖHM, P. CHARLOT, A. COLLIOUD, J. GIPSON, R. HAAS, T. HOBIGER, Y. KOYAMA, D. MACMILLAN, Z. MALKIN, T. NILSSON, A. PANY, G. TUCCARI, A. WHITNEY and J. WRESNIK (2009). *Design Aspects of the VLBI2010 System. Progress Report of the IVS VLBI2010 Committee*. NASA/TM-2009-214180. 62 pp.

RISHBETH, H. and O. K. GARRIOTT (1969). *Introduction to Ionospheric Physics*. Academic Press, New York.

ROCKEN, C., S. SOKOLOVSKIY, J. M. JOHNSON and D. HUNT (2001). 'Improved Mapping of Tropospheric Delays'. In: *Journal of Atmospheric and Oceanic Technology* 18 (7), pp. 1205–1213. DOI: 10.1175/1520-0426(2001)018<1205:IMOTD>2.0.CO;2.

ROEDEL, W. and T. WAGNER (2011). 'Die vertikale Struktur der Atmosphäre'. In: *Physik unserer Umwelt: Die Atmosphäre*. Springer-Verlag Berlin Heidelberg. Chap. 2, pp. 65–97. ISBN: 978-3-642-15728-8. DOI: 10.1007/978-3-642-15729-5_2.

ROGERS, A. E. E. (1975). *A Receiver Phase and Group Delay Calibrator for Use in Very Long Baseline Interferometry*. Tech. rep. Version Haystack Observatory Technical Note. Haystack Observatory, Westford, MA.

ROGERS, A. E. E. (1970). 'Very Long Baseline Interferometry with Large Effective Bandwidth for Phase-Delay Measurements'. In: *Radio Science* 5.10, pp. 1239–1247. ISSN: 1944-799X. DOI: 10.1029/RS005i010p01239.

ROSETTA CODE (2014a). *Sorting algorithms/Merge sort*. Rosetta Code. URL: http://rosettacode.org/wiki/Sorting_algorithms/Merge_sort (visited on 12/11/2014).

— (2014b). *Sorting algorithms/Quicksort*. Rosetta Code. URL: http://rosettacode.org/wiki/Sorting_algorithms/Quicksort (visited on 06/11/2014).

— (2014c). *String case*. Rosetta Code. URL: http://rosettacode.org/wiki/String_case (visited on 11/11/2014).

ROTHACHER, M., T. A. SPRINGER, S. SCHAER and G. BEUTLER (1998). 'Processing Strategies for Regional GPS Networks'. In: *Advances in Positioning and Reference Frames. IAG Scientific Assembly Rio de Janeiro, Brazil, September 3-9, 1997*. Ed. by F. K. BRUNNER. Vol. 118. International Association of Geodesy Symposia. Springer-Verlag Berlin Heidelberg, pp. 93–100. ISBN: 978-3-642-08425-6. DOI: 10.1007/978-3-662-03714-0_14.

RÜEGER, J. M. (2002a). 'Refractive Index Formulae for Radio Waves'. In: *Proceedings of the FIG XXII International Congress*. FIG. Washington, D.C., USA.

— (2002b). *Refractive Indices of Light, Infrared and Radio Waves in the Atmosphere*. UNISURV Report S-68. School of Surveying and Spatial Information Systems, The University of New South Wales, Australia. 92 pp.

SAASTAMOINEN, J. (1972). 'Atmospheric Correction for the Troposphere and Stratosphere in Radio Ranging of Satellites'. In: *The Use of Artificial Satellites for Geodesy*. Ed. by S. W. HENRIKSEN, A. MANCINI and B. H. CHOVITZ. Vol. 15. Geophysical Monograph Series. American Geophysical Union, Washington, D.C., pp. 247–251. ISBN: 9780875900155. DOI: 10.1029/GM015p0247.

SALSTEIN, D. (2013). Foreword. In: *Atmospheric Effects in Space Geodesy*. Ed. by J. BÖHM and H. SCHUH. Springer Atmospheric Sciences. Springer-Verlag Berlin Heidelberg, pp. vii–ix. ISBN: 978-3-642-36931-5. DOI: 10.1007/978-3-642-36932-2.

SCHELLENG, J. C., C. R. BURROWS and E. B. FERRELL (1933). 'Ultra-Short-Wave Propagation'. In: *Proceedings of the Institute of Radio Engineers* 21.3, pp. 427–463. ISSN: 0731-5996. DOI: 10.1109/JRPROC.1933.227639.

SCHUH, H. (1987). *Die Radiointerferometrie auf langen Basen zur Bestimmung von Punktverschiebungen und Erdrotationsparametern*. DGK Reihe C, Nr. 328. Verlag der Bayerischen Akademie der Wissenschaften, München.

— (2000). 'Geodetic Analysis Overview'. In: *International VLBI Service for Geodesy and Astrometry 2000 General Meeting Proceedings*. Ed. by N. R. VANDENBERG and K. D. BAVER. NASA/CP-2000-209893, pp. 219–229.

SCHUH, H. and J. BÖHM (2013). 'Very Long Baseline Interferometry for Geodesy and Astrometry. Innovations and Future Developments'. In: *Sciences of Geodesy - II*. Ed. by G. XU. Springer-Verlag Berlin Heidelberg. Chap. 7, pp. 339–376. ISBN: 978-3-642-27999-7. DOI: 10.1007/978-3-642-28000-9_7.

SCHULKIN, M. (1952). 'Average Radio-Ray Refraction in the Lower Atmosphere'. In: *Proceedings of the IRE* 40 (5), pp. 554–561. ISSN: 0096-8390. DOI: 10.1109/JRPROC.1952.273820.

SMITH, E. K. and S. WEINTRAUB (1953). 'The Constants in the Equation for Atmospheric Refractive Index at Radio Frequencies'. In: *Proceedings of the IRE* 41 (8), pp. 1035–1037. ISSN: 0096-8390. DOI: 10.1109/JRPROC.1953.274297.

SOLHEIM, F. S., J. VIVEKANANDAN, R. H. WARE and C. ROCKEN (1999). 'Propagation delays induced in GPS signals by dry air, water vapor, hydrometeors, and other particulates'. In: *Journal of Geophysical Research: Atmospheres* 104.D8, pp. 9663–9670. ISSN: 2156-2202. DOI: 10.1029/1999JD900095.

SOVERS, O. J., J. L. FANSELOW and C. S. JACOBS (1998). 'Astrometry and geodesy with radio interferometry: experiments, models, results'. In: *Reviews of Modern Physics* 70.4, pp. 1393–1454. DOI: 10.1103/RevModPhys.70.1393.

TANIR, E., V. TORNATORE and K. TEKE (2009). 'Analyses on the Time Series of the Radio Telescope Coordinates of the IVS-R1 and -R4 Sessions'. In: *Proceedings of the 19th European VLBI for Geodesy and Astrometry Working Meeting*. (24th–25th Mar. 2009). Ed. by G. BOURDA, P. CHARLOT and A. COLLIOUD. Bordeaux, France: Université Bordeaux 1 - CNRS - Laboratoire d'Astrophysique de Bordeaux, pp. 122–126.

THAYER, G. D. (1967). 'A Rapid and Accurate Ray Tracing Algorithm for a Horizontally Stratified Atmosphere'. In: *Radio Science* 1 (2), pp. 249–252.

TORGE, W. and J. MÜLLER (2012). *Geodesy*. 4th ed. De Gruyter Textbook Graduate. De Gruyter Berlin/Boston. 433 pp. ISBN: 978-3-11-020718-7.

VAUGHAN, W. W. (2003). *Standard Atmosphere*. In: *Encyclopedia of Atmospheric Sciences*. Ed. by J. R. HOLTON. Oxford Academic Press, pp. 2107–2113. ISBN: 978-0-12-227090-1. DOI: 10.1016/B0-12-227090-8/00379-1.

WALLACE, J. M. and P. V. HOBBS (2006). 'Atmospheric Thermodynamics'. In: *Atmospheric Science. An Introductory Survey*. 2nd ed. Academic Press. Chap. 3, pp. 63–111. ISBN: 978-0-12-732951-2. DOI: 10.1016/B978-0-12-732951-2.50008-9.

WHEELON, A. D. (2001). *Geometrical Optics*. Vol. 1: *Electromagnetic Scintillation*. Cambridge University Press. ISBN: 9780521801980.

WHITNEY, A., C. BEAUDOIN, S. DOELEMAN, A. HINTON, A. NIELL and A. ROGERS (2009). 'Wide-Band VLBI Digital Backend Systems'. Fifth IVS Technical Operations Workshop, April 27-30, 2009, Haystack Observatory, Westford, Massachusetts, USA. Lecture notes.

WIJAYA, D. D., J. BÖHM, M. KARBON, H. KRÀSNÀ and H. SCHUH (2013). 'Atmospheric Pressure Loading'. In: *Atmospheric Effects in Space Geodesy*. Ed. by J. BÖHM and H. SCHUH. Springer Atmospheric Sciences. Springer-Verlag Berlin Heidelberg, pp. 137–157. ISBN: 978-3-642-36931-5. DOI: 10.1007/978-3-642-36932-2_4.

WIKIMEDIA COMMONS (2015). *Atmosphere with Ionosphere*. Wikimedia Commons. URL: https://commons.wikimedia.org/wiki/File:Atmosphere_with_Ionosphere.svg (visited on 22/10/2015).

WIKIPEDIA (2016). *Weighted arithmetic mean*. Wikimedia Foundation, Inc. URL: https://en.wikipedia.org/wiki/Weighted_arithmetic_mean (visited on 02/05/2016).

Curriculum vitae

Personal details

Name:	Dipl.-Ing. Armin Hofmeister BSc
Date of birth:	September 25, 1987
Place of birth:	Vienna, Austria
Nationality:	Austria

University and education

since 03/2013	Doctoral programme in Engineering Sciences Surveying and Geoinformation, Technische Universiät Wien.
04/2011 – 03/2013	Master programme Geodesy and Geophysics, Technische Universiät Wien. Graduated with distinction, granted degree: Dipl.-Ing. (equivalent to MSc). Thesis title: "Bestimmung von himmelsfesten Referenzrahmen mit VLBI" ("Determination of celestial reference frames with VLBI").
10/2007 – 03/2011	Bachelor programme Geodesy and Geomatics Engineering, Technische Universiät Wien. Graduated with distinction, granted degree: BSc. Thesis title: "Wiederholbarkeit von Basislinienlängen in der VLBI" ("Baseline length repeatability in VLBI").
08/2006 – 02/2007	Compulsory military service in the Austrian Federal Armed Forces.
09/1998 – 06/2006	Bundesrealgymnasium (grammar school) in Perchtoldsdorf, Austria. Reifeprüfung (school-leaving examination) passed with distinction.

Employment record

since 05/2013	Project Assistant at the research group Advanced Geodesy at the Department of Geodesy and Geoinformation, Faculty of Mathematics and Geoinformation, Technische Universiät Wien. Employed as scientific research assistant in the Austrian Science Fund (FWF) project "Ray-traced Delays in der Atmosphäre für geodätische VLBI" (RADIATE VLBI) (P25320)

GEOWISSENSCHAFTLICHE MITTEILUNGEN

Bisher erschienen:

Heft 1 Kolloquium der Assistenten der Studienrichtung Vermessungswesen. 1970 - 1973, Dezember 1973.

Heft 2 EGGER-PERDICH-PLACH-WAGENSOMMERER, Taschenrechner HP 45 und HP 65, Programme und Anwendungen im Vermessungswesen. 1. Auflage, März 1974, Special Edition in English, Juli 1974, 2. verbesserte Auflage, November 1974.

Heft 3 Kolloquium der Assistenten der Studienrichtung Vermessungswesen 1973 - 1974, September 1974.

Heft 4 EGGER-PALFINGER-PERDICH-PLACH-WAGENSOMMERER, Tektronix-Tischrechner TEK 31, Programmbibliothek für den Einsatz im Vermessungswesen, November 1974.

Heft 5 K. LEDERSTEGER, Die horizontale Isostasie und das isostatische Geoid, Februar 1975.

Heft 6 F. REINHART, Katalog von FK4 Horrebow-Paaren für Breiten von +30 bis +60, Oktober 1975.

Heft 7 Arbeiten aus dem Institut für Höhere Geodäsie, Wien, Dezember 1975.

Heft 8 Veröffentlichungen des Instituts für Photogrammetrie zum XIII. Internationalen Kongreß für Photogrammetrie in Helsinki 1976, Wien, Juli 1976.

Heft 9 W. PILLEWIZER, Felsdarstellung aus Orthophotos, Wien, Juni 1976.

Heft 10 PERDICH-PLACH-WAGENSOMMERER, Der Einsatz des programmierbaren Taschenrechners Texas Instruments SR-52 mit Drucker PC100 in ingenieurgeodätischen Rechentechnik, Wien, Mai 1976.

Heft 11 Kolloquium der Assistenten der Studienrichtung Vermessungswesen 1974 - 1976, November 1976.

Heft 12 Kartographische Vorträge der Geodätischen Informationstage 1976, Wien, Mai 1977.

Heft 13 Veröffentlichung des Instituts für Photogrammetrie anläßlich des 80. Geburtstages von Prof. Dr.h.c. K. Neumaier, Wien, Januar 1978.

Heft 14 L. MOLNAR, Self Checking Analytical Relative Orientation and Strip Formation, Wien, Dezember 1978.

Heft 15 Veröffentlichung des Instituts für Landesvermessung anläßlich des 80. Geburtstages von Prof. Dr. Alois Bavir, Wien, Januar 1979.

Heft 16 Kolloquium der Assistenten der Studienrichtung Vermessungswesen 1976 - 1978, Wien, November 1979.

Heft 17 E. VOZIKIS, Die photographische Differentialumbildung gekrümmter Flächen mit Beispielen aus der Architekturbildmessung, Wien, Dezember 1979.

Heft 18 Veröffentlichung des Instituts für Allgemeine Geodäsie anläßlich des 75. Geburtstages von Prof. Dipl.-Ing. Dr. F. Hauer, Die Höhe des Großglockners, Wien, 1981.

Heft 19 H. KAGER, Bündeltriangulation mit indirekt beobachteten Kreiszentren, Wien, April 1981.

Heft 20 Kartographische Vorträge der Geodätischen Informationstage 1980, Wien, Mai 1982.

Heft 21 Veröffentlichung des Instituts für Kartographie anläßlich des 70. Geburtstages von Prof. Dr. Wolfgang Pillewizer: Glaziologie und Kartographie, Wien, Dezember 1982.

Heft 22 K. TEMPFLI, Genauigkeitsschätzung digitaler Höhenmodelle mittels Spektralanalyse, Wien, Mai 1982.

Heft 23 E. CSAPLOVICS, Interpretation von Farbinfrarotbildern, Wien, November 1982.

Heft 24 J. JANSA, Rektifizierung von Multispektral-Scanneraufnahmen - Entwicklung und Erprobung eines EDV-Programms, Wien, Mai 1983.

Heft 25 Zusammenfassung der Diplomarbeiten, Dissertationen und Habilitationen an den geodätischen Instituten der TU Wien, Wien, November 1984.

Heft 26 T. WUNDERLICH, Die voraussetzungsfreie Bestimmung von Refraktionswinkeln, Wien, August 1985.

Heft 27 G. GERSTBACH (Hrsg.), Geowissenschaftliche/geotechnische Daten in Landinformationssystemen - Bedarf und Möglichkeiten in Österreich, Juni 1986.

Heft 28 K. NOVAK, Orientierung von Amateuraufnahmen ohne Paßpunkte, Wien, August 1986.

Heft 29 Veröffentlichung des Instituts für Landesvermessung und Ingenieurgeodäsie, Abt. Ingenieurgeodäsie, anläßlich des 80. Geburtstages von Prof. Dipl.-Ing. Dr. F. Hauer, Wien, Oktober 1986.

Heft 30 K.-H. ROCH, Über die Bedeutung dynamisch ermittelter Parameter für die Bestimmung von Gesteins- und Gebirgseigenschaften, Wien, Februar 1987.

Heft 31 G. HE, Bildverbesserung mittels digitaler Filterung, Wien, April 1989.

Heft 32 F. SCHLÖGELHOFER, Qualitäts- und Wirtschaftlichkeitsmodelle für die Ingenieurphotogrammetrie, Wien, April 1989.

Heft 33 G. GERSTBACH (Hrsg.), Geowissenschaftliche/geotechnische Daten in Landinformationssystemen - Datenbestände und Datenaustausch in Österreich, Wien, Juni 1989.

Heft 34 F. HOCHSTÖGER, Ein Beitrag zur Anwendung und Visualisierung digitaler Geländemodelle, Wien, Dezember 1989.

Heft 35 R. WEBER, Lokale Schwerefeldmodellierung unter Berücksichtigung spektraler Methoden zur Geländereduktion, Wien, April 1990.

Heft 36 o.Prof. Dr. Hans Schmid zum 70. Geburtstag. Veröffentlichung der Abteilung für Landesvermessung, Wien, Oktober 1990.

Heft 37 G. GERSTBACH, H. P. HÖLLRIEGL und R. WEBER, Geowissenschaftliche Informationsbörse - Eine Nachlese zu GeoLIS II, Wien, Oktober 1990.

Heft 38 R. ECKER, Rastergraphische Visualisierungen mittels digitaler Geländemodelle, Wien, August 1991.

Heft 39 Kartographische Forschungen und Anwendungsorientierte Entwicklungen, herausgegeben von W. Stams und F. Kelnhofer zum 80. Geburtstag von Prof. Dr. W. Pillewizer, Wien, Juli 1991.

Heft 39a W. RIEGER, Hydrologische Anwendungen des digitalen Geländemodelles, Wien, Juli 1992.

Heft 40 K. STEINNOCHER, Methodische Erweiterungen der Landnutzungsklassifikation und Implementierung auf einem Transputernetzwerk, Wien, Juli 1994.

Heft 41 G. FORKERT, Die Lösung photogrammetrischer Orientierungs- und Rekonstruktionsaufgaben mittels allgemeiner kurvenförmiger Elemente, Wien, Juli 1994.

Heft 42 M. SCHÖNER, W. SCHÖNER, Photogrammetrische und glaziologische Untersuchungen am Gàsbre (Ergebnisse der Spitzbergenexpedition 1991), Wien, Mai 1996.

Heft 43 M. ROIC. Erfassung von nicht signalisierten 3D-Strukturen mit Videotheodoliten, Wien, April 1996.

Heft 44 G. RETSCHER, 3D-Gleiserfassung mit einem Multisensorsystem und linearen Filterverfahren, Wien, April 1996.

Heft 45 W. DAXINGER, Astrogravimetrische Geoidbestimmung für Ingenieurprojekte, Wien, Juli 1996.

Heft 46 M. PLONER, CCD-Astrometrie von Objekten des geostationären Ringes, Wien, November 1996.

Heft 47 Zum Gedenken an Karl Killian "Ingenieur" und "Geodät" 1903-1991, Veröffentlichung der Fachgruppe Geowissenschaften, Wien, Februar 1997.

Heft 48 A. SINDHUBER, Ergänzung und Fortführung eines digitalen Landschaftsmodelles mit multispektralen und hochauflösenden Fernerkundungsaufnahmen, Wien, Mai 1998.

Heft 49 W. WAGNER, Soil Moisture Retrieval from ERS Scatterometer Data, Wien, Dezember 1998.

Heft 50 R. WEBER, E. FRAGNER (Editoren),Prof. Bretterbauer, Festschrift zum 70. Geburtstag, Wien, Juli 1999.

Heft 51 Ch. ÖHRENEDER, A Similarity Measure for Global Image Matching Based on The Forward Modeling Principle, Wien, April 1999.

Heft 52 M. LECHTHALER, G. GARTNER, Per Aspera ad Astra, Festschrift für Fritz Kelnhofer zum 60. Geburtstag, Wien, Jänner 2000.

Heft 53 F. KELNHOFER, M. LECHTHALER, Interaktive Karten (Atlanten) und Multimedia – Applikationen, Wien, März 2000.

Heft 54 A. MISCHKE, Entwicklung eines Videotheodlit-Meßsystems zur automatischen Richtungsmessung von nicht signalisierten Objektpunkten, Wien, Mai 2000.

Heft 55 Veröffentlichung des I.P.F. anlässlich der Emeritierung von Prof. Dr. Peter Waldhäusl, Wien.

Heft 56 F. ROTTENSTEINER, Semi-automatic Extraction of Buildings Based on Hybrid Adjustment Using 3D Surface Models and Management of Building Data in a TIS, Wien, Juni 2001.

Heft 57 D. LEGENSTEIN, Objektrekonstruktion aus perspektiven Bildern unter Einbeziehung von Umrisslinien, Wien, Mai 2001.

Heft 58 F. KELNHOFER, M. LECHTHALER und K. BRUNNER (Hrsg.), Telekartographie und Location Based Services, Wien, Jänner 2002.

Heft 59 K. BRETTERBAUER, Die runde Erde eben dargestellt: Abbildungslehre und sphärische Kartennetzentwürfe, Wien, 2002.

Heft 60 G. GARTNER, Maps and the Internet 2002, Wien 2002.

Heft 61 L. DORFFNER, Erzeugung von qualitativ hochwertigen 3D Photomodellen für Internetbasierte Anwendungen mit besonderem Augenmerk auf Objekte der Nahbereichsphotogrammetrie, Wien, Jänner 2002.

Heft 62 K. CHMELINA, Wissensbasierte Analyse von Verschiebungsdaten im Tunnelbau, Wien 2002.

Heft 63 A. NIESSNER, Qualitative Deformationsanalase unter Ausnutzung der Farbinformation, Wien 2002.

Heft 64 K. BRETTERBAUER, R. WEBER, A Primer of Geodesy for GIS-Users, Wien 2003.

Heft 65 N. PFEIFER, 3D Terrain Models on the basis of a triangulation, Wien, Jänner 2002.

Heft 66 G. GARTNER (Hrsg), Lacation Based Services & Telecartography, Wien 2004.

Heft 67 I. KABASHI, Gleichzeitig-gegenseitige Zenitwinkelmessung über größere Entfernungen mit automatischen Zielsystemen, Wien 2004.

Heft 68 J. BÖHM, Troposphärische Laufzeitverzögerungen in der VLBI, Wien 2004.

Heft 69 R. WEBER, W. SCHLÜTER, U. SCHREIBER, O. TITOV Evolving Space Geodesy Techniques (EGS XXVII General Assembly, Nice, France, 2002), Wien 2004.

Heft 70 G. WEINWURM, Amalthea's Gravity Field and its Impact on a Spacecraft Trajectory, Wien 2004.

Heft 71 Forschungsgruppe Ingenieurgeodäsie, Festschrift anlässlich des 65. Geburtstages von Herrn o.Univ. Prof. Dr.-Ing. Heribert Kahmen, Wien 2005.

Heft 72 A. REITERER, A Knowledge-Based Decision System for an On-Line Video-Theodolite-Based Multisensor System, Wien 2005.

Heft 73 M. HABERLER, Einsatz von Fuzzy Methoden zur Detektion konsistenter Punktbewegungen, Wien 2005.

Heft 74 G. GARTNER, Location Based Services & Telecartography, Proceedings of the Symposium 2005, Wien 2005.

Heft 75 Th. HOBIGER, VLBI as a tool to probe the ionosphere, Wien 2006.

Heft 76 E. KLAFFENBÖCK, Troposphärische Laufzeitverzögerung von GNSS-Signalen – Nutzen aktiver Referenzstationsnetze für die Meteorologie, Wien 2006.

Heft 76a P. J. MENDES-CERVEIRA, Tidal and non-tidal contributions to surface loading processes on station coordinates, Wien 2006.

Heft 78 G. KOSTOV, G. BOURDA, L. FERNANDEZ, T. KONDO, Research Projects at IGG Reports, Wien 2007.

Heft 79 J. BÖHM, A. PANY, H. SCHUH (Editors), Proceedings of the 18th European VLBI for Geodesy and Astrometry Working Meeting, 12-13 April 2007, Wien 2007.

Heft 80 J. BÖHM, Tropospheric Delay Modelling at Radio Wavelengths for Space Geodetic Techniques, Wien 2007.

Heft 81 G. Retscher, Mobile Multi-sensor Systems for Personal Navigation and Location-based Services, Wien 2007.

Heft 82 R. HEINKELMANN, Bestimmung des atmosphärischen Wasserdampfes mittels VLBI als Beitrag zur Klimaforschung, Wien 2008.

Heft 83 F. ROTTENSTEINER, Automatic extraction of buildings from airborne laserscanner data and aerial images, Wien 2008.

Heft 84 S. TODOROVA, Kombination geodätischer Weltraumverfahren für globale Karten der Ionosphäre, Wien 2009.

Heft 85 J. WRESNIK, Simulationen für die neue Generation von VLBI-Systemen, Wien 2009.

Heft 86 A. KARABATIC, Precise Point Positioning (PPP). An alternative technique for ground based GNSS troposphere monitoring, Wien 2011.

Heft 87 K. TEKE, Sub-daily Parameter Estimation in VLBI Data Analysis, Wien 2011.

Heft 88 G. THALER, Echtzeit Bahn- und Uhrberechnung der GPS-Satellitenkonstellation basierend auf Beobachtungsdaten des RTIGS-Stationsnetzwerkes, Wien.

Heft 89 P. SWATSCHINA, Dynamic and Reduced-Dynamic Precise Orbit Determination of Satellites in Low Earth Orbits, Wien 2012.

Heft 90 S. BÖHM, Tidal excitation of Earth rotation observed by VLBI and GNSS, Wien 2012.

Heft 91 H. KRÁSNÁ, Estimation of solid Earth tidal parameters and FCN with VLBI, Wien 2013.

Heft 92 J. SUN, VLBI scheduling strategies with respect to VLBI2010, Wien 2013.

Heft 93 M.M. ALIZADEH ELIZEI, Multi-Dimensional modeling of the ionospheric parameters, using space geodetic techniques, Wien 2013.

Heft 94 M. KARBON, Atmospheric effects on measurements of the Earth gravity field, Wien 2013.

Heft 95 L. PLANK, VLBI satellite tracking for the realization of frame ties, Wien 2014.

Heft 96 M. SCHINDELEGGER, Atmosphere-induced short period variations of Earth rotation, Wien 2014.

Heft 97 M. MADZAK, Short period ocean tidal variations in Earth rotation, Wien 2016.

Heft 98 A. HOFMEISTER, Determination of path delays in the atmosphere for geodetic VLBI by means of ray-tracing, Wien 2016.